

NORTHWESTERN UNIVERSITY

Expanding Functionalities in Heteroanionic Materials Through First-Principles Design

A DISSERTATION

SUBMITTED TO THE GRADUATE SCHOOL
IN PARTIAL FULFILLMENT OF THE REQUIREMENTS

for the degree

DOCTOR OF PHILOSOPHY

Field of Materials Science and Engineering

by

Jaye Kimiko Harada

EVANSTON, ILLINOIS

June 2021

Abstract

Advancements in the understanding and synthesis of transition metal compounds have allowed materials engineers to design functional materials with a range of properties, such as ferroelectricity, non-linear optical activity, colossal magnetoresistance, and superconductivity. Conventional routes to tune and design functional materials includes chemical cation substitution and heterostructuring of oxide thin films. Anion engineering has recently been identified as another route to design materials with targeted properties by coordinating anions of different size, charge, and electronegativity to the same transition metal cation. Because of the similar sizes of fluorine and nitrogen to oxygen, anion substitutions also adds additional design variables, such as anion order, that are absent in homoanionic (i.e. oxide) compounds. Heteroanionic materials design provides an opportunity to expand the chemical design space for functional materials and to realize enhanced or unanticipated electronic, optical, and magnetic phenomena through its complex structural space. However, an understanding of the crystal-chemistry principles that govern the structure and properties of heteroanionic materials are still in their infancy.

In this dissertation, I utilize first principles calculations to explore the materials physics associated with anion engineering in oxyfluorides. Oxyfluorides are an intriguing class of heteroanionic materials due to their similarity to transition metal oxides and potential structural complexity from anion ordering. This work 1) adapts crystal-chemistry principles from homoanionic materials to heteroanionic materials and uses them to predict novel oxyfluorides, 2) investigates known mechanisms for ferroelectricity in bulk and thin film oxyfluorides and formulates new ones and,

3) evaluates the effect of anion (dis)order on the electronic states of oxyfluorides. My research advances our understanding of oxide-fluoride structures and their properties, motivating future experimental and materials design efforts on heteroanionic materials.

Acknowledgements

I would first and foremost like to thank my research advisors James Rondinelli and Kenneth Poeppelmeier for their support and guidance during my graduate studies. Both have been excellent mentors and have shown me that great professors invest in both the personal and professional development of their students. They have helped me become a better scientist, communicator, and mentor through their advice, encouragement, and accommodation.

Next, I would like to recognize the members of the Materials Theory and Design group for their friendship and fruitful (scientific and otherwise) discussions over the years. Nenan Charles was a wonderful mentor and friend to me in my first years in the group, teaching me DFT and everything he knew about heteroanionic materials. Danilo Puggioni was another invaluable mentor throughout my time in the group, I learned much about physics in our discussions and always had a good time doing so. Richard Saballos became an excellent friend and colleague over the years, I will miss our chats about life and oxyfluorides. I would also like to thank Mingqiang (Kurt) Gu, Liang-Feng Huang, Michael Waters, Alex Georgescu, Joshua Young, Nick Wagner, Xuezheng Lu, Emrys Tennessen, Yongjin Shin, Nathan Koocher, Daniel Hickox-Young, Yiqun (Raymond) Wang, Lauren Walters, Kathleen Mullin, Kyle Miller, and Sean Koyama for their companionship and conversations over the years. Likewise, I would like to thank the members of the Poeppelmeier group, who were always happy to answer my questions and help me get around lab. Allison Wustrow and Steven Flynn helped me tremendously in getting started in lab and with the synthesis projects I pursued. I would also like to thank Michael Yeung, Kent Griffith, Karl Rickert, Michael Holland, Jared Inorvati, James McCarthy, Jackie Cantwell, Ryan Paull, Fenghua Ding, Justin Hancock, Matt Nisbet, Yiran (Ella) Wang, Chi Zhang, Emily Greenstein.

I would also like to thank my previous research advisor, Ram Seshadri, who inspired me to pursue computational solid state materials research. Without his patience, mentorship, and support, I likely would not have pursued graduate school.

I am eternally grateful to my parents, John and Susan, and my siblings, Bryan and Mac, for their love and support throughout my life. I would also like to thank my partner, Max Garber, for his love, support, and understanding over the years. I am also thankful to all my family and friends for their humor, encouragement, and companionship over the course of my graduate studies.

This work was enabled by numerous financial supporters and high performance computing (HPC) resources. Funding was provided by the National Science Foundation through grants DMR-1454688, DMR-2011208, and the MRSEC program, DMR-1720139, through the Materials Research Center of Northwestern University. I was also supported by the Association for Computing Machinery's SIGHPC/Intel Computational and Data Science Fellowship. Computational resources were provided by Northwestern University through the Quest high performance computing facility which is jointly supported by the Office of the Provost, the Office for Research, and Northwestern University Information Technology; the Extreme Science and Engineering Discovery Environment (XSEDE), which is supported by National Science Foundation grant number ACI-1548562; and the Center for Nanoscale Materials (Carbon cluster), an Office of Science user facility, was supported by the U.S. Department of Energy, Office of Science, Office of Basic Energy Sciences, under Contract No. DE-AC02-06CH11357.

Contents

Abstract	3
Acknowledgements	5
List of Figures	10
List of Tables	18
1 Introduction	20
1.1 Motivation	20
1.2 Organization	22
2 First Principles Electronic Structure Methods	25
2.1 The Many-Body Schrödinger Equation	25
2.2 Density Functional Theory	27
2.2.1 The Hohenberg-Kohn Theorem	27
2.2.2 The Kohn-Sham Equations	30
2.2.3 Exchange-Correlation Functionals	32
2.3 Practical Aspects of Density Functional Theory	35
2.3.1 Plane Wave Basis Set	35
2.3.2 Brillouin Zone Sampling	37
2.3.3 Pseudopotentials	37
3 Heteroanionic Materials Design	39
3.1 Atomic Structure Considerations with Anion Engineering	39
3.1.1 Nonidealities	45
3.1.1.1 Polar Displacements	45
3.1.1.2 Octahedral Tilts	46
3.2 Electronic Structure Changes	47
3.3 Bulk and Thin Film Synthetic Methods	56
3.4 Description and Characterization of the Anion Sublattice	59
3.5 Functional Properties of Oxyfluoride Materials	64

3.5.1	Electronic and Magnetic Transitions	64
3.5.2	Acentric Functionalities	68
3.5.3	Phosphors for Solid State Lighting	72
3.5.4	Battery Materials	73
4	Predicting the Structure Stability of Layered Heteroanionic Materials Exhibiting Anion Order	76
4.1	Introduction	76
4.2	Methods	79
4.2.1	Group Theoretical Methods	79
4.2.2	GII Optimizations	80
4.2.3	Density Functional Theory Calculations	83
4.3	Results and Discussion	84
4.3.1	Group Theoretical Analysis	84
4.3.1.1	Polar and Antipolar Distortions	86
4.3.1.2	Rotations and Tilts	89
4.3.2	Stability Assessment with GII	92
4.3.3	DFT Assessment of GII Performance	96
4.3.4	Thermodynamic Assessment and Synthetic Attempts	101
4.4	Conclusion	103
5	Phase Transitions and Potential Ferroelectricity in Noncentrosymmetric KNaNbOF_5	105
5.1	Introduction	105
5.2	Methods	108
5.2.1	Computational Details	108
5.2.2	Synthesis of KNaNbOF_5	109
5.2.3	Experimental Details	110
5.3	Results and Discussion	111
5.3.1	Symmetry Analysis and Energetics	111
5.3.2	Approximate <i>Ab Initio</i> Phase Diagram	115
5.3.3	In-situ Characterization of the Transition	118
5.3.4	Intermediate Phase Verification	121
5.3.5	Electric Polarization	124
5.3.6	Potential Ferroelectric Switching Path	127
5.4	Conclusion	128
6	Heteroanionic Ruddlesden-Popper Ferroelectrics From Anion Order and Octahedral Tilts	130
6.1	Introduction	130
6.2	Methods	134
6.3	Results and Discussion	135
6.3.1	Improper Anion-Ordered Ferroelectricity	135
6.3.1.1	Symmetry Analysis	135

6.3.1.2	Energetic Stability Analysis	139
6.3.2	Energetic Contributions Stabilizing Octahedral Tilts with Differing Anion Orders	141
6.3.3	Polar Displacements Stabilize Octahedral Tilts	145
6.4	Conclusion	153
7	Exploring the Phase Space of Epitaxially Strained $n = 2$ Ruddlesden-Popper Oxyfluorides	155
7.1	Introduction	155
7.2	Methods	157
7.3	Results	158
7.3.1	$\text{Ba}_3\text{In}_2\text{O}_5\text{F}_2$	158
7.3.2	$\text{Sr}_3\text{In}_2\text{O}_5\text{F}_2$	161
7.4	Discussion	166
8	Investigating Insulator-Metal Transitions in Anion Disordered and Ordered TiOF	169
8.1	Introduction	169
8.2	Methods	170
8.3	Results and Discussion	172
8.3.1	Modeling Anion Disordered TiOF using a VCA	172
8.3.2	Modeling Anion Ordered TiOF	177
9	Conclusions and Outlook	180
	Bibliography	184
A	Predicting the Structure Stability of Layered Heteroanionic Materials Exhibiting Anion Order	237
B	Phase Transitions and Potential Ferroelectricity in Noncentrosymmetric KNaNbOF_5	241
C	Heteroanionic Ruddlesden-Popper Ferroelectrics From Anion Order and Octahedral Tilts	249
D	Exploring the Phase Space of Epitaxially Strained $n = 2$ Ruddlesden-Popper Oxyfluorides	253
E	Investigating Insulator-Metal Transitions in Anion Disordered and Ordered TiOF	255
	Vita	259

List of Figures

- 3.1 From homoanionic to heteroanionic building units for the assembly of oxide-derived heteroanionic materials: Heteroanionic materials are constructed from building units that exhibit unique local coordination chemistry with multiple anions surrounding a metal center (left) of the same (a, homoleptic) or different (b, heteroleptic) species. Typically, the number of oxide anions (red) govern: (c) the out-of-center metal displacements that may occur toward a face, edge, or corner of the polyhedron, which reduces the local symmetry for the metal d -orbitals, particularly in heteroanionic materials with d^0 electronic configurations. Local symmetry of the building units also depends on the geometric isomerism of the unit, e.g., *cis* or *trans* coordination. Illustration of the structural and chemical diversity in oxide-derived heteroanionic materials (HAMs), including: (d) a subset of those p -block anions, which combine with the oxide ion to form the structurally and chemically diverse oxynitride (e), oxy-sulfide (f), and oxyfluoride (g) materials from heteroleptic polyhedra. (h) BiCuOSe is a heteroanionic material comprised of homoleptic polyhedra, which distinguishes it from the other materials (broken line). The annotated slice of the periodic table in (d) indicates the anion electronegativities based on the Pauling scale, ionic radii for four-fold coordination (S^{2-} based on sixfold coordination), and the bound coherent scattering lengths. In these materials, the exchange of an anion for oxide as in $O^{2-} \rightarrow N^{3-}$ ($O^{2-} \rightarrow F^{1-}$) requires compensation of excess (deficit) charge, which often necessitates that binary heteroanionic oxynitrides are composed of cations with high oxidation states (Ti^{4+} , Zr^{4+} , Ta^{5+} , Nb^{5+} , $Mo^{4+,5+}$, $W^{5+,6+}$) as in TaON. In oxyfluorides, on the other hand, late transition metal cations are compatible with lower oxidation states. 40

- 3.2 Electronic-structure changes due to additional anions within a polyhedral unit used to construct the heteroanionic material: modifications to the transition metal d orbital structure induced by arranging different chemical species on a lattice can alter electronic, magnetic, and optical properties. (a-c) The schematic density-of-states (DOS) for d^0 (a) and d^n compounds exhibiting Mott-insulating (b) or charge-transfer insulating (c) character depict the changes in the cation d orbital and anion p orbital energies and bandwidth, indicated by the arrows in the first row, compared to their oxide analogue. The orange and blue boxes in (c) differentiate positive charge-transfer and negative charge-transfer insulators, respectively. The broken lines in the negative charge-transfer insulator section indicate the splitting of the O $2p$ band to form a gap. The inset in (b) is a modified version of the Zaanen-Sawatzky-Allen diagram, showing the metal-insulator phase boundaries based on values of U and Δ_{CT} . The colored dots represent the qualitative change in Δ_{CT} upon anion exchange into the homoanionic oxide. The inset in (b) is adapted with permission. [1] Copyright 1994, American Physical Society. 49
- 3.3 Crystal field effects in heteroanionic compounds with multiple anions in a single coordination unit: (a) Changes in d orbital degeneracies and energy splitting for a transition metal (M) cation with d^1 electronic configuration in the regular octahedral coordination with no bond distortions, $[MO_xF_{6-x}]$ ($x = 1-6$). (b,c) Calculated crystal field energy, Dq , under tetragonal distortion of the octahedral unit for a *trans*- $[MO_4F_2]$ (b) and *trans*- $[MO_4N_2]$ (c) heteroanionic building unit, where two fluoride or nitride ions, respectively, are located at the apical sites and four oxide ions occupy the equatorial sites as illustrated in the insets of (b) and (c). 54
- 3.4 Electronic and optical property control in heteroanionic oxyfluorides: a) Formation of the molecular orbitals from the high-temperature monoclinic and the low-temperature triclinic phases in $Nb_2O_2F_3$. The $[NbO_3F_3]$ polyhedra shown in the upper right exhibit cooperative distortions with symmetric metal-anion bond stretching in the charge ordered state. b) The transmittance spectra of the deep-ultraviolet nonlinear optical materials β - BaB_2O_4 and $KBe_2BO_3F_2$. The inset shows the $KBe_2BO_3F_2$ crystal grown for these measurements. c) The structure of $KBe_2BO_3F_2$, where the $[BeO_3F]$ tetrahedra link together with a $[BO_3]$ borate network through a shared oxide ion. a) Adapted with permission. [2] Copyright 2016, Elsevier. b,c) Adapted with permission. [3] Copyright 2009, Springer Nature. 65
- 3.5 Heteroanionic oxyfluorides for lighting and energy applications: a) Excitation and emission spectra of the solid-solution phosphor $Sr_{2.975}Ce_{0.025}Al_{1-x}Si_xO_{4+x}F_{1-x}$ with various x values indicated. The $Sr1X_8$ and $Sr2X_{10}$ polyhedra looking down the $[100]$ direction show the change in coordination environment (right inset). Light gray, black, orange, and green spheres represent Sr1, Sr2, O, and F atoms, respectively. Fluoride exchange leads to a decrease in peak excitation/emission wavelength with increase in fluoride content (lower panel). b) Theoretical capacities of Mn-redox based cathode materials with decreasing oxidation state. c) Voltage profiles and capacity retention of $Li_2Mn_{2/3}Nb_{1/3}O_2F$ when cycled from 1.5 to 4.6 V at 20 mA g^{-1} . a) Adapted with permission [4]. Copyright 2011, Wiley. b,c) Adapted with permission [5] Copyright 2018, Springer Nature. 71

4.1	Polar and antipolar structures which have distortions commensurate with the site symmetry breaking of the a , X2 and A sites, which have the same Wyckoff site, and b , the X1 anion site. The structures show the off-centering of the B-site. Below each structure is the irrep, OPD, and space group.	86
4.2	Octahedral rotation patterns of structures with rotational distortions that break the symmetry of the anion sites. A-site cations are omitted and the polyhedra are opaque for clarity. Arrows indicate tilting of the octahedra with the lines and dotted lines representing tilts of the opposite sense.	90
4.3	GII values for A_2BO_3F oxyfluoride structures obtained from the volumetric GII minimization. The GII of a distinct chemistry in the heat map is located at the intersection of a particular A- (column) and B-site (row) cation. Darker colors indicate a smaller GII value and a more stable structure. Structures with GII values greater than 0.6 v.u. are not shown and entries in the heat maps outlined with red indicate that the corresponding compound has been synthesized and is anion disordered with space group $I4/mmm$. Heat maps with only one structure outlined in red, such as Sr_2FeO_3F , are anion ordered with the indicated space group.	93
4.4	GII values for A_2BO_3N oxynitrides with $Cmma$ symmetry obtained from the volumetric GII minimization. The GII of a distinct chemistry in the heat map is located at the intersection of a particular A- (column) and B-site (row) cation. Darker colors indicate a smaller GII value and a more stable structure. Structures with GII values greater than 0.6 v.u. are not shown and entries in the heat maps outlined with red indicate that the corresponding compound has been synthesized and is anion disordered and the average structure has symmetry $I4/mmm$, except Nd_2AlO_3N which has space group $I4mm$	94
4.5	Correlation between the GII and total energies of the d^0 oxyfluorides before (circles) and after (squares) DFT relaxation with $P4/nmm$ symmetry. The movement of the GII minimized structure relative to the DFT relaxed structure is indicated by arrows of the same color. The energy of the structures is given relative to the DFT relaxed value of Sr_2ScO_3F . The horizontal line at 0.3 v.u. indicates our proposed GII cutoff value for synthesizable heteroanionic materials.	96
4.6	Correlation between the GII and total energies of the d^n oxyfluorides before (circles) and after (squares) the DFT relaxation in the $P4/nmm$ symmetry. The movement of the GII minimized structure relative to the DFT relaxed structure is indicated by arrows of the same color. The energy of the structures is relative to the DFT relaxed value of Sr_2FeO_3F . The horizontal line at 0.3 v.u. indicates our proposed GII cutoff value for synthesizable heteroanionic materials.	98
4.7	Correlation between the GII and total energies of the oxynitrides before (circles) and after (squares) DFT relaxations in the $Cmcm$ symmetry. The movement of the GII minimized structures relative to the DFT relaxed structures is indicated by arrows of the same color. The energy of the structures is relative to the DFT relaxed value of Sr_2TaO_3N . The horizontal line at 0.3 v.u. indicates our proposed GII cutoff value for synthesizable heteroanionic materials.	100
5.1	The a $Pna2_1$ (NCS) and b $Cmcm$ (HT) structures of $KNaNbOF_5$	112

- 5.2 Mode decomposition and energetics of KNaNbOF_5 . **a** The irreps associated with each intermediate structure are shown in blue. **b** Energetics of each of the modes associated with this transition. The atomic displacements associated with the unstable modes from force constant eigenvectors are also shown in the atomic structures on the left. Atoms are designated as in Figure 5.1. 113
- 5.3 Approximate phase diagram of the displacive transition in KNaNbOF_5 in which $\alpha_{\Gamma_2^-} = 0.6 \text{ meV \AA}^{-2}$. The red dot at (0,0) corresponds to the position in the phase diagram through which a direct transition between the high temperature ($Cmcm$) and ground state ($Pna2_1$) phases occurs. The red arrow represents a possible path of the phase transition through an intermediate centrosymmetric phase. 116
- 5.4 High-resolution ^{19}F MAS (25 kHz) NMR spectrum of noncentrosymmetric (NCS) sample of KNaNbOF_5 . Calculated ^{19}F NMR chemical shifts of NCS KNaNbOF_5 are also shown for reference. Asterisks (*) denotes spinning side bands. ^{19}F MAS (25 kHz) NMR spectrum of centrosymmetric (CS) KNaNbOF_5 is shown in (Appendix B) for comparison. 118
- 5.5 In situ monitoring (heating process) of the phase transition in KNaNbOF_5 from noncentrosymmetric (NCS) phase ($Pna2_1$) to the high-temperature (HT) phase ($Cmcm$) by variable-temperature ^{19}F MAS (5 kHz) NMR. 120
- 5.6 High-resolution ^{19}F MAS (25 kHz) NMR spectra of NCS phase KNaNbOF_5 quenched (q) at $T_q = 150^\circ\text{C}$, 250°C , 310°C , and 360°C . Asterisks * denote spinning side bands. 122
- 5.7 Structure and properties of the coherent monodomain switching pathway. The top panel shows key structures along the switching pathway, as indicated by the letters. 125
- 6.1 (a) Group-subgroup relationships among anion ordered structures coupled to octahedral tilts. Each anion ordering (second row) is associated with an irrep of the (b) parent phase, $n = 1$ RP with space group $I4/mmm$. The third row couples the anion order to an octahedral tilt, irrep X_3^+ , with the order parameter direction indicated below each space group label. Orange shaded space groups are polar and blue shaded space groups are nonpolar-noncentrosymmetric. Lines connecting space groups indicate that the phase transition is allowed to be continuous in Landau theory. 133
- 6.2 Octahedral tilt patterns and energetics of the derivative structures relative to their anion ordered structures. The octahedral tilt patterns associated with the modes (a) $X_3^+(\eta_1, 0)$ or $(0, \eta_1)$ and (b) $X_3^+(\eta_1, \eta_1)$. The tilts in Glazer notation are noted next to each perovskite layer. (c) The difference in energy ΔE between the relaxed derivative structures relative to their anion ordered structures. The larger the difference, the more the derivative structure is stabilized by the indicated octahedral tilt pattern. The graph is separated into the two compounds, $\text{Sr}_2\text{ScO}_3\text{F}$ and $\text{Ca}_2\text{ScO}_3\text{F}$, then further separated into the induced tilt pattern and anion orders (colors). 138

6.3	Decomposed energetics of $\text{Sr}_2\text{ScO}_3\text{F}$ and $\text{Ca}_2\text{ScO}_3\text{F}$ relative to the undistorted anion ordered structures. The top panel divides the energy stabilization into the primary mode contributions (anion order, Γ_3^- , M_3^- , or X_2^- , and octahedral tilts, X_3^+) and the contribution from the coupling of these primary modes. The bottom panel takes the difference between the lattice energy of the relaxed structures and the unstrained structures with the primary modes shown here. The gain in energy in the bottom panel is from fully symmetric ionic displacements and strain accommodation. . . .	141
6.4	Energetics of (a)-(c) $\text{Sr}_2\text{ScO}_3\text{F}$ and (d)-(f) $\text{Ca}_2\text{ScO}_3\text{F}$ with octahedral tilts in the presence and absence of Sc displacements due to the heteroleptic $[\text{ScO}_5\text{F}]^{8-}$ octahedron. The circles represent the prototypical $I4/mmm$ structure and the squares represent the $I4/mmm$ structure with the Sc displacements from the given composition and anion order. (a) and (d) have polar anion order, (b) and (e) have antipolar interlayer order, and (c) and (f) have antipolar intralayer order.	148
6.5	(a-d) Illustrations of a $[\text{ScO}_5\text{F}]^{8-}$ octahedron showing how local polar displacements and octahedral tilts induce in-plane polar distortions into it. Octahedron without (a) and with (c) local polar displacements along the z axis. Corresponding structures with octahedral tilts are shown without (b) and with (d) polar Sc displacements. (e) and (f) illustrate how an in-plane polar displacement increases the Sc–O _{eq} π -bonding interactions between Sc d_{xz} and O _{eq} p_z orbitals. When Sc^{3+} is in the center of the octahedra (e), the Sc–O bonds are equidistant and thus, the net overlap between the π bonds is zero. When Sc^{3+} displaces along the x direction, the net overlap is non-zero.	150
6.6	Comparison of the energetic stabilization of octahedral tilts from Sc displacements, ΔE , to the increase in our covalency metric, $\Delta(-\text{ICOHP}_{\text{net}})$, from the same displacements. The magnitude of the Sc displacement is listed next to each data point and the marker size is proportional to the square of the magnitude of the Sc displacements.	151
7.1	The (a) atomic structure and corresponding (b) phonon dispersion of the conventional cell of $\text{Ba}_3\text{In}_2\text{O}_5\text{F}_2$	158
7.2	Total energy evolution with epitaxial strain for $\text{Ba}_3\text{In}_2\text{O}_5\text{F}_2$ polymorphs. The dotted lines delineate regions of stability for each polymorph of $\text{Ba}_3\text{In}_2\text{O}_5\text{F}_2$	160
7.3	The phonon dispersions of the primitive cell of $\text{Sr}_3\text{In}_2\text{O}_5\text{F}_2$ with LO/TO splitting.	161
7.4	Atomic structures of the metastable phases, $Cmc2_1$ (a) and $Pnma$ (b), and ground state phase, $P2_1/c$ (c), of $\text{Sr}_3\text{In}_2\text{O}_5\text{F}_2$	162
7.5	(a) Total energy evolution with epitaxial strain for $\text{Sr}_3\text{In}_2\text{O}_5\text{F}_2$ polymorphs. The dotted lines delineate regions of stability for each polymorph of $\text{Sr}_3\text{In}_2\text{O}_5\text{F}_2$. The atomic structures of the $P\bar{1}$ (b) and $P1$ (c) polymorphs of $\text{Sr}_3\text{In}_2\text{O}_5\text{F}_2$	164
7.6	Octahedral tilt (top) and rotation (bottom) angles as a function of strain for $\text{Sr}_3\text{In}_2\text{O}_5\text{F}_2$ polymorphs.	166
8.1	Phonon dispersions of rutile, anion disordered TiOF with the VCA	173

8.2	Atomic and electronic structures of the rutile and monoclinic phases of anion disordered TiOF. Relaxed anion disordered rutile $P4_2/mnm$ (a) and monoclinic $P2_1/c$ (b) structures of TiOF. The corresponding DOS of the rutile (c) and monoclinic (d) phases of TiOF. The gray shaded portion is the total DOS and the Fermi level is at 0 eV.	174
8.3	Density of states of the monoclinic phases of TiOF with varying Hubbard U . The gray shaded portion is the total DOS.	176
8.4	(a) Atomic and (b) electronic structures of the ground state configuration of anion ordered TiOF.	178
A.1	The compound phase diagram from the binary phases, SrO, SrF ₂ , and Al ₂ O ₃ , which are used to create Sr ₂ AlO ₃ F. Green circles indicate that the compound is on the convex hull and red squares are above the hull. SrAl ₄ O ₇ is 0.001 eV per atom above the hull and Sr ₃ AlO ₄ F is 0.172 eV per atom above hull.	240
B.1	Approximate phase diagrams of the transition upon parametrically changing the trilinear coupling coefficients $\gamma_{\Gamma_2^-Y_2^+Y_1^-}$ to be equal to a 15 meV Å ⁻³ , and b 27 meV Å ⁻³ . c Approximate phase diagram using Landau coefficients fit to SCAN energies. The third quadratic coefficient, $K_{\Gamma_2^-}$, is set to 0.6 meV Å ⁻² , as described in the main text.	243
B.2	The a $Pna2_1$, b $Pnma$, c $Pnna$, and d $Cmcm$ structures of KNaNbOF ₅ with symmetrically inequivalent fluoride sites labeled.	244
B.3	Difference in energy (blue, left) and volume (red, right) between the various centrosymmetric phases of KNaNbOF ₅ and the $Pna2_1$ phase.	245
B.4	In situ ¹⁹ F NMR spin-lattice relaxation rate ($R_1 = 1/T_1$) measurements on the NCS to HT phase transition upon heating (0 °C to 450 °C) and the HT to NCS transition upon cooling (450 °C to 0 °C) in KNaNbOF ₅ . The apical F (blue square) experiences negligible motion as revealed by its unaltered ¹⁹ F T_1 throughout the measurements. In line with our previous studies [6], it suggests that the apical F _{5NCS} ion stays as if it is static in the axial rotation about the F _{apical} -Nb-O axis and no dynamic O/F disorder is expected for this fluoride ion. Note that the ¹⁹ F T_1 signals from the equatorial fluoride ions in the NCS phase is not traceable due to the interference of CSA. The jump in the ¹⁹ F T_1 signal (red circles) at ~360 °C till about 390 °C is associated with the the reconstructive phase.	245
B.5	High-resolution ¹⁹ F MAS (25 kHz) NMR spectra of noncentrosymmetric (NCS; bottom) and centrosymmetric (CS; top) KNaNbOF ₅ . The assignment of ¹⁹ F NMR signals of CS KNaNbOF ₅ can be found in literature. [6] Asterisks (*) denotes spinning side bands. Top panel is reproduced with permission from Chien, P.-H. et.al. Chem. Mater., DOI: 10.1021/acs.chemmater.0c01439. Copyright 2020 American Chemical Society.	246

- B.6 In situ monitoring (cooling process) of the phase transition in KNaNbOF_5 from non-centrosymmetric (NCS) phase ($Pna2_1$) to the high-temperature (HT) phase ($Cmcm$) by variable-temperature ^{19}F MAS (5 kHz) NMR. Note that the ^{19}F resonance at -143.2 ppm is not identified at 358.8°C (cf. Fig. 2). The removal of this ^{19}F chemical shift during the cooling process indicates that the reconstructive phase transition from $P4/nmm$ to $Cmcm$ (a secondary phase transition from the $P4/nmm$ polymorph of KNaNbOF_5 , not the focus of this article) is irreversible, as confirmed previously [6, 7]. 246
- B.7 ^{19}F MAS (5 kHz) NMR spectra of KNaNbOF_5 acquired at 440°C in different phase transition routes ($P4/nmm$ to HT and $Pna2_1$ to HT). The new signal (marked with # to indicate the isotropic shift) detected in the transition from NCS to HT route is shown in blue. Asterisks (*) denotes the spinning side bands. 247
- B.8 High-resolution ^{19}F MAS (25 kHz) NMR spectra of $Pna2_1$ KNaNbOF_5 before/after in situ high-temperature ^{19}F MAS NMR experiments. Calculated ^{19}F NMR chemical shifts are also shown for reference. Asterisks (*) denote spinning side bands. 247
- B.9 High-resolution ^{19}F MAS (25 kHz) NMR spectra of the perovskite-derived polymorph of KNaNbOF_5 with symmetry $P4/nmm$ quenched at 150°C , 250°C , 310°C , 340°C , and 370°C . Asterisks (*) denote spinning side bands. The spectra of the $P4/nmm$ samples quenched at 340°C , 310°C , 250°C , and 150°C do not show any additional phases other than the $P4/nmm$ phase. Multiple phases appear in the spectra of the sample quenched at 370°C . In order of highest to lowest percentage of the sample, we see the $Pnna$, $Pnma$, NCS phases along with a small amount of remaining $P4/nmm$ sample. This is distinctive from the results of the NCS quenching experiment, as the $Pnna$ phase makes up by far the largest percentage of the sample when the $P4/nmm$ sample is quenched. 248
- C.1 Potential derivative structure path to obtain a polar phase ($Cmc2_1$) from a centrosymmetric anion ordered structure ($Cmcm$) from the homoanionic parent phase ($I4/mmm$). The polarization in the $Cmc2_1$ structure arises as the fluorides all move to the right while the apical oxides all move to the left. The calculated Berry phase polarizations for the relaxed polar structures are 2.70 and $2.58 \mu\text{C cm}^{-2}$ for the $Cmc2_1$ and $Pna2_1$ phases of $\text{Sr}_2\text{ScO}_3\text{F}$, respectively, and $4.82 \mu\text{C cm}^{-2}$ for the $Cmc2_1$ phase of $\text{Ca}_2\text{ScO}_3\text{F}$ 249
- C.2 Relative energies of the $\text{Sr}_2\text{ScO}_3\text{F}$ $Cmc2_1$ structure as a function of the polar (Γ_5^-) mode with varying amounts of a hybrid order parameter, $\lambda Q_{X_3^+} Q_{X_2^-}$ 250
- C.3 Energetics of Ca_2TiO_4 with octahedral tilts. The anion order labels indicate the pattern of B -site displacements and all B -site displacements are 0.178 \AA 252
- C.4 (a) Schematic of the molecular orbital diagram for a $[\text{ScO}_5\text{F}]$ octahedra. The diagram is not drawn to scale. Partial density of states of the relaxed (b) polar, (c) interlayer, and (d) intralayer anion ordered structures of $\text{Sr}_2\text{ScO}_3\text{F}$ on a per atom basis. 252
- D.1 Structure with condensed $A2$ mode from the $\text{Sr}_3\text{In}_2\text{O}_5\text{F}_2$ ground state $P2_1/c$ structure. The lines shows the wave-like displacive modulation of the equatorial O ions in the foreground on the (101) plane. 253

E.1	Disordered TiOF with condensed instability at $k = (0.26, 0.26, 0.6)$ on a $4 \times 4 \times 2$ supercell. The distortions are exaggerated to make them clearer.	255
E.2	Energetics of anion disordered TiOF structures modulated with the unstable phonon modes from VCA phonon dispersions.	256

List of Tables

3.1	Common synthetic routes to realize heteroanionic materials. A check mark in the corresponding synthetic method row and products column indicate that there is a published report of the synthetic method producing a heteroanionic oxide compound.	56
4.1	Structural information of the prototypical $n=1$ Ruddlesden Popper structure with space group $I4/mmm$. Positions are given in fractional units; u, v are free parameters.	80
4.2	Polar and antipolar irreps that alter the site-symmetry of the anions. Irrep labels correspond to the following wavevectors (primitive basis): $\Gamma = (0, 0, 0)$, $M = (1/2, 1/2, -1/2)$, and $X = (0, 0, 1/2)$. Lattice vectors are given relative to the primitive cell of the aristotype $n=1$ Ruddlesden-Popper structure.	85
4.3	Rigid rotations and tilts of the anions also reduce the site symmetry of the anions. Lattice vectors are relative to the primitive cell of the prototypical $n = 1$ RP Ruddlesden-Popper structure.	89
6.1	The effect of individual irreps on the Wyckoff sites of the ideal $I4/mmm$ Ruddlesden-Popper A_2BX_4 compound due to anion ordering (O) and atomic displacements (D). The \times indicates that the irrep does not modify the specified Wyckoff site. Ligand sites X are either apical (ap) or equatorial (eq).	136
6.2	Dipole-dipole (DD) and short-range (SR) contributions to the total (tot) change in energy in Sr_2ScO_3F structures with tilts relative to the anion ordered structures. All values are in meV.	146
6.3	Dipole-dipole (DD) and short-range (SR) contributions to the total (tot) change in energy in Ca_2ScO_3F structures with tilts relative to the anion ordered structures. All values are in meV.	147
8.1	Comparison of the experimental and DFT relaxed lattice parameters of the rutile ($P4_2/mnm$) anion disordered TiOF.	172
A.1	Table of all published heteroanionic $n=1$ Ruddlesden-Popper compounds. RT = room temperature	238
A.2	Summary of statistics from varying bond valence parameters by 0.05 \AA . The ‘‘GII minimized’’ and ‘‘DFT’’ label in the first column indicate from which step of the materials discovery procedure the structure originates. All values are in units of v.u.	240
A.3	Attempted syntheses for Sr_2AlO_3F and products identified from powder x-ray diffraction. Starting materials for all synthetic attempts were stoichiometric amounts of $SrCO_3$, SrF_2 , and Al_2O_3 . Products are in order of weight percent.	240

B.1	Summary of each eigenmode's contribution to the symmetry adapted modes using the force constant matrix of the <i>Cmcm</i> phase.	242
B.2	Crystallographic information for the DFT relaxed structures of <i>Pna2₁</i> (NCS) and <i>Cmcm</i> (HT) structures of KNaNbOF_5	242
B.3	Landau coefficients of the free energy expansion fit to DFT total energy calculations using different functionals.	243
B.4	Crystallographic information for the DFT relaxed structures of <i>Pnma</i> and <i>Pnna</i> structures of KNaNbOF_5	244
B.5	Summary of ^{19}F NMR isotropic chemical shifts, δ , in KNaNbOF_5 . Bolded values indicate fluoride sites that are <i>trans</i> to the oxide in the $[\text{NbOF}_5]^{2-}$ octahedra. Although it is difficult to resolve the equatorial fluoride ions (i.e., all fluoride ions that are not <i>trans</i> to the apical oxide ions in the $[\text{NbOF}_5]^{2-}$ unit), because of their close proximity in terms of chemical shifts in the NMR spectra, we can readily resolve the phases using the chemical shifts of the apical fluoride ions (i.e., the fluoride ion <i>trans</i> to the oxide ion).	244
B.6	Summary of the calculated Born effective charges in KNaNbOF_5 in units of e at the DFT-PBEsol level.	248
C.1	The energetics of the prototypical anion ordered structures and their equilibrium structures relative to the highest energy anion order of $\text{Ca}_2\text{ScO}_3\text{F}$. $\Delta E_{\text{anion orders}}$ is the energy of the relaxed anion ordered structures relative to the highest energy anion ordered structure (intralayer antipolar). ΔE_{eq} (meV/f.u.) is the energy of the equilibrium structures relative to the highest energy anion ordered structure.	250
C.2	The energetics of the prototypical anion ordered structures and their equilibrium structures relative to the highest energy anion order of $\text{Sr}_2\text{ScO}_3\text{F}$. $\Delta E_{\text{anion orders}}$ is the energy of the relaxed anion ordered structures relative to the highest energy anion ordered structure (intralayer antipolar). ΔE_{eq} (meV/f.u.) is the energy of the equilibrium structures relative to the highest energy anion ordered structure.	250
C.3	Separation of dipole-dipole and short-range contributions to the total change in energy in the Sr_2SnO_4 structure with tilts relative to the prototypical <i>I4/mmm</i> structure.	251
D.1	Lowest energy phases obtained from derivative structure search of $\text{Sr}_3\text{In}_2\text{O}_5\text{F}_2$	254
D.2	Lowest energy phases obtained from derivative structure search of $\text{Sr}_3\text{In}_2\text{O}_5\text{F}_2$	254
E.1	Energetics of alternative anion ordered configurations of TiOF . All structures have only <i>fac</i> - $[\text{TiO}_3\text{O}_3]$ octahedral units.	255

Chapter 1: Introduction

1.1 Motivation

Advances in materials development are key to continue the technological advancement of society (i.e. Moore's law) and solve critical challenges to mankind, such as global warming. Transition metal oxides (TMOs) are a fruitful class of materials that display a wide variety of intrinsic and functional properties that are used in a range of applications, for example as paint pigments, magnetic storage materials, semiconductors, and Li-ion batteries [8–10]. TMOs that adopt the perovskite structure and its derivatives (e.g. Brownmillerties, Ruddlesden-Poppers, etc.) have been of particular interest to researchers because they accommodate a variety of chemistries and host properties such as superconductivity, metal-insulator transitions, multiferroism, and colossal magnetoresistance [11–14]. The study of perovskite-structured materials has allowed researchers to understand existing structure-property relationships and develop methodologies to rationally design new TMOs with enhanced properties.

Cation engineering, or the partial or complete substitution of a cation site for another cation species, has been very successful in tuning or enhancing functional properties and creating emergent phenomena at oxide interfaces [15–18]. Unexpected phenomena may arise in solid solutions or substituted materials due to the strong coupling between the lattice and electronic degrees of

freedom. Although many significant advances in this field were made before the broad adoption and availability of accurate electronic structure methods and widespread access of high-performance computing processing power, *ab initio* calculations have enhanced the quality and speed of understanding and discoveries in this area. Computational techniques such as density functional theory (DFT) in tandem with advances in materials synthesis, such as molecular beam epitaxy (MBE) and plasma layer deposition (PLD), have allowed researchers to observe and disentangle the underlying physical mechanisms for complex and emergent phenomena such as exotic magnetic orderings, two dimensional electron gasses, superconductivity and ferroelectricity [15, 19–24]. Structure-property relationships and materials design guidelines are well established for property control via cation engineering.

Recently, anion engineering in inorganic materials been identified as another paradigm for property control, because of the subtle chemical and physical differences between the anions [25–27]. Although this approach has been successful in a number of applications, such as Li-ion battery electrodes, second-harmonic generation materials, and solid-state phosphor materials [4, 28–34], understanding and control over structure-property relationships in mixed anion or heteroanionic materials is still developing and finding applications in condensed-matter physics areas such as magnetism [35, 36], topology [37], and superconductivity [38]. Additional challenges are imposed by the tendency for some heteroanionic materials, in particular oxyfluorides and oxynitrides, to have disordered anion sublattices or have statistically random distributions over the anion sites. The appearance of long-range anion order (or lack thereof) is often key to the appearance of a targeted property, particularly those which require acentricity such as ferroelectricity, piezoelectricity, and nonlinear optical phenomena.

In this dissertation, I use *ab initio* calculations to explore changes to the structure and functionality of heteroanionic materials that can be obtained by engineering the metal–ligand interactions through anionic substitution of oxygen by fluorine. Specifically, I adapt or leverage existing TMO crystal-chemistry principles for property control in oxyfluoride materials and predict new, functional oxyfluorides for synthesis.

1.2 Organization

This thesis is organized as follows:

- In Chapter 2, I review the fundamental aspects of density functional theory, ranging from the Schrödinger equation to exchange-correlation functionals. I also review practical aspects of DFT calculations such as plane wave basis sets, Brillouin zone sampling, and pseudopotentials.
- In Chapter 3, I provide an overview of heteroanionic materials design, focusing on oxygen-based compounds, such as oxyfluorides, oxynitrides, and oxysulfides. First, I discuss fundamental changes to the atomic and electronic structure that occur upon anion substitution and how these may be leveraged to engineer enhanced functional properties. I describe synthetic methods for bulk and thin film oxyfluorides, oxynitrides, and oxysulfides and characterization techniques that can distinguish between different species in the anion sublattice. Last, I review oxyfluorides whose properties have been engineered through anion substitution.
- In Chapter 4, I predict novel, synthesizable $n = 1$ Ruddlesden-Popper oxyfluorides using a workflow that filters for candidate compounds using an approach based on Pauling’s second rule. This filtering process significantly reduces computational cost and is based on a minimization scheme using the global instability index (GII), which filters and is able to eliminate

50% of highly unstable candidate compositions. I validate this minimization scheme using DFT calculations and find that the GII of stable heteroanionic compounds is higher than that of homoanionic oxides owing to significant charge redistribution in compounds containing more than one anion.

- In Chapter 5, I investigate potential ferroelectricity in noncentrosymmetric KNaNbOF_5 . To determine a potential ferroelectric switching pathway for the transition, I first use first principles calculations to create a model of the centrosymmetric to noncentrosymmetric phase transition. From this model, I construct a phase diagram of the transition that predicts the appearance of a previously unseen intermediate phase. The existence of the intermediate phase is confirmed using ^{19}F MAS NMR. Finally, I model a monodomain ferroelectric switching pathway through the predicted intermediate phase and find that its energetics and strain are similar to known ferroelectrics, suggesting that this compound may be switchable.
- In Chapter 6, I describe a strategy to design ferroelectric heteroanionic materials based on the coupling of anion order and octahedral tilts in $n = 1$ Ruddlesden-Popper structures with chemical formula ABO_3F . This would allow for noncentrosymmetric and polar compounds to arise from centrosymmetric anion ordered structures. I computationally examine the relative phase stability of the polymorphs derived from this coupling using the compositions $\text{Sr}_2\text{ScO}_3\text{F}$ and $\text{Ca}_2\text{ScO}_3\text{F}$.
- In Chapter 7, I explore the phase space of heteroanionic $n = 2$ Ruddlesden-Popper compounds under ambient and epitaxially strained conditions. Competition between antiferroelectric and ferroelectric distortions are well known in the analogous homoanionic oxide structures and

find similar competition occurs in these materials with chemical composition $\text{Ba}_3\text{In}_2\text{O}_5\text{F}_2$ and $\text{Sr}_3\text{In}_2\text{O}_5\text{F}_2$.

- In Chapter 8, I investigate the anion-ordered and anion-disordered variants of TiOF for a potential insulator-metal transition.
- In Chapter 9, I summarize the findings of my investigations and discuss future opportunities enabled by my work.

Chapter 2: First Principles Electronic Structure Methods

This section briefly reviews the foundations and practical aspects of performing first principles density functional theory (DFT) calculations methods, which are used throughout this thesis. It does not rigorously prove all the mathematical theorems behind DFT, rather it focuses on the principle concepts, equations, and common approximations. More detailed descriptions and rigorous mathematical proofs can be found in journal articles, textbooks, and review papers including Refs [39–42]. Throughout this thesis, I use density functional theory calculations as implemented in the Vienna *Ab Initio* Software Package (VASP) [43, 44]. Specific computational details such as choice of pseudopotential, plane-wave cutoff, k -point meshes, etc. are specified in each chapter.

2.1 The Many-Body Schrödinger Equation

The behavior of quantum particles can be described by solving the Schrödinger equation. In its simplest, time-independent form, the Schrödinger equation can be written as follows:

$$\hat{H}\Psi = E\Psi \tag{2.1}$$

where $\Psi(\mathbf{R}_I, \mathbf{r}_i)$ is the many body wavefunction with \mathbf{R}_I and \mathbf{r}_i representing the positions of the ions (I) and electrons (i), respectively. The total energy of the system, E , can then be computed by operating the Hamiltonian \hat{H} on Ψ .

The Hamiltonian which describes a system of interacting electrons (e) and nuclei (N) includes kinetic (\hat{T}) and Coulombic interaction (\hat{V}) terms:

$$\hat{H} = \hat{T}_e + \hat{T}_N + \hat{V}_{NN} + \hat{V}_{ee} + \hat{V}_{eN} \quad (2.2)$$

The electronic and nuclear kinetic terms are as follows,

$$\hat{T}_e = -\frac{\hbar^2}{2m_e} \sum_i \nabla_i^2; \hat{T}_N = -\sum_I \frac{\hbar^2}{2M_I} \nabla_I^2 \quad (2.3)$$

where m_e and M_I are the mass of the electron and ion, respectively, and \hbar is the reduced Planck constant. The Coulombic interaction terms, nuclear-nuclear (NN), electron-electron (ee), and nuclear-electron (eN) are as follows:

$$\hat{V}_{NN} = \frac{1}{2} \sum_{I \neq J} \frac{Z_I Z_J e^2}{|\mathbf{R}_I - \mathbf{R}_J|}; \hat{V}_{ee} = \frac{1}{2} \sum_{i \neq j} \frac{e^2}{|\mathbf{r}_i - \mathbf{r}_j|}; \hat{V}_{eN} = \sum_{i, I} \frac{Z_I e^2}{|\mathbf{r}_i - \mathbf{R}_I|} \quad (2.4)$$

where Z_I is the nuclear charge and e is the electron charge.

Given that the nuclear mass is much larger than the electronic mass, the inverse mass of the nuclei $1/M_I$ can be regarded as small. If the mass of the nuclei is set to infinity, the kinetic energy of the nuclei can be ignored. This is known as the Born-Oppenheimer or adiabatic approximation [45] and allows one to separate the motion of the atomic nuclei and electrons, which partly simplifies the calculation of the electronic wavefunctions. In this approximation, the electrons can be thought

of as moving through an external field imposed by the nuclei at fixed positions. The resulting Hamiltonian, which can be referred to as the electronic Hamiltonian, consists of \hat{T}_e , \hat{V}_{ee} , \hat{V}_{eN} , a classical interaction of the nuclei (replacing \hat{V}_{NN}), and any further contributions to the total energy independent of the problem of describing electrons.

Although this does speed up the calculation of the electronic wavefunctions, these approximations are still insufficient to allow for *useful* calculations of complex systems. This is largely because of the computational cost of calculating real systems, as the number of electrons is on the order of 10^{23} and the electron-electron interaction term requires the 3 coordinate positions of each electron. Furthermore, each electron interacts with each other, making the calculation completely intractable. The most successful method of approximating this electron-electron interaction problem is density functional theory, which provides a good tradeoff between reliability and computational cost.

2.2 Density Functional Theory

Although the original density functional theory functional was a method developed by Thomas [46] and Fermi [47] in 1927 and Dirac in 1930 [48], the modern formulation of density functional theory originated from Pierre Hohenberg and Walter Kohn in 1964 [49]. A year later, Kohn and Lu J. Sham published a derivation of a self-consistent scheme for the calculation of the electronic structure of real materials, not only model systems [50].

2.2.1 The Hohenberg-Kohn Theorem

The first theorem of Hohenberg and Kohn states that for any system of interacting particles in an external potential $V_{\text{ext}}(\mathbf{r})$, the potential $V_{\text{ext}}(\mathbf{r})$ is determined uniquely, except for a constant, by the ground state particle density $n_0(\mathbf{r})$. It follows that since the hamiltonian is fully determined, except

for a constant shift of energy, the many-body wavefunctions for all states (ground and excited) are also determined. Therefore all properties of the system are completely determined given only the ground state density $n_0(\mathbf{r})$.

The proof of this theorem is straightforward. Suppose there are two different external potentials, $V_{\text{ext}}^{(1)}(\mathbf{r})$ and $V_{\text{ext}}^{(2)}(\mathbf{r})$, that differ by a constant and have the same ground state density $n(\mathbf{r})$. The two potentials lead to two different hamiltonians, $\hat{H}^{(1)}$ and $\hat{H}^{(2)}$, and two different wavefunctions, $\Psi^{(1)}$ and $\Psi^{(2)}$, which are hypothesized to have the same ground state density $n_0(\mathbf{r})$. From the variational principle, we can write that

$$E^{(1)} = \langle \Psi^{(1)} | \hat{H}^{(1)} | \Psi^{(1)} \rangle < \langle \Psi^{(2)} | \hat{H}^{(1)} | \Psi^{(2)} \rangle \quad (2.5)$$

The strict inequality indicates our assumption that the ground state is non-degenerate. The last term can be written as

$$\langle \Psi^{(2)} | \hat{H}^{(1)} | \Psi^{(2)} \rangle = \langle \Psi^{(2)} | \hat{H}^{(2)} | \Psi^{(2)} \rangle + \langle \Psi^{(2)} | \hat{H}^{(1)} - \hat{H}^{(2)} | \Psi^{(2)} \rangle \quad (2.6)$$

$$= E^{(2)} + \int d^3r [V_{\text{ext}}^{(1)}(\mathbf{r}) - V_{\text{ext}}^{(2)}(\mathbf{r})] n_0(\mathbf{r}) \quad (2.7)$$

such that

$$E^{(1)} < E^{(2)} + \int d^3r [V_{\text{ext}}^{(1)}(\mathbf{r}) - V_{\text{ext}}^{(2)}(\mathbf{r})] n_0(\mathbf{r}) \quad (2.8)$$

We can write $E^{(2)}$ in the exact same way and we find the same resulting equations with the superscripts interchanged:

$$E^{(2)} < E^{(1)} + \int d^3r [V_{\text{ext}}^{(2)}(\mathbf{r}) - V_{\text{ext}}^{(1)}(\mathbf{r})] n_0(\mathbf{r}) \quad (2.9)$$

If we add together Equation 2.8 and Equation 2.9, we obtain $E^{(1)} + E^{(2)} < E^{(1)} + E^{(2)}$, an inherently contradictory inequality. This proves the first theorem by *reductio ad absurdum*; there cannot be two different external potentials differing by more than a constant which give rise to the same non-degenerate ground state charge density. The density must uniquely determine the external potential to within a constant.

The second theorem states that independent of the external potential, $V_{\text{ext}}(\mathbf{r})$, there exists a universal function for the energy $E[n(\mathbf{r})]$ in terms of the density $n(\mathbf{r})$. For any $V_{\text{ext}}(\mathbf{r})$, the exact ground state energy of the system is the global minimum value of this functional and the density $n(\mathbf{r})$ that minimizes the functional is the exact ground state density $n_0(\mathbf{r})$. We define this energy functional as follows:

$$E[n(\mathbf{r})] = F[n(\mathbf{r})] + \int d^3\mathbf{r} V_{\text{ext}}(\mathbf{r})n(\mathbf{r}) + E_{II} \quad (2.10)$$

where E_{II} is the interaction energy of the nuclei, $F[n(\mathbf{r})] = T[n(\mathbf{r})]$ is the kinetic and potential energy of the interacting electron system, which must be universal as they are functionals only of the density. Suppose we define a unique ground state density, $n^{(1)}(\mathbf{r})$, corresponding to the external potential $V_{\text{ext}}^{(1)}(\mathbf{r})$. The expectation value of the Hamiltonian of this ground state corresponds to

$$E^{(1)}[n(\mathbf{r})] = \langle \Psi^{(1)} | \hat{H}^{(1)} | \Psi^{(1)} \rangle \quad (2.11)$$

By the variational principle, a different density, $n^{(2)}(\mathbf{r})$, which has a different wavefunction, $\Psi^{(2)}$, will have a higher energy than $n^{(1)}(\mathbf{r})$ ($E^{(1)} < E^{(2)}$). It follows then that the density that minimizes the energy is the true ground state density, $n_0(\mathbf{r})$.

2.2.2 The Kohn-Sham Equations

The Hohenberg-Kohn theorem establishes that ground state properties can be determined from only the electronic density, however it does not tell us how to extract those properties from the density. Kohn and Sham proposed that this many-body interaction term could be replaced with an independent-particle equation of non-interacting electrons with the many-body terms being incorporated into an exchange-correlation functional of the density. This is then the basis for the application of the Hohenberg-Kohn Theorem.

There are two assumptions made in the construction of the Kohn-Sham auxiliary system. The first is that the ground-state electron density can be represented by the ground state density of an auxiliary system of non-interacting particles with wavefunctions ϕ . The second is that the auxiliary hamiltonian is chosen to have a *local* potential and the usual kinetic operator. The local form of the potential is essential to have a one-to-one correspondence of the potential. The density of this auxiliary system can be expressed as

$$n(\mathbf{r}) = \sum_{i=1}^N |\phi_i(\mathbf{r})|^2 \quad (2.12)$$

and the independent-particle kinetic energy T_S is

$$T_S = \frac{1}{2} \sum_{i=1}^N \int d^3r |\nabla \phi_i(\mathbf{r})|^2. \quad (2.13)$$

The Kohn-Sham approach rewrites the many-body Hohenberg-Kohn expressing for the ground state energy into the form:

$$E_{\text{KS}} = T_S[n] + \int d\mathbf{r} V_{\text{ext}}(\mathbf{r})n(\mathbf{r}) + E_{\text{Hartree}}[n] + E_{II} + E_{\text{XC}}[n] \quad (2.14)$$

where $V_{\text{ext}}(\mathbf{r})$ is the external potential due to the nuclei and any other external fields and E_{II} is the interaction between nuclei. $E_{\text{Hartree}}[n]$ is the classical treatment of the electron density,

$$E_{\text{Hartree}} = \frac{1}{2} \int d^3r d^3r' \frac{n(\mathbf{r})n(\mathbf{r}')}{|\mathbf{r} - \mathbf{r}'|} \quad (2.15)$$

Lastly, E_{XC} is the exchange-correlation energy which contains all the many-body effects of exchange and correlation.

Using the variational principle on Equation 2.14 and Equation 2.12, Equation 2.13, and Lagrange multipliers, we can obtain the Kohn-Sham Schrödinger-like equations:

$$(H_{\text{KS}} - \epsilon_i)\phi_i(\mathbf{r}) = 0, \quad (2.16)$$

where ϵ_i are the eigenvalues and H_{KS} is the effective hamiltonian,

$$H_{\text{KS}} = -\frac{1}{2}\nabla^2 + V_{\text{KS}}(\mathbf{r}), \quad (2.17)$$

with

$$V_{\text{KS}}(\mathbf{r}) = V_{\text{ext}}(\mathbf{r}) + \frac{\delta E_{\text{Hartree}}}{\delta n(\mathbf{r})} + \frac{\delta E_{\text{XC}}}{\delta n(\mathbf{r})}. \quad (2.18)$$

The solution to these system of equations can be solved iteratively until self-consistency is reached.

From there, the ground state electron density, total minimized energy, and all derivable quantities are obtained.

2.2.3 Exchange-Correlation Functionals

The Kohn-Sham equations transform the Hohenberg-Kohn theorem into a tractable problem, with all terms containing independent-particle expressions. The exchange-correlation energy $E_{XC}[n]$, however, which contains the many-body interacting electron problem remains to be specified. The exact form of $E_{XC}[n]$ is exceedingly complex and non-analytical, however with a number of assumptions, we can successfully approximate the exchange-correlation functional. There are a range of functionals from those which have simple approximations of exchange and correlation to those which use exact exchange. These functionals, forming so-called Jacob's ladder of density functional approximations [51–53], generally sacrifice computational cost for higher accuracy. This section will review several exchange-correlation functionals, especially those that are used in this thesis.

One of the first proposals for the exchange and correlation energies relies on the assumption that solids can often be considered close to the limit of the homogeneous electron gas. In that limit, the effects of exchange and correlation are local in character. Kohn and Sham therefore proposed the local density approximation (LDA) for the exchange-correlation functional forming the first run of the ladder. This energy functional simply integrates over all space with the exchange correlation energy density at each point assumed to be the same as a homogeneous electron gas with that density:

$$E_{XC}^{\text{LDA}}[n] = \int n(\mathbf{r})\epsilon_{XC}^{\text{hom}}[n(\mathbf{r})]d^3r. \quad (2.19)$$

The exchange-correlation energy density can be separated into the exchange and correlation contributions, which are known analytically and quantum Monte-Carlo methods, respectively [54, 55].

Perhaps surprisingly, this simple approximation works well for predicting properties in a wide range of materials [40]. LDA tends to overestimate the binding energy between atoms in a solid, therefore underestimating bond lengths, lattice parameters, and overpredicting phonon frequencies, elastic moduli, and cohesive energies [56].

The next step up Jacob’s ladder is the semi-localized generalized gradient approximation (GGA). As its name suggests, it incorporates information about the gradient of the charge density, $\nabla n(\mathbf{r})$, into the functional. The exchange-correlation energy has the form:

$$E_{\text{XC}}^{\text{LDA}}[n] = \int n(\mathbf{r}) \epsilon_{\text{XC}}^{\text{hom}}[n(\mathbf{r})] d^3r \quad (2.20)$$

Unlike LDA, there are multiple GGA functionals [57–60] as the exchange-correlation energy density is dependent on an exchange and correlation enhancement factor, which differs depending on the choice of functional. The GGA functional developed by Perdew, Burke, and Ernzerhof (PBE) is one of the most commonly used functionals and has been used to benchmark many DFT codes [61]. GGA functionals fix the overbinding error of LDA functionals, but tend to slightly underbond and overestimate cell volumes. In this thesis, we typically use the PBE functional revised for solids (PBEsol), which is a version of PBE that improves the accuracy of bond lengths and surface energies [62]. Although GGA functionals are more computationally expensive than LDA, the increased cost is nearly negligible compared to the improvement in overall accuracy.

Beyond GGAs, the next rung in Jacob’s ladder of functionals is the meta-GGAs, which in addition to the energy density and gradient of the energy density included in GGA, includes the kinetic energy density, $t[n(\mathbf{r})]$. In order to uniquely define the kinetic energy density, it can be considered as the sum of two parts, $t[n(\mathbf{r})] = t_n[n(\mathbf{r})] + \tau_x[n(\mathbf{r})]$ where all the nonuniqueness is

in the term $t_n(\mathbf{r})$ which depends on the density $n(\mathbf{r})$. The “exchange kinetic energy per particle,” $\tau_x(\mathbf{r})$, has a physical meaning; it is the curvature of the exchange hole and the basis for the electron localization function (ELF) [63]. $\tau_x(\mathbf{r})$ is defined by the Kohn-Sham orbitals, $\phi_i(\mathbf{r})$:

$$\tau_x(\mathbf{r}) = \frac{1}{2} \sum_{i=1}^N |\nabla \phi_i(\mathbf{r})|^2 \quad (2.21)$$

MetaGGAs aim to have more accurate predictions than GGA for a wider range of applications and chemical systems. Some metaGGAs such as TPSS are more accurate in predicting the properties of bulk solids and surfaces [64, 65], but often fail to capture van der Waals’ bonding in layered compounds [66]. Although modern metaGGAs, such as MS2 [67] and SCAN [65] show great promise, they are still in the process of being validated for various chemical systems and applications [68–71].

The final functional type discussed here is hybrid functionals, which increase the accuracy of calculations by including some percentage of non-local exact exchange. The non-local exact exchange is obtained from Hartree-Fock theory, which are very expensive for extended solids meaning hybrid functional cost significantly more than any of the previous functionals mentioned here. Note also that Hartree-Fock pertains to only exchange, there is no term to improve correlation in these calculations. However, exchange generally contributes to the energy more than correlation. Hybrid functionals also work best for insulators with little correlation, giving significant improvements in band gaps and excitation energies. Metals require screened-Fock exchange to give reasonable results. Like GGAs and metaGGAs, there are many different implementations of hybrid functionals, but I will focus only on the functionals proposed by Heyd, Scuseria, and Ernzerhof, HSE03 and HSE06 [72, 73]. HSE is a “range separated” hybrid functional, meaning the exchange energy is

separated into components from the short- and long-range parts of the Coulomb interaction. This is based on the idea that screening is dependent on the distance, with little screening at short distances and reaching macroscopic values at large distances. Within HSE, the long-range non-local is eliminated and the exchange correlation energy is represented as

$$E_{XC} = E_{XC}^{\text{PBE}} + a(E_X^{\text{HF,SR}} - E_X^{\text{PBE,SR}}) \quad (2.22)$$

The a term can be tuned based on the property and material being studied [59, 74–76], meaning that this functional is semi-empirical, unlike the other functionals discussed thus far.

2.3 Practical Aspects of Density Functional Theory

In the previous section, I described the theory behind DFT along with the assumptions and approximations that are made in order to obtain a practical self-consistent implementation of it. This section focuses on the numerical approximations that are necessary in the practical implementation of the Kohn-Sham equations, which requires convergence testing to ensure accurate results.

2.3.1 Plane Wave Basis Set

Because we are modeling crystalline materials, we take advantage of their lattice periodicity and significantly reduce the number of atoms and electrons under consideration. Given the periodicity, we apply Bloch’s theorem [77] to further reduce the complexity. Bloch’s theorem states that any solution to the Schrödinger equation in a periodic potential must take the form of a plane wave

modulated by a periodic function, $u_{n,\mathbf{k}}(\mathbf{r})$,

$$\phi_{n,\mathbf{k}}(\mathbf{r}) = u_{n,\mathbf{k}}(\mathbf{r})e^{i\mathbf{k}\cdot\mathbf{r}}, \quad (2.23)$$

where n is the index for an electron in a band and k is a reciprocal lattice wave vector confined to the first Brillouin zone. The periodic part of Bloch's theorem is typically expanded in terms of the reciprocal lattice vector \mathbf{G} ,

$$u_{n,\mathbf{k}}(\mathbf{r}) = \sum_{\mathbf{G}} c_{n,\mathbf{G}} e^{i\mathbf{G}\cdot\mathbf{r}}. \quad (2.24)$$

Combining Equation 2.23 and Equation 2.24, we obtain,

$$\phi_{n,\mathbf{k}}(\mathbf{r}) = \sum_{\mathbf{G}} c_{n,\mathbf{k}+\mathbf{G}} e^{i(\mathbf{k}+\mathbf{G})\cdot\mathbf{r}}. \quad (2.25)$$

The Kohn-Sham equations and the wavefunctiona can now easily be solved for using this plane wave expansion. However an exact solution would require *infinite* plane waves, which is obviously impractical. To make this problem tractable and ensure an accurate calculation, one must truncate the plane wave expansion in a DFT calculations to include only solutions with plane wave kinetic energies (E_{cut}) less than some value:

$$\frac{\hbar^2}{2m} |\mathbf{k} + \mathbf{G}|^2 \leq E_{\text{cut}} \quad (2.26)$$

Care must be taken to ensure the chosen E_{cut} is converged with respect to the properties of interest.

2.3.2 Brillouin Zone Sampling

Now that we have the plane wave basis set, we can integrate over the first Brillouin zone (BZ) rather than all of real space in order to obtain the energy, charge density, and derivative properties. The first BZ can be further reduced by taking into account the point group symmetry of the periodic lattice, obtaining the *irreducible* Brillouin zone (IBZ). Although we have reduced the area that we need to integrate over, to obtain an exact solution, the integration would still technically need to be performed over an infinite number of k -points in the IBZ. However, we can reduce the number of integrations needed to obtain an accurate result by appropriately weighting a mesh of k -points in the IBZ and interpolating between them. The choice of k -point placement and weighing significantly influences the efficiency of the calculations, and there are many approaches to determine the most efficient set of k -points [78–83]. In this thesis, I primarily use the method developed by Monkhorst and Pack in 1976 [79] to determine k -point meshes.

2.3.3 Pseudopotentials

Although we have reduced the number of plane waves needed for an accurate calculation through the use of a basis set, the number of plane waves is still too many for practical calculations. This is because wavefunctions of electrons near the core of an atom are highly oscillating, meaning a large number of plane waves would be needed to accurately capture its behavior. Valence electrons, however, have relatively smooth wavefunctions and could be treated with a reasonable number of plane waves if not for the core electrons. Additionally, bonding interactions are largely determined by the valence electrons so accurate calculations are typically not dependent on accurate representation of the core states. Pseudopotentials (PP) increase the efficiency of calculations by attempting to describe the valence states without explicitly treating the core states, thereby reducing the number

of plane waves needed in a given calculation. The core states are instead “frozen” and replaced with an effective potential.

There are multiple pseudopotentials formalisms, among the most influential are norm-conserving [84], ultrasoft [85,86], and the projector-augmented wave (PAW) method [87]. The two former formalisms suffer some limitations in DFT calculations in the “semi-core” region from nonlinearity of the exchange-correlation functional [88]. To correct this error, elaborate nonlinear core-corrections are required when the overlap between core and valence electrons is non-negligible, such as $4s$ states in $3d$ transition metals [89]. However, the PAW method reconstructs the full all-electron density by essentially separating the smooth valence functions from the oscillatory core functions and allowing them to be treated by a rough grid and fine grid, respectively, improving both the efficiency and accuracy of calculations. The PAW method can be seen as a balance between the computational efficiency of the pseudopotential method and the accuracy of the computationally expensive full-potential linearized augmented-plane wave (FLAPW) method [90]. For all calculations in VASP, I use the PAW method as implemented by Kresse [91].

Chapter 3: Heteroanionic Materials Design

This chapter is composed of sections from Ref. [27], which has been adapted with permission. Sections from the manuscript have been updated with recent publications. This work was written in collaboration with Dr. Nenian Charles. Copyright 2019 Wiley-VCH.

This chapter covers fundamental aspects of heteroanionic materials design, focusing primarily on oxyfluorides, oxynitrides, and oxysulfides. First, I review the fundamental changes to the atomic and electronic structures that occur with anion substitution and how these changes may be leveraged to enhance functional properties. Then, I cover synthetic methods and characterization techniques that can discern similar anions in the same sublattice. Finally, I review a number of functional properties that have been enhanced through anion engineering in oxyfluorides.

3.1 Atomic Structure Considerations with Anion Engineering

Before examining changes to the the long-range structure of materials upon partial substitution of a secondary anion, we first consider the fundamental differences between the anions. In general, we consider the homoanionic analogues or basis structures to be oxide materials, as they are the most well studied of the homoanionic materials. To create a heteroanionic material (HAM), we choose a homoanionic (oxide) analogue as our base structure, then either insert the secondary anion

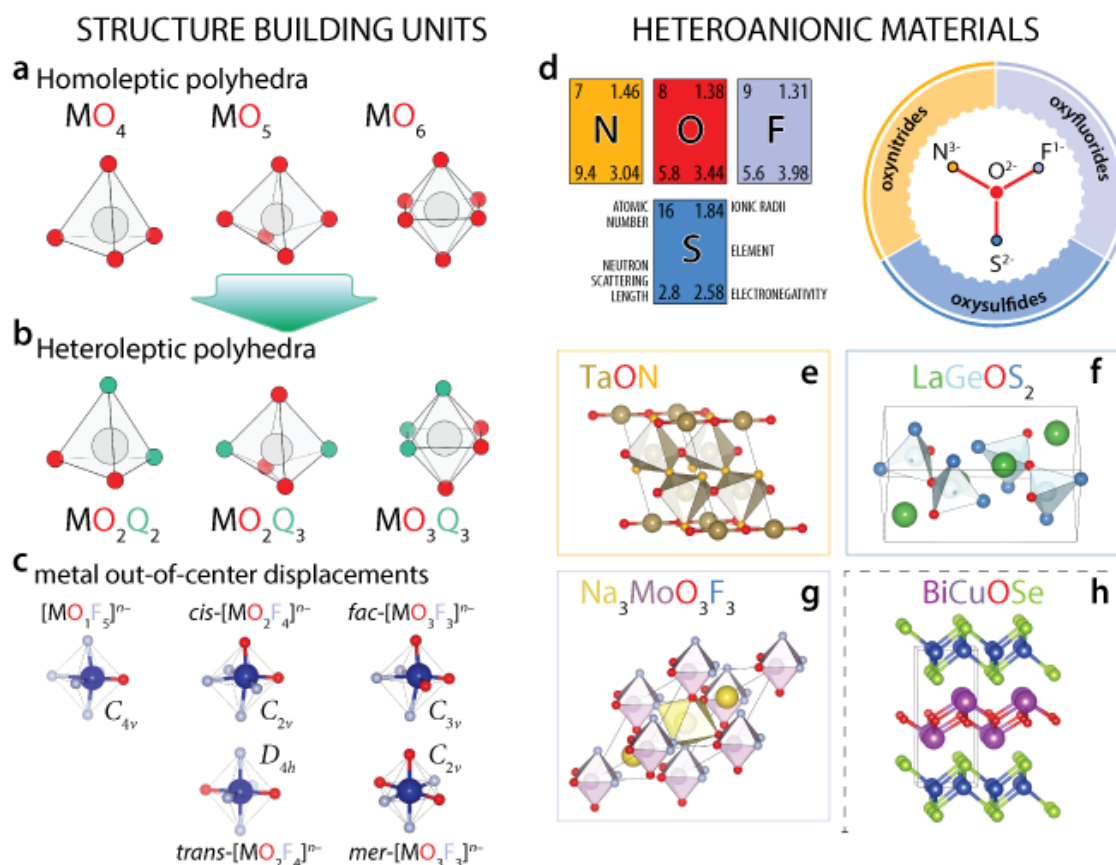


FIGURE 3.1: From homoanionic to heteroanionic building units for the assembly of oxide-derived heteroanionic materials: Heteroanionic materials are constructed from building units that exhibit unique local coordination chemistry with multiple anions surrounding a metal center (left) of the same (a, homoleptic) or different (b, heteroleptic) species. Typically, the number of oxide anions (red) govern: (c) the out-of-center metal displacements that may occur toward a face, edge, or corner of the polyhedron, which reduces the local symmetry for the metal d -orbitals, particularly in heteroanionic materials with d^0 electronic configurations. Local symmetry of the building units also depends on the geometric isomerism of the unit, e.g., *cis* or *trans* coordination. Illustration of the structural and chemical diversity in oxide-derived heteroanionic materials (HAMs), including: (d) a subset of those p -block anions, which combine with the oxide ion to form the structurally and chemically diverse oxynitride (e), oxysulfide (f), and oxyfluoride (g) materials from heteroleptic polyhedra. (h) $BiCuOSe$ is a heteroanionic material comprised of homoleptic polyhedra, which distinguishes it from the other materials (broken line). The annotated slice of the periodic table in (d) indicates the anion electronegativities based on the Pauling scale, ionic radii for four-fold coordination (S^{2-} based on sixfold coordination), and the bound coherent scattering lengths. In these materials, the exchange of an anion for oxide as in $O^{2-} \rightarrow N^{3-}$ ($O^{2-} \rightarrow F^{1-}$) requires compensation of excess (deficit) charge, which often necessitates that binary heteroanionic oxynitrides are composed of cations with high oxidation states (Ti^{4+} , Zr^{4+} , Ta^{5+} , Nb^{5+} , $Mo^{4+,5+}$, $W^{5+,6+}$) as in $TaON$. In oxyfluorides, on the other hand, late transition metal cations are compatible with lower oxidation states.

or exchange it with some portion of the oxide anion sublattice. However, successfully exchanging one anion for another requires careful consideration of the size, electronegativity, and valence with the global composition of the heteroanionic material in determining the final crystallography of the structure. The portion of the periodic table appearing in Figure 3.1d illustrates the inherent physical and chemical differences of a subset of the elemental *p*-block anions to combine with the oxide anion in heteroanionic materials.

The relative size of anions affects the number and shape of the coordination polyhedra, which may be justified by applying Pauling’s radius-ratio rule. Common polyhedral unit shapes found in HAMs include tetrahedra, square pyramids, and octahedra. For oxyfluorides with metal anionic octahedral units, these heteroleptic units may be $[MO_3F_3]$, $[MO_2F_4]$, or $[MOF_5]$ units (Figure 3.1c). Owing to the ionic size of the anion, usually only the nitride and fluoride anions are able to substitute easily for the oxide anion in these units (Figure 3.1e-g). Other suitable halides and chalcogenides are typically too large to coordinate the same transition metal ion, and thus layered structures tend to crystallize with various homoleptic polyhedral motifs in the unit cell (Figure 3.1h).

Additional implications of the size similarities of the anions are that co-occupancy of the same ligand site by two different anions may occur and give rise to disorder about the metal center. Naively, one anticipates that heteroanionic materials should exhibit complete disorder of the anion sublattice defining the polyhedral network; however, even in the dilute insertion or exchange limit, the substituted anions demonstrate site preferences about the metal centers [28, 29] and partial or complete order of the heteroleptic unit occurs [92]. Generally, long-range anion order tends to occur in heteroanionic materials when the difference in ionic radius of the two anions is significantly large. For example, oxysulfides tend to have long-range order owing to the significantly larger ionic radius of S^{2-} (1.84 Å) compared to O^{2-} (1.35 Å) despite the same formal oxidation state, and

oxynitrides and oxyfluorides tend to be disordered. Nonetheless, oxynitrides and oxyfluorides do exhibit short-range order and the degree of long-range order is sensitive to processing conditions. These changes in ionic radii and the (an)isotropic distribution of multiple anions can affect both the equilibrium lattice constants (of the global crystal structure) relative to the homoanionic oxide and local structure in heteroanionic materials.

There are multiple configurations of anions about the metal centers (i.e., geometric isomers) available for the $[MO_2F_4]$ and $[MO_3F_3]$ units. For $[MO_2F_4]$, *cis* and *trans* configurations are possible and for $[MO_3F_3]$, *fac* and *mer* units can form (Figure 3.1a,b). Changes to the local anion order in the heteroleptic unit lead to different local site symmetries for the cations (Figure 3.1c). In general, *cis* and *fac* units are more favored [93,94], particularly when the cation is a d^0 transition metal, because having anions with similar Pearson hardness [95] near each other maximizes the π -hybridization in the M–anion bonds. The hybridization is reinforced by allowing atomic relaxations toward characteristic bond lengths [96–103]. The inherent contrast between the anions also causes displacive nonidealities such as rotations and distortions to the polyhedral units, which are discussed later. π -hybridization favors the *cis* configuration for more electronegative anions over the *trans* anion arrangement in heteroanionic materials with d^0 transition metal cations, for example in for Mo-centered $[MoO_2F_4]$ heteroleptic units. In contrast, the *trans* anion arrangements with $4/mmm$ (D_{4h}) point symmetry are observed in $Pb_5W_3O_9F_{10}$ where *trans*-oxide anions bridge ribbons of *trans*- $[WO_2F_4]$ and $[WO_6]$ units [104].

The atomic number and coherent neutron scattering length serve as proxies for the ability of typical structural characterization techniques, X-ray and neutron diffraction, respectively, to distinguish between anions in heteroanionic materials. The larger the difference between each respective parameter, the easier it is to distinguish the elements using each technique. For example,

although it is difficult to distinguish N^{3-} from O^{2-} using X-ray diffraction techniques, neutron diffraction will readily distinguish the two. Sulfide ions are readily distinguishable from oxide ions owing to their higher atomic scattering factor. As a result, anion ordering in oxysulfide materials is more easily determined experimentally than in oxyfluorides and oxynitrides. Additional characterization techniques to distinguish species in the anionic sublattice will be discussed later.

Heteroanionic materials can exhibit one or several types of polyhedra, e.g., tetrahedra, square-pyramids, and octahedra, linked in some fashion. The units may share corners, edges, and faces, making connections to form 1D chains, 2D layers, and complex 3D networks [105]. Other coordination polyhedra are also possible. Here we use simplified crystal coordination formula [106] when convenient to describe the building blocks and their linkages. This notation places the polyhedral units in square brackets and separates the coordination geometry of nonequivalent ligands from the stoichiometric coefficients of the chemical formula. For example the infinite 3D homoanionic perovskite $\text{CaTiO}_3 = {}^3_{\infty}\text{Ca}[\text{TiO}_3] = {}^{33}_{\infty}\text{Ca}[\text{TiO}_{6/2'}]$, where the prefixes indicate the material is an infinite 3D solid and the $[\text{TiO}_3]$ unit in brackets is the building unit generating the octahedral framework with Ti coordinated by six oxide anions (6 subscript) and the oxide anion coordinated linearly by two Ti ($2'$ subscript). The superscripts, here 3 followed by another 3, indicate the dimensionality of the unit in brackets followed by the dimensionality of the total structure.

Owing to the multiple anions in the heteroleptic polyhedral units, misassembled units can lead to a variety of disorder, which will affect crystal symmetry and often properties. The assembly of heteroleptic polyhedral building units typically occurs through the most anionic (negative) ligand. These anions preferentially form linkages to “direct” the assembly of the extended structure [107]. Although we expect the nuanced polyhedral packing principles to vary among different structure types and compositions as the optimization of relevant energy scales (electrostatic, strain, etc.)

can vary, there are some general features common to the assembly of extended structures using heteroleptic polyhedra of the same or different type.

The manner in which polyhedral units assemble is sensitive to the other cations not in the polyhedra, which are often considered to only provide the necessary countercharge balancing and structural rigidity. An example of the importance of the *A*-cation in ternary HAMs governing long-range connectivity is found in the $A\text{NaNbOF}_5$ family ($A = \text{K}, \text{Cs}$) with $[\text{NbOF}_5]$ and $[\text{NaOF}_5]$ octahedra. Both crystals exhibit long-range order of the heteroleptic polyhedra owing to the preference of fluoride to interact with the Na^+ cations. Interestingly, the *A*-site cation also determines the distinct equilibrium structures of each member of this family. Although the family can be written stoichiometrically to resemble perovskite with an ordered *A*-site vacancy, the equilibrium structure for KNaNbOF_5 is polar and noncentrosymmetric [108] with edge-shared polyhedra, whereas CsNaNbOF_5 is centrosymmetric with perovskite-like corner connectivity of the polyhedra. Chemical hardness in this case is important for achieving ordered heteroleptic units that assemble into nonisostructural compounds with nominally the same chemistry. This change in connectivity alters spatial parity, which is a symmetry that must be lifted for many acentric functionalities, e.g., piezoelectricity, nonlinear optical (NLO) responses, etc. The absence of additional cations to participate in ion-hardness matching may explain why anion ordered polyhedra are difficult to realize in some binary heteroanionic materials, for example, the ReO_3 -structured oxyfluoride NbO_2F . Although local anion order of oxide and fluoride about Nb can be realized experimentally, it is likely synthesis dependent [109] and random distributions of the oxide and fluoride ions frequently occur [110] with short-range correlated order [111].

Chemical hardness differences between oxide and fluoride ions also guide how polyhedral units connect in the oxyfluorides $\text{Rb}_3\text{Na}(\text{NbOF}_5)_2 \cdot \text{H}_2\text{O}$ and $\text{Rb}_3\text{Na}(\text{MO}_2\text{F}_4) \cdot \text{H}_2\text{O}$ ($M = \text{Mo}, \text{W}$) [112],

which exhibit partial anion order. These materials would be isostructural if their $[\text{NbOF}_5]$ and *cis*- $[\text{MO}_2\text{F}_4]$ octahedra, respectively, were homoleptic. However, these materials show both anion order and disorder about different inequivalent Nb/*M* sites. The partial anion order is largely directed by chemical hardness, the preferential bonding between Na and F, as in the $A\text{NaNbOF}_5$ family. Secondary factors affecting the connectivity of the units, and thus the anion order, are based on how “well-matched” the residual charges of the *A*-site and closest anion site are. The residual charges can be calculated based on bond valence sums and the nominal valence of the ions. When the positive residual charge was large and about equal to the negative residual charge, the sites were ordered. When they were unequal or quite small, the sites were mixed.

3.1.1 Nonidealities

Nonidealities must be considered in designing new heteroanionic materials from polyhedral assembly. These include the polar displacements of transition metal centers, polyhedral distortions (rotations and shape or size distortions from electronic and magnetic instabilities), and anion sublattice order or disorder among the linked building units, which we explore further. The latter behavior leads to nontrivial dependencies on the former two secondary intra- or interpolyhedral distortions. Ultimately, the interplay among all of these degrees-of-freedom determines the equilibrium crystal symmetry and properties.

3.1.1.1 Polar Displacements

Many heteroanionic materials with heteroleptic polyhedra of varying anion-to-oxide ratios exhibit acentric metal displacements. Metal off-centering within the $[\text{BO}_3\text{F}_3]$ units appears to be ubiquitous among compounds in the previously described $A_2BB'O_3F_3$ family. In addition, oxyfluorides

with anion ordered $[BOF_5]$ octahedral units (KNaNbOF₅, CsNaNbOF₅, and Rb₂KTiOF₅) exhibit B cations displaced toward the oxide ion forming a polar unit with $4mm$ (C_{4v}) symmetry. In oxynitrides AMO_2N ($A = \text{Er, Sr}$; $M = \text{Nb, Ta}$) perovskites [25] with ordered *cis*- $[MO_4N_2]$ octahedra, the polyhedra exhibit out-of-center metal displacements towards the N^{3-} anion, resulting in shorter $M-N$ bonds and local $mm2$ (C_{2v}) symmetry. In all cases, the inherent contrast in the covalent interactions between the transition metals and multiple anions leads to the formation of local dipoles within heteroleptic polyhedra that are useful for designing noncentrosymmetric materials [113].

3.1.1.2 Octahedral Tilts

The perovskite oxynitrides SrNbO₂N and SrTaO₂N exhibit a high-temperature tetragonal structure [103], with space group $P4/nmm$ rather than the expected cubic $Pm\bar{3}m$ owing to preferential (incomplete) anion order in the $[BO_4N_2] = \frac{3}{\infty}[BO_{4/2'}N_{2/2'}]$ octahedra ($B = \text{Nb or Ta}$). A change in the metric shape of the unit cell occurs because the oxide anion is smaller than the nitride anion and when the $[BO_4N_2]$ units arrange the c and a lattice constants cannot change identically. At room temperature, these two heteroanionic materials exhibit octahedral rotations about the tetragonal axis ($a^0a^0c^-$ in Glazer notation [114]), which were found to depend on the *cis*-ordering of the two nitrides in each $[BO_4N_2]$ and the successive connectivity of these polyhedra. Interestingly, this tilt pattern is the same as that found in the low-temperature polymorph of the homoanionic oxide perovskite SrTiO₃, which is known to be an incipient ferroelectric, and may have motivated searches for ferroelectricity in thin film SrTaO₂N [115]. One consequence of the octahedral tilts in heteroanionic materials is that the structural distortion will lift crystal-site symmetries that require some anion positions to be equivalent. As a result, these oxynitrides are strictly not tetragonal but rather exhibit monoclinic symmetry. In addition, the type of octahedral tilting can be tuned

with metal chemistry as in homoanionic materials such as alkaline-earth and rare-earth titanate oxides; for example, the substitution of Sr with Ca (and other smaller ionic radii metals like La, Ce, and Pr) cause additional tilts to occur, specifically the pervasive orthorhombic $a^-a^-c^+$ $Pbnm$ tilt pattern [29, 93, 116]. As before, long-range anion order results in symmetry reductions (although usually with preservation of inversion symmetry) depending on whether the octahedral $[\text{TaO}_4\text{N}_2]$ units arrange in two or three dimensions [117]. Similar interplays between (partial) anion order and octahedral tilt patterns are observed in transition metal oxyfluorides [118].

3.2 Electronic Structure Changes

The essence of electronic structure design in transition metal compounds (TMCs) is rooted in the modulation of electronic states near the Fermi energy by changing the chemical interactions between transition metal d states and ligand p states. In solids, the choice of anion can greatly determine the size of bandgaps, orbital hybridization, band dispersions, crystal field splitting, etc., because the anion p levels are completely filled and lie below those of the metal. The combination of transition metals with d levels that are either empty or filled with n d electrons (d^n -electron configuration) and multiple anions will lead to a variety of electronic structures and physical properties of heteroanionic materials. In this section, we review the consequences of the metal valence (electron filling) and the exchange of anions with electronegativities and charge that differ from O^{2-} on the distribution of the low-energy orbital states and electronic properties of heteroanionic materials.

First, we note that even in relatively simple heteroanionic materials, one does not find that the material's electronic structure is described simply as a superposition of the electronic properties of the homoanionic components. Although prior work has established that the difference between the cation and anion electronegativities correlate well with the size of bandgaps of many insulating

solids [119], the application of Vegard’s law often fails to provide an adequate description of the electronic structure [120].

Consider for example the “simple” binary oxynitride Si_2ON_2 . Electronic structure calculations based on density functional theory (DFT) show that the electronic density-of-states (DOS) of the oxynitride Si_2ON_2 cannot be reproduced by a superposition of the homoanionic constituents, Si_3N_4 and SiO_2 [121]. How does the crystal and local structure of the heteroanionic material compare to that of the closest binary homoanionic materials? The silicon nitride (Si_3N_4) and oxide (SiO_2) both exhibit tetrahedral bonded networks of homoleptic ${}^3_{\infty}[\text{SiN}_{4/3}]$ and ${}^3_{\infty}[\text{SiO}_{4/2}]$ units, respectively. The polar oxynitride Si_2ON_2 (space group $Cmc2_1$) also exhibits a tetrahedral silicate-like network; however, it is composed of heteroleptic ${}^3_{\infty}[\text{SiO}_{1/2'}\text{N}_{3/3'}]$ units. The structure is assembled from units that are corner-connected in a manner that allows Si to be surrounded by three triple-bridging nitride anions and one linear bridging oxide anion. This connectivity leads to an effectively layered anion sublattice in the 3D structure and the absence of inversion symmetry. Now, how does the change in atomic structure affect the electronic structure? [Add dos?](#) Because the electronegativity of N^{3-} is less than that of O^{2-} , the Si–N bonds are more covalent than the Si–O bonds. The covalency (or ionicity) of Si_2ON_2 is not the same as the average covalency of Si_3N_4 and SiO_2 owing to the inductive effect [122], which causes a redistribution of charge in the chemical bonds. In homoanionic d^0 oxides, the valence band electronic structure is nominally O $2p$ character (discussed further below), and the inductive effect will destabilize the N $2p$ states relative to the O $2p$ states such the nitride states form the band edge (Figure 3.2a). The net effect is to reduce the overall size of the charge-excitation gap in the material, shifting the absorption edge from the UV to the visible. This materials understanding of the role of anion chemistry makes it possible to design optical gaps by control of anion-to-oxide ratios [97]. In addition, the added anion-order

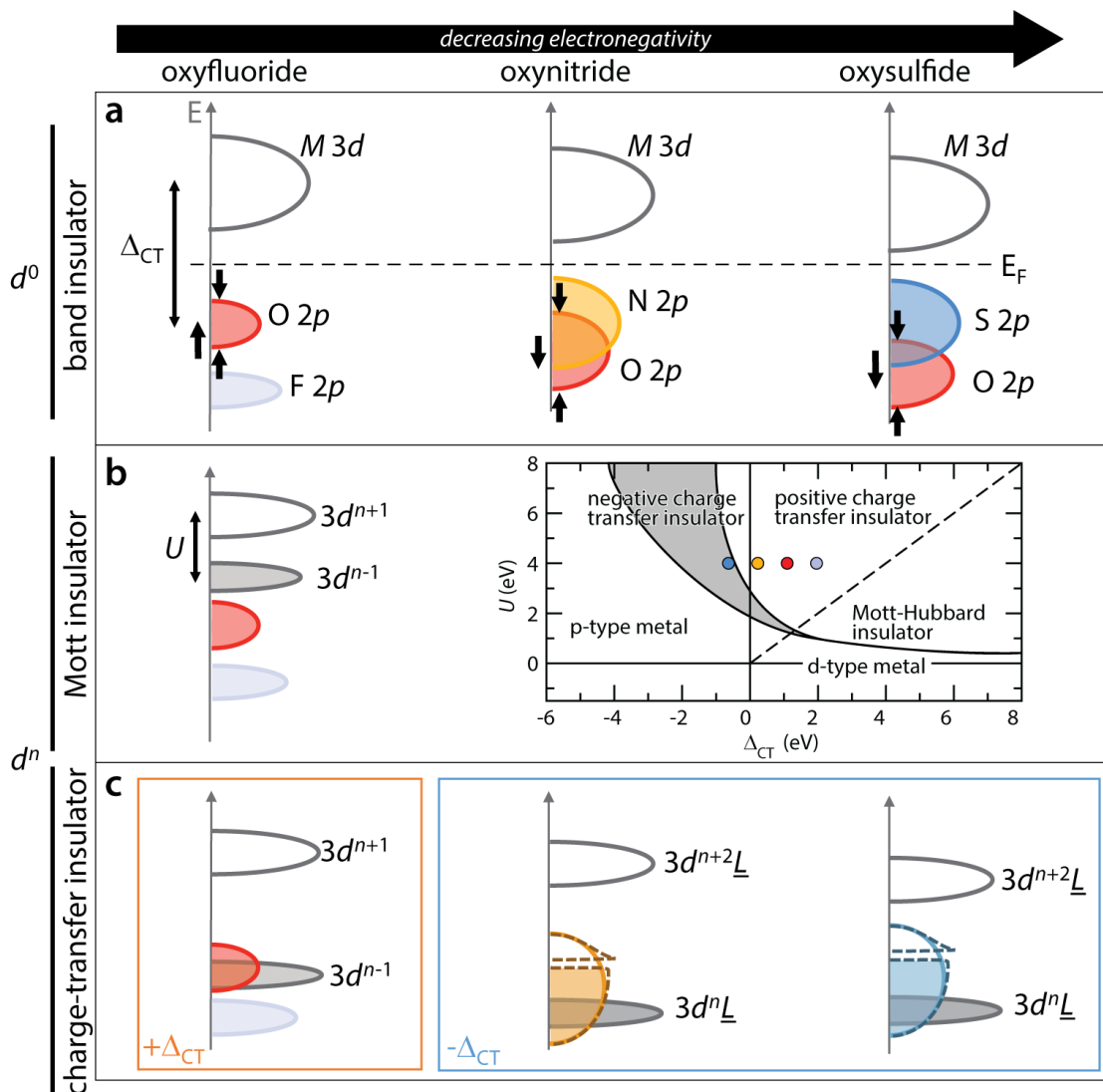


FIGURE 3.2: Electronic-structure changes due to additional anions within a polyhedral unit used to construct the heteroanionic material: modifications to the transition metal d orbital structure induced by arranging different chemical species on a lattice can alter electronic, magnetic, and optical properties. (a-c) The schematic density-of-states (DOS) for d^0 (a) and d^n compounds exhibiting Mott-insulating (b) or charge-transfer insulating (c) character depict the changes in the cation d orbital and anion p orbital energies and bandwidth, indicated by the arrows in the first row, compared to their oxide analogue. The orange and blue boxes in (c) differentiate positive charge-transfer and negative charge-transfer insulators, respectively. The broken lines in the negative charge-transfer insulator section indicate the splitting of the O $2p$ band to form a gap. The inset in (b) is a modified version of the Zaanen-Sawatzky-Allen diagram, showing the metal-insulator phase boundaries based on values of U and Δ_{CT} . The colored dots represent the qualitative change in Δ_{CT} upon anion exchange into the homoanionic oxide. The inset in (b) is adapted with permission. [1] Copyright 1994, American Physical Society.

degree of freedom makes it possible to access a variety of bandgaps because the manner in which the heteroleptic polyhedra assemble together affects the symmetry allowed orbital hybridizations between ligand p and metal d states [117].

Second, the size and character of the bandgap depend on the d -band filling. For stoichiometric d^0 compounds, one expects the bandgap size to decrease with decreasing electronegativity from fluorides to sulfides (Figure 3.2a). The electronic structure of d^n TMCs with interacting electrons requires additional considerations and is often rationalized within the Zaanen, Sawatzky, and Allen (ZSA) framework, which was originally introduced to understand the energy scales leading to metal-insulator transitions in homoanionic oxides [123]. The ZSA scheme is sufficiently complete, such that it includes the main energy scale often used to understand the electronic structure of many materials, that it can be extended to heteroanionic compounds with heteroleptic polyhedra as we show below. In this section, we briefly summarize this scheme and show how the framework can be used to rationalize and design the electronic structure of HAMs, focusing on compounds with heteroleptic building units. For a more detailed introduction to the ZSA scheme, readers can refer to Refs. [12, 124].

The first important energy scale is the on-site Coulomb energy (U), which acts to localize electrons onto the metal site and produce insulating behavior in non- d^0 transition metal compounds. In such Mott-Hubbard insulators, the bandgap scales with U , which is the energetic cost to doubly occupy a metal orbital manifold with an additional electron from another metal site via the charge transfer process, $d^n d^n \rightarrow d^{n-1} d^{n+1}$. This energy scale competes with the electronic bandwidth (kinetic energy) of the system, W , which is dictated by the interatomic hopping strength t . The main hopping interaction favoring electron delocalization is between anion p and metal d , therefore $t_{pd} \propto W$ depends on the orbital overlap between the transition metal and coordinating anion,

i , which for a heteroanionic material becomes anion dependent W_i . Generally, Mott insulating behavior arises when the bandwidth is less than the U interaction, i.e., with localized d electrons and localized moments, as in early transition metal compounds.

In addition, the filled dispersing anion p bands arise from pp hopping, and therefore, another key energy scale is the charge transfer energy (Δ_{CT}), which corresponds to the energy needed to transfer an electron from a filled anion band to an empty d band. The charge transfer energy is directly related to the electronegativity of the anion [123] and will have the largest effect on the electronic structure of heteroanionic materials. A simplified description of Δ_{CT} within a single-particle framework is given by the reaction $d^n p^6 \rightarrow d^{n+1} p^5$. Chemically one may consider this as $O^{2-} \rightarrow O^{1-}$ for the oxide anion or equivalently as the formation of a ligand hole L on the anion p orbital and a metal $d^{n+1}L$ configuration. The sensitivity of the electronic structure on this energy scale is explicitly seen in isovalent homoanionic transition metal oxides and sulfides, which are expected to have comparable U values; late transition metals such as Co, Ni, and Cu oxides are insulating whereas the corresponding sulfides are metallic [123, 125].

In non- d^0 materials, the ZSA scheme reveals that the balance of U/W versus Δ_{CT}/W determines if a material will be metallic or insulating. The insulator, as discussed above, is either Mott-Hubbard-like or charge-transfer-like depending on whether the U or Δ_{CT} energy scale is greater. Note that U systematically increases from left to right along a transition metal row while Δ_{CT} decreases for homoanionic materials due to increased nuclear charge. For $\Delta_{CT} < U$, the lowest energy excitation is from a filled p band to an empty d orbital, which leads to the “charge-transfer insulator” classification for such compounds. In contrast, the charge gap will be $d-d$ when $\Delta_{CT} > U$ (Figure 3.2b). Electronic insulator-metal transitions then occur for critical values of Coulomb strength $U^c < U < \Delta$ (Mott-Hubbard insulators) and $U > \Delta_{CT} > \Delta_{CT}^c$. For $\Delta_{CT} > 0$,

strong bonding-antibonding splitting of the $pd\sigma$ orbitals leads to bonding orbitals far below the Fermi level and antibonding d -derived orbitals as the low-energy electronic structure. The antibonding states may then be partially occupied by selecting various cation valence states, which makes it possible to design the electronic and magnetic states of homoanionic compounds. As described below, these states can be further tuned when more than one anion is present in the coordination polyhedra.

As one reduces U or Δ_{CT} , the material should become metallic owing to orbital overlap (see inset, Figure 3.2). Indeed, one would anticipate that as Δ_{CT} decreases from a finite value (and $U \neq 0$), a metallic or semimetallic state should emerge, but a significant number of oxides remain insulating in this regime owing to p - d orbital hybridization that opens a covalent-bonding gap with a negative charge transfer energy ($\Delta_{CT} < 0$). In these compounds, an electron has fully transferred to the transition metal, making the ground state $d^{n+1}L$. This behavior is also known as self-doping [126], and may result in negative charge transfer insulators that are distinct from the other aforementioned insulators (Figure 3.2c). Compounds with $\Delta_{CT} < 0$ are of increasing interest to chemists and physicists. For example, the anion-hole character has recently been exploited for cathode design [127–129] and new charge and orbital ordering states [130] have been reported in compounds exhibiting unusually high metal oxidation states.

Typically, negative charge-transfer oxides contain transition metals with a high formal valence and are found near the end of the $3d$ transition metal series, such as NaCuO_2 [131] and rare earth nickelates [132]. Small or negative Δ_{CT} energies can be designed by selecting transition metals with large electron affinities (obtained by a high oxidation state) and/or anions with smaller electronegativities. Because of their lower electronegativities, oxynitrides and oxysulfides with late transition metals are expected to be negative charge transfer insulators. Note that Ni^{3+} , Cu^{3+}

and formally Co^{4+} and Fe^{4+} will be negative charge transfer insulators or exhibit mixed-valency, which will lead to metallicity or narrow gap semiconductivity. In contrast, oxyfluorides are likely to be positive charge-transfer insulators (Figure 3.2c). Although there are theoretical examples of positive charge transfer insulators in oxyfluorides [94], we are unaware at this time of any published oxynitrides or oxysulfides that are negative charge transfer insulators.

An example of heteroanionic materials design of electronic properties is in the performance of layered transparent *p*-type semiconducting oxychalcogenide LnCuOQ ($\text{Ln} = \text{La, Bi}$; $\text{Q} = \text{S, Se}$) [133–137]. It was designed and realized by exchanging oxygen with an isovalent and less electronegative anion to reduce the tendency toward hole-carrier localization at the top of the valence band. Several compounds in the LnCuOQ family were found to be wide bandgap materials with a highly dispersive valence band [137] and *p*-type electrical conductivity [134, 136], demonstrating the advantage of moving a materials science focus from cation to anion design strategies.

In addition to the U and Δ_{CT} energy scales, crystal field interactions and spin-orbit coupling may be exploited for electronic structure and spin-crossover control. In heteroanionic materials, the choice of anion and degree of anion order can significantly affect the crystal field splitting and antibonding *d*-derived orbital energies, which govern the magnetic and electronic properties in d^n materials. There are two contributions to the crystal field splitting: the large Coulomb interaction of the *d* electron with the charged anions and the smaller *pd* hybridization (covalency), which may be equally important for some negative charge transfer insulators [138]. The spectrochemical series approximates the amount by which the electrostatic fields generated by the different ligands modify the energy difference among the metal *d*-orbitals. Note that of the anions discussed in this review, the nitride ion is the strongest ligand while the sulfide is the weakest. The N^{3-} anion therefore induces the largest orbital modifications (crystal field splitting) and S^{2-} induces the smallest

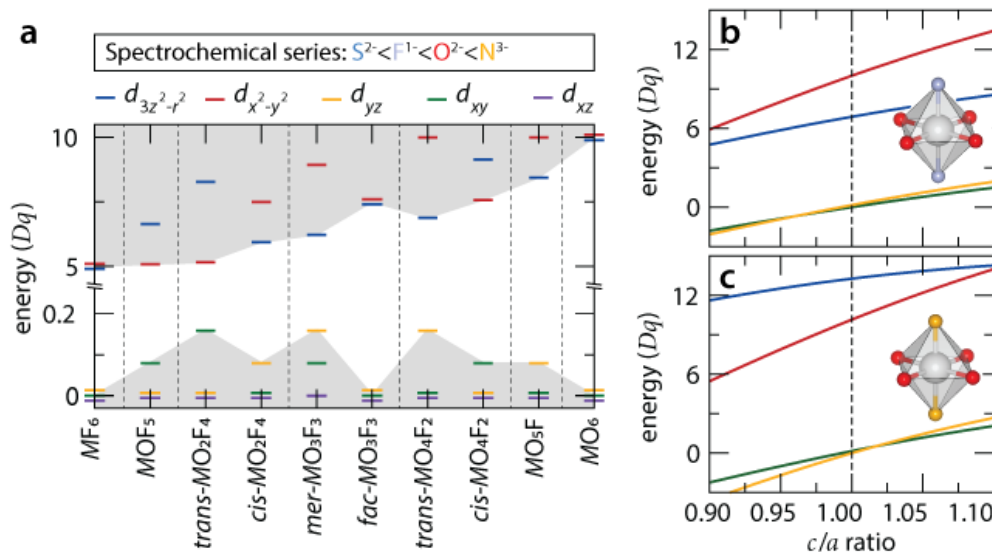


FIGURE 3.3: Crystal field effects in heteroanionic compounds with multiple anions in a single coordination unit: (a) Changes in d orbital degeneracies and energy splitting for a transition metal (M) cation with d^1 electronic configuration in the regular octahedral coordination with no bond distortions, $[MO_xF_{6-x}]$ ($x = 1-6$). (b,c) Calculated crystal field energy, Dq , under tetragonal distortion of the octahedral unit for a $trans$ - $[MO_4F_2]$ (b) and $trans$ - $[MO_4N_2]$ (c) heteroanionic building unit, where two fluoride or nitride ions, respectively, are located at the apical sites and four oxide ions occupy the equatorial sites as illustrated in the insets of (b) and (c).

(Figure 3.3). Given a hypothetical oxyfluoride compound AMO_xF_{3-x} where the anion sublattice possesses a statistical distribution of oxide and fluoride ions, the crystal field splitting varies linearly with anion concentration. However, if the heteroleptic polyhedra are ordered, then the relationship between crystal field splitting energy and anion concentration is considerably different, to the advantage of the electronic structure designer.

Figure 3.3a illustrates the evolution of the crystal field splitting for a transition metal cation octahedrally coordinated by oxide and fluoride ions with varying anion configurations with uniform metal–anion distances. Here only the electrostatic effect is included. The e_g orbitals exhibit stronger electrostatic repulsions (and larger hybridization, not shown) than the t_{2g} orbitals because the ligands are pointed directly at them. As dictated by the spectrochemical series, the crystal field splitting energy (CFSE) of the e_g ($d_{x^2-y^2}$ and $d_{3z^2-r^2}$) and t_{2g} (d_{xy} , d_{xz} , d_{yz}) is smallest ($5Dq$) for

the $[MF_6]$ fluoride unit compared to the $[MO_6]$ oxide (10Dq). In an ideal octahedral geometry, the constituent orbitals of the e_g and t_{2g} manifolds are degenerate for the homoanionic oxide and fluoride compounds. However, the electrostatic anisotropy introduced by the ordering of oxide and fluoride ions lifts the degeneracy of the orbitals in the e_g and t_{2g} manifolds. We note that the hierarchy of orbitals is also anion-order dependent. For example, the energy splitting between e_g and t_{2g} is straddled by the $d_{x^2-y^2}$ and d_{xy} orbitals for *trans*- $[MO_2F_4]$ and $d_{3z^2-r^2}$ and d_{yz} for *cis*- $[MO_2F_4]$ configurations.

Figure 3.3b,c further demonstrates how the choice of anion within a specific octahedral configuration affects the evolution of the crystal field splitting energy in a lattice under a tetragonal distortion, corresponding to the constraint found in many layered structures or mechanically imposed by thin-film epitaxy. In the *trans*- $[MO_4F_2]$ configuration with 4 in-plane oxide ions, the substitution of fluoride ions on the apical sites results in a lowering of the electrostatic repulsion along the z direction, thus lowering the energy of the $d_{3z^2-r^2}$ orbital relative to that of the $d_{x^2-y^2}$ orbital (Figure 3.3b). On the other hand, substituting the higher valence N^{3-} anion on the apical sites instead of F^- results in a larger CFSE and lowering of the $d_{x^2-y^2}$ orbital compared to the $d_{3z^2-r^2}$ (Figure 3.3c). In addition, the evolution of the CFSE is markedly different for the oxyfluoride compared to the oxynitride under the tetragonal distortion. These features indicate that reliable control of anion order in heteroanionic materials offers a platform for bandstructure design. In the following sections, we further highlight how heteroanionic materials can enhance technologically useful properties and induce new exotic phenomena.

TABLE 3.1: Common synthetic routes to realize heteroanionic materials. A check mark in the corresponding synthetic method row and products column indicate that there is a published report of the synthetic method producing a heteroanionic oxide compound.

	Synthetic method	Products		
		Oxynitride	Oxysulfide	Oxyfluoride
Bulk	Solid state synthesis	✓	✓	✓
	Hydrothermal and Solvothermal	✓	✓	✓
	Nidridation/fluorination	✓		✓
Thin Film	Pulsed laser deposition	✓		
	Chemical vapor deposition	✓	✓	
	RF Sputtering	✓	✓	

3.3 Bulk and Thin Film Synthetic Methods

Synthesizing materials with multiple anions presents new challenges compared to typical homoanionic synthesis. Typically, HAMs are metastable owing to the increased entropy from decorating the anion sites with two different anions and thus may require more than typical solid state synthesis in order to produce the desired phase. Another barrier to entry for materials scientists may be equipment needed to handle the extremely hazardous starting materials that are often needed to synthesize HAMs, such as F_2 gas, aqueous HF, and H_2S gas. Here we provide an overview of common solid state and thin film synthetic techniques that are used to prepare the three classes of HAMs discussed in this manuscript (Table 3.1). Synthetic methods have an effect on sample quality and whether the anion site on interstitial sites (particularly in oxyfluorides) [139], it appears to have little to no effect on the degree of anion order in the compound.

By far the most common preparation for bulk materials is solid state synthesis. Solid state reactions are suitable for synthesizing materials in which the heteroanionic compound is the most thermodynamically stable compound of the starting materials. Because nitrogen, fluorine, and sulfur are all liable to react with ambient air, these reactions often take place in non-ambient

atmospheres, such as vacuum sealed quartz or a flowing inert gas (N_2 , Ar). For example, the synthesis of R_2AlO_3N (R = rare earth) took place in sealed nickel tubes under N_2 gas, Sr_2FeO_3F was synthesized under Ar gas [140], and $Ln_2Ti_2S_2O_5$ (Ln = Nd, Pr, Sm) was prepared in an evacuated quartz tube [141,142]. To access metastable phases using solid state synthetic methods, external forces can be applied during the sintering step. High pressure solid state syntheses have been very successful in reaching metastable, heteroanionic phases. This method has synthesized a family of $n = 1$ Ruddlesden-Popper type oxyfluorides, Sr_2MO_3F (M =Mn, Co, Ni) [143–145]. We note that other members of this structural family, Sr_2ScO_3F [146] and Sr_2FeO_3F [147], have been prepared through typical solid state syntheses. Oxynitrides have also recently been synthesized using high pressure synthesis [148].

Hydrothermal and solvothermal methods have also been successful in synthesizing heteroanionic materials, particularly oxyfluorides. Solvothermal synthesis refers to the heterogeneous reactions in an aqueous media in a sealed or closed system [149]. When the system is heated above the boiling point of aqueous media, the vapor pressure of the system increases which has a significant effect on the mobility and solubility of the reacting species. Hydrothermal refers to syntheses where water is the aqueous media and solvothermal refers to any other solvent. Hydrothermal methods often produce higher quality samples compared to solid state methods [150] and have the advantage of accessing metastable phases without external forces. For example, the hydrothermal method can produce both the (metastable) centrosymmetric and (ground state) noncentrosymmetric polymorphs of $KNaNbOF_5$ while solid state synthesis can only produce the noncentrosymmetric polymorph [108,151]. For oxyfluorides, hydrothermal methods have been very successful because the reactions can take place in HF, which acts as both a fluorine source and mineralizer. Solvothermal synthesis have been used to synthesize a few oxysulfides, however these are the layered-type

oxysulfides, such as BiCuOS [152] and Bi₂O₂S [153], where O and S do not bond to the same cation.

Topotactic synthesis methods such as nitridation and fluorination have had some success in generating heteroanionic materials. These methods start with a precursor oxide that has an analogous cation chemistry and structure as the desired heteroanionic phase. From this point, nitridation or fluorination can take place, or the oxide can be reduced to try and control the insertion of the second anion into specific sites, as done in the synthesis of Sr₇Mn₄O₁₃F₂ [154]. Syntheses of oxynitrides typically attempt to reduce and insert nitrogen in the same step. Oxynitrides are typically prepared using so-called gas-reduction nitridation or ammonolysis in which NH₃ or NH₃–CH₄ act as both a reducing and nitriding agent. Another method for oxynitride synthesis is carbothermal reduction and nitridation, which uses carbon powder as a reducing agent and N₂ gas as a nitriding agent [155]. In oxyfluorides, the reducing step (if done) takes place separately from the fluorination step. In the synthesis of anion ordered Sr₇Mn₄O₁₃F₂ [154], the oxide analogue is reduced using CaH₂, then fluorinated with 5% F₂/N₂ at elevated temperatures. Fluorination can take place through gas-solid or solid-solid reactions with common fluorinating agents including F₂ gas, XeF₂ [156], NH₄F [157], MF₂ ($M = \text{Ni, Cu, Zn, Ag}$) [158,159], polyvinylidene fluoride (PVDF) [160,161], and polytetrafluoroethylene (PTFE) [162]. These methods will often partially or fully substitute fluorine or nitrogen into anion sites. They may also insert a layer of the fluorine or nitrogen into the structure, as in the fluorination of $n = 2$ RP La₃Ni₂O₇, which inserts an interlayer fluorine sheet into the structure as well as substituting 25% fluorine onto the apical oxygen sites [118].

Thin film synthetic methods: Oxynitrides are the only class of HAMs that have been reliably synthesized in good quality, stoichiometric films with controlled anion order [163]. Pulsed laser deposition (PLD) and nitrogen plasma assisted PLD (NPA-PLD) have been successful in synthesizing epitaxial perovskite oxynitrides ($ATaO_2N$ where $A = \text{Ca, Sr, Ba}$) on a variety of

substrates [115, 164–166]. Studies suggest that the anion coordination (i.e. *trans* vs. *cis*) may be controlled via epitaxial strain in perovskite oxynitrides [166]. Reactive frequency (RF) sputtering has been used to synthesize oxynitrides, with varying degrees of success in achieving stoichiometric films [167–169]. Chemical vapor deposition (CVD) and atomic layer deposition (ALD) have been used to synthesize oxynitrides, particularly SiO_xN_y , but like RF sputtering, these systems are still non-stoichiometric.

Stoichiometric oxysulfide films have not been synthesized to our knowledge. Non-stoichiometric oxysulfide $\text{Zn}(\text{O},\text{S})$ films have been prepared using atomic layer deposition (ALD) by reacting of diethylzinc ($\text{Zn}(\text{C}_2\text{H}_5)_2$) with deionized water and hydrogen sulfide [170]. Oxyfluoride thin films have been made by fluorinating an oxygen deficient thin film made by molecular beam epitaxy [161, 171] or pulsed laser deposition [172–177], however, these all produced non-stoichiometric films. To our knowledge, there is only one known case of fluorinating an oxide thin film to produce a stoichiometric oxyfluoride, which is the fluorination of epitaxially thin films of Sr_2RuO_4 to produce $\text{Sr}_2\text{RuO}_3\text{F}_2$ [35, 178].

3.4 Description and Characterization of the Anion Sublattice

Ordering in heteroanionic materials must be specified on both the local and long-range scales. Often in heteroanionic materials, only one type of ordered metal-anion polyhedra (e.g., $[\text{MO}_5\text{X}]$, *cis*- $[\text{MO}_4\text{X}_2]$, *trans*- $[\text{MO}_4\text{X}_2]$, etc.) exists in the structure, but the average structure shows fully disordered anion sites or multiple sites with partial anion occupancy. This indicates that although the local polyhedral units are ordered, disorder can still occur on a longer length scale through the random alignment of units (also called orientational disorder). In order to fully describe ordering on the anion sublattice, ordering must be specified on the local (i.e., polyhedral unit) scale and in

the long-range crystal structure. Here, we define the different types of anion order and disorder that can occur in heteroanionic materials and identify some of the techniques that can characterize the local and long-range order.

In the context of heteroanionic materials, ordered local structure indicates that the structure only contains one configuration of a polyhedral unit. This specifies the anion order about the metal cation, meaning that structures containing both *cis*- and *trans*-[MO₂X₄] are not included. On the local scale, disorder in these systems comes in two different flavors. The first is polyhedral disorder, in which multiple configuration of polyhedral units are observed in the crystal structure. For example, NbO₂F exhibits local anion order (–OOFOOFOOF–) along columns in the <001> direction with no correlation between columns [179]. This leads to the structure having multiple configurations of its octahedral units within the structure. We represent this as a polyhedra with fully disordered anion sites. Dynamic disorder overall appears similar to polyhedral disorder, except the origin of the disordered sites is from the polyhedral units rotating or vibrating on a shorter timescale than the measurement. This is observed in the high temperature phase of KNaNbOF₅, where if the temperature is lowered, the degree of disorder is slightly reduced. This is explored more in Chapter 5.

Long-range ordering is viewed in the context of the “average” structure over multiple unit cells. On this scale, the anion sublattice can be broken into components with anion order or disorder. Ordered anions occur when each anion site is fully occupied by one anionic element. Descriptions of disordered systems come in few different flavors. In a fully disordered system, all anion sites have equal fractional occupancies. In a partially disordered system, one or more anion sites are fully occupied and the other sites are occupied by equal fractional occupancies. In a preferentially disordered system, all anion sites are fractionally occupied but the sites have the different fractional

occupancies.

Characterizing anion order in heteroanionic materials typically requires more than one technique to verify the local and long-range order. Long-range or “average” structural techniques such as x-ray and neutron diffraction are very common, but often gives an incomplete description of anion ordering in a heteroanionic material. Characterizing the anion sublattice with x-rays is particularly difficult in oxynitrides and oxyfluorides because the electron density surrounding the anions is very similar. Anion order can sometimes be determined using a combination of structure refinements from high resolution x-ray diffraction (single crystal or powder) and bond valence sums [151], but this typically only works for structures with fully ordered anions. Unlike x-rays, neutrons can distinguish oxygen and nitrogen, making it a common technique in oxynitride research [25, 103, 180]. However, neutron diffraction requires a large volume of sample that may or may not be feasible for a given compound.

Local structural probes are extremely useful in the case of oxyfluorides because it can help distinguish between the two anions. Pair distribution function (PDF) analysis is becoming more common in oxyfluoride research because of its ability to determine the local structure [4, 101, 181]. ^{19}F NMR, when coupled with an additional structural probe such as PDF, can distinguish anion ordering and identify the correct fluorine site [4, 182]. A couple of microscopy techniques have been used to probe local anion order. Electron diffraction, including diffuse scattering, has also been helpful in determining anion order [93, 179, 183, 184]. Recent publications have also used inverse photoelectron holography to probe the local structure throughout SrTaO_2N thin films [185].

Spectroscopic characterization methods have been used as a method of determining the local coordination of metal–ligand polyhedra. Oka et al. used linearly polarized X-ray near-edge

structure (LP-XANES) and electron energy loss spectroscopy combined with scanning transmission electron microscopy electron (STEM-EELS) to reveal an increase in the N occupancy of apical sites in epitaxial thin films of $\text{Ca}_{1-x}\text{SrTaO}_2\text{N}$ with increased compressive strain. Previous studies using neutron diffraction failed to evaluate the local coordination of the $[\text{TaO}_4\text{N}_2]$ octahedra. DFT calculations and X-ray linear dichroism (XLD) measurements suggest that a higher proportion of *trans*- $[\text{TaO}_4\text{N}_2]$ octahedra is the origin of the higher N occupancy. More recently in 2021, linearly polarized x-ray absorption spectroscopy was used to successfully characterize the anion order in oxyfluoride thin films, and similarly shows that strain affects anion order in oxyfluorides [83]. In addition to the spectroscopic methods, these studies further highlights the ability to manipulate the local coordination of heteroleptic polyhedral in thin films as an additional motivation for developing epitaxial thin-film oxyfluoride and oxysulfide growth procedures, of which there are no published stoichiometric films.

In addition to experimental techniques, computational tools can provide insight into the atomic and electronic structure of HAMS and aid experimentalists in the synthesis of new materials. Density functional theory has been used frequently to determine the most likely structure adopted by a compound from candidate structures determined from experimental studies. It can also predict stable configurations of novel heteroanionic materials and potential synthetic routes to produce the desired phase. Recent studies have verified the accuracy of first-principles calculated Pourbaix diagrams [186], which can aid the synthesis of heteroanionic materials in hydrothermal reactions or other syntheses in aqueous conditions. Medium- and high-throughput techniques, which have shown success in discovering novel materials with enhanced properties in oxides [187], have also begun to be used in HAMS [188]. Derivative structure algorithms such as *enumlib* [189–191] and SOCCR [192] can be used to generate the large structure set of potential anion orderings from

which, high-throughput DFT calculations can be used to evaluate their stability. Virtual crystal approximations, creating a new ion that is a mix of two or more pseudopotentials, can be used to model mixed occupancy anion sites, this approach is time consuming as it requires rigorous testing and benchmarking to determine how “correct” the ion behaves compared to experiment.

Other computational methods include using molecular dynamic (MD) simulations, which can model temperature and dynamical effects on longer time scales. MD has been used in combination with experimental techniques and DFT to successfully determine the structure of high temperature phases in KNaNbOF_5 [7] and BaTaO_2N [96]. However, we note that this method requires that suitable atomic potentials exist to describe the interatomic interactions. Although ab initio MD methods (AIMD) can be performed, most MD simulations use empirical potentials, which may have difficulty in capturing the different chemical bonding environments of the anions. For example, high-pressure experiments were needed to obtain accurate interatomic potentials in KNaNbOF_5 from which subsequent MD simulations were carried out [7]. Monte Carlo methods can also take into account temperature effects and are most often used to calculate transport phenomena in solids and to assess phase transitions (structural order, ferroic, etc.). In heteroanionic materials, Monte Carlo simulations have previously been used to confirm the measured structure of locally ordered, long-range disordered $\text{K}_3\text{MoO}_3\text{F}_3$ given a set of constraints determined from electron diffraction studies [179]. A combination of one or more of the aforementioned computational materials approaches is likely required to understand the full temperature, pressure, and field dependence of structure-property relationships in heteroanionic materials.

3.5 Functional Properties of Oxyfluoride Materials

3.5.1 Electronic and Magnetic Transitions

Phase transitions driven by changes in chemical composition, temperature, pressure, and magnetic fields are of broad technological interest [12], because they offer access to different spin, charge, and conductivity states. In this context, chemical doping through a small amount of anion substitution has sought to induce or enhance electronic and magnetic responses in TMCs. Insulator-to-superconductor transitions occur in Nd_2CuO_4 [193] and $\text{Cd}_2\text{Re}_2\text{O}_7$ [194] upon fluorine doping, as well as in other oxyhalides such as $(\text{Ca,Na})_2\text{CuO}_2\text{Cl}_2$ with hole doping [195]. In designing magnetic oxyfluorides, researchers are limited to open shell transition metal cations (d^1 - d^9). In practice, there are few non- d^0 oxyfluorides in the current literature compared to the abundance of d^0 Nb^{5+} and Ta^{5+} compounds. One avenue to obtain a d^n electronic configuration in an oxyfluoride includes starting with a non- d^0 transition metal or reducing Nb^{5+} and Ta^{5+} to produce a magnetic HAM. In this section, we highlight one material from each approach and emphasize that these are intended to be illustrative examples: $\text{Sr}_2\text{CoO}_3\text{F}$, which exhibits spin multiplets, and an electronic phase transition in $\text{Nb}_2\text{O}_2\text{F}_3$, in which the niobium cations possess an average oxidation state of +3.5 that leads to a charge-order instability.

To rationally achieve spin-state transitions, we start with a transition metal ion that can access multiple spin states of similar energies arising from crystal field splitting energy (CFSE), Hund's exchange, and thermal energy. Co^{3+} and Fe^{2+} transition metal cations are ideal as they can access low- ($S = 0$), intermediate- ($S = 1$), and high-spin ($S = 2$) configurations under a cubic crystal field (octahedral coordination). For example, $\text{Sr}_2\text{CoO}_3\text{Cl}$ exhibits the layered $m = 1$ Ruddlesden-Popper structure with corner-connected heteroleptic $[\text{CoO}_5\text{Cl}] = \frac{2}{\infty}[\text{CoO}_{4/2'}\text{O}_{1/1'}\text{Cl}_{1/1'}]$ units [196].

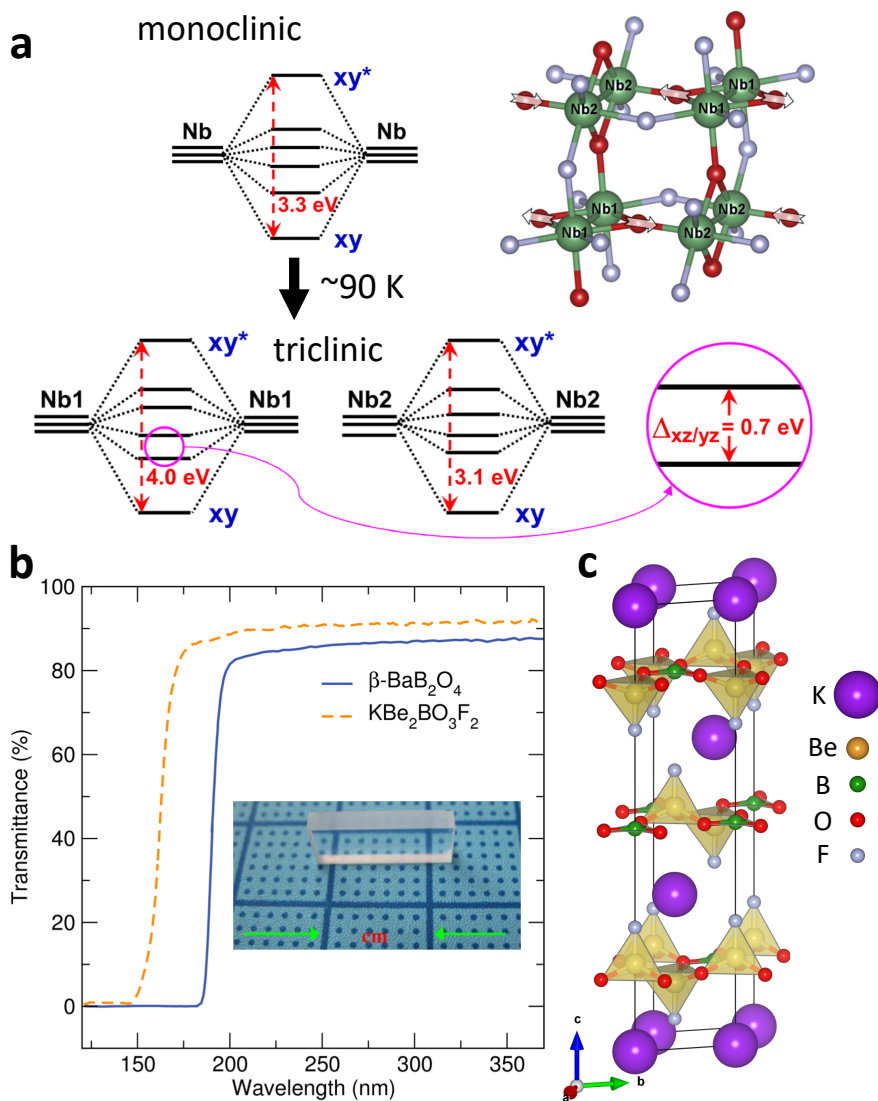


FIGURE 3.4: Electronic and optical property control in heteroanionic oxyfluorides: a) Formation of the molecular orbitals from the high-temperature monoclinic and the low-temperature triclinic phases in $\text{Nb}_2\text{O}_2\text{F}_3$. The $[\text{NbO}_3\text{F}_3]$ polyhedra shown in the upper right exhibit cooperative distortions in the charge ordered state. b) The transmittance spectra of the deep-ultraviolet nonlinear optical materials $\beta\text{-BaB}_2\text{O}_4$ and $\text{KBe}_2\text{BO}_3\text{F}_2$. The inset shows the $\text{KBe}_2\text{BO}_3\text{F}_2$ crystal grown for these measurements. c) The structure of $\text{KBe}_2\text{BO}_3\text{F}_2$, where the $[\text{BeO}_3\text{F}]$ tetrahedra link together with a $[\text{BO}_3]$ borate network through a shared oxide ion. a) Adapted with permission. [2] Copyright 2016, Elsevier. b,c) Adapted with permission. [3] Copyright 2009, Springer Nature.

The terminal chloride anion in the octahedral unit forms a relatively long Co–Cl bond such that the polyhedra are closer to square pyramids than octahedra in the structure. The layered crystal habit and the reduced coordination number stabilize the high-spin state, limiting access to a spin-state transition and supporting a transition from short-range 2D spin correlations to long-range 3D order [197]. Additional perturbations to either the chemistry or structure (bond lengths) of the building unit are required to achieve a transition to $S = 0$ or 1.

Increasing the ligand strength from Cl^- to F^- in the spectrochemical series increases the CFSE, which could favor lower spin configurations, e.g., in the oxyfluoride $\text{Sr}_2\text{CoO}_3\text{F}$. The constituent polyhedra forming this structure are similar to the oxychloride, with octahedral ${}^2_{\infty}[\text{CoO}_{4/2'}\text{O}_{1/1'}\text{F}_{1/1'}]$ units and the fluoride ions also located at the terminal apical sites [92]. Although the heteroleptic $[\text{CoO}_5\text{F}]$ octahedra are ordered, partial ordering of the long-range structure occurs with a 50/50 O/F occupancy on the apical sites. Magnetic susceptibility and electrical resistivity measurements reveal that $\text{Sr}_2\text{CoO}_3\text{F}$ is an antiferromagnetic insulator with a Néel temperature, $T_N = 323$ K [139]. Because the octahedra are locally ordered, the Co ions off-center, forming $[\text{CoO}_5]$ square pyramids such that the Co–F (~ 2.48 Å) bond is weak, but nonetheless shorter than the Co–Cl distance (~ 3.10 Å) in the isoelectronic oxychloride. Upon increasing hydrostatic pressure, the Co–F bond length shortens gradually to transform the $[\text{CoO}_5]$ square pyramids into $[\text{CoO}_5\text{F}]$ octahedra without a symmetry change to drive a spin-crossover transition [198]. The high spin Co^{3+} cation ($S = 2$) gradually evolves to a low-spin state ($S = 0$) at 12 GPa similar to the well-known spin-crossover transition in the homoanionic LaCoO_3 . The anion sublattice plays an important role in the spin crossover transition in the heteroanionic oxyfluoride because the enhanced CFSE is due to the changes in ligand covalency. This leads to abrupt changes in the long apical Co–(O/F) bond lengths and in-plane O–Co–O bond angle above 10 GPa [198]. Such anisotropic pressure effects on

the electronic structure are difficult to achieve in homoanionic analogues.

For transition metal cations with d^1 and d^2 electron configurations, temperature controlled electronic MITs often occur when the correlation strength is comparable to or greater than the bandwidth of the compound. Early transition metals such as Nb^{4+} and Nb^{3+} exhibit orbital degeneracies and strong metal-metal bonding, which can be utilized to design electronic transitions relying on charge fluctuations from the instabilities derived from formally mixed-valence cation configurations [166]. The charge fluctuations will often support a metallic state and the insulating phase will emerge as the electrons localize over one or more (atom-center or bond-centered) sites in the crystal due to U , which leads to a gap in the electronic structure and often crystal symmetry breaking. The design of these types of MIT materials requires combining cations with instabilities to the ordered state that are not so strong that the metallic state is never accessible. One avenue to realize such materials is to use reduced oxides, which can be achieved by anion control rather than through (co)substitution of cations.

To this end, Tran et al. reduced Nb^{5+} (d^0) to produce the magnetic oxyfluoride $\text{Nb}_2\text{O}_2\text{F}_3$ using a flux growth synthesis method known for producing reduced Nb compounds [199]. The room-temperature crystal structure is monoclinic ($I2/a$) with a fully disordered anion sublattice and $[\text{Nb}_2\text{O}_4\text{F}_6]$ dimeric units consisting of two NbX_6 (X being the ligand) octahedra that are collapsed onto each other by sharing edges. This building unit allows for short Nb–Nb distances ($\sim 2.57 \text{ \AA}$) and the units are then linked through shared vertices to produce a quasi-2D structure similar to the homonanoic oxide $\zeta\text{-Nb}_2\text{O}_5$ [200]. Although the heteroleptic units are likely ordered, the site specificity could not be determined using their X-ray diffraction methods.

Temperature-dependent magnetic measurements show an increase in the magnetic susceptibility upon cooling from a paramagnetic $S = 1/2$ insulating state with a precipitous drop below 90 K,

indicating a transition that quenches the magnetic moment ($S = 0$). The quenching of the moment resembles the formation of a spin-gap, typically seen in spin-Peierls materials, and coincides with the observed semiconductor-to-metal transition in the transport data. Below 90 K, $\text{Nb}_2\text{O}_2\text{F}_3$ single crystals transition from monoclinic ($I2/a$) to triclinic ($P\bar{1}$) symmetry and the loss of a the body-centering operation permits two inequivalent Nb_2X_{10} dimers with dissimilar Nb–Nb bond lengths in the triclinic structure (Figure 3.4a). The dissimilar bond lengths suggest a charge density wave state emerges from the localized Nb dimerized state according to $2[\text{Nb}_2]^{7+}$ (semiconducting) \rightarrow $[\text{Nb}_2]^{6+} + [\text{Nb}_2]^{8+}$ (semimetallic), where the different “charge ordered” $[\text{Nb}_2]^{6+}$ (d^2) and $[\text{Nb}_2]^{8+}$ (d^1) dimers have double and single bonds, respectively. Owing to the orbital overlap of these dimerized molecular orbitals in momentum space, the material transforms into a semimetallic state upon cooling.

3.5.2 Acentric Functionalities

In order for materials to exhibit properties such as piezoelectricity, ferroelectricity, and second harmonic generation (SHG), it is necessary that they crystallize in a noncentrosymmetric space group [201]. Although noncentrosymmetry is common mathematically, i.e., 16 out of 32 crystallographic point groups are either polar or chiral (21 are noncentrosymmetric), less than 20% of known inorganic materials exhibit polar or chiral symmetries [202]. Heteroanionic materials are attractive because of their inherently polar polyhedral units; in particular, the study of oxyfluoride materials that possess the octahedral heteroleptic units $[\text{MO}_x\text{F}_{6-x}]$ ($x = 1, 2, 3$), where M is a d^0 early transition metal, has intensified over the last three decades [203–205]. Despite exhibiting building units with large local dipoles (e.g., *fac*- $[\text{MoO}_3\text{F}_3]$ has a dipole moment of ~ 6.1 debye [206]) only a few oxyfluorides are found in noncentrosymmetric structures. This is due in large part to

our limited knowledge of the mechanisms that control the cooperative assembly of the units and the tendency for order-disorder transitions.

Aligning the assembly of polar polyhedral units to a noncentrosymmetric structure will generate a large polarization, however, we note that this polarization is nonswitchable under electric fields. As of this publication we are unaware of any successfully switched polar oxyfluorides. The measured ferroelectric hysteresis loop of $\text{Na}_3\text{MoO}_3\text{F}_3$, which crystallizes in the $R\bar{3}$ space group is a “banana,” thus it does not conclusively indicate a true electric-field-induced polarization reversal [207, 208]. Because the polarization arises from the order of the anions in the lattice, a possible switching mechanism would require rearrangement of ions through some diffusional mechanism. Moreover, the measured polarization for polar oxyfluorides is typically small compared to ferroelectrics like BaTiO_3 . The approximated spontaneous polarizations (P_s) of $\text{Na}_3\text{MoO}_3\text{F}_3$ and KNaNbOF_5 are $P_s = 0.021 \mu\text{C cm}^{-2}$ [207] and $P_s = 0.21 \mu\text{C cm}^{-2}$ [209] respectively, compared to $P_s = 26 \mu\text{C cm}^{-2}$ in BaTiO_3 [210]. Piezoelectric strain measurements found a d_{33} value of $\pm 6.3 \text{ pC N}^{-1}$ for KNaNbOF_5 . Although larger than α -quartz, the response is small compared to industrial standards such as lead zirconate titanate (PZT), where the d_{33} component of the tensor can be as large as $\pm 480 \text{ pC N}^{-1}$ [211].

Interestingly, noncentrosymmetric oxyfluorides have found greater utility in SHG applications. According to Chen’s anionic group theory, the design of efficient SHG-active crystals requires strong uniaxial orientational alignment of polar anionic units, which would be an advantage of ordered oxyfluorides [212]. Indeed, noncentrosymmetric oxyfluorides routinely display SHG responses rivaling crystalline quartz, however few demonstrate phase matching, which is necessary to achieve highly efficiently nonlinear optical processes [213]. For instance, $\text{NaVOF}_4(\text{H}_2\text{O})$ and $\text{NaVO}_{2-x}\text{F}_{2+x}$ originate from identical reagent mixtures, but are synthesized at different temperatures. Although

both display SHG responses, only $\text{NaVO}_{2-x}\text{F}_{2+x}$ is phase matchable [214].

A particularly active research area focuses on synthesizing NLO crystals for deep-ultraviolet (deep-UV) frequency conversion for use in semiconductor photolithography, attosecond pulse generation, and advanced instrument applications [215–219]. For noncentrosymmetric crystals to be efficiently used in deep-UV NLO applications, the following attributes are necessary: i) wide bandgap, ii) large SHG response, iii) moderate birefringence, iv) high laser damage threshold, and v) large single crystals [215]. Currently, many of the best performing UV NLO materials are borate crystals [218]. However, the incorporation of boron-oxide anionic groups also has a tendency to induce a redshift in the absorption edge, thus reducing the possibility for deep-UV applications [218]. Perhaps the most promising pure oxide borate was $\beta\text{-BaB}_2\text{O}_4$ owing to a large birefringence of 0.1127 [220]. However, $\beta\text{-BaB}_2\text{O}_4$ exhibits a highly anisotropic thermal expansion and is only transparent down to 189 nm [215]. As a result $\beta\text{-BaB}_2\text{O}_4$ cannot directly produce deep-UV coherent light by second-harmonic generation [3].

The first suitable deep-UV birefringent crystal was the oxyfluoride $\text{KBe}_2\text{BO}_3\text{F}_2$ (KBBF) engineered by Chen et al. [221]. Here, the addition of fluorine aids in shifting the band edge further into the deep UV region (Figure 3.4b) [221]. KBBF has a relatively large SHG coefficient, moderate birefringence, a bandgap of ~ 8.3 eV, and exhibits phase matchability over a wide range of wavelengths. In addition, KBBF has a high laser damage threshold and relatively high thermal conductivity [3]. The excellent NLO properties of KBBF stem from the $2\text{D}_{\infty}^2[(\text{BeO}_{3/[2'+1]}\text{F}_{1/1'})_2\text{BO}_{3/[1'+2]}]$ layers, which are composed of $[\text{BO}_3]$ and $[\text{BeO}_3\text{F}]$ units (Figure 3.4c) [219]. However, this layered morphology leads to a major shortcoming of KBBF: difficulty in growing large single crystals [222,223]. Moreover, the high toxicity of beryllium oxide used during synthesis places limitations on the practical use of KBBF in many technologies. These challenges have motivated the search for

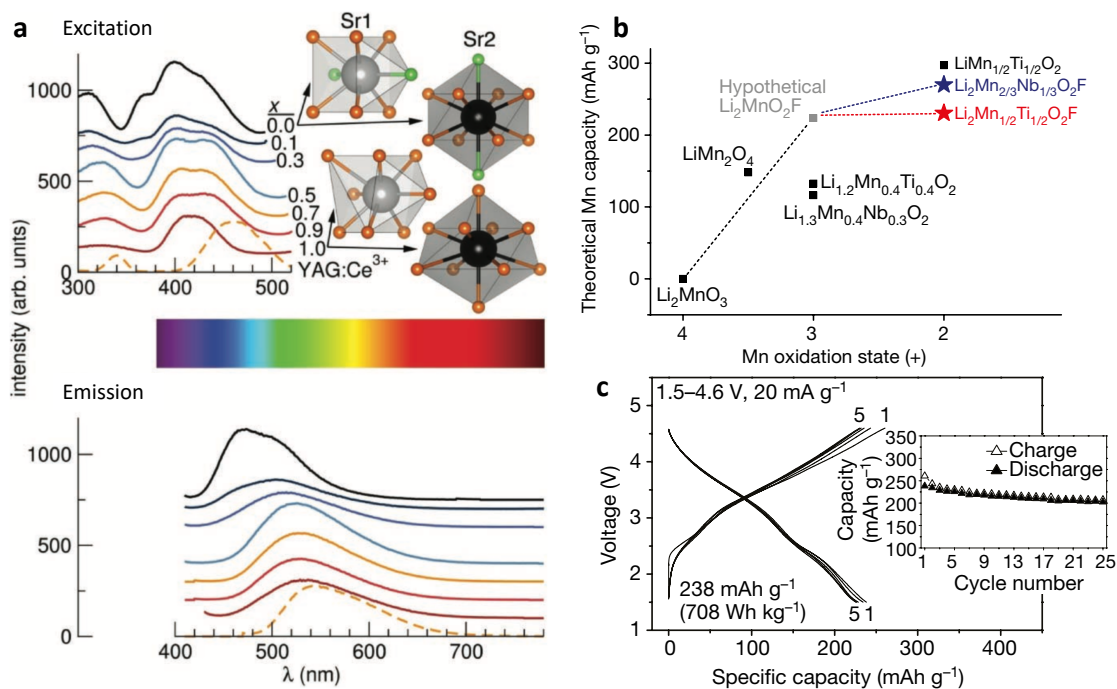


FIGURE 3.5: Heteroanionic oxyfluorides for lighting and energy applications: a) Excitation and emission spectra of the solid-solution phosphor $\text{Sr}_{2.975}\text{Ce}_{0.025}\text{Al}_{1-x}\text{Si}_x\text{O}_{4+x}\text{F}_{1-x}$ with various x values indicated. The Sr1X_8 and Sr2X_{10} polyhedra looking down the $[100]$ direction show the change in coordination environment (right inset). Light gray, black, orange, and green spheres represent Sr1, Sr2, O, and F atoms, respectively. Fluoride exchange leads to a decrease in peak excitation/emission wavelength with increase in fluoride content (lower panel). b) Theoretical capacities of Mn-redox based cathode materials with decreasing oxidation state. c) Voltage profiles and capacity retention of $\text{Li}_2\text{Mn}_{2/3}\text{Nb}_{1/3}\text{O}_2\text{F}$ when cycled from 1.5 to 4.6 V at 20 mA g^{-1} . a) Adapted with permission [4]. Copyright 2011, Wiley. b,c) Adapted with permission [5] Copyright 2018, Springer Nature.

alternative oxyfluorides and other heteroanionic materials with improved properties for NLO application [32, 188, 217–219, 222]. This research has led to many new and interesting phases including $\text{Na}_3\text{Ba}_2(\text{B}_3\text{O}_6)_2\text{F}$, which can be grown as large single crystals and exhibits large birefringence ($\Delta n = 0.0750\text{--}0.2554$) from the IR ($3.35 \mu\text{m}$) to the deep UV (175 nm) range [224].

3.5.3 Phosphors for Solid State Lighting

To design new heteroanionic phosphors for solid-state lighting, the methodology must be changed slightly because the coordination environment around the activator ion, rather than the transition metal, is key in understanding the relevant properties in these materials. Typical activator ions in phosphor materials are Ce^{3+} or Eu^{2+} , because the transition between $4f$ and $5d$ states is largely responsible for the down conversion of light [34]. Additionally, activator ion-ligand polyhedral units are rarely octahedral, tetrahedral, or other standard polyhedra; they typically sit on the A site owing to their large size. In typical phosphor materials, the principle governing the shift of emission spectra is the centroid shift and crystal field splitting in the $5d$ states. The centroid shift, or the change of the $5d$ levels because of a change in interelectron repulsion, generally shifts downward (redshifting the emission spectra) with decreasing anion electronegativity; in other words, (oxy)nitrides would emit the highest wavelength of light, oxides would be slightly lower, and (oxy)fluorides would be the lowest. As discussed in § 3.2, the choice of ligand affects the crystal field splitting between the highest and lowest d orbital. In phosphor materials, the distortion of the coordination geometry about the activator ion may have a larger effect on the CFSE. Overall, an oxyfluoride structure will likely blueshift the emission spectra, though it is dependent on the degree of anisotropy of the activator ion coordination. Additional properties needed for efficient solid state lighting, such as quantum efficiency (QE) and good thermal stability, are largely determined by the structure of the host lattice.

To investigate the effects of fluoride substitution in a phosphor material, Seshadri et al. [4] studied solid solutions of the anion-ordered oxyfluoride $\text{Sr}_3\text{AlO}_4\text{F}$ and Sr_3SiO_5 as hosts for Ce^{3+} activator ions. These materials are isostructural and charge balanced with fluoride substitution

though a stoichiometric substitution of the *B*-site cation. The resulting phosphor materials, $\text{Sr}_{2.975}\text{Ce}_{0.025}\text{Al}_{1-x}\text{Si}_x\text{O}_{4+x}\text{F}_{1-x}$ (SASF:Ce³⁺), emitted yellow-green light, had high quantum yield values, and tunable excitation and emission wavelengths with fluorine content. ¹⁹F NMR confirmed the fluorine sits in a single crystallographic site in all compositions and confirmed the oxyfluoride end member has a fully ordered long-range structure. The excitation wavelengths range from 390 to 450 nm with increasing *x* (or decreasing F content, Figure 3.5a), which agrees well with excitation sources in LED chips. The emission spectra in these materials were generally broad (comparable to commercial materials) and the peaks ranged from 474 to 537 nm with increasing *x*. As expected, a redshift in emission spectra occurs with a decrease in fluoride content. The crystal field splitting also contributes to the increased redshift with decreased fluoride content. Somewhat surprisingly, coordination about both Sr sites becomes increasingly anisotropic as the fluoride content decreases. Room-temperature QE measurements of the oxyfluoride and oxide end-members shows that the oxyfluoride has a higher QE (83% and 62%, respectively), though this only increases monotonically until *x* = 0.5, which has a maximum QE of 85%. Previous work on a related compound has attributed this to the softer phonon modes associated with the fluorine atoms [225]. Thermal quenching of QE is also generally diminished in compositions with more fluoride, for the same reasons. Similar trends in fluoride content and excitation wavelength, emission wavelength, QE, and thermal quenching have been obtained from other oxyfluoride solid solutions [182].

3.5.4 Battery Materials

The benefits of fluoride substitution in battery materials can be initially assessed with Vegard's law. Assuming oxyfluorides will lie somewhere between its oxide and fluoride end members, fluoride battery cathode materials feature higher (theoretical) specific capacities and higher reduction

potentials compared to oxides. However, they also suffer from worse electrode cycle life, lower conductivities, and large hysteresis of lithiation/delithiation voltages, which makes them poor candidates for commercial applications [10, 226]. The goal of oxyfluoride research in battery materials has therefore been to maintain the higher capacities and potentials of fluorides while avoiding their pitfalls. To generate novel oxyfluorides for battery materials, the transition metal cation must have multiple attainable oxidation states to enable the necessary redox reactions. Here, the coordination of the polyhedra facilitates the anion order in the structure. For intercalation batteries, which lithiate through insertion of Li into the crystal, the units are typically assembled into a layered structure-type. Many oxyfluorides investigated as battery cathodes phase separate or decompose as they are charge and discharged, indicating that the materials are likely lithiating the fluorine through a conversion mechanism [181].

Silver vanadium oxyfluorides such as $\text{Ag}_4\text{V}_2\text{O}_6\text{F}_2$ (SVOF) have been proposed as cathode materials for implantable cardioverter defibrillator in primary batteries. To improve over the current industry standard, $\text{Ag}_2\text{V}_4\text{O}_{11}$ (SVO), new materials need higher volumetric capacities and greater capacities over 3 V. Fluoride substitution is an ideal candidate for this application because it generally increases the cell potential. $\text{Ag}_4\text{V}_2\text{O}_6\text{F}_2$ contains isolated chains of corner connected $[\text{VO}_4\text{F}_2]$ octahedra and $[\text{VO}_4]$ tetrahedra, with Ag ions between the chains forming a relatively open structure. Preliminary Li insertion electrochemical results as a primary cathode were promising; SVOF exhibited a higher capacity above 3 V and a higher silver reduction potential (48 mAh g^{-1} and 300 mV, respectively, higher than SVO) [227]. However, upon further investigation of SVOF as a secondary battery cathode, it was found that nearly half of the capacity is irreversible on the second charge, largely owing to the irreversible Ag reduction [31]. A combination of in situ XRD and EPR revealed an Ag^+/Li^+ displacement lithiation mechanism occurs from $\text{Li}_0\text{Ag}_4\text{V}_2\text{O}_6\text{F}_2$ to

$\text{Li}_{\sim 4.0}\text{Ag}_4\text{V}_2\text{O}_6\text{F}_2$ and appears to be nearly entirely irreversible. The reversible capacity arises from a redox mechanism (V^{5+} to V^{3+}), but it is accompanied by an unfavorable decrease in the cathode polarization.

Fluorine can also be used to stabilize low-valence transition metals for improved capacity in Li-ion cathode materials. A new strategy for high capacity Mn-based Li-ion cathode materials has been to stabilize the Mn^{2+} state, such that a double oxidation reaction can be triggered and achieve high theoretical capacities (Figure 3.5b) without O redox. Although O redox can improve the capacity of the materials, it also causes O loss, which results in voltage and capacity fade. Lowering the Mn valence can be achieved through incorporation of a high-valent cation and by substitution of O^{2-} with F^- . Recent experiments on $\text{Li}_2\text{Mn}_{2/3}\text{Nb}_{1/3}\text{O}_2\text{F}$ and $\text{Li}_2\text{Mn}_{1/2}\text{Ti}_{1/2}\text{O}_2\text{F}$ show high reversible capacities of 238 and 259 mAh g^{-1} (Figure 3.5c), respectively, with little O redox [5]. Additionally, X-ray absorption spectroscopy measurements show that the electrochemical process is reversible with Mn^{2+} being fully recovered on discharge and minimal oxygen redox over electrochemical cycling.

Chapter 4: Predicting the Structure Stability of Layered Heteroanionic Materials Exhibiting Anion Order

Reprinted with permission from Ref. [228]. Copyright 2019 American Chemical Society.

4.1 Introduction

Heteroanionic materials, which are an emerging inorganic materials class, aim to deliver enhanced material function through the incorporation of multiple anions of different size, charge, and electronegativity [26, 229]. Anion engineering aims to combine the advantageous properties of each anion species or create unexpected phenomena through the incorporation of multiple anions in ordered arrangements [27]. This approach has been successful in generating new materials for water splitting (such as TaON) [230], second-harmonic generation ($\text{Ba}_4\text{B}_{11}\text{O}_{20}\text{F}$) [188], and energy storage ($\text{Li}_2\text{Mn}_{2/3}\text{Nb}_{1/3}\text{O}_2\text{F}$) [5], among others technologies.

One major challenge that has hampered the exploration of this family of compounds is the inability to accurately predict (the appearance or lack of) anion ordering in heteroanionic compounds. Anion order can be critical to the appearance of technologically relevant properties, particularly those which require a noncentrosymmetric structure in order to appear, such as piezoelectricity,

multiferroicity, and second-harmonic generation. Density functional theory based high-throughput methods potentially offer a solution to this problem, as it can reliably and nearly autonomously assess the relative stability of different anion orders and the thermodynamic stability (i.e. a large negative formation energy or convex hull distance) of the lowest-energy polymorph. These techniques have been successful in predicting novel oxide materials with desirable properties, such as high- ZT materials for thermoelectric applications [231] and high quantum yield phosphor materials for solid state white lighting [232]. However, enumeration of all possible anion orders, including (quasi)random geometries, generates about an order of magnitude more structures [192,233] than a conventional high-throughput structure search. Consequently, the computational cost is also at an order of magnitude greater (or more), depending on the scaling of the anion order configurational space. This motivates the search and evaluation of computationally cheaper methods for assessing material stability. Established methods, such as Ewald sums [234] or bond valence based methods [235,236], may be effective screening approaches to reduce the number of advanced quantum mechanical calculations required to predict the electronic, magnetic, and optical properties of novel heteroanionic compounds.

Previous research in heteroanionic materials has shown that bond valence sums (BVS) and Pauling’s second crystal rule (PSCR) can be used to *a priori* predict the distribution of anions in systems with anions of different charge [237]. For example, consider $\text{Sr}_2\text{TaO}_3\text{N}$ (or ${}^{33}\text{Sr}_2[\text{TaO}_{2/2'}\text{O}_{2/1'}\text{N}_{2/2'}]$ when written in the crystal coordination formulation) [106] which adopts the Ruddlesden-Popper structure, defined by two-dimensional sheets of *cis*- $[\text{TaO}_{2/2'}\text{O}_{2/1'}\text{N}_{2/2'}]$ octahedra. Experimentally, it exhibits apical anion sites that are fully occupied by O (hence the terminal 1-coordination) and equatorial anion sites with a statistical 50/50 O/N occupancy. PSCR predicts that the N anions in $\text{Sr}_2\text{TaO}_3\text{N}$ will prefer to occupy the equatorial sites; however, the rule cannot distinguish whether

there will be complete anion order on those sites, because PSCR only accounts for the coordination environments of each Wyckoff site (the apical and equatorial anion sites have different orbits, $4e$ and $4c$, respectively, with site symmetries $4mm$ and mmm). Because recent studies have shown that BVS and DFT lattice energetics are correlated [238,239], it is likely that the crystal-chemistry method is able to grossly discern bonding preferences by assessing how well local bond constraints are satisfied, for example, through the so-called global-instability index (GII) [240,241]. These facts together suggest that *a posteriori* BVS methods could be used to distinguish between anion ordered structures, accelerating the search process and arriving at a set of low-energy structures for further computational or experimental interrogation.

Here we show that global instability indices (GII), which rely on bond valence methods, can quickly and reliably assess the structure stability of heteroanionic materials. We evaluate the performance of GII using the the $n = 1$ Ruddlesden-Popper (RP) structure with composition $A_2BX_1_2X_2_2$ as the model structure, because $n = 1$ oxyfluorides and oxynitrides show preferential anion ordering. In addition, the two-dimensional perovskite layers (either ${}^2_{\infty}A[BX_{1_2/2'}X_{1_2/1'}X_{2_2/2'}]$ or ${}^2_{\infty}A[BX_{1_4/2'}X_{2_2/1'}]$) provide more degrees of freedom for lifting inversion symmetry [242]. We first present a group theoretical analysis of this structure type, highlighting irreducible representations (irreps) that have displacive and anion ordering character. A subset of the distorted structures obtained from this analysis are then used to assess the ability of the global instability index to discriminate stable and unstable structures. To that end, we describe a computational filtering process, which utilizes both GIIs and DFT calculations to assess the thermodynamic stability of a $n = 1$ Ruddlesden-Popper heteroanionic material. We show that the inclusion of an additional screening step based on BVS and GII reduces the computational cost of heteroanionic composition screening by 50% and predicts new stable oxyfluorides for synthesis.

4.2 Methods

4.2.1 Group Theoretical Methods

We use representation theory to investigate hypothetical symmetry-lifting transitions from the aristotype homoanionic $n = 1$ (high symmetry) structure (Table 4.1) to an anion ordered structure. The translation of ${}^3_{\infty}[\text{BX}_{6/2'}]$ perovskite layers perpendicular to their stacking direction naturally stratifies the anion Wyckoff sites into those located on the equatorial $4c$ and apical $4e$ positions in the B-centered octahedra. We then construct hettotype (low-symmetry) structures from the $I4/mmm$ aristotype that would further split the $4c$ and $4e$; here, we assume there exists a group-subgroup relationship, characterized by an irreducible representations (irreps) and a corresponding order parameter direction (OPD).

There are two methods to identify all irreps and OPDs that alter the X1 and X2 site symmetry such that the four equivalent anions on each site are no longer required by symmetry to be identical. This site splitting then permits the occupancy of the new Wyckoff positions by chemically distinct species, which we denote by a prime, e.g., X1' or X2'. The first method utilizes a derivative-structure algorithm, such as `enumlib` [189–191] or `SOCCR` [192], which generates all possible hettotypes compatible within a supercell given as a multiple of the $I4/mmm$ cell and then removes all symmetric duplicates. This process generates all structures suitable for the subsequent stability analysis, but in order to identify the irreps, OPDs, and mode representations between the aristotype and derivative structures, the user must run a separate mode analysis on the structures. The second method is to enumerate all combinations of irreps and OPD and then identify those which independently or together reduce the symmetry of the anion sites. This approach can

TABLE 4.1: Structural information of the prototypical $n=1$ Ruddlesden Popper structure with space group $I4/mmm$. Positions are given in fractional units; u, v are free parameters.

atom	Wyckoff site	site symmetry	x	y	z
A	$4e$	$4mm$	0	0	u
B	$2a$	$4/mmm$	0	0	0
X1 (equatorial)	$4c$	mmm	0	$\frac{1}{2}$	0
X2 (apical)	$4e$	$4mm$	0	0	v

be more cumbersome but has been successfully applied to classify anion order in perovskite compounds [233]. We select the latter method for the present study and utilize the group theoretical packages ISOTROPY [243] and ISODISTORT [244] to facilitate the analysis. Throughout, we use the Miller and Love convention [245] for irrep labeling.

4.2.2 GII Optimizations

To reduce computational cost, we have created a GII minimizer which relaxes the lattice parameters of a given structure to minimize the GII value while keeping the ionic positions fixed. This ensures a moderately accurate GII value while screening the chemical composition space on identical starting structures. The GII minimizer is based on bond valence sums, which are a quantitative measure of ideal bonding in inorganic solids [240]. Each cation-anion pair has a unique set of empirically determined bond valence parameters, B and R_0 , from which the bond valence of a unique pair, s_{ij} , can be determined from their experimental bond lengths, R_{ij} :

$$s_{ij} = e^{(R_{ij}-R_0)/B} \quad (4.1)$$

In our implementation, we use a slightly modified version of the bond valence parameter (BVP) dataset from the International Union of Crystallography [246], which is a collection bond valence parameters from the literature. The dataset contains many bond valence parameters from Ref. 247,

which states that the bond valence parameters for cations paired with anions less electronegative than oxygen (e.g. N, Br, S, etc.) will in general not vary between different cation oxidation states (i.e. the bond valence parameters for $\text{Ta}^{+9}\text{-N}^{-3}$, should be the same as $\text{Ta}^{+5}\text{-N}^{-3}$). Therefore, we have modified the dataset to include multiple cation oxidation states when paired with nitrogen. This modified data set is available in Appendix A. For example, the database only lists BVP for $\text{Ta}^{+9}\text{-N}^{-3}$ despite the source of these parameters stating that it should be used for multiple oxidation states. In these cases, we create a new bond-valence pair with the same anion but now with a cation of a lower oxidation state (e.g., $\text{Ta}^{+5}\text{-N}^{-3}$) and the same BVP value. When multiple BVPs are available for the same cation-anion pair, our code attempts to pick the parameters in which $B=0.37$, which is considered a universal value [248]. If it is unable to do so, then GII implementation selects the first parameter that appears in the database.

Once the BVPs are chosen, the bond valence sum of an ion, $V_{i(\text{calc})}$, is computed by summing over all the individual bond valences about each ion as $V_{i(\text{calc})} = \sum_j s_{ij}$. The bond valence sums approximate the valence of an ion, i . In our bond valence sum implementation, we sum over all atomic pairs whose bond lengths are less than 6 \AA , which at least captures the first and second nearest neighbors in the $n=1$ RP structures. After the bond valence sums of all ions in the structure are evaluated, the global instability index (GII) is calculated as the root-mean-square error of the bond valence sum from the nominal valence, $V_{i(\text{ox})}$, over all ions in the structure:

$$\text{GII} = \left\{ \frac{\sum_{i=1}^N (V_{i(\text{ox})} - V_{i(\text{calc})})^2}{N} \right\}^{1/2} \quad (4.2)$$

The GII value then represents the extent from which the structure presents deviations from ideal bonding between all cation-anion pairs. This value can be also interpreted as a measure of the

amount of internal strain in the system [240]. Typically, unstrained stable structures exhibit GII values less than 0.1 v.u. (valence units), but strain stabilized structures can have GII values ranging up to 0.2 v.u. [240].

Given these thresholds for experimentally observed compounds, researchers have attempted to use GII as a pseudo-energy upon which to predict new phases [249, 250] or for structure optimization [238]. These have largely focused on using GII and BVS to determine ideal atomic positions and evaluate the stability of compounds. Although our GII minimizer attempts to minimize lattice stresses by changing the lattice parameter, it could be adapted to optimize both the lattice and atomic degrees of freedom simultaneously. Thus, the general functional form of GII is $\text{GII}(a, b, c, \alpha, \beta, \gamma, \{r_i\})$, such that it is dependent on the lengths of the cell edges (a, b, c) , the interaxial angles (α, β, γ) , and the fractional coordinates of the ions $(\{r_i\})$. Because we fix the interaxial angles and fractional coordinates of our structures and relax only the axial lengths, the GII is a function of three cell parameters: $\text{GII}(a, b, c)$. (Note that the interaxial angles are all fixed to 90 because all the structures we consider are either tetragonal or orthorhombic). In the analysis that follows, we account for atomic relaxations using a first-principles energy method, because the GII minimization of the atomic positions requires semi-empirical constraints to ensure the optimization is convex [251].

Our GII minimizer uses the sequential least squares programming (SLSQP) minimization scheme, as implemented by SciPy [252], to optimize the lattice parameters and minimize the GII. At its core, this method approximates the first derivative (Jacobian) and second derivative (Hessian) to find the direction and size of the next minimization step. If we consider the GII as a pseudo-energy, the internal energy of the system can be expanded as a Taylor series about our

vector $\mathbf{x} = (a, b, c)$:

$$\text{GII}(\mathbf{x} + d\mathbf{x}) = \text{GII}(\mathbf{x}) + \frac{\partial \text{GII}}{\partial \mathbf{x}} d\mathbf{x} + \frac{\partial^2 \text{GII}}{\partial \mathbf{x}^2} (d\mathbf{x})^2, \quad (4.3)$$

where the first derivative is the force and the second derivative is the Hessian matrix. Here, the force F between ions i and j can be approximated by $F = V_{i(ox)} - \Sigma s_{ij}$, such that if $F < 0$, then the bond is too short and if $F > 0$, then the bond is too long. To prevent the lattice from diverging and becoming unphysical, we set bounds on the lattice parameter relaxation such that the short axes must be between 3 and 6 Å (or 4 and 7 Å for cells that were $\sqrt{2} \times \sqrt{2} \times 1$) and the long axis between 11.5 and 14.5 Å. We also note that we included a penalty in the GII minimization process, which increases as the a/b ratio (or the ratio of the short-axes) deviates from 1. Our rationale for this penalty is that all synthesized compounds are tetragonal and if unpenalized, the GII relaxed structures have unphysical elongations of the long axis and a/b ratios as large as 0.7. Our GII minimization code is available at https://github.com/MTD-group/GII_Minimizer-relax_lattice.

4.2.3 Density Functional Theory Calculations

Density functional theory (DFT) calculations are used to validate the results of the GII optimizer and further identify candidate materials for synthesis. DFT calculations are performed using the projector-augmented wave (PAW) formalism [87, 91] as implemented in the Vienna *Ab initio* Simulation Package (VASP) [43, 44] within the generalized gradient approximation (GGA) of Perdew-Burke-Ernzerhof (PBE) for densely packed solids (PBEsol) [62], as recommended for oxyfluorides. [253]. A 600 eV plane-wave cutoff was used, and k -space integrations were performed on a $6 \times 6 \times 3$ Monkhorst-Pack mesh [79] with Gaussian smearing (10 meV width) for Brillouin zone integrations. For all calculations, total energies were converged to 10^{-8} eV. In all structural

relaxations, forces on the ions were converged to within $1 \text{ meV } \text{\AA}^{-1}$ and lattice stresses to below 0.1 kbar . For systems with open d shells, we impose a collinear antiferromagnetic (AFM) ordering within a $\sqrt{2} \times \sqrt{2} \times 1$ supercell for the oxyfluorides and collinear ferromagnetic (FM) ordering for the oxynitrides. Convex hulls and phase diagrams were created using `Pymatgen` [254]. All crystal structure information is available in the Appendix A.

4.3 Results and Discussion

4.3.1 Group Theoretical Analysis

Previous work suggests that displacive distortions may be a practical method to control anion ordering in heteroanionic materials [192, 233]. Commonly, researchers have held that short-range interactions, such as second-order Jahn-Teller distortions, drive ordering in local polyhedral units [102, 107], with long range anion order largely being determined by secondary cations [151, 255]. However, recent studies on anion order in compounds with octahedral rotations have suggested that these cooperative distortions may also promote or suppress anion ordering in heteroanionic perovskites and Ruddlesden-Popper materials [25, 118]. We therefore choose to enumerate and categorize those irreps which represent cooperative displacements of anions or cations that alter the site symmetry of one or both Wyckoff sites, $X1 \rightarrow X1'$ and $X2 \rightarrow X2'$, of the ideal $I4/mmm$ aristotype.

There are a total of 111 unique combinations of irreps and OPDs which split one or both of the anion sites. The number of unique OPDs and irreps which split the apical anion site is 85 whereas 95 alter the equatorial anion site. (Many of the irreps lower the symmetry of both sites.) Of the possible irreps considered, only 17 lead to noncentrosymmetric hettotypes.

TABLE 4.2: Polar and antipolar irreps that alter the site-symmetry of the anions. Irrep labels correspond to the following wavevectors (primitive basis): $\Gamma = (0, 0, 0)$, $M = (1/2, 1/2, -1/2)$, and $X = (0, 0, 1/2)$. Lattice vectors are given relative to the primitive cell of the aristotype $n=1$ Ruddlesden-Popper structure.

irreps	OPD	lattice vectors	space group	B-site symmetry reduction
Γ_3^-	(η_1)	$\sqrt{2}a \times \sqrt{2}b \times c$	$I4mm$	$4mm$
Γ_5^-	$(\eta_1, 0)$	$\sqrt{2}b \times c \times \sqrt{2}a$	$Imm2$	$mm2$
Γ_5^-	(η_1, η_2)	$2b \times c \times \sqrt{2}a$	Cm	m
M_3^-	(η_1)	$\sqrt{2}a \times \sqrt{2}b \times c$	$P4/nmm$	$4mm$
M_5^-	(η_1, η_1)	$c \times \sqrt{2}a \times \sqrt{2}b$	$Pmnm$	$mm2$
M_5^-	(η_1, η_2)	$\sqrt{2}b \times c \times \sqrt{2}a$	$P2_1/m$	m
X_2^-	$(0, \eta_1)$	$2b \times c \times 2a$	$Cmcm$	$m2m$
X_2^-	(η_1, η_1)	$2a \times 2b \times c$	$P4/nmm$	$\bar{4}m2, 4mm$
X_2^-	(η_1, η_2)	$2a \times 2b \times c$	$Pmnm$	$mm2, mm2$
X_3^-	$(0, \eta_1)$	$c \times 2a \times 2b$	$Cmcm$	$m2m$
X_3^-	(η_1, η_1)	$2a \times 2b \times c$	$P4_2/mnm$	$m.2m$
X_3^-	(η_2, η_1)	$2a \times 2b \times c$	$Pnmm$	$..m$
X_4^-	$(0, \eta_1)$	$c \times 2a \times 2b$	$Cmma$	$mm2$

Below we discuss the mode representations (i.e., polar and antipolar distortions, octahedral tilts, etc.) in more detail; however, we first make a few caveats: (1) We exclude structures whose B-site have a site symmetry of 1. (2) We constrain our analysis to displacive modes that uniformly alter the symmetry of all octahedra; distortions that break the equivalence between perovskite layers, allowing the structure to have inequivalent heteroleptic $trans$ -[BX₁₄X₂'] and $trans$ -[BX₁₄X₂'] octahedra, are not included. (3) The splitting and occupancy is based on a symmetry argument and in the ensuing analysis we make no immediate claim on stability, which requires a proper treatment of the chemistry of the cations, anions, and the occupied sites as we show later. (4) When possible, we also list the experimentally known compounds that adopt symmetries induced by these representations. All known heteroanionic $n=1$ RP compounds are also listed in Appendix A

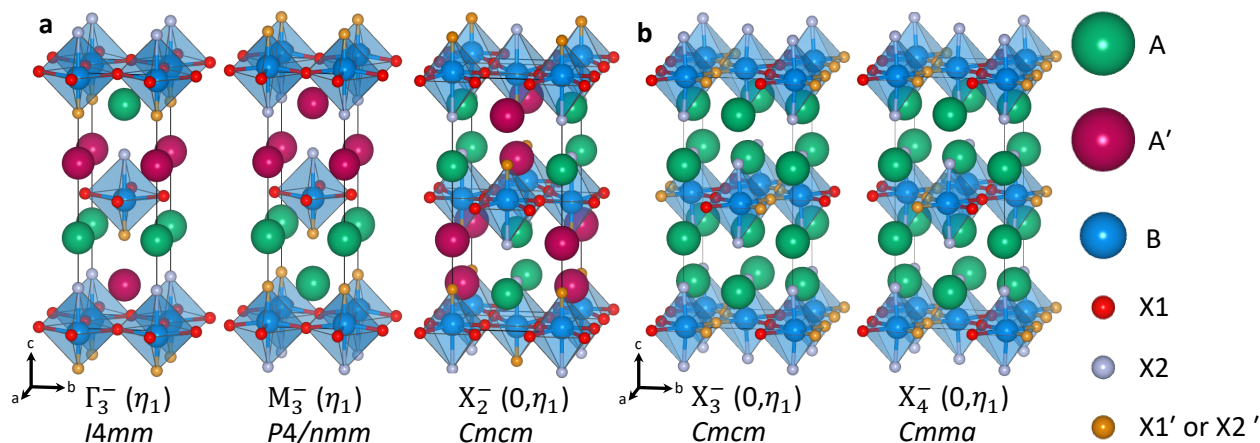


FIGURE 4.1: Polar and antipolar structures which have distortions commensurate with the site symmetry breaking of the **a**, X2 and A sites, which have the same Wyckoff site, and **b**, the X1 anion site. The structures show the off-centering of the B-site. Below each structure is the irrep, OPD, and space group.

4.3.1.1 Polar and Antipolar Distortions

Many ordered heteroanionic materials (not just the RPs) show polar and antipolar distortions accompanied by anion order and so we focus on these first (Table 4.2). The ordering occurs because the displacive metal off-centering found in noncentrosymmetric heteroleptic polyhedra [102] favors cation displacements towards the less electronegative anion to facilitate orbital hybridization. Table 4.2 shows that multidimensional irreps can lift the anion site symmetry in different ways, e.g., $M_5^- (\eta_1, \eta_1) \neq M_5^- (\eta_1, \eta_2)$. Experimentally at a fixed temperature, however, we would expect only one OPD of such an irrep to be present,¹ because the direction of the cation off-centering must be commensurate with the anion order. For example, in the structure with $Imm2$ symmetry induced by Γ_5^- , the B-site would off center in a polar manner such that it moves towards one equatorial anion. The anion order supported by this distortion, however, causes the equatorial anions sites to form a *trans* configuration, which is inconsistent with this symmetry of the B-site displacement.

¹We note, however, that the OPD of a multidimensional irrep can change with external influence (temperature, pressure, etc.)

Figure 4.1 depicts only those structures within this reduced irrep space where the displacements are compatible with the anion ordering. We do not show structures in which the displacements are incompatible with the anion ordering, because they are unlikely to exist within the heteroanionic materials family. Figure 4.1a depicts the $n = 1$ structures exhibiting a reduced site-symmetry on the X2 apical anion. The only polar structure with broken symmetry exhibits the $I4mm$ space group, such that the X2' anion is positioned below the equatorial anion plane of all octahedra, making the c -axis the polar axis. The resulting crystal coordination formula is ${}_{\infty}^{33}AA'[BX_{1/2}X_{2/1}X_{2'/1'}]=AA'BX_1X_2X_2'$ Although typically oxyfluorides break the site symmetry of the apical anion sites [237], only the oxynitride, Nd_2AlO_3N ($X_1=X_2=O$ and $X_2'=N$) adopts this polar structure [256, 257].

The apical anion site symmetry can also be reduced such that there is an antipolar arrangement of the X2' anions as for the $P4/nmm$ and $Cmcm$ structures (Figure 4.1a). The $P4/nmm$ structure exhibits an *interlayer* antipolar anion ordering, where within each perovskite layer, the X2' anion is located on the top or bottom apical positions (relative to the equatorial anions in that layer), but in the next adjacent layer, X2' occupies the alternative apical position. There are a number of anion ordered heteroanionic materials which adopt this structure: Sr_2FeO_3F [147], Sr_2FeO_3Cl [258], Sr_2MnO_3Cl [259], Sr_2CoO_3Cl [143], Sr_2NiO_3Cl [145], Ba_2InO_3F [260], Ba_2InO_3Cl , and Ba_2InO_3Br [261]. In all cases, $X_1=X_2=O$ and $X_2'=F, Cl, \text{ or } Br$, the compound has symmetry $P4/nmm$, and the B-site cations exhibit off-centering towards the less electronegative anion. The $Cmcm$ structure exhibits an *intralayer* antipolar anion ordering, where X2' occupies both the top and bottom apical positions within each perovskite layer. The alignment of X2' in adjacent perovskite layers is out-of-phase owing to the C-face centering operation and hence there are more formula units in the conventional cell. There are no known synthesized heteroanionic materials that adopt

this symmetry.

Among the distortions that break the site symmetry of the *equatorial* anion, we find none of them have commensurate displacements and anion orderings to permit a polar axis. Figure 4.1b shows the only compatible antipolar and centrosymmetric structures. Unlike the structures obtained from splitting of the apical site symmetry, these variants can exhibit equatorial sites with either a *cis* or *trans* configuration of X1 and X1' anions: the X1' anions are either adjacent to or across from one another, respectively. Both *Cmcm* and *Cmma* structures exhibit *cis* arrangement of the X1' anions. Although both structures possess intralayer antipolar ordering, they exhibit different anion ordering owing to the combination of the C-face centering and glide operations. The X1' anions alternate in layers along the *c*-axis in the *Cmcm* structure forming a zig-zag network, whereas the anions spans columns (stripes) in the *Cmma* structure. There are no known ordered oxynitrides which adopt either of the structures, which we explain as follows: The connectivity of the equatorial anions requires each anion is linked to two B-site cations; however, splitting this anion site requires the distribution of two anions among the four sites, which only leaves a *cis* and *trans* configuration. In either case, we are only able to obtain two structures which differ in the stacking of their perovskite layers, which itself does not affect the local coordination polyhedra of the A-site. The result is that the lattice energies for these two geometries should be very similar.

In contrast to this scenario, site splitting of the *apical* anions enables different polar or antipolar anion ordering within the perovskite layer. If the stacking of the polar perovskite layers changes (i.e., polar versus interlayer antipolar structures), then the coordination polyhedra of the A-site is significantly different between the structures; in this situation, the lattice energies should be markedly different. We confirm this hypothesis in a more quantitative manner below. However, there are a number of known disordered oxynitrides which can be viewed as adopting an average of

TABLE 4.3: Rigid rotations and tilts of the anions also reduce the site symmetry of the anions. Lattice vectors are relative to the primitive cell of the prototypical $n = 1$ RP Ruddlesden-Popper structure.

irreps	OPD	lattice vectors	SG	modified Glazer tilt	B-site symmetry reductions
X_3^+	(η_1, η_1)	$2a \times 2b \times c$	$P4_2/ncm$	$a^-b^0b^0/b^0a^-b^0$	$..2/m$
X_3^+	(η_1, η_2)	$2a \times 2b \times c$	$Pccn$	$a^-b^-c^0/b^-a^-c^0$	$\bar{1}$
X_4^+	(η_1, η_1)	$2a \times 2b \times c$	$P4_2/nnm$	$a^-b^0b^0/b^0a^-b^0$	$..2/m$
X_4^+	(η_1, η_2)	$2a \times 2b \times c$	$Pnnn$	$a^-b^-c^0/b^-a^-c^0$	$\bar{1}$

the $Cmcm$ and $Cmma$ structures. Although these structures are refined to $I4/mmm$ symmetry, meaning they may not on average exhibit off-centering of the B cation, the O/N occupancy on the equatorial anion sites is 50/50 and the octahedra generally present a *cis*-[BX_{1_{2/2'}}X_{1'_{2/2'}}X_{2_{1/1'}}] heteroleptic unit (Appendix A).

4.3.1.2 Rotations and Tilts

Rotation and tilts of the B-centered polyhedra in $n = 1$ RP materials can produce unique symmetry effects not found in perovskites [262, 263]. Here we show that these displacive modes coexist with anion ordering in $n=1$ RPs, which is not possible in either perovskites or double perovskites [192, 233]. Table 4.3 lists the rotations that alter the site symmetry of the equatorial anions and Figure 4.2 depicts the octahedral rotation patterns and anion ordering of the resulting structures. In all cases, the equatorial anion sites are broken in a *trans* manner, such that the equatorial anions form *trans*-[BX_{1₂}X_{1'₂'}] square planes. The equatorial anions in the parent phase have a site symmetry of mmm . Rotations about an in-plane axis break the two mirror planes parallel to the axis of rotation and exposes the intrinsic $2/m$ site symmetry along the perpendicular direction, making the new site symmetry of the equatorial sites $2/m...$

In the structures representing the X_3^+ and X_4^+ with order parameter (η_1, η_1) (right panels of Figure 4.2), we can consider the two perovskite layers separately to describe the rotations using

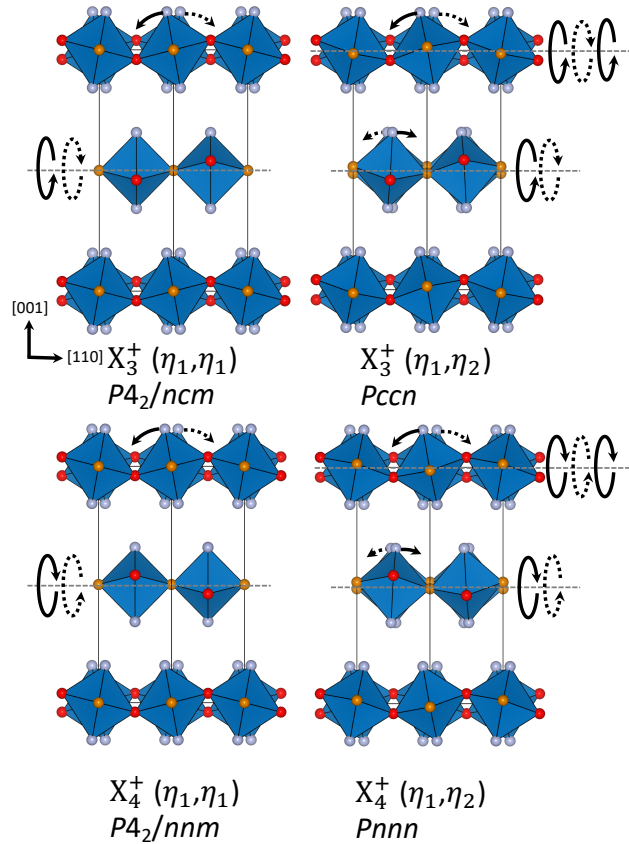


FIGURE 4.2: Octahedral rotation patterns of structures with rotational distortions that break the symmetry of the anion sites. A-site cations are omitted and the polyhedra are opaque for clarity. Arrows indicate tilting of the octahedra with the lines and dotted lines representing tilts of the opposite sense.

conventional Glazer notation [114]. Both have $a^-b^0b^0$ rotations, however there is a 90° rotation about the c -axis between the two layers. We can therefore represent the tilts in the structure using a modified Glazer notation, where a slash separates the adjacent perovskite layers, conventional Glazer notation persists within each perovskite layer (i.e., the first, second, and third indices represent the rotations about the a , b , and c axes, respectively) and the magnitudes of the rotations are coherently maintained, then we can nearly fully represent the rotation patterns in RP structures. In the case of X_3^+ and X_4^+ with order parameter (η_1, η_1) , these structures would be represented by $a^-b^0b^0/b^0a^-b^0$ using this modified Glazer notation, where a^- switching between the first and

second position between layers indicates that the rotation axis changes between layers, but the magnitude of the rotation remains the same. The rotation patterns of the remaining irreps and OPDs, $X_3^+(\eta_1, \eta_1)$ and $X_4^+(\eta_1, \eta_1)$, is $a^-b^-b^0/b^-a^-b^0$, where there are two rotation axes within each perovskite layers, which are exchanged in adjacent layers. The differing magnitudes of the two in-plane rotation axes also explains why the symmetry of the equatorial anions is broken; if the magnitude of these rotations are the same, as in $X_3^+(0, \eta_1)$, then the symmetry of the equatorial sites remains unbroken.

The only subtlety in this notation is that it does not capture the difference between the *sense* of the rotations in adjacent layers. The X_3^+ and X_4^+ distortions differ in the sense of the rotation between adjacent layers. This difference is clearly discerned in the structures on the right of Figure 4.2, $X_3^+(\eta_1, \eta_1)$ and $X_4^+(\eta_1, \eta_1)$. The tilt patterns of the top and bottom perovskite layers of X_3^+ and X_4^+ are the same, whereas the sense of the rotation of the center layer is opposite.

We are unaware of any heteroanionic materials that adopt the aforementioned structures. Derivative structures with *trans* anion ordering in the equatorial anion plane are generally unfavorable because having anions with similar Pearson hardness [95] next to each other maximizes the π hybridization in the B-X bonds. For this reason, the large majority of oxyfluorides and oxynitrides exhibit *cis* or *fac* heteroleptic units [93, 94], although recent studies have shown that strain can induce *trans* anion ordering [166, 264]. Aschauer and coworkers have predicted the ground state of the anion disordered and ordered variants of $\text{Sr}_2\text{TaO}_3\text{N}$ to have these rotations and *trans*- $[\text{TaO}_4\text{N}_2]$ octahedra, which agrees with the structures presented here [265]. Time-of-flight neutron diffraction experiments at 291 K on this compound suggest that it adopts the prototypical RP structure without rotations and with 50/50 O/N occupancy on the equatorial anion sites [180]. Given that DFT calculations suggest a different ground state, low temperature measurements may

a reveal a phase transition to a structure with rotations, but we unaware of any experimental reports in the literature.

4.3.2 Stability Assessment with GII

We now evaluate the performance of the GII as a predictor of heteroanionic material stability. First, we generate all charge balanced compositions with the chemical formula A_2BO_3X , where $X=N, F$ from a list of candidate A and B chemistries. To simplify our analysis, we restrict our structure search to anion-ordered geometries with polar and antipolar distortions (see Figure 4.1), because these anion-ordered variants (or a disordered average of them) are the most commonly observed hettotypes among $n=1$ RP heteroanionic materials. For the oxyfluorides, we restrict our search to structures that alter the symmetry of the X2 site such that the fluoride ion occupies an apical site. In particular, we chose the the following structures with space groups (irreps and OPD in parenthesis) from Table 4.2: $I4mm$ (Γ_3^- (η_1)) with a polar distortion along the c -axis and polar anion order, $P4/nmm$ (M_3^- (η_1)) with an interlayer antipolar distortion along the c -axis, and $Cmcm$ (X_2^- ($0, \eta_1$)) with an intralayer antipolar distortion along the c -axis. For the oxynitrides, we chose structures that alter the symmetry of the X1 site such that the nitride anions occupy equatorial sites. From Table 4.2 these hettotypes correspond to: $Cmcm$ (X_3^- ($0, \eta_1$)) with an intralayer antipolar distortion in the a or b -axis and $Cmma$ (X_4^- ($0, \eta_1$)) with an intralayer antipolar distortion in the a or b -axis.

Next we use the charge balanced oxynitride or oxyfluoride chemistries and generate initial compounds from a pre-distorted trial structure. These trial structures contain an appropriate metal off-centering by the cation occupying the B site (i.e., the B cation is distorted towards the less electronegative anion). The displacements lengths are based on DFT relaxed structures of

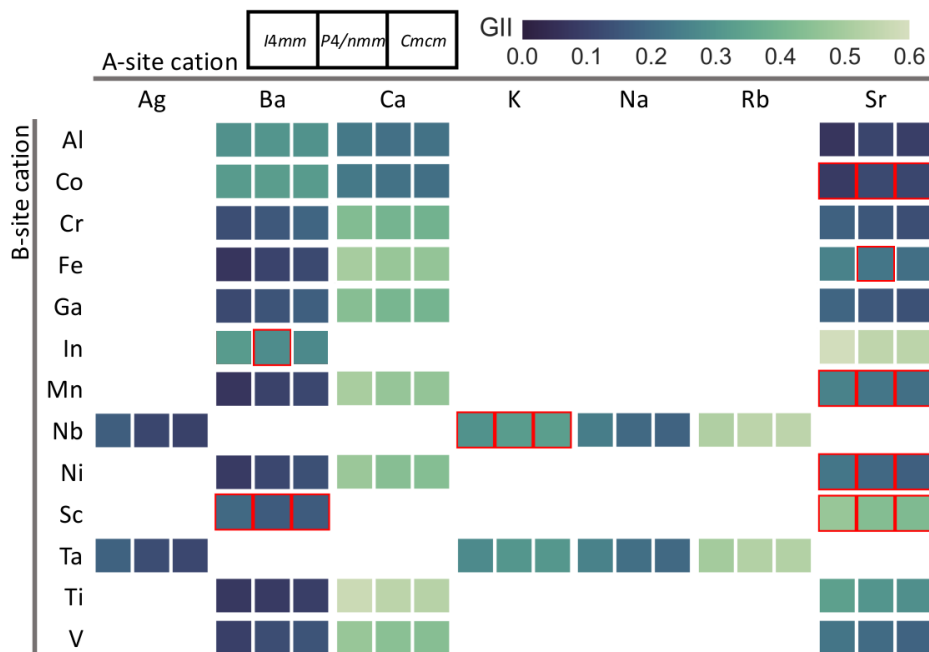


FIGURE 4.3: GII values for A_2BO_3F oxyfluoride structures obtained from the volumetric GII minimization. The GII of a distinct chemistry in the heat map is located at the intersection of a particular A- (column) and B-site (row) cation. Darker colors indicate a smaller GII value and a more stable structure. Structures with GII values greater than 0.6 v.u. are not shown and entries in the heat maps outlined with red indicate that the corresponding compound has been synthesized and is anion disordered with space group $I4/mmm$. Heat maps with only one structure outlined in red, such as Sr_2FeO_3F , are anion ordered with the indicated space group.

varying chemistries, so the displacements of the B-sites may differ depending on the structure and anion ordering. The oxyfluoride structures with symmetry $I4mm$ have a B-site displacement of 0.0180 fractional units or 0.226 Å in the base structure, $P4/nmm$ has a B-site displacement of 0.0238 fractional units (0.300 Å), and $Cmcm$ has a B-site displacement of 0.0168 fractional units (0.212 Å). Both oxynitride structures have a B-site displacement of 0.0257 fractional units (0.324 Å) in the base structure. To account for the different cation and anion sizes, we utilize our in-house lattice relaxation algorithm based on the minimization of GII given by Equation 4.2 to determine optimal cell volumes for a given anion arrangement.

We set a cutoff of $GII=0.6$ v.u. to filter our candidate structures to a set of more probable geometries. This cutoff value is larger than that typically accepted for stable, solid state inorganic

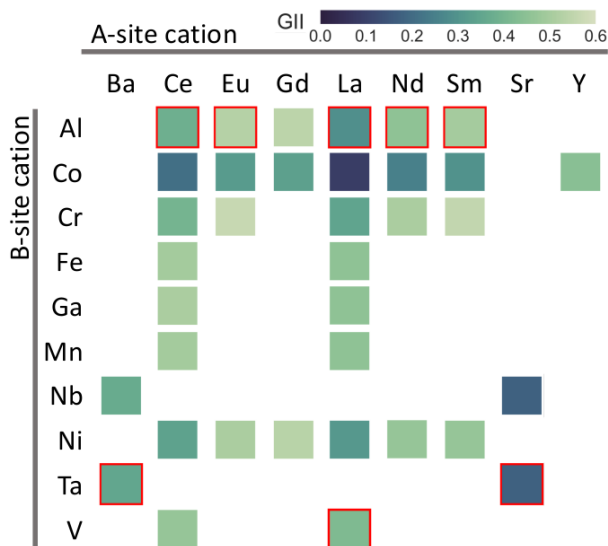


FIGURE 4.4: GII values for A_2BO_3N oxynitrides with $Cmma$ symmetry obtained from the volumetric GII minimization. The GII of a distinct chemistry in the heat map is located at the intersection of a particular A- (column) and B-site (row) cation. Darker colors indicate a smaller GII value and a more stable structure. Structures with GII values greater than 0.6 v.u. are not shown and entries in the heat maps outlined with red indicate that the corresponding compound has been synthesized and is anion disordered and the average structure has symmetry $I4/mmm$, except Nd_2AlO_3N which has space group $I4mm$.

compounds [240] (0.2 v.u.), which we justify being necessary to account for the inherent error in the ionic positions of the trial structures.

Using this screening method, we reduce the 54 (86) candidate oxyfluoride (oxynitride) compositions to 39 (38). The oxyfluoride and oxynitride results obtained with this GII-relaxation are shown in Figure 4.3 and Figure 4.4, respectively. With a cutoff of 0.6 v.u., the algorithm successfully captures all known synthesized oxynitrides and oxyfluorides with the $n = 1$ RP stoichiometry. Interestingly, the oxyfluoride results do not show significant variation among the anion ordered variants, which suggests that we cannot use the GII to discriminate and predict the most stable anion ordering for a fixed chemistry. In fact, the results of the algorithm for Sr_2FeO_3F show that the structure with the lowest GII is the *intralayer* antipolar anion ordering, when the experimental structure has *interlayer* antipolar anion ordering. This discrepancy is likely because of the limited

bond lengths that are accessible to the GII minimizer because only the lattice parameters are relaxed. Ideally, the length of the Fe-F bond would prefer to be much longer relative to the Fe-O, which would cause significant strain with *intralayer* antipolar anion order, but that strain would be reduced in the *interlayer* antipolar anion order. This is verified after relaxing the atomic coordinates and lattice parameters with DFT, which shows that *interlayer* antipolar anion ordering is the most stable configuration and has the smallest GII of the anion ordered structures.

Although there are two unique oxynitrides structures, their GII values are generally within 0.01 v.u. of each other, because the coordination about each cation is the same. As we show below, the energetics of the fully relaxed structures obtained at the DFT level do vary slightly (typically by 1-15 meV per formula unit), but under the fixed atomic positions used in this screening step, the GII always yield the same values and the DFT energies only vary by 1-4 meV per formula unit. Therefore, we only present the results of one structure (*Cmcm*) in Figure 4.4. As with the oxyfluorides, a GII cutoff of 0.6 v.u. captures all the known synthesized oxynitrides with this chemical formula. However, the results of both the oxyfluoride and oxynitride GII minimizations show synthesized compounds with relatively high GII values. For example, the GII of the synthesized oxyfluoride $\text{Sr}_2\text{ScO}_3\text{F}$, [146] when averaged over the *I4mm*, *P4/nmm*, and *Cmcm* anion ordered structures after the GII minimization procedure, is 0.45 v.u. To compare to the experimental structure, which is anion disordered, we ordered the anions of the experimental structure into the three variants used in Figure 4.3 and calculated their GII with no change to the lattice parameters or ion positions. Averaging the GII of these three anion ordered variants, the GII of the experimental structure is effectively 0.29 v.u. with little variation between the anion orders (less than 0.01 v.u.). Given the remarkable similarity in some of the lattice parameters of the experimental and GII minimized structures (short-axes vary by less than 0.07 Å or about 2% and long-axes vary by less

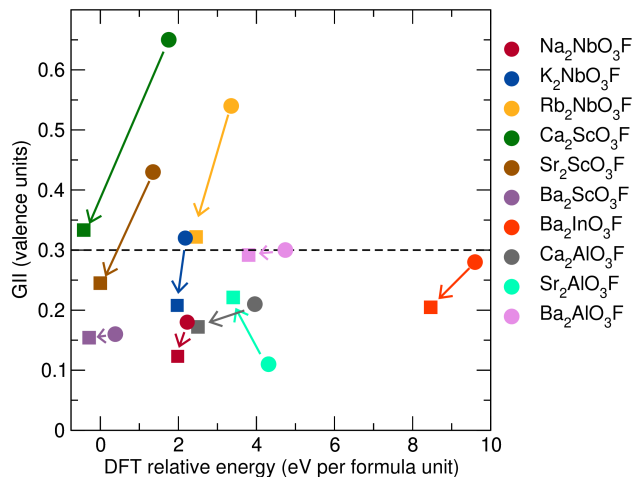


FIGURE 4.5: Correlation between the GII and total energies of the d^0 oxyfluorides before (circles) and after (squares) DFT relaxation with $P4/nmm$ symmetry. The movement of the GII minimized structure relative to the DFT relaxed structure is indicated by arrows of the same color. The energy of the structures is given relative to the DFT relaxed value of $\text{Sr}_2\text{ScO}_3\text{F}$. The horizontal line at 0.3 v.u. indicates our proposed GII cutoff value for synthesizable heteroanionic materials.

than 0.765 Å or about 6%) and minor variation in GII between anion orderings, the reduction in the GII may be largely attributed to the atomic displacements and motivates an additional relaxation of the internal atomic degrees-of-freedom.

4.3.3 DFT Assessment of GII Performance

Next, we re-optimize the trial structures by minimizing the total energy subjected to variable volume and atomic positions at the DFT level. We initialize our DFT calculations with the GII minimized structures from the previous section. We first relax the oxyfluoride compositions with d^0 B-site cations. Figure 4.5 shows both the correlation and the trajectory from the GII minimized structures to the DFT relaxed structures. We only show the results of the $P4/nmm$ structure in Figure 4.5, as the energy difference between the anion ordered structures is typically less than 100 meV per formula unit and the difference in GII is less than 0.03 v.u. The DFT relaxed structures are always lower in energy than the GII minimized structures (square symbols are to the left of the

circles), as expected. The GII also typically decreases after the DFT relaxation (downward arrow), except in the case of $\text{Sr}_2\text{AlO}_3\text{F}$ which shows that the GII increases by about 0.1 v.u.

The increase in the GII of $\text{Sr}_2\text{AlO}_3\text{F}$ is not due to a specific displacement that occurs in this material; rather, it appears to originate in how well the B-site BVS matches the nominal oxidation state. In most of these compounds, the B-site cation is extremely overbonded in the starting structure and because the minimization procedure does not allow for atomic displacements, it remains so until the DFT relaxation. The DFT relaxation procedure typically results in a large change in the BVS of the B-site cation toward its ideal oxidation state, which decreases the GII along with additional large displacements of the A cation that can increase or decrease the GII. In the specific case of $\text{Sr}_2\text{AlO}_3\text{F}$, the BVS of Al before the DFT relaxation is already quite close to its nominal oxidation state, which means that other changes in the structure, such as a short bond distance between the equatorial O and Sr ions (leading to an overbonded Sr), dominate the GII and cause it to increase.

Next, if we use the GII values from the DFT structural relaxations as the reference values, we find that the root-mean-square error of the GII minimizer in the oxyfluoride compounds is very large, around 0.5 v.u., which justifies the high GII cutoff in the step prior to the DFT relaxation. Interestingly, the compounds that have been synthesized all lie below 0.3 v.u. after the DFT relaxation (horizontal broken line in Figure 4.5). Of the compounds which have GII values less than 0.3 after DFT relaxations, only $\text{Na}_2\text{NbO}_3\text{F}$, $\text{Ca}_2\text{AlO}_3\text{F}$, $\text{Sr}_2\text{AlO}_3\text{F}$, and $\text{Ba}_2\text{AlO}_3\text{F}$ have not been synthesized, which makes them compelling targets for materials synthesis. We assess the thermodynamic stability of some of these compounds in the next section and attempt to synthesize those with negative formation energies.

We repeat this DFT relaxation procedure for oxyfluoride compounds with a d^n B-site cation.

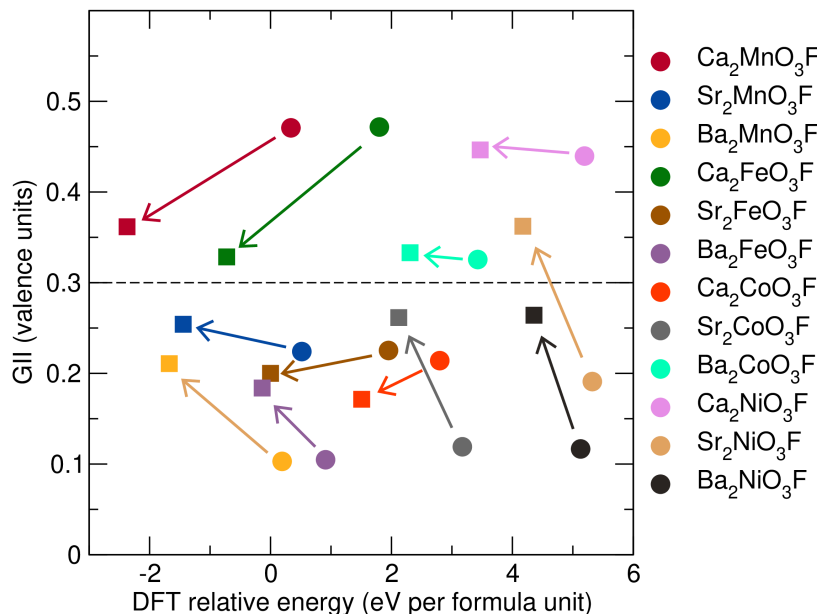


FIGURE 4.6: Correlation between the GII and total energies of the d^n oxyfluorides before (circles) and after (squares) the DFT relaxation in the $P4/nmm$ symmetry. The movement of the GII minimized structure relative to the DFT relaxed structure is indicated by arrows of the same color. The energy of the structures is relative to the DFT relaxed value of $\text{Sr}_2\text{FeO}_3\text{F}$. The horizontal line at 0.3 v.u. indicates our proposed GII cutoff value for synthesizable heteroanionic materials.

We anticipate most of these compounds to be antiferromagnets based on the known oxyfluorides in this family [143, 144, 258], so we require this magnetic order to ensure a correct qualitative description of the spin polarized relaxations. Figure 4.6 shows the resulting GII and relative energetics of the spin polarized DFT structure relaxation. The energy is reduced in all cases and there is a mix of the GII increasing and decreasing after the DFT relaxation. The increase in the GII values occurs for similar reasons as the increase in the GII of $\text{Sr}_2\text{AlO}_3\text{F}$; the BVS B-site cation is already close to its nominal oxidation state allowing other overbonded ions (typically one of the A-site cations or the equatorial O) to dominate the GII.

The only known synthesized d^n oxyfluorides are $\text{Sr}_2\text{MnO}_3\text{F}$, $\text{Sr}_2\text{FeO}_3\text{F}$, $\text{Sr}_2\text{CoO}_3\text{F}$, and $\text{Sr}_2\text{NiO}_3\text{F}$, and all except the Ni compound lie below the 0.3 v.u. cutoff. There may be a few reasons for the high GII, the most likely justification being that these compounds, with the exception of $\text{Sr}_2\text{FeO}_3\text{F}$, are

metastable compounds, because they were synthesized at high pressure and temperatures (6 GPa and $> 1500^\circ\text{C}$ for the Co and Ni variants). As with other metastable compounds, we should expect slightly higher GII values [249,266]. Additionally, we find that $\text{GII}=0.261$ v.u. for the ordered experimental structure of the Ni compound. This may be because the magnetic and/or electronic structure is not being reproduced accurately. A spin glass transition is observed at low temperatures in the Ni compound, meaning that the ground state has both FM and AFM character, perhaps originating from the disordered O and F anions [145]. Accurately representing the magnetism in the structure may improve the GII. Finally, although the Ni compound may be metallic (as the powder samples are black [145]), adding correlation to the calculation through the inclusion of a Hubbard U or the use of a meta-GGA functional such as SCAN may improve the calculations such that they are closer to their ordered experimental structures. Relaxations with the SCAN functional produce a lower GII of 0.305 v.u.

The results of the oxynitride DFT relaxations are shown in Figure 4.7 for both compounds with d^0 and d^n B-site cations. There are no known magnetic oxynitrides of this structure type, so we constrained the magnetic order to be ferromagnetic for simplicity. Like in the oxyfluorides, we find that the GII values of the d^0 compounds generally decrease and the GII values of the d^n compounds either increase or decrease after the DFT relaxation. Of the compounds presented here, only $\text{Sr}_2\text{TaO}_3\text{N}$, $\text{Ba}_2\text{TaO}_3\text{N}$, and $\text{La}_2\text{AlO}_3\text{N}$ have been synthesized and all have GIIs less than 0.3 v.u. after DFT structural relaxations.

The increase in the GII cutoff to 0.3 v.u. from the typically accepted value of 0.2 v.u. may be due to an inherent error in the parameterization of bond valence. If the bond-valence parameters are fit to homoanionic compounds or simply to compounds with homoleptic polyhedra, it may not accurately model the bond lengths of heteroanionic materials owing to the inductive effect [122], or

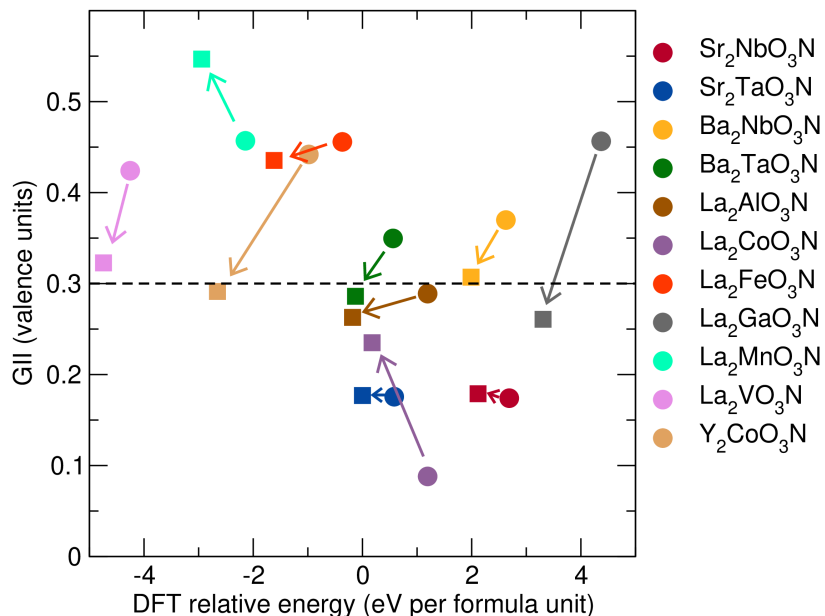


FIGURE 4.7: Correlation between the GII and total energies of the oxynitrides before (circles) and after (squares) DFT relaxations in the $Cmcm$ symmetry. The movement of the GII minimized structures relative to the DFT relaxed structures is indicated by arrows of the same color. The energy of the structures is relative to the DFT relaxed value of Sr_2TaO_3N . The horizontal line at 0.3 v.u. indicates our proposed GII cutoff value for synthesizable heteroanionic materials.

a redistribution of charge from the inherent differences in the electronegativity of the ions. Indeed, the influence of additional counter cations beyond the first nearest neighbors has been shown to significantly affect the empirical bond-valence parameters [267, 268].

To test this hypothesis, we re-calculated the GII values of the GII minimized and DFT relaxed structures using slightly smaller and larger BV parameters. We varied both the R_0 and B bond valence parameters of all cation and anion pairs by $\pm 0.05 \text{ \AA}$ and enumerated all possible combinations of bond valence parameters to ascertain what an ‘error bar’ for the BV parameterization may look like (results are in Appendix A). We chose Sr_2ScO_3F , Sr_2AlO_3F , Ba_2ScO_3F , Sr_2InO_3F as our test cases because they all lie below our cutoff GII value and most of them have been synthesized. In all cases, the average GIIs are slightly higher than the actual value, which is consistent with the exponential nature of bond valence sums. The standard deviation of the values, which we interpret

as the error in the GII value owing to an incorrect bond valence parameterization, is about 0.1 v.u. which may explain why the 0.3 v.u. cutoff found for synthesized heteroanionic materials is higher than the typical cutoff for homoanionic oxide materials.

From the DFT-based analysis of the results from the GII minimizer, we have shown that the GII minimizer acts as an effective screening tool to reduce the computational cost of high-throughput analysis. Using the GII minimizer, we can quickly remove a large percentage of highly unstable compounds from the list of synthetic candidates. We also show, however, that further relaxations, for example at the DFT level, are required both to achieve equilibrium ionic positions and to accurately capture electrostrictive and magnetostrictive effects in the compounds. For the latter case, accurately capturing the spin configurations are necessary in assessing phase stability. We also show that heteroanionic materials exhibit a slightly higher GII cutoff value of 0.3 v.u., which we explained as arising from an inaccurate bond valence parameterization. Future determination of improved bond valence parameters for heteroanionic systems, where the inductive effect has a large influence on the cation-anion bond lengths, may be needed for more accurate results.

4.3.4 Thermodynamic Assessment and Synthetic Attempts

Our analysis of the GII and its performance against DFT relaxed structures motivates us to recommend that heteroanionic compounds exhibiting GII values less than 0.3 v.u. after DFT structural relaxations are viable targets for experimental synthesis. To further guide synthetic efforts, we next calculate the formation energy and convex hull of some of these candidate compounds to confirm their thermodynamic stability. We choose to target oxyfluoride compounds rather than oxynitrides for experiment because their synthesis is more easily achieved with solid-state methods [258, 261]. Oxynitrides typically require an additional or concurrent ammonolysis step which

would add more tunable parameters to the synthesis [27]. We choose $\text{Sr}_2\text{AlO}_3\text{F}$ and $\text{Ca}_2\text{AlO}_3\text{F}$ as synthetic candidates because of their low GII values (0.221 v.u. and 0.172 v.u., respectively).

The formation energy for $\text{A}_2\text{AlO}_3\text{F}$ ($\text{A} = \text{Sr}, \text{Ca}$) is given by

$$H_f^{\text{A}_2\text{AlO}_3\text{F}} = E(\text{A}_2\text{AlO}_3\text{F}) - 1.5\mu_{\text{AO}} - 0.5\mu_{\text{Al}_2\text{O}_3} - 0.5\mu_{\text{AF}_2}, \quad (4.4)$$

where $E(\text{A}_2\text{AlO}_3\text{F})$ is the total energy of the RP phase and μ_i is the chemical potential of compound i . In this case, the chemical potentials are equal to the DFT energies of their ground state electronic energies and no corrections are used. Additionally, we calculate the formation energies using the binary oxides and fluorides as references to better approximate the experimental synthesis. From Equation 4.4, we obtain $H_f^{\text{Sr}_2\text{AlO}_3\text{F}} = -57.6$ meV per atom and $H_f^{\text{Ca}_2\text{AlO}_3\text{F}} = 0.7$ meV per atom. We therefore focus most of our synthetic efforts on $\text{Sr}_2\text{AlO}_3\text{F}$, but also attempt the synthesis of $\text{Ca}_2\text{AlO}_3\text{F}$ a few times because its formation energy is nearly zero.

We used a general solid-state approach for synthesizing $\text{Sr}_2\text{AlO}_3\text{F}$ and $\text{Ca}_2\text{AlO}_3\text{F}$, using sintering temperatures resembling similar $n=1$ oxyfluoride compounds [146,147,260,261] and varying atmospheric conditions (e.g., air, Ar gas). Detailed experimental synthesis information for $\text{Sr}_2\text{AlO}_3\text{F}$ is presented in Appendix A, however, none of our attempts were able to synthesize either compound successfully as revealed from powder x-ray diffraction. Most likely, $\text{Ca}_2\text{AlO}_3\text{F}$ is simply unstable, but our calculations indicated that $\text{Sr}_2\text{AlO}_3\text{F}$ should be enthalpically very stable. To understand why the synthesis of $\text{Sr}_2\text{AlO}_3\text{F}$ was likely unsuccessful, we examined the complex hull of these compounds (the compound phase diagram with hull distances can be found in Appendix A). Using our synthetic results as a guide for our convex hull calculations, we only include the DFT energies of the compounds observed in the powder x-ray diffraction results of our synthetic attempts. $\text{Sr}_2\text{AlO}_3\text{F}$ is

still stable according to our convex hull calculations, however, when calculating the driving force for a reaction from $\text{Sr}_3\text{Al}_2\text{O}_6$, which is the major phase present in most of our synthetic attempts, we find that the driving force is small, about -3 meV per atom. Therefore, the synthesis of $\text{Sr}_2\text{AlO}_3\text{F}$ may still be achievable, similar to other compounds with low driving forces such as MgCr_2S_4 [30], although it may take a long time to form.

4.4 Conclusion

Using group theoretical methods, we generated all derivative structures which break the site symmetry of one or both of the anion sites of the parent $n = 1$ Ruddlesden-Popper structure. We identified that polar, antipolar, and octahedral tilts and rotations can lift the site symmetry of the anions and use the generated polar and antipolar structures as the base structure for the screening study. We then used the global instability index, GII, to efficiently screen out candidate compositions from a high-throughput exploration of $\text{A}_2\text{BO}_3\text{X}$ ($\text{X} = \text{N}, \text{F}$) compounds in the aforementioned structures, eliminating highly unstable compounds from our list of candidates and reducing the number of compositions for further DFT calculations by up to 50%. The GII values for these structures are obtained by relaxing the lattice parameters of a candidate structure and eliminate structures with a GII greater than 0.6 v.u. from our subsequent structure search. Then the remaining structures are relaxed using density functional theory, and the resulting GII values for those optimized structures are used to further downselect to viable structures ($\text{GII} < 0.3$ v.u.). Using this scheme, we capture nearly all the known oxyfluorides and oxynitrides, with the exception of a couple of metastable structures. The higher GII cutoff value defining the boundary between stable and likely unstable heteroanionic materials may be due to the significant charge redistribution and asymmetric orbital hybridization that occurs in this class of materials. Finally, we identify $\text{Sr}_2\text{AlO}_3\text{F}$ as an unreported

yet viable candidate for synthesis, which is further supported by our DFT calculated formation energies. To that end, we attempted a general solid-state synthesis of the $\text{Sr}_2\text{AlO}_3\text{F}$, but found it did not form, likely because of the small thermodynamic driving force.

Chapter 5: Phase Transitions and Potential Ferroelectricity in Noncentrosymmetric KNaNbOF_5

This work was done in collaboration with the following individuals: Dr. Po-Hsiu Chien, Haoyu Liu, Sawankumar Patel, and Professor Yan-Yan Hu from Florida State University performed the ^{19}F NMR MAS spectroscopy measurements, calculated the DFT isotropic shifts for the KNaNbOF_5 polymorphs, and assisted in writing the manuscript; Ching-Hwa (Anita) Chen refined the synthesis of noncentrosymmetric KNaNbOF_5 ; and Dr. Nenian Charles identified and outlined the problem, and performed preliminary DFT phonon calculations.

5.1 Introduction

A ferroelectric material requires a spontaneous polarization under zero applied electric field and the polarization must be “switchable,” meaning the material can switch between different polarization states through an applied electric field [269]. Additionally, other technologically relevant properties such as piezoelectricity and second harmonic generation are also active in ferroelectric materials, however they do not rely on a switchable electric polarization [270]. Strategies to design and synthesize new ferroelectrics has largely focused producing polar off-centering displacements in

ABO₃ perovskite and perovskite-derived structures. Common ferroelectrics such as BaTiO₃ rely on a d^0 transition metal B sites to induce polarity into the structure through a second order Jahn-Teller (SOJT) mechanism; however, this restricts the B-site chemistry to select elements. Hybrid improper ferroelectricity allows for a wider chemistry and coupling to other properties, e.g., magnetism, as it relies on rotations and tilting of the BO₆ octahedra to drive polar A-site displacements [23, 271–273].

Recent work has gone beyond traditional perovskite-type oxides and fluorides, and has shown polar and/or noncentrosymmetric (NCS) structures may be realized by controlled modification of the anion-sublattice composition and structure. Anion vacancy ordering combined with A-site chemical ordering has been used successfully to generate NCS Ba₂YFeO_{5.5} and (SrFeO_{2.5})₁/(CaFeO_{2.5})₁ thin films and superlattices [159, 274], respectively. Anion substitution alone can be used to create polar-building-block units within a structure and their directed assembly can stabilize compounds without inversion symmetry [275, 276]. NCS anion-substituted compounds, which we refer to as heteroanionic materials (HAMs), however, are still relatively rare [27]. For that reason, there are few conclusively demonstrated ferroelectric HAMs. Ferroelectric oxynitrides have been studied and proposed as relaxor ferroelectrics with a switchable polarization [277–279], but to our knowledge there are no known switchable ferroelectric oxyfluorides. Na₃MoO₃F₃ has been proposed to be a ferroelectric [184], however, its field-polarization hysteresis loop neither saturates nor exhibits a region with a large change in concavity. [208, 280]. Upon our microscopic analysis of the polarization in Na₃MoO₃F₃, we find that it arises from aligned [MoO₃F₃]⁻⁶ units. For polarization reversal, significant mass transport (i.e., 180°C rotations of the all [MoO₃F₃]⁻⁶ units) would be required, which is difficult to achieve. It would involve disassembling the structure and reconnecting it in a manner analogous to how the the structure of zinc blende is noncentrosymmetric and permits a

static polarization, but cannot be reversed. Thus, in order to find a ferroelectric oxyfluoride, we not only require a polar structure, but the electronic polarization must be switchable below the break-down voltage of the material with small displacive distortions.

KNaNbOF_5 is one of these rare polar heteroanionic materials [151], which is also polymorphic. It exhibits a metastable centrosymmetric (CS) phase [108] and a polar structure at room temperature [281, 282]. This polar ground state structure has $Pna2_1$ symmetry and exhibits a reversible, temperature-driven phase transition to a high temperature (HT) centrosymmetric (CS) phase with symmetry $Cmcm$ [7, 282], which makes it a potential candidate for switchable ferroelectricity. Our analysis of the group-subgroup relationships for the HT and NCS phases, which we present in detail below, reveals that a complex phase transition with either proper or hybrid-improper character may occur depending on whether the relevant unstable modes driving the transition condense sequentially or simultaneously. If two or more modes condense together at the same temperature, KNaNbOF_5 would exhibit an unusual avalanche transition [271, 283, 284]. If the modes do not condense together, then an intermediate phase would appear and the transition becomes proper. Ferroelectric switching would also be more likely, as the intermediate phase could provide for a low energy CS pathway.

Here we investigate ferroelectricity in KNaNbOF_5 by examining the sequence of possible phase transitions occurring between its ground state NCS phase and its HT phase. We first investigate the character of possible phase transitions by constructing a Landau model using order parameters and interactions obtained from density functional theory (DFT) calculations. Our model suggests an intermediate phase with $Pnma$ symmetry should appear between the previously identified HT and NCS phases upon cooling. We then verify the symmetry of this phases experimentally using high-resolution and in-situ ^{19}F magic-angle spinning (MAS) NMR. Furthermore, we show the

electric polarization in the compound arises from the antipolar displacements of oxygen and fluorine atoms and that a low-energy monodomain ferroelectric switching path occurs through the potential intermediate phase by reversal of these antipolar displacements. Our results suggest that KNaNbOF_5 is an ideal ferroelectric oxyfluoride candidate.

5.2 Methods

5.2.1 Computational Details

All calculations were performed using density functional theory (DFT) as implemented in the Vienna *Ab initio* Simulation Package (VASP) [43,44]. We used the generalized gradient approximation of the exchange correlation functional of Perdew, Burke, and Ernzerhof revised for solids (PBEsol) [62], and the meta-GGA functional SCAN [65] as recommended by recent computational studies of oxyfluorides [253]. We also use projector augmented wave (PAW) potentials [87] with the following valence configurations: $3s^23p^64s^1$ for K, $2p^63s^1$ for Na, $4p^65s^24d^4$ for Nb, $2s^22p^4$ for O, and $2s^22p^5$ for F. A plane-wave cutoff of 600 eV and a $5 \times 3 \times 5$ Monkhorst-Pack mesh [79] were used for structure relaxations and total energy calculations. Structure relaxations were converged to have forces less than $1 \text{ meV } \text{\AA}^{-1}$ on each atom.

To investigate the energetics of the monodomain switching path, a generalized solid-state nudged elastic band (G-SSNEB) method was used [285]. Forces on ions in the G-SSNEB calculation were converged to less than $10 \text{ meV } \text{\AA}^{-1}$. Phonon frequencies were calculated using the frozen phonon method with 0.03 \AA displacements in $2 \times 2 \times 2$ supercells of the primitive cell. The Phonopy software package [286] was used to calculate the force constants and dynamical matrices from the DFT calculations. Wannier centers and maximally localized Wannier functions were

obtained using the Wannier90 code [287]. The chemical shifts were determined by magnetic shieldings using perturbation theory (linear response) [288,289]. The calculated isotropic shifts, which included the contribution of $\mathbf{G} = 0$ and PAW cores, were then calibrated with a calibration factor of +15 ppm according to our previous work [6].

Crystallographic symmetry-adapted modes were analyzed using ISODISTORT [244,290]. Landau free energy expansion was generated using the INVARIANTS tool [291,292]. In our analysis of the Landau free energy expansion, we utilize the unstable phonon eigenvectors which are obtained from the force constant matrices of the fully relaxed $Cmcm$ structure. Under a given irrep, these modes are allowed to mix to form the symmetry-adapted modes. We use the eigenvectors because the using the symmetry-adapted modes alone were found to be stable with the mode distortion. Details on the linear combination of these eigenvectors to fulfill the symmetry-adapted modes is described in Appendix B. Landau coefficients are obtained by a least-squares fit of a mesh of *ab initio* energy calculations to the Landau function. Quadratic coefficients were fit to at least 20 data points, biquadratic to more than 400, and trilinear terms to more than 1000 data points.

5.2.2 Synthesis of KNaNbOF_5

Caution: Hydrofluoric acid is toxic and corrosive and must be handled with extreme caution and the appropriate protective gear! If contact with the liquid or vapor occurs, proper treatment procedures should immediately be followed [293–295].

The reagents NaF (99%, Aldrich), KNO_3 (99.9%, Mallinckrodt), Nb_2O_5 (99.5%, Strem) and aqueous hydrofluoric acid (HF) (48% HF by weight, Aldrich) were used as received. All reactants were sealed in Teflon pouches as previously described [296]. The precursor Na_2NbOF_5 was synthesized hydrothermally via a previously published procedure by combining 0.1344 g NaF, 0.4254 g

Nb_2O_5 , and 1.2 ml aqueous HF in a Teflon pouch [7, 282]. Six pouches were placed in a 125 ml Teflon-lined Parr pressure vessel filled with 42 ml deionized water as backfill, and heated at 5 °C per minute to 150 °C, held for 24 h, and slowly cooled to room temperature at 5 °C per min. The cooled products were left in the pouches at room temperature to crystallize over 2 weeks. The product was recovered by vacuum filtration in air.

NCS KNaNbOF_5 was synthesized by combining 0.0496 g Na_2NbOF_5 , 0.0929 g KNO_3 , and 0.12 ml deionized H_2O in a Teflon pouch [151]. Six pouches were placed in the Parr pressure vessel with 49 ml deionized water as backfill and heated at 5 °C per minute to 150 °C, held for 24 h, and slowly cooled to room temperature at a slower rate of 1 °C per hour. The pouches were then removed from the pressure vessel and left undisturbed at room temperature for 1-2 weeks. Crystals were recovered by vacuum filtration in air. Sample purity was confirmed by powder X-ray diffraction (PXRD) measurements on an Ultima IV X-ray diffractometer (Rigaku) with $\text{Cu K}\alpha$ radiation from 10 °C to 60 °C.

5.2.3 Experimental Details

The collection of ex situ ^{19}F magic-angle-spinning (MAS of 25 kHz) NMR spectra of KNaNbOF_5 (including as-synthesized $Pna2_1$, heated $Pna2_1$, and quenched samples as discussed below) was performed using the same experimental protocol as described previously [6]. In situ (heating and cooling) high-temperature ^{19}F MAS NMR and ^{19}F T_1 relaxation time measurements were employed to track the displacive $Pna2_1$ (NCS) to $Cmcm$ (HT) transition with the LASMAS probe [297]. Detailed experimental conditions (pulse sequence, heating/cooling control, etc.) are reported in Ref. [6]. After the in situ ^{19}F MAS NMR experiments, the heated sample was measured again with ^{19}F MAS (25 kHz) NMR experiments for post-mortem phase identification.

To capture potential intermediate phases arising during the NCS-to-HT phase transition, as-synthesized NCS KNaNbOF_5 was heated to select temperatures (150 °C, 250 °C, 310 °C, and 360 °C) and quickly quenched in an ice bath (~ 0 °C). The as-synthesized NCS KNaNbOF_5 sample (~ 20 mg) was first placed in a ZrO_2 tube, then loaded in a quartz tube and sealed under vacuum for quenching experiments. The tubes were then loaded into a tube furnace (Carbolite MTF 10/25/130) and held at the target temperature for 5 minutes before quenching. Then, the quenched samples were packed into 2.5 mm ZrO_2 rotors in a glovebox (Mbraun Inc., $\text{H}_2\text{O} < 1$ ppm, $\text{O}_2 < 1$ ppm) for the ^{19}F MAS (25 kHz) NMR experiments. To describe the fluoride ions in the ^{19}F MAS NMR spectra of different phases of KNaNbOF_5 we use the notation: $\text{F}(\text{site number})_{\text{phase name}}$ throughout, e.g., F1_{NCS} , corresponds to the first crystallographic fluoride position in the NCS with $Pna2_1$ symmetry.

We note that our starting material contains both the centrosymmetric perovskite-derived $P4/nmm$ phase and NCS phase, however we are confident that we can distinguish the irreversible, reconstructive ($P4/nmm \rightarrow Cmcm$) from the reversible, displacive ($Pna2_1 \leftrightarrow Cmcm$) transitions given that these transitions have been studied using the same technique [6]. We show equivalent experiments results for the reconstructive phase transition and discuss their potential impacts on the results in the displacive phase transition in the Appendix B.

5.3 Results and Discussion

5.3.1 Symmetry Analysis and Energetics

To understand the nature of the $Pna2_1$ to $Cmcm$ phase transition in KNaNbOF_5 , we first examine the relationship between the structures using mode analysis [298, 299]. For the analysis of the

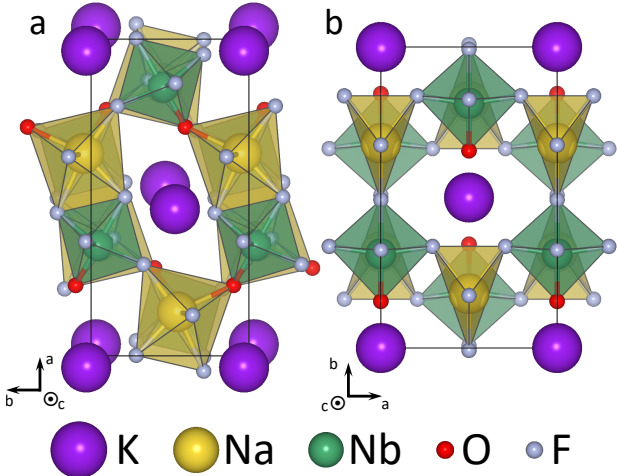


FIGURE 5.1: The **a** $Pna2_1$ (NCS) and **b** $Cmcm$ (HT) structures of $KNaNbOF_5$.

displacive motion of atoms that reduce the $Cmcm$ structure to $Pna2_1$, we use the DFT optimized structures in Appendix B. Although the HT structure exhibits corner-connecting heteroleptic and homoleptic units and the NCS structures exhibits only edge- and corner-connected heteroleptic units (Figure 5.1), the transition between these distinct structures maintains a group-subgroup relationship.

Figure 5.2 shows the results of the mode-decomposition analysis for the high symmetry ($Cmcm$) to low symmetry ($Pna2_1$) transition. Unlike a proper phase transition, which typically requires the condensation of only one mode, this transition requires the condensation of at least two (of a possible three) modes to obtain the $Pna2_1$ space group as shown in the group-subgroup tree (Figure 5.2a). Each mode displaces atoms according to a particular sub-group symmetry, which are labeled according to the irreducible representations (irreps) of the high-symmetry $Cmcm$ phase. The modes are Y_2^+ , Y_1^- , and Γ_2^- . Their corresponding atomic displacements, obtained from the lowest frequency phonon eigenvectors of the $Cmcm$ force constant matrices, are shown on the left of Figure 5.2. The Y_2^+ mode is an out-of-phase rotation of the $[NbOF_5]^{2-}$ and $[NaF_5]^{4-}$ polyhedra about the c axis. The Y_1^- mode is an in-phase rotation of the polyhedra about the b -axis, and

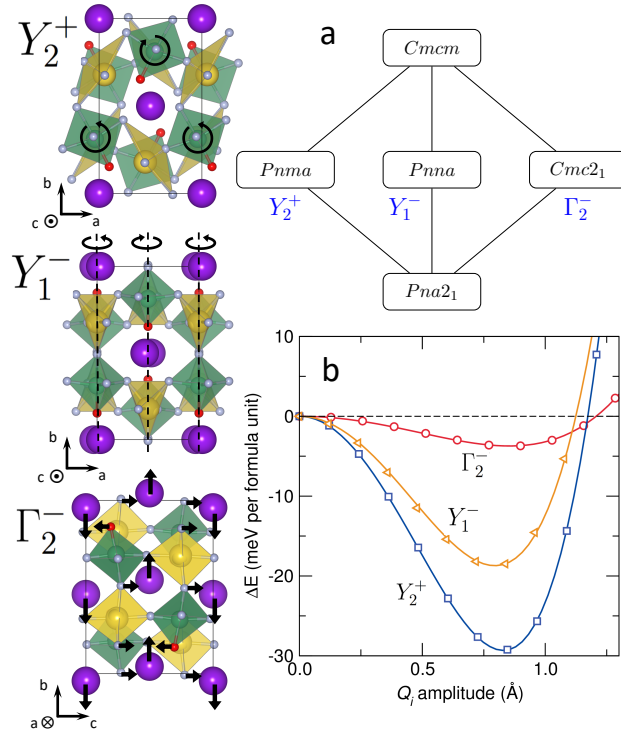


FIGURE 5.2: Mode decomposition and energetics of KNaNbOF₅. **a** The irreps associated with each intermediate structure are shown in blue. **b** Energetics of each of the modes associated with this transition. The atomic displacements associated with the unstable modes from force constant eigenvectors are also shown in the atomic structures on the left. Atoms are designated as in Figure 5.1.

the Γ_2^- mode induces polar displacements into the high temperature structure, primarily through uncompensated anti-polar displacements of the O^{2-} and F^- ions as denoted by the black arrows. The polar displacements are accompanied by large anti-polar displacements of the K^+ ions along the *b* axis (black arrows).

Condensing these modes individually into the $Cmcm$ structures shows the expected energy lowering behavior (Figure 5.2b). The Y_2^+ mode is the most unstable, with its minimum around an amplitude of 0.83 \AA , followed by Y_1^- with its minimum around 0.80 \AA . The polar mode, Γ_2^- is the least energy stabilizing, exhibiting a shallow energy well at a slightly higher amplitude of 0.86 \AA and depth of $\approx -3.72 \text{ meV}$ per formula unit. Based on these energetics it is likely that the nonpolar

modes transforming as Y_2^+ and Y_1^- drive the NCS-to-CS transition as they are considerably more unstable than the polar Γ_2^- mode.

To determine the character of this phase transition in KNaNbOF_5 , we follow a procedure used to investigate the sequence of phase transitions in $\text{SrBi}_2\text{Ta}_2\text{O}_9$ and $\text{SrBi}_2\text{Nb}_2\text{O}_9$, which also exhibit a complex energy landscape with multiple mode couplings. The approach involves computing the 0 K free energy Landau expansion using *ab initio* DFT energy calculations to obtain the coefficients for symmetry-permitted terms that involve the active order parameters and their coupled interactions. Based on this Landau model, and an approximate phase diagram with variable quadratic coefficients is constructed to reveal whether a direct transition between the high and low symmetry phases is allowed [283].

Following this procedure, we first construct a zero-temperature energy model (ΔE_{0K}) using the relevant unstable modes, Y_2^+ , Y_1^- , and Γ_2^- , to model the transition as follows:

$$\Delta E_{0K} = E_{\Gamma_2^-} + E_{Y_2^+} + E_{Y_1^-} + E_{\Gamma_2^- Y_2^+} + E_{Y_2^+ Y_1^-} + E_{Y_1^- \Gamma_2^-} + E_{\Gamma_2^- Y_2^+ Y_1^-} . \quad (5.1)$$

The homogeneous terms (E_i) are:

$$\begin{aligned} E_{\Gamma_2^-} &= \alpha_{\Gamma_2^-} Q_{\Gamma_2^-}^2 + \beta_{\Gamma_2^-} Q_{\Gamma_2^-}^4 , \\ E_{Y_2^+} &= \alpha_{Y_2^+} Q_{Y_2^+}^2 + \beta_{Y_2^+} Q_{Y_2^+}^4 , \\ E_{Y_1^-} &= \alpha_{Y_1^-} Q_{Y_1^-}^2 + \beta_{Y_1^-} Q_{Y_1^-}^4 , \end{aligned}$$

and the biquadratic terms (E_{ij}) are:

$$\begin{aligned} E_{\Gamma_2^- Y_2^+} &= \delta_{\Gamma_2^- Y_2^+} Q_{\Gamma_2^-}^2 Q_{Y_2^+}^2, \\ E_{Y_2^+ Y_1^-} &= \delta_{Y_2^+ Y_1^-} Q_{Y_2^+}^2 Q_{Y_1^-}^2, \\ E_{Y_1^- \Gamma_2^-} &= \delta_{Y_1^- \Gamma_2^-} Q_{Y_1^-}^2 Q_{\Gamma_2^-}^2. \end{aligned}$$

Last, the the trilinear term (E_{ijk}) coupling each order parameter is

$$E_{\Gamma_2^- Y_2^+ Y_1^-} = \gamma_{\Gamma_2^- Y_2^+ Y_1^-} Q_{\Gamma_2^-} Q_{Y_2^+} Q_{Y_1^-},$$

5.3.2 Approximate *Ab Initio* Phase Diagram

We now approximate the zero temperature free energy of the system using coefficients for α , β , and γ calculated from DFT at 0K. Values for all coefficients are listed in Appendix B. Using the zero-temperature model in the previous section, we can approximate a phenomenological free energy under the assumptions of the Landau theory of phase transitions. Then, the temperature renormalization is solely contained in the quadratic terms, such that $\alpha_i = a_i(T - T_{0,i})$ for a given mode i , where a_i is a constant and $T_{0,i}$ is the critical temperature. Under this approximation, the free energy is:

$$F = \sum_i^3 \left[\frac{a_i}{2} (T - T_{0,i}) Q_i^2 + \beta_i Q_i^4 \right] + E_{\Gamma_2^- Y_2^+} + E_{Y_2^+ Y_1^-} + E_{Y_1^- \Gamma_2^-} + E_{\Gamma_2^- Y_2^+ Y_1^-} \quad (5.2)$$

Because we are approximating a zero temperature system, the coefficients obtained from the fits to the *ab-initio* data from the unstable eigenvectors are directly related to the stiffness coefficient and

transition temperature, $\alpha_{0,i} = -a_i T_{0,i}$. Given that the quadratic stiffness coefficient is linear with temperature, we can construct a phase diagram in a region near $\alpha_i = 0$ to predict if a continuous, direct phase transition is possible between the high temperature $Cmcm$ and ground state $Pna2_1$ phases.

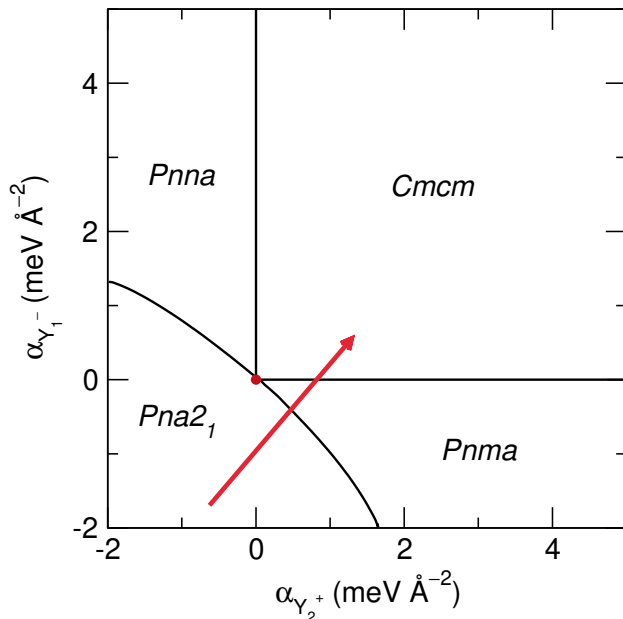


FIGURE 5.3: Approximate phase diagram of the displacive transition in KNaNbO_5 in which $\alpha_{\Gamma_2^-} = 0.6 \text{ meV \AA}^{-2}$. The red dot at $(0,0)$ corresponds to the position in the phase diagram through which a direct transition between the high temperature ($Cmcm$) and ground state ($Pna2_1$) phases occurs. The red arrow represents a possible path of the phase transition through an intermediate centrosymmetric phase.

Figure 5.3 presents the phase diagram of our 0 K Landau model for the transition in the space of the two most negative stiffness constants Y_2^+ and Y_1^- . Presenting the phase diagram in a two-dimensional space with three potential stiffness coefficients, requires we impose a constraint between one of the coefficients of these order parameters and the amplitude of Γ_2^- . The slice presented in Figure 5.3 gives the “best case scenario” for a direct phase transition between the HT and NCS phases, where $\alpha_{\Gamma_2^-} = 0.6 \text{ meV \AA}^{-2}$. Here we find a singular point at the origin, which allows for a direct phase transition between the phases. This scenario also exists under the following conditions:

$0 < \alpha_{\Gamma_2^-} < 6 \text{ meV } \text{\AA}^{-2}$; $\alpha_{\Gamma_2^-} = \alpha_{Y_2^+} + n$ where $0 < n < 0.6 \text{ meV } \text{\AA}^{-2}$; and $\alpha_{\Gamma_2^-} = \alpha_{Y_1^-} + m$ where $0 < m < 0.6 \text{ meV } \text{\AA}^{-2}$. The only condition for this point to open and permit passage between *Cmcm* and *Pna2₁* is when the trilinear coupling coefficient is increased (Appendix B), which is also seen in the case of $\text{SrBi}_2\text{Ta}_2\text{O}_9$ [283]. Given that we do not know the exact physical path the phase transition follows, we assume that the larger the gap between the two phases, the more likely it is for a direct transition to occur. Because the gap between the phases is restricted to a singular point at the DFT-calculated trilinear coupling amplitude, we conclude that a hybrid-improper transition does not occur. The two unstable modes Y_2^+ and Y_1^- do not condense at the same temperature; therefore, an intermediate phase must exist to accommodate the transition between *Pna2₁* and *Cmcm*. Given the single mode energetics in Figure 5.2b, we predict it to be one of the centrosymmetric phases *Pnma* or *Pnna*. This makes it a proper ferroelectric transition driven by the condensation of a single mode.

To confirm the appearance of the gap is not functional or volume dependent, we repeat this procedure using the SCAN functional, which has been shown to give more accurate phonon frequencies in oxyfluoride materials [253]. Appendix B gives the Landau coefficients and approximate phase diagram obtained using the SCAN functional, respectively. The trilinear coupling coefficient from the SCAN functional is slightly smaller than the PBEsol equivalent (18.95 and 20.17 $\text{meV } \text{\AA}^{-3}$). As a result, the SCAN phase diagram is essentially similar to that we obtained using PBEsol; there is a single point in which a direct transition can occur. Increasing the trilinear coupling coefficient is the only way to open passage between the *Pna2₁* and *Cmcm* phases through a hybrid improper transition. Therefore, our conclusion remains the same and we expect an intermediate phase of either *Pnma* or *Pnna* symmetry, whose DFT relaxed structures and crystallographic information can be found in Appendix B. As described previously, the structures differ in the $[\text{NbOF}_5]^{-2}$ axis

of rotation, which is about the c in $Pnma$ and the b axis in $Pnna$. When the structures are relaxed, the $Pnma$ structure is lowest in energy (93.3 and 282.2 meV per formula unit relative to $Pna2_1$, see Appendix B).

5.3.3 In-situ Characterization of the Transition

First, we confirm structure assignments of the $Pna2_1$ and $Cmcm$ phases and the reversibility between these phases using in-site ^{19}F NMR. Previous experiments have shown the technique is able to distinguish among the known symmetries, $P4/nmm$, $Cmcm$, and $Pna2_1$ of KNaNbOF_5 [6]. Appendix B shows the calculated and observed isotropic chemical shifts of $Pna2_1$ and $Cmcm$ and the proposed intermediate phases, $Pnma$ and $Pnna$. Appendix B shows the fluoride sites in the structures. Although it is difficult to resolve the equatorial fluoride sites, i.e., all fluoride sites that are not *trans* to the oxide in the $[\text{NbOF}_5]^{2-}$ octahedra, because of their close proximity in the NMR spectra, we can readily resolve the phases using the chemical shifts of the apical fluoride, i.e., the fluoride *trans* to the oxide anion. We also note that the apical fluoride anion is static throughout the phase transition (Appendix B), indicating that there is no dynamic O/F disorder in the HT phase.

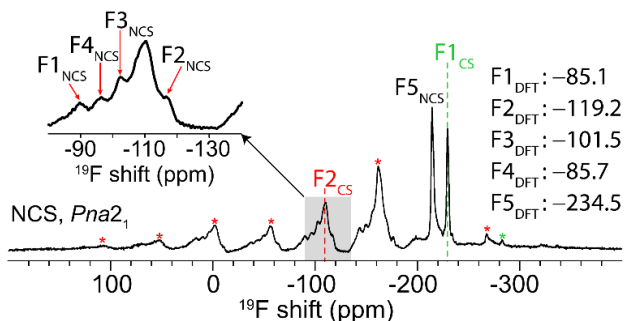


FIGURE 5.4: High-resolution ^{19}F MAS (25 kHz) NMR spectrum of noncentrosymmetric (NCS) sample of KNaNbOF_5 . Calculated ^{19}F NMR chemical shifts of NCS KNaNbOF_5 are also shown for reference. Asterisks (*) denotes spinning side bands. ^{19}F MAS (25 kHz) NMR spectrum of centrosymmetric (CS) KNaNbOF_5 is shown in (Appendix B) for comparison.

Figure 5.4 shows the high-resolution ^{19}F MAS (25 kHz) NMR spectrum of the NCS KNaNbOF_5 . Among seven recognizable ^{19}F resonances, the peaks at -229.2 and -109.5 ppm can be assigned to the fluoride ions F1_{CS} and F2_{CS} , respectively, of the centrosymmetric (CS) $P4/nmm$ (perovskite-derived) phase of KNaNbOF_5 (see also Appendix B). These assignments agree well with our previous results. [6] The remaining five ^{19}F chemical shifts at -89.8 , -115.8 , -100.1 , -95.8 , and -214.2 ppm are assigned to the fluoride ions at sites F1_{NCS} to F5_{NCS} in the NCS phase. The isotropic shifts to which F_{NCS} ions are assigned are verified by the calculated results from DFT (Appendix B).

The $Pna2_1$ KNaNbOF_5 exhibits five crystallographically distinct sites with no mixed occupancy; thus, the ratio among the five fluorine atoms is 1:1:1:1:1. In other words, the apical fluoride ion, F5_{NCS} , should ideally share 20% of the total ^{19}F integral in the NCS KNaNbOF_5 spectra. Experimentally, the percentage of the ^{19}F integral (including both isotropic shift and spinning side bands) of the apical fluorine atom F5_{NCS} over the sum of all fluorine atoms is 19.4%. The ratio among the equatorial fluorine atoms (F2_{NCS} , F3_{NCS} , F4_{NCS} , and F1_{NCS}) is 1.02:0.83:1.13:1.15, which confirms the assignments of the ^{19}F resonances in the NCS phase.

Next, we performed in situ high-temperature ^{19}F MAS (5 kHz) NMR on the as-synthesized NCS KNaNbOF_5 to examine the reversibility of the $Pna2_1$ to $Cmcm$ transition. The heating process is summarized in Figure 5.5 and the cooling process is displayed in Appendix B. From room temperature to $\sim 350^\circ\text{C}$, no phase transition is observed. The only detectable ^{19}F resonance at -259.2 ppm is assigned to the apical fluoride ion, F5_{NCS} , in KNaNbOF_5 (Appendix B). The ^{19}F signals for the equatorial fluoride ions in the NCS phase (F2_{NCS} , F3_{NCS} , F4_{NCS} , and F1_{NCS}), which are supposed to emerge from -85 ppm to -120 ppm (Appendix B) are not discernible. Indeed, this can be explained by the large chemical shift anisotropy (CSA). From simulations of ^{19}F MAS NMR

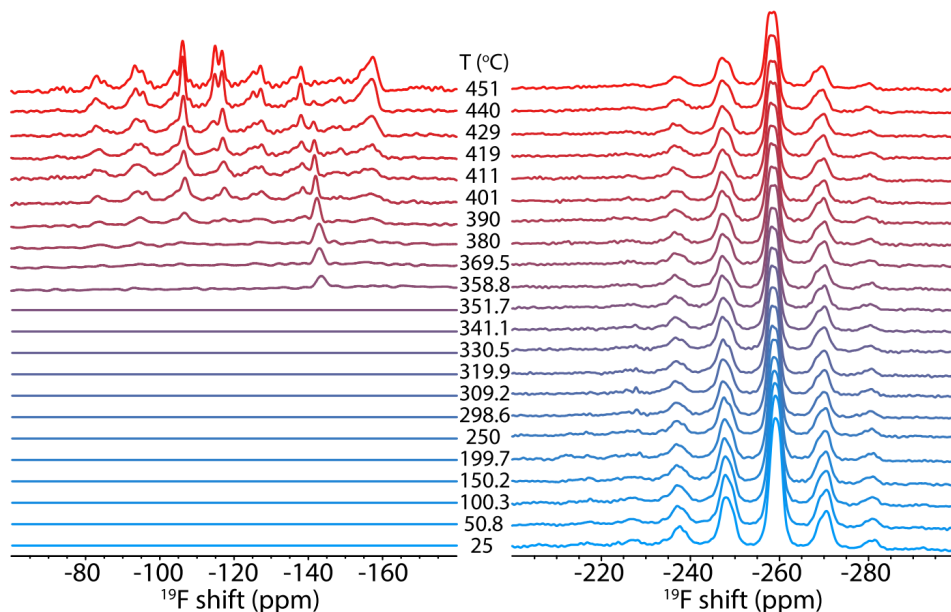


FIGURE 5.5: In situ monitoring (heating process) of the phase transition in KNaNbOF_5 from non-centrosymmetric (NCS) phase ($Pna2_1$) to the high-temperature (HT) phase ($Cmcm$) by variable-temperature ^{19}F MAS (5 kHz) NMR.

spectrum of NCS KNaNbOF_5 (Figure 5.4), the obtained CSA of F5_{NCS} is only 29.7 kHz, whereas the summed CSA of the equatorial fluorine atoms, F2_{NCS} , F3_{NCS} , F4_{NCS} , and F1_{NCS} , is 98.9 kHz. We attribute the spread of the ^{19}F signals over nearly 99 kHz for F2_{NCS} , F3_{NCS} , F4_{NCS} , and F1_{NCS} to both the slow spinning rate of 5 kHz, slow spinning rate of 5 kHz, and the relatively large CSA, leading to low sensitivity.

Upon heating the NCS KNaNbOF_5 up to 450 °C, the ^{19}F NMR linewidth of the F5_{NCS} signal remains unchanged. This temperature-independent lineshape, which is consistent with our previous studies [6], indicates that the $[\text{NbOF}_5]^{2-}$ unit in the NCS phase experiences an axial rotation about the $\text{F}_{\text{apical}}\text{-Nb-O}$ axis. Several additional features in the downfield spectra, however, emerge upon heating. At ~ 360 °C, a ^{19}F peak at -143.2 ppm appears. We assign this peak to a phase associated with the reconstructive transition, further details can be found in Appendix B. At 390 °C, the HT phase appears with a ^{19}F chemical shift at -116.7 ppm (Appendix B). Upon further heating, fast

axial rotations of the $[\text{NbOF}_5]^{2-}$ units occur, which gradually reduce the CSA of the equatorial fluoride ions and leads to an ‘observable’ isotropic shift together with residual spinning side bands. This feature mirrors the growth of the HT phase in the irreversible reconstructive transition reported in Ref. [6] (Appendix B), confirming the assignment of the -116.7 ppm resonance to the HT phase.

Additionally, another unknown ^{19}F peak at -114.8 ppm becomes visible at a higher temperature of 419°C . Whether this ^{19}F signal suggests a new KNaNbOF_5 phase is currently under investigation. Overall, the evolution of the ^{19}F signals shown from -100 ppm to -160 ppm are reversible with temperature except for the peak associated with the reconstructive transition (Appendix B), consistent with a second-order proper ferroelectric transition.

After in situ high-temperature ($T_{\text{max}} = 451^\circ\text{C}$) ^{19}F MAS NMR experiments, post-mortem analysis on the heated NCS was investigated with ^{19}F MAS (25 kHz) NMR. Appendix B shows that the ^{19}F resonances (F1_{CS} and F2_{CS}) of the CS phase vanish from the pristine sample, leaving a clean signature of five ^{19}F signals (F1_{NCS} to F5_{NCS}), which further support our previous findings [6]. This observation indicates that the CS phase converted to the NCS phase during in situ high-temperature experiments. Finally, the chemical shifts of all the ^{19}F signals in the NCS phase remain identical before/after the heat-treatment ($T_{\text{max}} = 451^\circ\text{C}$). This means that the local environment of each fluorine atom in the NCS KNaNbOF_5 is unaltered, and therefore the $Pna2_1$ -to- $Cmcm$ transition is fully reversible.

5.3.4 Intermediate Phase Verification

We performed heating-and-quenching experiments on KNaNbOF_5 followed by ^{19}F NMR to identify the potential intermediate phases with $Pnna$ and $Pnma$ symmetry. First, we quenched (q) the $Pna2_1$ KNaNbOF_5 samples in ice bath after heating to the following select temperatures: $T_q =$

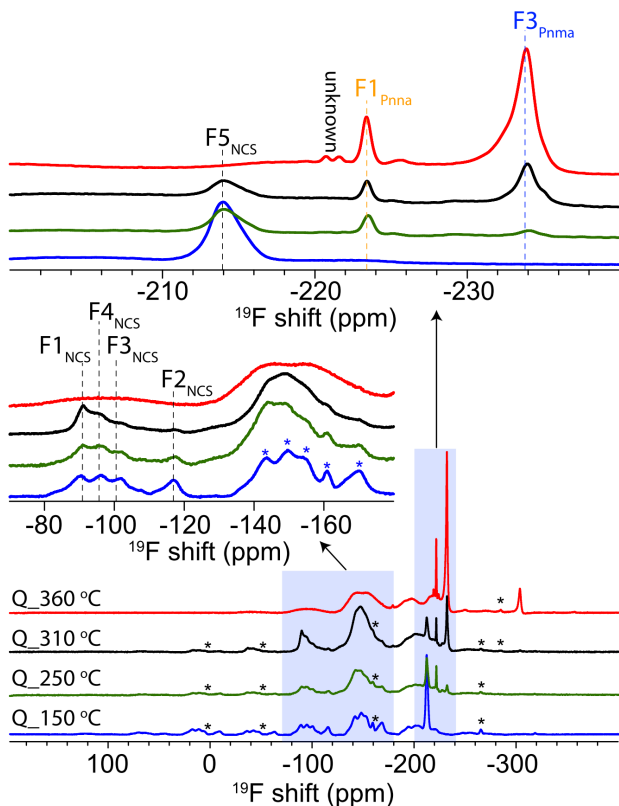


FIGURE 5.6: High-resolution ^{19}F MAS (25 kHz) NMR spectra of NCS phase KNaNbOF_5 quenched (q) at $T_q = 150^\circ\text{C}$, 250°C , 310°C , and 360°C . Asterisks * denote spinning side bands.

360°C , 310°C , 250°C , and 150°C . The quenched samples, denoted as for example $Pna2_1(360^\circ\text{C})$, were then studied with ^{19}F MAS (25 kHz) NMR. Figure 5.6 shows there are three characteristic ^{19}F signals, which correspond to the apical fluoride ions in the $Pnna$ phase (-223.5 ppm), $Pnma$ phase (-233.8 ppm), and $Pna2_1$ phase (-214.2 ppm). In contrast, the equatorial fluoride ions among the three phases manifest in broad and featureless ^{19}F resonances due to severe signal overlap from -80 ppm to -130 ppm (Appendix B). The superimposed ^{19}F NMR peaks of the equatorial fluorides create a source of ambiguity in quantifying the individual phases. Therefore, we reference the phase fraction between intermediates ($Pnna$ and $Pnma$) and the ending form of KNaNbOF_5 ($Pna2_1$) to the ^{19}F integral of the apical fluoride ions.

First, our quenching study reveals that quenching at lower temperatures leads to a greater phase

fraction of the $Pna2_1$ phase compared to the intermediate phases ($Pnna$ and $Pnma$). Specifically, when quenched from 360 °C, the $Pnma$ phase consumed 81% of the total ^{19}F integral with the remaining 19% assigned to the $Pnna$ phase. At a lower quenching temperature of 310 °C, all three phases, $Pnna$, $Pnma$, and $Pna2_1$, were detected. The $Pna2_1$ phase grew and accounted for 53% of the total ^{19}F integral, whereas the ^{19}F integral of the $Pnna$ and $Pnma$ phases decreased from 19% to 13% (−6% reduction) and from 81% to 34% (−47% reduction), respectively. It should be noted that the overall loss of the intermediate phases is consistent with a transformation to the $Pna2_1$ phase. We observed a further increase (53% to 69%) of the $Pna2_1$ phase at the expense of the $Pnma$ phase (34% to 19%) and the $Pnna$ phase (13% to 12%) in the $Pna2_1(250\text{ °C})$ samples. Quenching the NCS phase at 150 °C resulted in the complete formation of the NCS KNaNbOF_5 . In sum, the phase transition onsets around 250 °C and fully transforms to an intermediate structure at 360 °C. Additionally, we observe that both the intermediates phases from our symmetry analysis, $Pnma$ and $Pnna$, occur experimentally.

The manner in which the ^{19}F integral varies among the apical fluoride ions (F3_{Pnma} , F1_{Pnna} , and F5_{NCS}) throughout the course of quenching experiments suggests one of the following scenarios: (i) the $Pnma$ structure is the likely intermediate phase in the proper ferroelectric transition or (ii) the energy barrier between the $Pnma$ and $Pnna$ phases is low and thus, both phase transition pathways are possible. Scenario (i) is supported by equivalent quenching experiments of the perovskite-derived $P4/nmm$ phase (Appendix B), which when quenched at 370 °C show a much larger fraction of the $Pnna$ phase compared to the $Pnma$. Because samples used in the quenching experiments on the polar phase contain some fraction of the $P4/nmm$ phase, it is difficult to discern if the appearance of the $Pnna$ phase is intrinsic to the NCS to HT phase transition, or if is due to the sample's contamination with the $P4/nmm$ phase. Additional support for this scenario

is also contained in the ^{19}F integral of the $Pnna$ phase, which remains comparatively unchanged compared to the opposing fluctuations of the $Pnma$ and $Pna2_1$ ^{19}F integrals. Likewise, scenario (ii) is supported by calculations of the energy barrier between the intermediate phases. Although the difference in energy between the relaxed phases is 189 meV/f.u., the energetic barrier may be smaller and allow for mixing of the two phases. This may also suggest that there is a first order phase transition between the $Pnma$ and $Pnna$ phases. Either way, the quenching experiments reveal the existence of a centrosymmetric intermediate phase.

We have confirmed that the displacive phase transition is reversible and consistent with previous measurements. By quenching the sample at various intermediate temperatures, we also confirm the existence of an intermediate phase, although its crystallographic symmetry remains to be determined as NMR is a short-range structural technique. We also identify an additional high temperature phase transition around 415 °C. Further attempts were made to determine the character of the phase transition through temperature-dependent second-harmonic generation (SHG) measurements, but due to the particular environmental conditions needed to keep the sample from degrading at high temperatures, we were unable to obtain reliable data at this time.

5.3.5 Electric Polarization

Next, we computed the Berry phase polarization [300, 301] and obtained $0.64 \mu\text{C cm}^{-2}$ along the c -axis, which differs from the previously reported calculation of $0.21 \mu\text{C cm}^{-2}$ [209]. The value is small, but not unaccepted as our analysis shows that the polarization in KNaNbOF_5 arises from the displacement of the anions. As seen in the structures of Figure 5.7, the $[\text{NbOF}_5]^{2-}$ octahedra can be thought of as dipoles, which are aligned in an anti-polar manner in the $Pnma$ phase. Using a vector sum model [302], we calculate the dipole moment of the $[\text{NbOF}_5]^{2-}$ unit in the $Pna2_1$

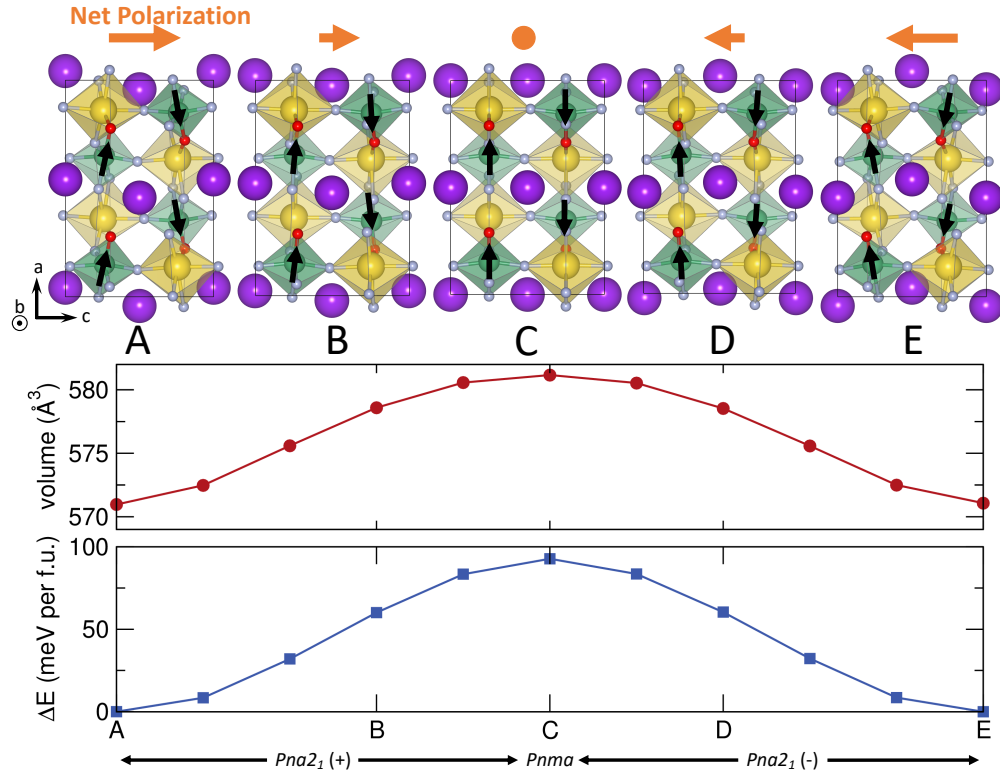


FIGURE 5.7: Structure and properties of the coherent monodomain switching pathway. The top panel shows key structures along the switching pathway, as indicated by the letters.

phase as 1.9 debye, which is consistent with other heteroleptic polyhedra [107, 302] and slightly smaller than the dipole of the unit in the $Pnma$ phase (2.2 debye). As the atoms displace to lift inversion symmetry to produce the $Pna2_1$ structure, the octahedra rotate with opposite sense about the b -axis in alternating rows along the a -axis. This rotates the dipoles such that they are no longer compensated equally, but sum to give a net polarization along the c -axis analogous to weak-ferromagnetism observed in canted antiferromagnets. The calculated born effective charges (Appendix B) are anomalous for the oxide and the fluoride ions that are not aligned with the arrow in the structures in Figure 5.7.

Although the calculated macroscopic polarization is small, we find both the electronic and ionic contributions to the polarization are large but of opposite signs, which is uncommon among simple

polar dielectrics. Using the Berry phase method, we found the ionic and electronic polarizations were $2.63 \mu\text{C cm}^{-2}$ and $-1.99 \mu\text{C cm}^{-2}$, respectively. We confirmed these polarization values by calculating the polarization using a Wannier representation [303]. In this method, the Wannier functions of all occupied pairs of valence electrons are calculated, and because they are localized, their average positions or Wannier centers can be found. We then obtain the electric polarization as the sum of the ionic polarization (from displacements of atomic sites) and electronic polarization (from displacements of the Wannier centers). This analysis resulted in an electronic polarization of $-1.99 \mu\text{C cm}^{-2}$ and total polarization of $0.64 \mu\text{C cm}^{-2}$, which is identical to the result of the Berry phase calculations. This significant contribution from the electronic polarization may be a common feature in heteroanionic materials, as this is also seen in calculations on LaTiO_2N , where the Berry phase polarizations are twice as large as the point charge model [264].

To our knowledge, a polarization arising from the displacement of anions is not often seen, particularly in homonanionic materials (e.g. oxides, fluorides). This mechanism is distinct from second order Jahn-Teller induced ferroelectricity, as well as improper or hybrid improper mechanisms as the octahedra in the centrosymmetric structure already have second order Jahn-Teller-like distortions, the polarization arises from a single soft mode, and the polarization does not originate from the uncompensated displacements of the A-site cations. This material may be categorized as a proper geometric ferroelectric, although unlike other proper geometric ferroelectric such as BaMF_4 ($M=\text{Mn, Fe, Co, Ni}$) [304], there is a large electronic polarization contribution and anomalous Born effective charges, indicating that the polar displacements may originate from changes in chemical bonding.

5.3.6 Potential Ferroelectric Switching Path

To investigate the feasibility of a switchable polarization in this compound, we calculate the energetics of a coherent ferroelectric domain reversal or the monodomain switching barrier. Although this approach is a very simple approximation of the ferroelectric switching mechanism, it provides a figure of merit that often indicates if polarization switching is possible in a material. For example, the well-known ferroelectrics PbTiO_3 and BaTiO_3 have coherent energetic barriers of 200 meV and 16 meV, respectively [305]. If a material has a comparable barrier, then the polarization may likely be a switchable, but materials with significantly higher barriers are less likely to be ferroelectric and simply pyroelectrics.

Because we are unsure of the structure of the intermediate phase, we first compare the energetics and volume of the relaxed HT and intermediate phases relative to ground state structure, as shown in Appendix B. $Cmcm$ has a large volume and energy difference relative to the ground state structure, suggesting that if the transition were direct, the phase may not be switchable due to a large energetic barrier or potential cracking from a large strain gradient in the sample. The candidate intermediate phases, $Pnma$ and $Pnna$, have an order of magnitude smaller volume change, and the energetic barrier is also reduced, by up to about 300 meV/f.u. in the case of $Pnma$. We therefore choose to investigate a potential ferroelectric switching pathway through the $Pnma$ phase, as is the lowest energy intermediate phase and the most likely intermediate candidate based on the energetics of the singular modes.

To ensure an accurate modeling of the fluctuations in lattice parameters through the transition, we use a generalized solid-state nudged elastic band (G-SSNEB) calculation to model the monodomain switching. The results of the G-SSNEB, shown in Figure 5.7, should predict the

minimum energy pathway to switch the polarization of the material. The ferroelectric switching path through the $Pnma$ structure proceeds smoothly along the minimum energy pathway. The maximum in both the volume and relative energy is at the CS intermediate and their values do not deviate much compared to their relaxed differences (Appendix B). The maximum difference in energy is about 93 meV, which is a bit less than half of the coherent energy switching barrier of $PbTiO_3$. This suggests that the polarization may be switchable, but further investigation is needed to confirm the material is a ferroelectric. Attempts were made to measure the polarization hysteresis of $KNaNbO_5$ under applied electric field, however due to the difficulty in sample processing, we were not able to confirm or refute its switchability.

5.4 Conclusion

We have investigated the character of the NCS to HT CS phase transition in $KNaNbO_5$ in order to gain insight into its potential switchable ferroelectricity. Using a Landau model constructed from DFT calculations of the relevant unstable modes, we determined that a direct transition was not possible and an intermediate phase should appear between these known phases. We verified the existence of an intermediate phase through in-situ and high resolution ^{19}F MAS NMR, which suggested the intermediate phase to be $Pnma$, however further long-range in-situ structural characterization would be needed to prove this definitively. We also identify another high temperature phase transition from the $Cmcm$ phase to an unknown higher temperature phase. Based on this proposed intermediate phase, we created a ferroelectric switching path and investigated its coherent energy switching barrier. Based on this simple metric, the material may be switchable as its energetic barrier is comparable to other known ferroelectrics. A hysteresis experiment would

be necessary to confirm its switchability and we hope that our work sparks further experimental investigation into this material and other potential ferroelectric oxyfluorides.

Chapter 6: Heteroanionic Ruddlesden-Popper Ferroelectrics From Anion Order and Octahedral Tilts

6.1 Introduction

The development of ferroic-based microelectronic components, such as non-volatile ferroelectric memory cells [306, 307], relies on advances in novel ferroelectric materials, i.e., materials whose spontaneous polarization is switchable through an external electric field. New mechanisms to induce ferroelectricity in known or novel compounds are therefore key to the development of better technologies. For example, the design and validation of alternative ferroelectric mechanisms such as improper [15] and hybrid improper ferroelectricity [272, 308] over proper ferroelectricity has expanded the design space for novel ferroelectric materials [309].

Designing novel ferroelectrics in ceramics has largely focused on homoanionic perovskite-derived oxide materials. Proper ferroelectrics, such as BaTiO_3 , are generally driven by the pseudo-Jahn-Teller (PJT) mechanism [310, 311], which stabilizes the off-centering of the Ti ion through covalent interactions [305, 312]. However, this interaction relies on d^0 transition metals in such materials, which severely limits the number of potential compounds and restricts routes to couple the electric

polarization to a net magnetization. To facilitate coupling to magnetism and expand the available design space, improper and hybrid improper ferroelectric mechanisms can be used, which induce polarity through an anharmonic (multi-)mode coupling of polarization to zone-boundary modes such as octahedral tilts or rotations [24, 271, 272, 313, 314]. In hybrid improper ferroelectrics, the polarization is induced through antipolar displacements of chemically distinct *A*-site cations, which removes the reliance on d^0 transition metals and may allow for magnetoelectric coupling [23, 273]. This research led to the discovery of similar anharmonic multimode couplings that induce polarization by coupling octahedral rotations to other types of distortions (e.g., Jahn-Teller, antiferroelectric modes, etc.) in both organic and inorganic perovskites and perovskite-derived phases [274, 315–319]. These polarizations are all typically induced by the *A*-site cations or cation order.

Heteroanionic or multi-anion materials have emerged as an active area of research as one can leverage anion substitution to enhance and design new materials with functional properties, including those rooted in acentricity such as ferroelectricity, piezoelectricity, and second harmonic generation [26, 27, 229]. A number of heteroanionic materials have been investigated for potential ferroelectricity, however many of their electronic polarizations originate from mechanisms observed in homoanionic materials. (Relaxor) ferroelectric behavior has been observed in SrTaO₂N in both epitaxial thin films and on the surface of bulk samples [277, 278]. Density functional theory (DFT) calculations and later measurements of the anion order [166] suggest that small domains of *trans*-type anion ordering with symmetry $P4mm$ was the origin of the electric polarization. The polarization in that structure is driven by the pseudo-Jahn-Teller effect, which drives polar distortions of the Ta⁵⁺ within the *trans*-[TaO₄N₂] octahedra. Likewise, the polar structure of BaWON₂ also originates from the PJT effect, but it is unknown if this material is a ferroelectric [320].

Computational studies of oxynitrides have also predicted polar oxynitrides. LaTiO_2N is predicted to be polar under high compressive strain with possible switchable ferroelectricity, but the polarity originates from the PJT effect [264]. $\text{Ca}_3\text{Nb}_2\text{O}_5\text{N}_2$ is predicted to exhibit a polar structure, although the polarization originates from antipolar A -site displacements as in other homoanionic, hybrid improper $n = 2$ Ruddlesden-Popper compounds [279]. $\text{Na}_3\text{MoO}_3\text{F}_3$ is a known polar oxyfluoride and has been investigated for switchable ferroelectricity [184]. However, the polarization arises from aligned dipoles formed from the $[\text{MoO}_3\text{F}_3]^{3-}$ heteroleptic units, which would require large mass transport in order to switch the direction of the polarization.

Recently, the polar oxyfluoride, KNaNbOF_5 , has found renewed interest as a potential ferroelectric [6, 7]. Unlike other known polar or ferroelectric heteroanionic compounds comprising oxygen and another main-group anion, the polarization arises from the coupling of in-phase and out-of-phase polyhedral rotations to a polar distortion—antipolar displacements of the O and F anions [209]. Motivated by these studies on polar heteroanionic materials, herein we describe a strategy to find stable ferroelectric phases in heteroanionic materials. The coexistence of anion order and octahedral tilts generates a polarization in centrosymmetric (CS) anion ordered compounds. This method of coupling of *anion* rather than cation order to other displacive order parameters to generate polar structures was previously proposed in Ref. [192] for double perovskites, however, the examination of these phase transitions was not pursued. It was also explored for a limited case of perovskite oxysulfides [321].

Here, we examine the interactions between anion order and octahedral tilts in $n = 1$ Ruddlesden-Popper oxyfluorides with chemical formula $A_2\text{BO}_3\text{F}$ and evaluate the relative energetics and driving forces to form the derivative phases through *ab initio* DFT calculations. We first enumerate the possible structures arising from the coupling of anion orders to octahedral tilts and determine which

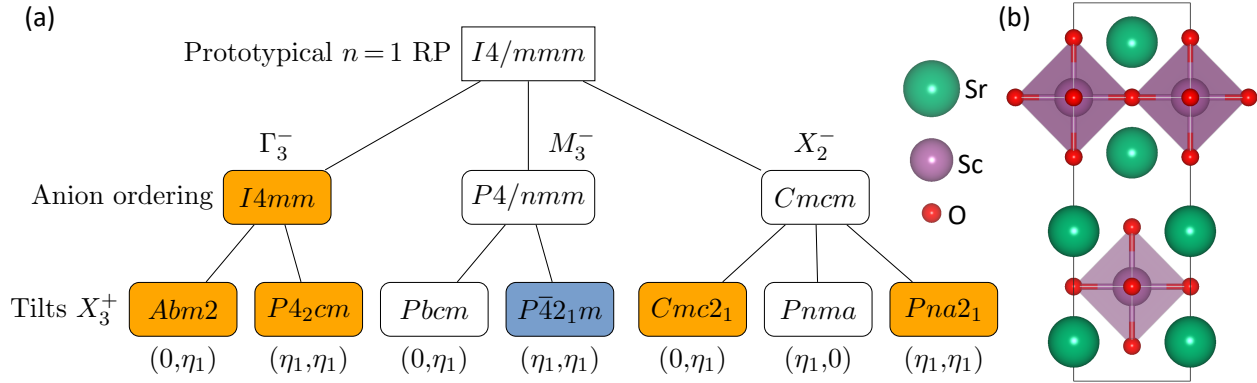


FIGURE 6.1: (a) Group-subgroup relationships among anion ordered structures coupled to octahedral tilts. Each anion ordering (second row) is associated with an irrep of the (b) parent phase, $n = 1$ RP with space group $I4/mmm$. The third row couples the anion order to an octahedral tilt, irrep X_3^+ , with the order parameter direction indicated below each space group label. Orange shaded space groups are polar and blue shaded space groups are nonpolar-noncentrosymmetric. Lines connecting space groups indicate that the phase transition is allowed to be continuous in Landau theory.

couplings generate a polar (or noncentrosymmetric) phases. We find that only antipolar intralayer anion orders generate polar compounds from CS anion orders. Next, we use DFT calculations to evaluate the energy of these phases relative to their anion ordered structures in $\text{Sr}_2\text{ScO}_3\text{F}$ and $\text{Ca}_2\text{ScO}_3\text{F}$. In $\text{Ca}_2\text{ScO}_3\text{F}$, the stabilization from the octahedral tilts are nearly great enough to switch the anion order from antipolar *interlayer* in $\text{Sr}_2\text{ScO}_3\text{F}$ to antipolar *intralayer* in $\text{Ca}_2\text{ScO}_3\text{F}$. This finding suggests that the choice of *A*-site cations and octahedral tilts can change the relative stability of the anion orders. We then investigate the driving force for these rotations to better understand the microscopic origin of the anion-order–octahedral-tilt stabilization. We find that covalent metal-ligand interactions within the $[\text{ScO}_5\text{F}]^{8-}$ octahedron play a key role in stabilizing the octahedral tilts.

6.2 Methods

All calculations were performed using DFT as implemented in the Vienna *ab initio* Simulation Package (VASP) [43,44]. We used the generalized gradient approximation of the exchange correlation functional of Perdew, Burke, and Ernzerhof revised for solids (PBEsol) [62], as recommended for computational studies of oxyfluorides [253], and the projector augmented plane-wave (PAW) potentials [87] for the separation of core and valence electrons. The valence configurations used for the elements are as follows: $4s^24p^65s^2$ for Sr, $3s^23p^64s^2$ for Ca, $3p^64s^23d^1$ for Sc, $2s^22p^4$ for O, and $2s^22p^5$ for F. We used a cutoff energy of 650 eV and a $6 \times 6 \times 3$ Monkhorst-Pack k -mesh [79] for structure relaxations and total energy calculations. Structure relaxations were converged by requiring forces to be less than $1 \text{ meV } \text{\AA}^{-1}$ on each atom and stresses of less than 10 MPa along each crystal axis. Phonon frequencies and eigenvectors were computed using the frozen phonon method. To ensure accurate phonon frequencies and eigenvectors across the Brillouin zone, $2 \times 2 \times 2$ supercells were used for all phonon-dispersion calculations. Phonon calculations were prepared and analyzed using the PHONOPY software package [286].

Symmetry-mode analyses of structures were carried out using the AMPLIMODES [298] and ISODISTORT [244,290] software packages. The electronic polarization was calculated according to the Berry phase method and the modern theory of polarization [300,301]. The procedure for the separation of interatomic force constants has been published previously and was followed here [322]. To evaluate the covalent interactions in the system, we computed the crystal orbital Hamiltonian populations (COHPs) using the LOBSTER code [323–326]. The COHP quantifies the orbital overlap in a given structure and projects these orbitals onto a particular atomic (or orbital) pairs (pCOHPs).

6.3 Results and Discussion

6.3.1 Improper Anion-Ordered Ferroelectricity

6.3.1.1 Symmetry Analysis

We propose a chemical ordering form of improper ferroelectricity, which we refer to as improper anion-ordered ferroelectricity. Similar to the hybrid improper ferroelectric mechanism, the mechanism active here relies on anharmonic multi-mode coupling to induce polar distortions in the compound. However, this mechanism relies on coupling an order parameter describing *anion* order to a displacive order parameter describing octahedral tilts, which makes it exclusive to heteroanionic materials and different from compounds where *cation* order facilitates broken inversion symmetry in the presence of nonpolar lattice distortions [272, 315, 319].

The main idea we follow is that a low-symmetry phase arises from distortions to an ideal high symmetry phase. Symmetry modes, which act as basis functions of irreducible representations or irreps of the space group of the ideal phase, then describe the symmetry breaking and serve as order parameters in the real or hypothetical phase transition used to “derive” the low-symmetry phase. The mechanical and permutation representations of these irreps may account independently or simultaneously for atomic displacements and atomic chemical ordering on different Wyckoff sites. As a result, there are interdependencies among the two representations that provide for the symmetry lowering through displacive or order/disorder mechanisms in a physical phase transition.

Figure 6.1 illustrates this coexistence and/or coupling. Here the minimum set of irreps that describe out-of-phase octahedral tilts and common anion ordering in heteroleptic $[BO_5F]$ octahedra [27] are combined into the ideal $n = 1$ A_2BO_3F Ruddlesden-Popper structure ($I4/mmm$ symmetry)

TABLE 6.1: The effect of individual irreps on the Wyckoff sites of the ideal $I4/mmm$ Ruddlesden-Popper A_2BX_4 compound due to anion ordering (O) and atomic displacements (D). The \times indicates that the irrep does not modify the specified Wyckoff site. Ligand sites X are either apical (ap) or equatorial (eq).

Species	Site	Γ_3^-	M_3^-	X_2^-	X_3^+
A	4e	D	D	D	D
B	2a	D	D	D	\times
X1 (ap)	4e	D,O	D,O	D,O	D
X2 (eq)	4c	D	D	\times	D

to produce lower symmetry derivative structures. The applied anion orders affect the ligand Wyckoff sites as given in Table 6.1. These anion-order modes appear as the polar anion order, irrep Γ_3^- , in which the fluoride ion is exclusively located at the top apical ligand position; the antipolar interlayer anion ordering, irrep M_3^- , in which the fluoride ion switches between the top and bottom apical positions between adjacent perovskite layers; and the antipolar intralayer anion ordering, irrep X_2^- , in which the fluoride ion switches between the top and bottom positions within the same perovskite layer. The interlayer anion ordering appears to be the most commonly observed among synthesized anion ordered heteroanionic materials [145, 258–261, 327, 328]. Polar anion order has also been observed [256, 257] whereas intralayer anion order has not been seen [27]. The octahedral tilts described by irrep X_3^+ always rotate about an in-plane axis and have two order parameter directions, $(0, \eta_1)$ or $(\eta_1, 0)$ and (η_1, η_1) , which correspond to the octahedral tilts $a^-a^-c^0/a^-a^-c^0$ and $a^-b^0c^0/b^0a^-c^0$, respectively, in a modified Glazer notation [114], where the slash between the Glazer tilts indicates the octahedral tilt patterns for adjacent perovskite layers (Figure 6.2a,b).

The derivative structures in the bottom row of Figure 6.1 can be stabilized if the octahedral tilt modes, X_3^+ , are unstable in the anion ordered structure (second row of Figure 6.1). The lines connecting these phases then implies a displacive phase transition occurs, in which the octahedral tilt modes condense to form the low symmetry phase. We show in the next section that most

of these octahedral tilt modes are unstable in the anion ordered structures, however, here we focus on the implications of these changes for potential phase transitions. Figure 6.1 shows that the polar anion order combined with the octahedral tilts always results in a polar structure. In contrast, the *interlayer* anion order and octahedral tilts produce centrosymmetric and nonpolar noncentrosymmetric structures. The *intrinsic* anion order and octahedral tilts can produce polar structures; the polarization arises from the antipolar displacements of the anions. The structures along the $Cmc2_1$ phase transition pathway are shown in Appendix C, and which indicate the polarization arises from all apical fluorides displacing along the [101] direction and the apical oxides displacing in the opposite $[\bar{1}0\bar{1}]$ direction. Because the polarization arises from small displacements, it may be switchable, in contrast to $\text{Na}_3\text{MoO}_3\text{F}_3$, in which the polarization arises from aligned dipolar heteroleptic units [184].

The nature of the coupling can be understood through a polynomial expansion of the free energy change (ΔF) in terms of the symmetry allowed invariants comprising different order parameters. Using anion order (O), out-of-phase octahedral tilts (T), and the polarization (P) as the order parameters and the parent $n = 1$ Ruddlesden-Popper structure with $I4/mmm$ symmetry serving as the reference structure, we obtain the following free energy expansion:

$$\Delta F = \alpha_0 O^2 + \alpha_1 T^2 + \alpha_2 P^2 + \beta_0 O^4 + \beta_1 T^4 + \beta_2 P^4 + \gamma_0 O^2 T^2 + \gamma_1 T^2 P^2 + \gamma_2 P^2 O^2 + \delta OTP, \quad (6.1)$$

where $\alpha_i, \beta_i, \gamma_i$, and δ are the order parameter (coupling) coefficients. The stability of the polar phase originates from a delicate balance of energetically favorable and unfavorable couplings, which we will probe in the next section. For example, in hybrid improper materials, the trilinear term (δ) typically plays a significant role in stabilizing the polar structure, as the biquadratic couplings (γ_i)

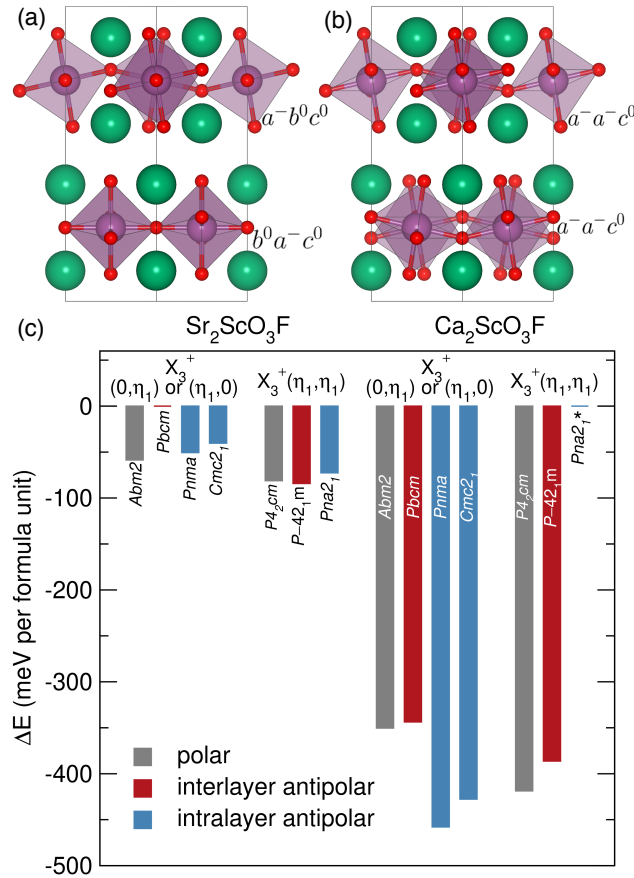


FIGURE 6.2: Octahedral tilt patterns and energetics of the derivative structures relative to their anion ordered structures. The octahedral tilt patterns associated with the modes (a) $X_3^+(\eta_1, 0)$ or $(0, \eta_1)$ and (b) $X_3^+(\eta_1, \eta_1)$. The tilts in Glazer notation are noted next to each perovskite layer. (c) The difference in energy ΔE between the relaxed derivative structures relative to their anion ordered structures. The larger the difference, the more the derivative structure is stabilized by the indicated octahedral tilt pattern. The graph is separated into the two compounds, $\text{Sr}_2\text{ScO}_3\text{F}$ and $\text{Ca}_2\text{ScO}_3\text{F}$, then further separated into the induced tilt pattern and anion orders (colors).

are typically energetically unfavorable [271, 272, 283]. Additionally, the homogeneous coefficients (i.e., α_i and β_i) also can be energetically unfavorable, so long as the biquadratic and/or trilinear term counterbalances the energy penalty and stabilizes the structure. If the free energy expansion is made with the antipolar intralayer anion ordered structure, then the change in translational periodicity causes the T mode to mix with P . As a result, a new order parameter P_T results, where the distinction between exclusively displacive and anion order parameters are lost. The new free-energy expansion then describes a proper ferroelectric with homogeneous quartic and quadratic

terms: $\Delta F = \alpha P_T^2 + \beta P_T^4$.

6.3.1.2 Energetic Stability Analysis

To determine if the anion-order ferroelectricity mechanism occurs, we evaluate the energetics of the various phases obtained by combination of the aforementioned irreps. We choose $\text{Sr}_2\text{ScO}_3\text{F}$ and $\text{Ca}_2\text{ScO}_3\text{F}$ as our test cases as the Sc^{3+} (d^0 configuration) ensures insulating character for all possible anion configurations. $\text{Sr}_2\text{ScO}_3\text{F}$ has also been synthesized, with locally ordered $[\text{ScO}_5\text{F}]^{8-}$ heteroleptic octahedra that are randomly oriented leading to the absence of long-range anion order [146]. The smaller ionic size of the Ca compared to Sr also allows us to examine how different tilt patterns and tilt magnitudes, owing to the *A*-site cations differences, affect and contribute to phase stability ¹.

Figure 6.2 shows the relative energies of the relaxed tilted structures obtained from different order parameter directions of X_3^+ for different anion ordered configurations (colored bars). Overall, the stability of the tilted polymorphs of $\text{Sr}_2\text{ScO}_3\text{F}$ is weaker than the corresponding phases of $\text{Ca}_2\text{ScO}_3\text{F}$, with a few notable exceptions. The $\text{Sr}_2\text{ScO}_3\text{F}$ *Pbcm* structure was not energetically favorable and the $\text{Ca}_2\text{ScO}_3\text{F}$ *Pna2₁* phase transforms into a different structure, indicated by the asterisk in Figure 6.2, albeit with the same symmetry. Therefore, we omit these two phases from further analysis. For both scandates, we also find that the $X_3^+(\eta_1, \eta_1) = a^-b^0c^0/b^0a^-c^0$ tilt pattern tends to stabilize the structure more than the $X_3^+(\eta_1, 0) = a^-a^-c^0/a^-a^-c^0$ tilts.

We first examine the anion-order-dependent octahedral tilt stability trends in the $\text{Ca}_2\text{ScO}_3\text{F}$ phases, because the variations are more obvious. The stability of the octahedral tilts is much greater

¹We attempted to synthesize both compounds and were successful at reproducing the synthesis of $\text{Sr}_2\text{ScO}_3\text{F}$, however we were unable to synthesize $\text{Ca}_2\text{ScO}_3\text{F}$ through solid state and ion-exchange methods. Convex hull calculations indicate that both compounds sit above the hull, the ground states of the compounds are at a distance of 9 meV per atom for $\text{Sr}_2\text{ScO}_3\text{F}$ and 67 meV per atom for $\text{Ca}_2\text{ScO}_3\text{F}$.

in the intralayer anion ordered structures compared to the other anion orders. In the structures with $X_3^+(\eta_1, 0)$ octahedral tilts, the tilts in the intralayer compounds are approximately 100 meV more stable compared to the interlayer and polar compounds. The $X_3^+(\eta_1, 0)$ tilts are more stable in the intralayer anion orders than the $X_3^+(\eta_1, \eta_1)$ tilts, which does not occur in $\text{Sr}_2\text{ScO}_3\text{F}$.

Control of octahedral tilts may be a viable method to tune the equilibrium anion order. By examining the stability of the anion ordered phases without rotations (Appendix C), we find the most stable anion order is the antipolar interlayer order (the relative energies are -117.4 , -204.8 , and 0 meV per formula unit for the polar, interlayer, and intralayer anion orders, respectively). When tilts are added to these structures, the tilts stabilize the intralayer anion order the most, but it is not enough to overcome the large initial energy difference between the interlayer and intralayer anion orders. However, we find that the ground state structure of $\text{Ca}_2\text{ScO}_3\text{F}$ has intralayer anion order (Appendix C), indicating that although the octahedral tilts alone are unable to change the most stable anion order, they increase the energetic competition among competing anion orders adopted in $\text{Ca}_2\text{ScO}_3\text{F}$.

The stability of tilts with differing anion order is weaker in $\text{Sr}_2\text{ScO}_3\text{F}$. In contrast to $\text{Ca}_2\text{ScO}_3\text{F}$, the octahedral tilt stability of intralayer anion orders are less stable compared to their polar and interlayer counterparts, although the difference is much smaller, on the order of 10s of meV. Like $\text{Ca}_2\text{ScO}_3\text{F}$, the interlayer and polar anion orders compete more closely with one another compared to the intralayer anion ordered phases. The most stable anion order without octahedral tilts is the interlayer antipolar order and this does not change when calculating the equilibrium and ground state structures (Appendix C).

The change in anion order of the ground states structures of $\text{Sr}_2\text{ScO}_3\text{F}$ and $\text{Ca}_2\text{ScO}_3\text{F}$ from interlayer to intralayer, is notable. The stability of the octahedral tilts in $\text{Ca}_2\text{ScO}_3\text{F}$ appears to be

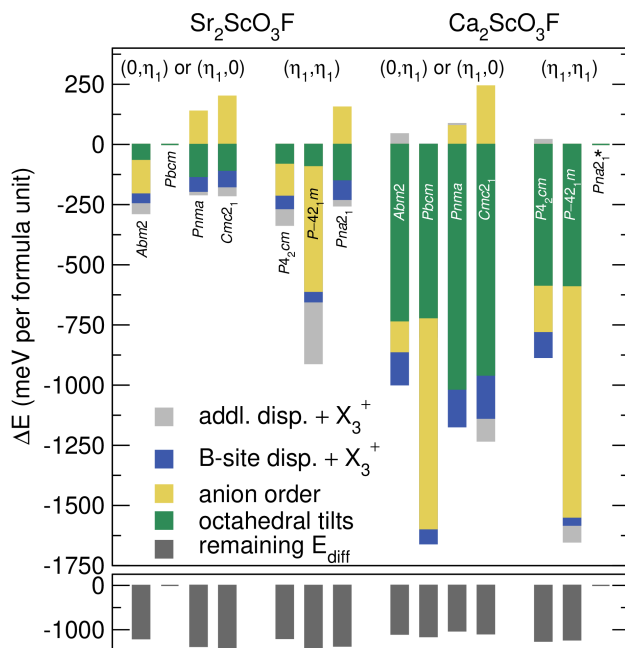


FIGURE 6.3: Decomposed energetics of $\text{Sr}_2\text{ScO}_3\text{F}$ and $\text{Ca}_2\text{ScO}_3\text{F}$ relative to the undistorted anion ordered structures. The top panel divides the energy stabilization into the primary mode contributions (anion order, Γ_3^- , M_3^- , or X_2^- , and octahedral tilts, X_3^+) and the contribution from the coupling of these primary modes. The bottom panel takes the difference between the lattice energy of the relaxed structures and the unstrained structures with the primary modes shown here. The gain in energy in the bottom panel is from fully symmetric ionic displacements and strain accommodation.

greater with intralayer anion ordering, although the origin of this behavior is not obvious. Likewise, the choice of *A*-site cation has a strong effect on the relative energetics of the system. To gain further insight into these problems, we further decompose the energetic contributions to the octahedral tilt stability.

6.3.2 Energetic Contributions Stabilizing Octahedral Tilts with Differing Anion Orders

The derivative structures compared to their parent phase have two main displacive mode contributions, as noted in Figure 6.1a. The anion ordering mode (O or Γ_3^- , M_3^- , and X_2^- for polar, interlayer, and intralayer anion orders, respectively), which includes the *B*-site displacement along

with additional displacements of the A , equatorial oxide (O_{eq}), apical oxides (O_{ap}), and F sites along the out-of-plane axis, and the octahedral tilt modes X_3^+ . The final relaxed structures typically include one or two additional secondary modes; however, these modes do not alter the symmetry of the structure and do not contribute much to the energy ($< 10\%$). To gain further insight into the influence of anion order on the stability of octahedral tilts, we calculate the change in energy due to these primary modes, O and X_3^+ , both individually and coupled together, relative to the undisplaced (i.e., appropriately O/F decorated prototypical $n = 1$ RP) $I4/mmm$ structure with rigid octahedra.

These relative energies are shown in Figure 6.3, with the different colors noting the individual or coupled contributions to the relative energy (ΔE). We find that the octahedral rotations, without any contribution from the anion ordered displacements (green bars in Figure 6.3), stabilize the intralayer anion orders the most. The polar and interlayer anion orders follow next in stability and are in close competition with one another. The close competition between the polar and interlayer anion orders makes sense as there is essentially no difference between their anion orders within each perovskite layer, unlike the intralayer anion order. In the polar and interlayer anion orders, the F^- ion always sits on either the top or bottom apical ligand site whereas in the intralayer anion order the position of the F^- ion switches between the apical sites within a perovskite layer.

The origin of the higher stability of the octahedral tilts in the intralayer compounds possibly originates in the alternating anion order in the perovskite layers. Our hypothesis is that in this ideal scenario, the electrostatic interactions of the apical sites, which move closer and further apart with the octahedral tilts, limit the degree of tilting. In the polar and interlayer compounds, the apical interactions are either O–O or F–F, and in the intralayer are always O–F. By using Coulomb’s law, which gives an energy proportional to the product of the two point charges and their distance, the

ratio of the average interaction of the apical sites in the polar and interlayer compounds compared to the intralayer compounds is 2.5:2 or 1.25. This means that the destabilizing electrostatic interactions from the ligands are stronger in the polar and interlayer compounds, which is consistent with our DFT results.

Interestingly, displacements from the anion ordering mode do not always stabilize the structure. With intralayer anion ordering, displacements from O (X_2^-) destabilize the structure. This likely explains why intralayer antipolar anion ordering has never been seen in synthesized heteroanionic RP compounds [27]. However, in the derivative structures, this destabilization is overcompensated by the stabilization gained from octahedral tilting and anharmonic coupling between O and X_3^+ . In $\text{Sr}_2\text{ScO}_3\text{F}$, the competition between these forces is close, but in $\text{Ca}_2\text{ScO}_3\text{F}$, the stabilizing forces far exceed the destabilizing ones, likely due to more acute octahedral tilting. The anion ordering displacements stabilize both the polar and interlayer anion orders, but the magnitude of the stabilization is several times larger in the interlayer anion ordered structures.

In all cases, coupling O and X_3^+ stabilizes the derivative structure. To help determine the origin of this stabilization, the ΔE from the coupling of primary order parameters has been separated into (i) B -site displacements from O (row B in Table 6.1) coupled to the octahedral tilts and (ii) the displacements of all other ions from O (rows A , $X1$, and $X2$ in Table 6.1) and coupled to the octahedral tilts. When octahedral tilts are coupled to the B -site displacements (blue bars in Figure 6.3), the structure always becomes more stable. Additionally, as the magnitude of the B -site displacements increase, ΔE also increases in a nearly linear manner. As will be explained and quantified in the next section, the coupling creates unequal *trans* Sc–O_{eq} bond lengths in the $[\text{ScO}_5\text{F}]^{8-}$ octahedra which stabilizes the structure through the PJT effect. Next, we consider all other ionic displacements in the anion-order mode coupled to the octahedral tilts (gray bars in the

upper panel of Figure 6.3). In most of the structures, this contribution is small and does not effect the relative energetics of the phases. There are a few exceptions, namely structures exhibiting $Cmc2_1$ and $P\bar{4}2_1m$ symmetry. This appears to be driven by the magnitude of the apical anion site displacements ($4e$), which makes sense as this will alter the bond lengths between Sc–O_{ap} and Sc–F and thus the strength of their covalent interactions. In general, it appears that the larger the apical anion site displacement, the larger the energetic gain.

In connecting this data back to Figure 6.2, we first note that the ΔE values obtained are different. Data in Figure 6.3 shows the energy change from specific modes without spontaneous lattice strains relative to an $I4/mmm$ -like structure, whereas data in Figure 6.2 shows the energy of the relaxed derivative structures relative to the relaxed anion ordered structures. The difference in energy between the fully relaxed derivative structures (i.e., Figure 6.2) and the structures with only primary mode contributions (i.e., Figure 6.3) are shown in the bottom panel of Figure 6.3. This energy contains contributions from the aforementioned secondary modes, but is primarily composed of contributions from strain and fully symmetric ionic displacements (i.e., those transforming at Γ_1^+).

The data in Figure 6.3 allows us to understand the connection between anion order and tilt stabilization. It clarifies that the trend in tilt stabilization is consistent between the Sr₂ScO₃F and Ca₂ScO₃F compounds, as intralayer anion ordering stabilizes the octahedral tilts the most in both compounds. The difference in the relative energetics of these phases likely lies in the energy scales and degree of rotations of the structures. In the Sr₂ScO₃F phases, the octahedral tilts are smaller and do not dominate the energetics, so competing factors have a much stronger effect on the overall energetics. In contrast, the degree of octahedral tilting in Ca₂ScO₃F is much greater owing to the small size of the *A*-site cation, thus the octahedral tilting dominates the relative energetics.

Through this analysis, we also learn how the $Cmc2_1$ and $Pna2_1$ phases are stabilized from terms in the Landau model (Equation 6.1). The homogeneous coupling constants (α_i and β_i) of X_3^+ are negative and are large in the case of $\text{Ca}_2\text{ScO}_3\text{F}$, so they likely contribute the most towards the stability of the polar phases. Interestingly, both the homogeneous coupling constants of O and P are energetically unfavorable (positive). In both compounds, destabilization energy from P is small. However in $\text{Sr}_2\text{ScO}_3\text{F}$, the destabilization from O is similar in magnitude to X_3^+ , which means additional, energetically favorable couplings are necessary to stabilize the polar phase. The biquadratic coupling coefficients (γ_i) between O and X_3^+ are energetically favorable, which also helps stabilize the polar phase in $\text{Sr}_2\text{ScO}_3\text{F}$. The coupling between X_3^+ and P is also weakly energetically favorable. (The coupling between O and P was not probed.) The trilinear term appears to also further stabilize the phase as the hard mode, P (Γ_5^-), softens when the two primary modes O and X_3^+ condense (Appendix C). Now that we understand a significant factor in the stabilization of the polar phases in $\text{Sr}_2\text{ScO}_3\text{F}$ comes from the coupling of O and X_3^- , we examine the origin of the stabilization and quantify it.

6.3.3 Polar Displacements Stabilize Octahedral Tilts

In a typical homoanionic perovskite-derived material such as a transition metal oxide, sterics [240, 329] and covalent interactions [330–332] are known to drive rotations and tilts. Furthermore, octahedral tilts can compete with or facilitate local off-centering of cations due to the PJT effect [333, 334]. Because $\text{Ca}_2\text{ScO}_3\text{F}$ and $\text{Sr}_2\text{ScO}_3\text{F}$ are heteroanionic, we should also consider the role of the ligand electrostatic interactions (O^{2-} versus F^-) on the octahedral tilt stability in the presence of steric, covalent, and cation off-centering.

TABLE 6.2: Dipole-dipole (DD) and short-range (SR) contributions to the total (tot) change in energy in $\text{Sr}_2\text{ScO}_3\text{F}$ structures with tilts relative to the anion ordered structures. All values are in meV.

	<i>Abm2</i>	<i>Pbcm</i>	<i>Pnma</i>	<i>Cmc2₁</i>	<i>P4₂cm</i>	<i>P$\bar{4}$2₁m</i>	<i>Pna2₁</i>
ΔE_{tot}	-22.5	–	-31.3	-28.3	-22.6	-23.4	-32.0
ΔE_{DD}	-0.9	–	5.6	-4.8	-1.2	-5.3	5.6
ΔE_{SR}	-21.6	–	-36.9	-23.5	-21.5	-18.1	-37.6

To determine which interaction drives the octahedral tilts, we decompose the energy stabilization into its dipole-dipole (electrostatic) and short-range contributions. The short-range contribution is essentially a catch-all term and encompasses all contributions which are not dipolar in nature, such as steric and covalent interactions [322, 335]. We analyze the octahedral tilts modes relative to their relaxed anion ordered structures. Because this method is based on calculating the energetics from harmonic force constants, we use displacements normalized to 0.25 Å, which is why their energy differences do not match those exactly in Figure 6.2. The separation of these contributions is shown in Table 6.2 and Table 6.3 for $\text{Sr}_2\text{ScO}_3\text{F}$ and $\text{Ca}_2\text{ScO}_3\text{F}$, respectively. The polar PJT distortions in BaTiO_3 are driven by dipole-dipole interactions which are nearly fully compensated by the short-range contribution [336]. Octahedral tilts are similarly driven by the PJT effect [330–332], so we may expect similar results here. However we instead observe that the short-range contribution is the major driving force for the octahedral tilts. The dipole-dipole interactions either de-stabilize the octahedral tilts or stabilize them only by a small amount. The only exception to this is the *Cmc2₁* and *P $\bar{4}$ 2₁m* structures of $\text{Sr}_2\text{ScO}_3\text{F}$, in which the electrostatic contribution is about 20% of the total stabilization.

For comparison, this procedure was repeated for the $X_3^+(0, \eta_1)$ mode in the homoanionic prototypical $n = 1$ RP Sr_2SnO_4 (Appendix C). In this oxide, tilts driven by either ligand electrostatic effects or covalent interactions through the PJT are unlikely as all ligands are equivalent and the d

TABLE 6.3: Dipole-dipole (DD) and short-range (SR) contributions to the total (tot) change in energy in $\text{Ca}_2\text{ScO}_3\text{F}$ structures with tilts relative to the anion ordered structures. All values are in meV.

	<i>Abm2</i>	<i>Pbcm</i>	<i>Pnma</i>	<i>Cmc2₁</i>	<i>P4₂cm</i>	<i>P$\bar{4}$2₁m</i>	<i>Pna2₁</i>
ΔE_{tot}	-44.9	-48.4	-54.6	-51.3	-56.1	-56.8	–
ΔE_{DD}	2.3	11.3	8.1	9.8	-1.5	9.3	–
ΔE_{SR}	-47.2	-59.7	-62.7	-61.1	-54.6	-66.1	–

orbitals are all occupied [330]. Nonetheless, the homoanionic case is very similar to the heteroanionic results as the short-range interaction stabilizes the tilt distortion more than the dipole-dipole interactions and these electrostatic interactions in fact act to destabilize the octahedral tilts. Although there should be no contribution from covalent interactions in the form of mixing ground and excited state wavefunctions, this approach does not allow us to fully disentangle the covalent interactions from steric interactions in the heteroanionic case. The covalent interaction would simply further stabilize the distortion through the short-range component. Therefore, from this data we can only conclude that electrostatic interactions do not drive the tilts in heteroanionic materials.

Aside from the charge difference from the anion substitution, the other major structural distinction from the prototypical homoanionic case is the local off-centering of Sc within the $[\text{ScO}_5\text{F}]^{8-}$ octahedra from the anionic substitution. (Note that this is accompanied by additional displacements of the *A*-site cations and equatorial anions). To clarify the role of the Sc displacement on the stability of the octahedral tilts, we freeze in rotations of varying amplitude into both the prototypical $I4/mmm$ structure with and without the Sc displacements under the imposed anion order and calculate the relative energy changes (Figure 6.4). The rotations are standardized to $X_3^+(\eta_1, \eta_1)$ and use the eigenvectors obtained from phonon calculations on a theoretical homoanionic analogue, Ca_2TiO_4 . The magnitudes of the local displacements match those in the relaxed anion-ordered structures. For $\text{Sr}_2\text{ScO}_3\text{F}$, the magnitudes of the local displacements are 0.23, 0.16,

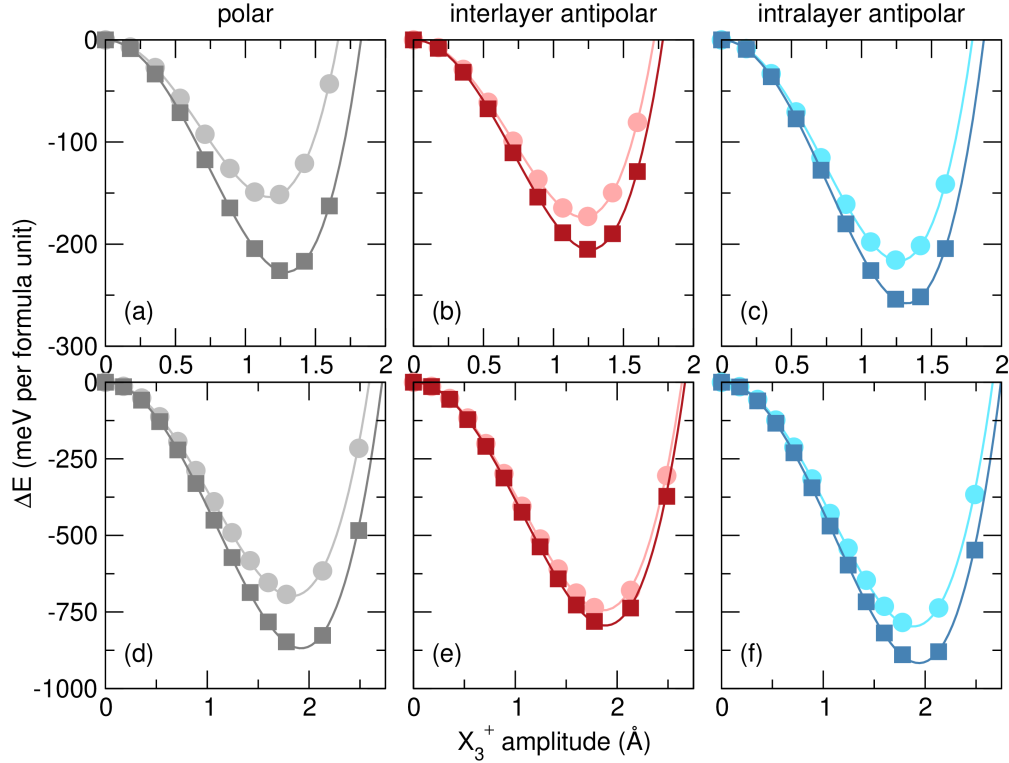


FIGURE 6.4: Energetics of (a)-(c) $\text{Sr}_2\text{ScO}_3\text{F}$ and (d)-(f) $\text{Ca}_2\text{ScO}_3\text{F}$ with octahedral tilts in the presence and absence of Sc displacements due to the heteroleptic $[\text{ScO}_5\text{F}]^{8-}$ octahedron. The circles represent the prototypical $I4/mmm$ structure and the squares represent the $I4/mmm$ structure with the Sc displacements from the given composition and anion order. (a) and (d) have polar anion order, (b) and (e) have antipolar interlayer order, and (c) and (f) have antipolar intralayer order.

and 0.21 Å for the polar, interlayer, and intralayer anion orders, respectively. For $\text{Ca}_2\text{ScO}_3\text{F}$, the magnitudes of the local displacements are 0.23, 0.10, and 0.21 Å for the polar, interlayer, and intralayer anion orders, respectively.

We find that within each composition, the magnitude of the Sc displacements increases the stability of the octahedral tilts (Figure 6.4). In all cases, the octahedral tilts are more stable in structures with local displacements (squares, darker lines) than in the structures without the Sc off-centering displacements (circles, lighter lines). The difference in energy minima between the $\text{Sr}_2\text{ScO}_3\text{F}$ structures with and without the displacements are -73.3, -31.7, and -58.1 meV in the polar, antipolar interlayer, and antipolar intralayer structures, respectively, which scales with the

size of the Sc displacement used in each anion order. Likewise, the energy differences for $\text{Ca}_2\text{ScO}_3\text{F}$ are -170.5, -49.1, and -119.5 meV in the polar, antipolar interlayer, and antipolar intralayer, respectively.

We repeat this experiment with the all-oxide analogue, Ca_2TiO_4 to show that this effect is not unique to heteroanionic materials. Although Ti^{4+} is PJT active, phonon calculations on $I4/mmm$ Ca_2TiO_4 reveal that the PJT distortion occurs along the in-plane direction [337]. The layered structure removes a driving force for out-of-plane polar distortions of the Ti^{4+} [338]. However, upon coupling the out-of-plane polar displacements to the octahedral tilts, we find the stabilization of the octahedral tilts in the structure (Appendix C). The differences between the minimum energies of the structures with and without local Ti displacements are -15.2, -25.5, and -38.5 meV for the homoanionic polar, interlayer, and intralayer displacement patterns, respectively. The stability of these variants differs from the heteroanionic case because the magnitude of the Ti displacements used in Ca_2TiO_4 are equivalent (0.18 Å). These trends indicate that anion order, or the pattern of out-of-plane polar displacements resulting from the anion order, have an influence on the tilt stability. However, the magnitude of the *B*-site displacement appears to have a much stronger affect on the tilt stability, based on Figure 6.4 and the results in the next section.

The origin of this effect lies in a relatively simple geometric argument: the combination of octahedral tilts about an in-plane axis and static polar displacements in a transverse out-of plane direction induces polar in-plane *B*-cation displacements through a PJT effect. This combination of displacive modes is illustrated in Figure 6.5a-d, where the Sc–O and Sc–F bond lengths within the *xz* plane of the $[\text{ScO}_5\text{F}]^{8-}$ octahedron are shown without and with the octahedral rotations and Sc displacements. Without Sc displacements, the Sc–ligand bond lengths are all equal (Figure 6.5a) and remain so with the octahedral tilt mode, X_3^+ , which involves equal but opposite directional

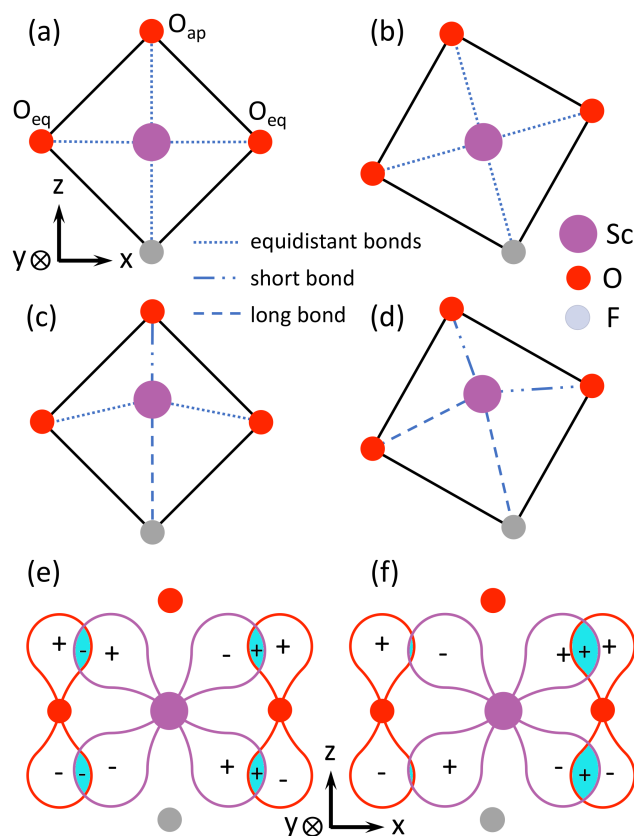


FIGURE 6.5: (a-d) Illustrations of a $[\text{ScO}_5\text{F}]^{8-}$ octahedron showing how local polar displacements and octahedral tilts induce in-plane polar distortions into it. Octahedron without (a) and with (c) local polar displacements along the z axis. Corresponding structures with octahedral tilts are shown without (b) and with (d) polar Sc displacements. (e) and (f) illustrate how an in-plane polar displacement increases the Sc– O_{eq} π -bonding interactions between Sc d_{xz} and O_{eq} p_z orbitals. When Sc^{3+} is in the center of the octahedra (e), the Sc–O bonds are equidistant and thus, the net overlap between the π bonds is zero. When Sc^{3+} displaces along the x direction, the net overlap is non-zero.

displacements of the equatorial anions (O_{eq}) along the out-of-plane direction (Figure 6.5b). Because the Sc displacement occurs along z to produce asymmetric apical Sc–O and Sc–F bond lengths (Figure 6.5c), the nominally rigid rotation removes the equivalence between the *trans* Sc– O_{eq} bonds and causes the bond lengths to become unequal (Figure 6.5d). This asymmetry in the bond lengths increases the covalency from dp orbital mixing due to the PJT effect (compare the orbital overlap in Figure 6.5e and f). This is the same effect that stabilizes the polar displacements in BaTiO_3 , where the mixing of occupied anion p orbitals and unoccupied metal d orbitals close to the Fermi

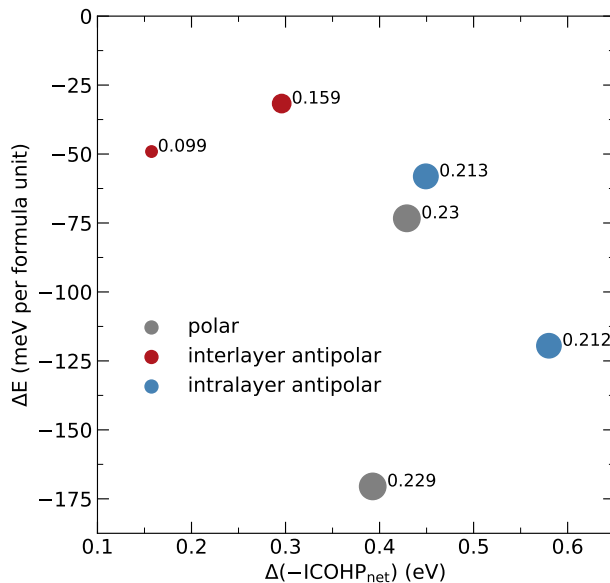


FIGURE 6.6: Comparison of the energetic stabilization of octahedral tilts from Sc displacements, ΔE , to the increase in our covalency metric, $\Delta(-\text{ICOHP}_{\text{net}})$, from the same displacements. The magnitude of the Sc displacement is listed next to each data point and the marker size is proportional to the square of the magnitude of the Sc displacements.

level also occurs [305, 312, 339]. In this case, the enhanced covalency is mediated by the octahedral tilting that occurs among the heteroleptic units shown in Figure 6.5e and f. When Sc is in the center of an octahedron, the positive orbital overlap of the Sc d_{xz} and $O_{\text{eq}} p_z$ cancels the negative overlap so the net overlap is zero. When the Sc is displaced in the x -direction, the net overlap is non-zero.

The PJT effect is stronger when the states that are mixing are energetically close together. We first examine the molecular orbital diagram and density of states (DOS) for the Sc displaced structures to determine which interactions dominate. Since we substitute a F^- for an O^{2-} , the symmetry of the octahedra is no longer O_h (or $m\bar{3}m$ in Hermann-Mauguin notation), which means the d orbitals do not split into an e_g doublet and a t_{2g} triplet. The symmetry of the octahedra with one substituted site is C_{4v} ($4mm$) and we derive the molecular orbital diagram in Appendix C, which matches the crystal field splitting of similar $[\text{MO}_5\text{X}]$ octahedra [340–342]. The molecular

orbital diagram predicts that the $3d$ orbitals (symmetry) from lowest to highest energy are ordered d_{xy} (b_2), $\{d_{xz}, d_{yz}\}$ (e), $d_{x^2-y^2}$ (b_1), and d_{z^2} (a_1), where the d_{xz} and d_{yz} orbitals are degenerate. The partial DOS for the anion ordered structures (Appendix C) supports this interpretation, although the center of mass of the the d_{xy} bands is at higher energy than that of the degenerate (d_{xz}, d_{yz}) orbitals, it does form the conduction band edge. For this reason, we consider only π -bonding interactions of the anions with the d_{xy} orbital. Additionally, because the apical F $2p$ and O_{ap} states exhibit a_1 and b_1 symmetries, we do not consider the σ -type Sc-F and Sc- O_{ap} interactions. Thus, we only consider the following π Sc- O_{eq} interactions in our analysis: d_{xy} - p_x or p_y (dependent upon which axis O_{eq} is located), d_{xz} - p_z , and d_{yz} - p_z .

To quantify these changes in chemical bonding, we integrate the $-pCOHP$ of the relevant π -bonding interactions (and obtain the $-ICOHP$) and take the difference between the Sc- O_{eq} bonds along the same axes, i.e., bonds where are *trans* to one another, to obtain the net overlap ($-ICOHP_{net}$). The difference is taken because the COHP does not account for the positive or negative phase of the orbital interactions. For consistency with the data in Figure 6.4, we also take the difference between the net overlap of the structures with and without the Sc displacements to obtain the increase in covalency due to the off centering and refer to it as $\Delta(-ICOHP_{net})$.

Figure 6.6 plots the energetic gain of the octahedral tilts with the Sc displacements (from Figure 6.4) against this increase in covalency due to the Sc displacements, along with the magnitude of the B -site displacement as the marker size. In general, the greater the increase in covalency, the more stabilizing the octahedral tilts. This trend is not perfectly linear, which may be due to missing secondary contribution to the overall change in energy or from A -site cations affecting the covalency of the Sc-O bonds via an inductive effect that is unaccounted for. Another possible missing energetic contribution is the change in covalency of the Sc- O_{ap} π -interaction, as discussed

earlier. The choice of *A*-site cation can also influence the covalency of the metal–anion bonds by reducing their bond formation through *A*-site *s* or *p* states hybridizing the occupied metal *3d* states [332] (or occupied *2p* states, in our case). However this seems unlikely, as “covalency-limiting” cations are generally those with large ionic size or high polarizability, and the largest outlier in Figure 6.6 is from a $\text{Ca}_2\text{ScO}_3\text{F}$ interlayer phase, which has a smaller ionic size and lower polarizability. We also plot the magnitude of the Sc displacements using the size of the data points. In general, we also find an increase in the stability of the tilts (and, thus, the covalency) with the size of the Sc displacements, which is understandable as the Sc–O_{eq} bond lengths are dependent on the magnitude of this displacement.

From these analyses, we conclude that the octahedral tilts are driven through short-range interactions described by sterics or covalent interactions rather than electrostatic forces. The local out-of-plane polar displacements induced by the anion order drive and further stabilize the octahedral tilts through the PJT effect as the coupling of tilts and local polar distortions induces in-plane polar displacements in the heteroleptic octahedra.

6.4 Conclusion

We have outlined a new mechanism for ferroelectricity in perovskite-derived heteroanionic materials, which we refer to as improper anion-order ferroelectricity. Anharmonic coupling between intralayer antipolar anion ordering and octahedral tilts generates polar displacements through antipolar displacement of O and F anions. We evaluated the feasibility of this mechanism through DFT calculations on $\text{Sr}_2\text{ScO}_3\text{F}$ and $\text{Ca}_2\text{ScO}_3\text{F}$ and found that intralayer anion ordering may be stabilized through large octahedral tilts. We also found that the driving force for octahedral tilts in these oxyfluoride appear to be no different than the driving force in homoanionic materials—sterics

and covalent interactions appear to drive octahedral tilting. We also found that out-of-plane local polar displacements, driven by the anion substitution, further stabilize octahedral tilting through the SOJT effect and the formation of unequal *trans* Sc–O_{eq} bonds. We showed that this stabilization is due to covalent effects through a COHP analysis and found that the magnitude of the *B*-site displacements serves as a useful descriptor for the relative stabilization effect of these out-of-plane local polar displacements. The link uncovered here between local polar displacements and octahedral tilts or rotations is intriguing and could have promising applications in multiferroic heteroanionic materials [343], as magnetic interactions could be tuned by rotations of the octahedra, which could be controlled through the magnitude of the transition metal cation displacements. We hope that these results spur interest in experimental synthesis and investigations into RP-type heteroanionic materials and anion order in complex transition metal compounds.

Chapter 7: Exploring the Phase Space of Epitaxially Strained $n = 2$ Ruddlesden-Popper Oxyfluorides

7.1 Introduction

Research into $n = 2$ Ruddlesden-Popper (RP) transition metal oxides surged after anharmonic multimode coupling of octahedral rotation, octahedral tilt, and polar modes was proposed as a method of inducing polarization into $A_3B_2O_7$ compounds [272]. This was particularly attractive because this mechanism does not rely on the chemistry of the B -site, as is the second-order Jahn-Teller driven ferroelectric such as $BaTiO_3$. This discovery led to many predictions of novel ferroelectrics, although this hybrid improper ferroelectric mechanism has been only recently experimentally confirmed in a handful of compounds, including $(Ca,Sr)_3Ti_2O_7$ single crystals [308], $(Sr,Ca)_3Sn_2O_7$, $Sr_3Zr_2O_7$ [344–346], $(Ca_{0.69}Sr_{0.46}Tb_{1.85}Fe_2O_7)$ [347], and $Ca_3(Ti,Mn)_2O_7$ [348]. To broaden the search for polar structures, approaches such as epitaxial-strain stabilization and cation engineering [273,347] were investigated as a method of tuning octahedral rotations and tilts to break the inversion symmetry of nominally centrosymmetric structures. Epitaxial strain was found to be an effective method for stabilizing ferroelectric phases from nonpolar dielectrics and tuning electronic polarizations, Curie temperatures, and ferroelectric switching barriers [349,350]. Recent work has

also uncovered an unexpected polar-to-nonpolar phase transition driven by epitaxial strain, suggesting that relatively trivial anharmonicity may have a significant effect on strain-polarization coupling [351].

In heteroanionic materials, exploring strain-lattice coupling relationships is just beginning. More progress has been made in oxynitride materials, as thin film growth of stoichiometric oxyfluorides is difficult due to the toxicity of F_2 gas (although recent progress has been made in the fluorination of phases with ordered oxygen vacancies [83, 161, 171, 352]). In perovskite oxynitrides, small domains of thin film $SrTaO_2N$ were found to exhibit ferroelectricity due to their *trans*- $[TaO_4N_2]$ anion order [277]. Later work confirmed that these *trans*-type anion orders were stabilized through compressive strain [166]. Computational investigations into perovskite oxynitrides has also suggested that polar oxynitrides can be stabilized through epitaxial strain due to the stabilization of *trans* anion orders [264, 353]. Recent work has also confirmed that $n = 2$ Ruddlesden-Popper oxynitrides, specifically $Ca_3Nb_2N_2O_5$, can adopt similar polar structures with $a^-a^-c^+$ octahedral rotations found in oxide analogues [76].

In this chapter, I investigate the lattice dynamics of $n = 2$ Ruddlesden-Popper oxyfluorides and explore their phase space with epitaxial strain using first principles calculations. I begin with $Ba_3In_2O_5F_2$, as it is one of the only synthesized $n = 2$ RP oxyfluorides [354], and then investigate $Sr_3In_2O_5F_2$, as its reduced *A*-site cation size should favor larger amplitude rotations and tilts in the structure. I first present the results of phonon and epitaxial strain calculations for these compounds separately, and then I discuss them in the context of homoanionic materials.

7.2 Methods

All calculations were performed using density functional theory (DFT) with projector augmented-wave (PAW) potentials [87] and PBEsol [62] as implemented in the Vienna *Ab initio* Simulation Package (VASP) [43, 44]. The valence electron configurations were as follows: $5s^25p^66s^2$ for Ba, $4s^24p^65s^2$ for Sr, $5s^25p^1$ for In, $2s^22p^4$ for O, and $2s^22p^5$ for F. For structural relaxations, I used a plane-wave cutoff of 650 eV and $5 \times 5 \times 1$ Monkhorst-Pack k -point mesh [79]. Structural relaxations were complete when the forces on each ion were less than $1 \text{ meV } \text{\AA}^{-1}$ and stresses were less than 10 MPa along each crystal axis. Metastable and ground state structures were derived from phonon calculations, which used Phonopy [286] to setup the finite-displacement calculations and for post-processing. Force constants were computed using the frozen phonon method on $2 \times 2 \times 2$ supercells with a higher plane-wave cutoff of 750 eV to ensure accurate forces.

Once derivative structures were identified, I examined the stability of the phases with epitaxial strain. To simulate strain on a cubic [001] perovskite substrate, the in-plane a and b lattice parameters are fixed while the out-of-plane c -axis and all ionic positions are allowed to relax. I relax in 1% and 2% increments between -4% and 4% strain, with the reference lattice parameter being the $a = b$ lattice parameters of the fully relaxed $I4/mmm$ structure of each compound (4.19 Å and 4.08 Å for $\text{Ba}_3\text{In}_2\text{O}_5\text{F}_2$ and $\text{Sr}_3\text{In}_2\text{O}_5\text{F}_2$, respectively).

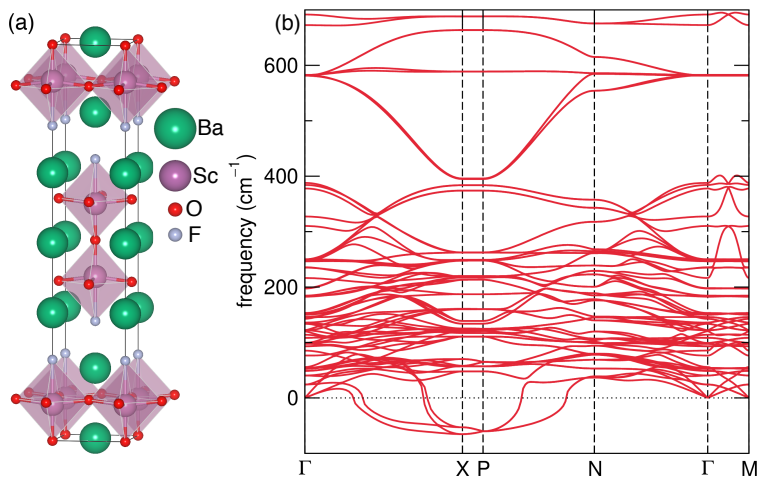


FIGURE 7.1: The (a) atomic structure and corresponding (b) phonon dispersion of the conventional cell of Ba₃In₂O₅F₂.

7.3 Results

7.3.1 Ba₃In₂O₅F₂

Ba₃In₂O₅F₂, whose structure is shown in Figure 7.1, is a known oxyfluoride that can be synthesized through a solid state method [354]. It has a distorted $n = 2$ RP structure with $I4/mmm$ symmetry and ordered anions, which drive the characteristic second-order Jahn-Teller distortions of the In³⁺ ions towards the oxide ion in the [InO₅F] heteroleptic octahedra. Because of its ordered anions, it is a good candidate for a DFT-based computational study. I first calculate its phonon dispersion across the whole Brillouin zone to determine which derivative phases maintaining octahedral connectivity may exist. These structures are then used to initialize structure relaxations to search for the 0 K ground state structure.

As shown in Figure 7.1b, there are only a few unstable modes in this compound: two pairs of degenerate modes at X ($k = (0.5, 0.5, 0)$ in the conventional basis) at $65i$ and $53i$ cm⁻¹ and four degenerate modes at P ($k = (0.5, 0.5, 0.5)$ in the conventional basis) at $60i$ cm⁻¹. All these modes

primarily consist of octahedral rotations with different rotation patterns. In Glazer notation [114], all modes have $a^-b^0c^0$ tilt patterns within their perovskite layers. The difference between the mode displacements is the axis of rotation and the sense (i.e. clockwise vs counterclockwise) of the rotation in adjacent (or further) perovskite layers. In the X modes, the adjacent layers have $b^0a^-c^0$ tilt patterns, relative to the first layer (i.e., the adjacent perovskite layers have the same degree of tilting about the orthogonal in-plane axis). The difference between the degenerate pairs is in the sense of the rotation, which is opposite in one layer and produces structures of symmetry $P4_2/mnm$ and $P4_2/mcm$. The degenerate P modes double the unit cell along the c axis with every other perovskite layer having opposite sense, producing structures with symmetry $I\bar{4}2m$.

I enumerate all possible combinations of these modes, condense them into structures, and relax them to obtain their ground state total energies. I then compare the energetics of these structures and find that the lowest energy structure is $P4_2/mnm$, whose energy difference is -30 meV relative to the $I4/mmm$ structure. Homoanionic compounds that adopt this $P4_2/mnm$ structure typically have two different A - or B -site cations [355–364], except in the case of $Ba_3Zr_2S_7$ [365]. I also compute its phonons and find that it is dynamically stable, so it is the ground state structure. The energy difference suggests a phase transition from the $P4_2/mnm$ to $I4/mmm$ phase should take place around 348 K, however investigations of the structure at room temperature show it is $I4/mmm$ [354]. I predict that the compound should show a phase transition to the $P4_2/mnm$ phase somewhere between room and liquid nitrogen (77 K) temperature.

Next, I explore the phase space of $Ba_3In_2O_5F_2$ with epitaxial strain. In addition to the phases mentioned previously ($P4_2/mnm$, $P4_2/mcm$, and $I\bar{4}2m$), I also consider $Cmcm$, $Ibam$, and $Cmma$ symmetries, as they can be condensed by combining instabilities found in the phonon calculations.

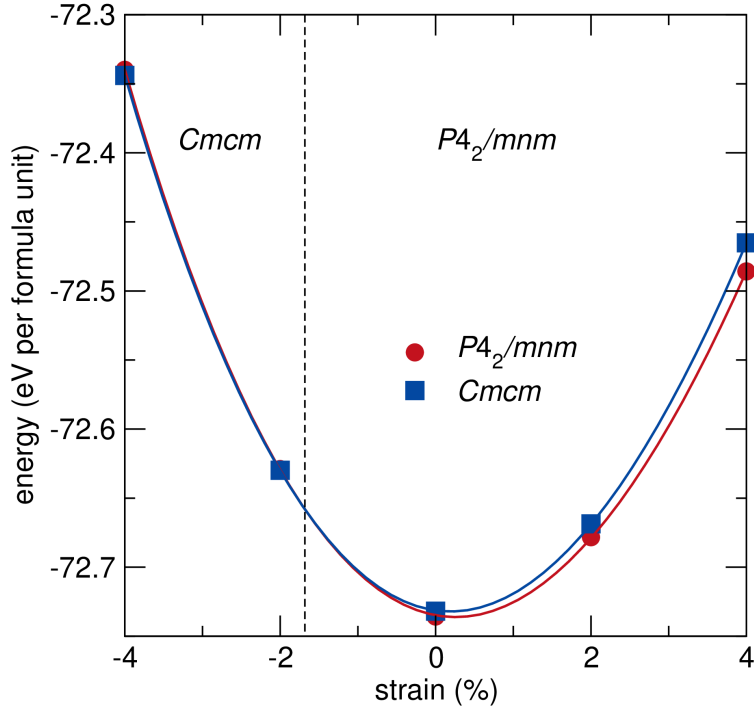


FIGURE 7.2: Total energy evolution with epitaxial strain for $Ba_3In_2O_5F_2$ polymorphs. The dotted lines delineate regions of stability for each polymorph of $Ba_3In_2O_5F_2$.

Like those phases discussed previously, these phases are also primarily composed of different patterns of in-phase octahedral tilts. The $Cmcm$ structure exhibits the $a^-a^-c^0$ octahedral rotation patterns in its perovskite layers, the $Cmma$ structure has the same rotation as $Cmcm$ with one layer having rotations of the opposite sense, and the $Ibam$ structure doubles the size of the unit cell by stacking a cell with $a^-a^-c^0/a^-a^-c^0$ tilt pattern on top of another unit cell with $a^-a^-c^0/a^-a^-c^0$ tilts in the opposite sense.

The evolution in the total energy of $Ba_3In_2O_5F_2$ polymorphs as a function of strain is shown in Figure 7.2. Under tensile strain, the ground state structure, $P4_2/mnm$, is the most stable phase. Under compressive strain, the $P4_2/mnm$ structure is the most stable phase until between -1% and -2% strain, where the stability changes to the $Cmcm$ structure, which is maintained under further compressive strain, up to -4%. This is consistent with observations in perovskite oxides, which show

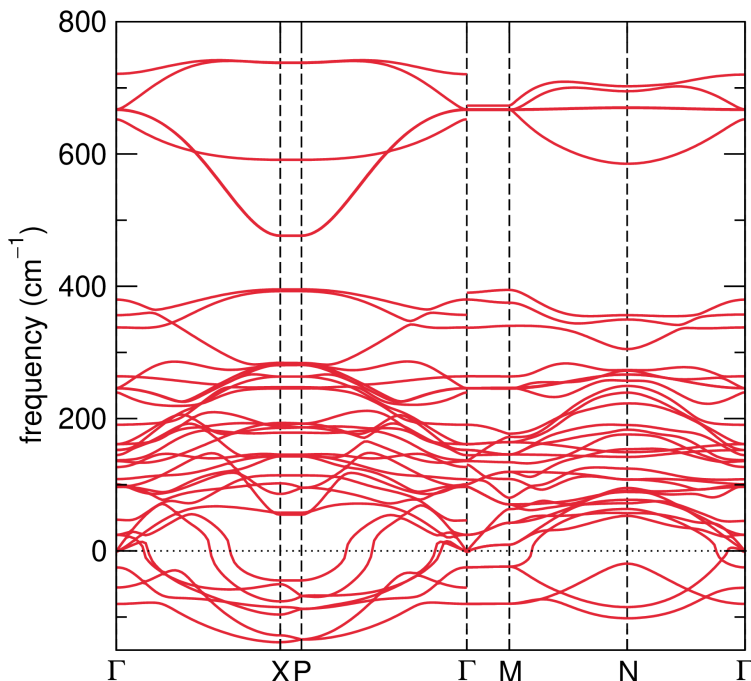


FIGURE 7.3: The phonon dispersions of the primitive cell of Sr₃In₂O₅F₂ with LO/TO splitting.

increase octahedral tilting under compressive strain [366,367]. This also can be explained by the *Cmcm* structure containing octahedral tilts about both in-plane axes within each perovskite layer. Assuming rigid octahedra, octahedral tilting would be compatible with a smaller unit cell size. Although *P4₂/mnm* also contains octahedral tilting, it only has in-plane tilts in each perovskite layer. Tilting about two, orthogonal in-plane axes would likely accommodate a smaller *ab* lattice parameters.

7.3.2 Sr₃In₂O₅F₂

Next, I explore the phase space of Sr₃In₂O₅F₂ and try to find its ground state structure. The phonon dispersions of the primitive cell of Sr₃In₂O₅F₂ are shown in Figure 7.3, whose unstable bands are more complex than those in Ba₃In₂O₅F₂. Although there are more unstable bands, the mode representations are still rather similar to those in Ba₃In₂O₅F₂; the modes largely contain

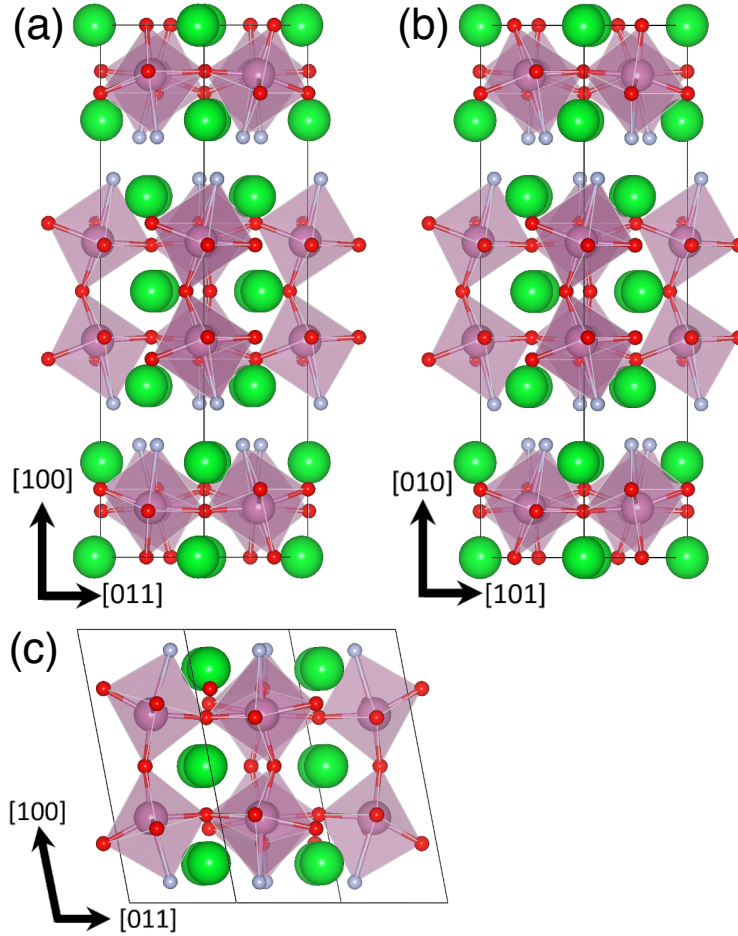


FIGURE 7.4: Atomic structures of the metastable phases, $Cmc2_1$ (a) and $Pnma$ (b), and ground state phase, $P2_1/c$ (c), of $Sr_3In_2O_5F_2$.

octahedral tilts about the in-plane axes (either about the central Sc ion or the central O_{ap} ion in the perovskite layers) with additional modes that induce octahedral shearing of the apical O_{ap} or F ions. The $a^0a^0c^+$ tilting distortion, which is commonly unstable in homoanionic materials, is stable in $Sr_3In_2O_5F_2$.

Because there are too many unstable modes to condense and enumerate all possible structures, I combine the modes below $100i\text{ cm}^{-1}$, relax the structures, and calculate the phonons of the lowest energy phase. I repeat this procedure until I find the lowest energy, dynamically stable structure which I identify as the ground state structure. A few of these metastable phases are shown in

Figure 7.4a,b. One structure is a direct analogue to a phase observed in homoanionic $n = 2$ RPs. The $Cmc2_1$ structure has the ubiquitous $a^-a^-c^+$ rotation pattern that induces polarity into the structure and has a relative energy of -700.8 meV per formula unit compared to the $I4/mmm$ phase. The $Pnma$ phase has a relative energy of -695.6 meV per formula unit and also exhibits the $a^-a^-c^+$ rotation pattern within its perovskite layers, however one of these in-plane rotations has the opposite sense compared to the $Cmc2_1$ phase (see the top perovskite layers of Figure 7.4a,b), which makes the A -site displacements antipolar and keeps the structure centrosymmetric. Interestingly, in homoanionic materials a centrosymmetric structure with $Pbcn$ symmetry is typically observed [346], which has a $a^-a^-c^-$ rotation pattern in its perovskite layers. In $Sr_3In_2O_5F_2$, the $Pbcn$ structure was about 50 meV higher in energy than $Pnma$.

It is interesting to note that in contrast to the homoanionic analogue, the primary order parameters that drive the phase transition to $Cmc2_1$ from the $I4/mmm$ parent phase in $Sr_3In_2O_5F_2$ are the octahedral tilts, X_3^- , and the polar distortion, Γ_5^- . The $Cmc2_1$ phase, relative to the $I4/mmm$ phase, is composed of three modes. The aforementioned X_3^- and Γ_5^- modes, and the octahedral rotation mode, X_2^+ , which induces $a^0a^0c^+$ octahedral rotations into the structure. In many oxide $n = 2$ RP compounds [272,346,351,368], the $Cmc2_1$ phase is stabilized by the condensation of the soft octahedral tilt and rotation modes and the trilinear coupling term, which decreases the overall energy of the child phase $Cmc2_1$ through the coupling of all three order parameters. However, the primary modes driving the phase transition are the soft (energetically favorable) octahedral tilts and rotations, X_3^- and X_2^+ , as the remaining polar mode is hard or energetically unfavorable. In $Sr_3In_2O_5F_2$, X_2^+ is always stable while X_3^- and Γ_5^- are unstable making them the primary ordering parameters for the $Cmc2_1$ phase and distinct from the homoanionic case.

The ground state structure with symmetry $P2_1/c$ is shown in Figure 7.4c, which has a relative

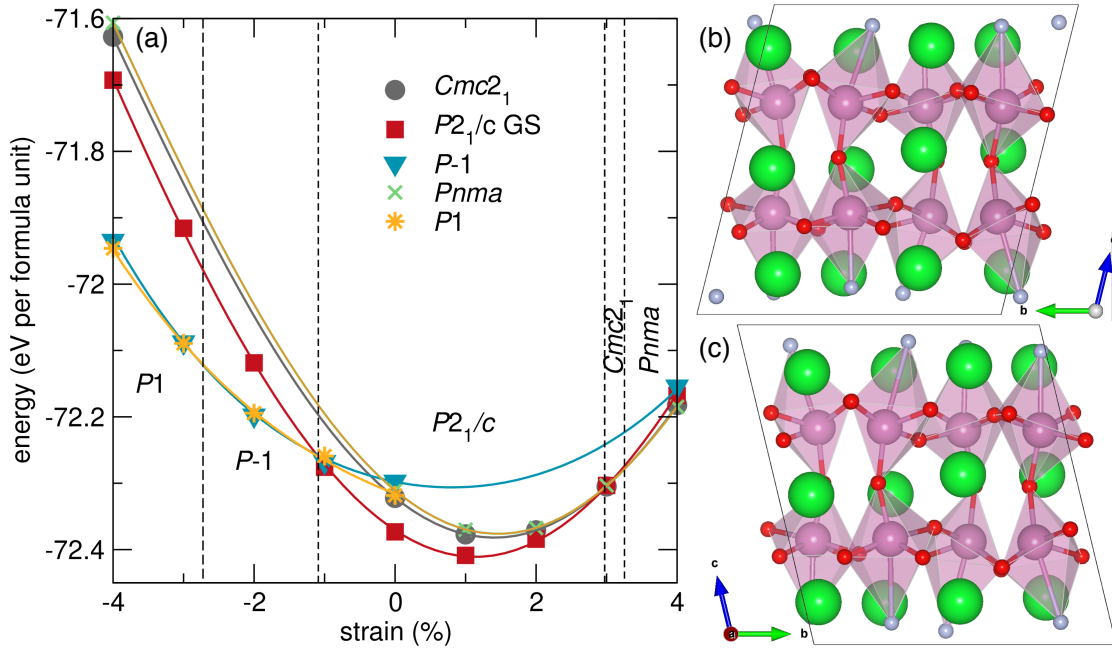


FIGURE 7.5: (a) Total energy evolution with epitaxial strain for $\text{Sr}_3\text{In}_2\text{O}_5\text{F}_2$ polymorphs. The dotted lines delineate regions of stability for each polymorph of $\text{Sr}_3\text{In}_2\text{O}_5\text{F}_2$. The atomic structures of the $P\bar{1}$ (b) and $P1$ (c) polymorphs of $\text{Sr}_3\text{In}_2\text{O}_5\text{F}_2$.

energy of -730.0 meV per formula unit. It is primarily composed of $a^-a^-c^0$ octahedral tilts (X_3^-) and a condensation of the $A2$ mode [$k = (0.25, 0.25, 0.5)$ in the conventional cell]. The $A2$ mode (shown in Appendix D) is composed of antipolar displacements of In, F, and Sr ions along the a -axis, a slight in-phase octahedral rotation, and a transverse, wave-like modulation of the equatorial O ions. This modulation occurs along the c axis, but the ions displace along the a -axis and significantly distort the $[\text{InO}_5\text{F}]$ octahedra.

Using these relaxed structures and the ten lowest energy phases I observed (see Appendix D), I now explore the phase space of $\text{Sr}_3\text{In}_2\text{O}_5\text{F}_2$ with epitaxial strain. Figure 7.5 shows the evolution of the total energy as a function of epitaxial strain. The $P2_1/c$ ground state structure is stable from about -1% to about 3% strain. Under tensile strain, the homoanionic analogue phases with $a^-a^-c^+$ rotations, $Pnma$ and $Cmc2_1$, are stabilized. The $Cmc2_1$ phase is stable from 3.0% to 3.3% strain,

while the $Pnma$ phase is stable at least until 4% strain, which was the largest strain value examined. In homoanionic perovskite and perovskite-derivative compounds, compressive strain will typically induce out-of-plane octahedral rotations (i.e. $a^0a^0c^-$ or $a^0a^0c^+$) into the structure [350, 366–368], so it may seem counterintuitive to observe structures with out-of-plane rotations under tensile strain. However, because the competing phases contain complex distortions including wave-like modulations and octahedral shearing, compressive strain may favor these highly distorted phases over those with only octahedral rotations and tilts. Indeed, if I plot the angles of the octahedral tilts and rotations with tensile strain (Figure 7.6), the trends are consistent with previous studies, i.e., with increasing tensile strain, the rotations decrease and the tilts increase. I note that this trend is qualitatively observed in the phase transitions that occur in $Sr_3In_2O_5F_2$ under compressive strain, but because those structures have highly distorted octahedra, quantitative measurements of the out-of-plane and in-plane octahedral rotations were difficult to directly compare compounds with more rigid octahedra.

Under compressive strain, the triclinic phase $P\bar{1}$ is stabilized at -1.1% and $P1$ at -2.7% to -4%. The phases are shown in Figure 7.5b,c and their mode decomposition are in Appendix D. The transition from the $P2_1/c$ structure to the $P\bar{1}$ structure condenses many modes but the largest distortions are due to the X_1^- mode, which produces out-of-phase octahedral rotation, and the $A1$ mode, which is a transverse, wave-like distortion of the apical fluorides whose direction is along the b axis and with displacements of F along the c axis. The primary difference between the $P\bar{1}$ and $P1$ phase comes from the condensation of a Γ_5^+ mode, which is a polar displacement of the In ions along the a -axis.

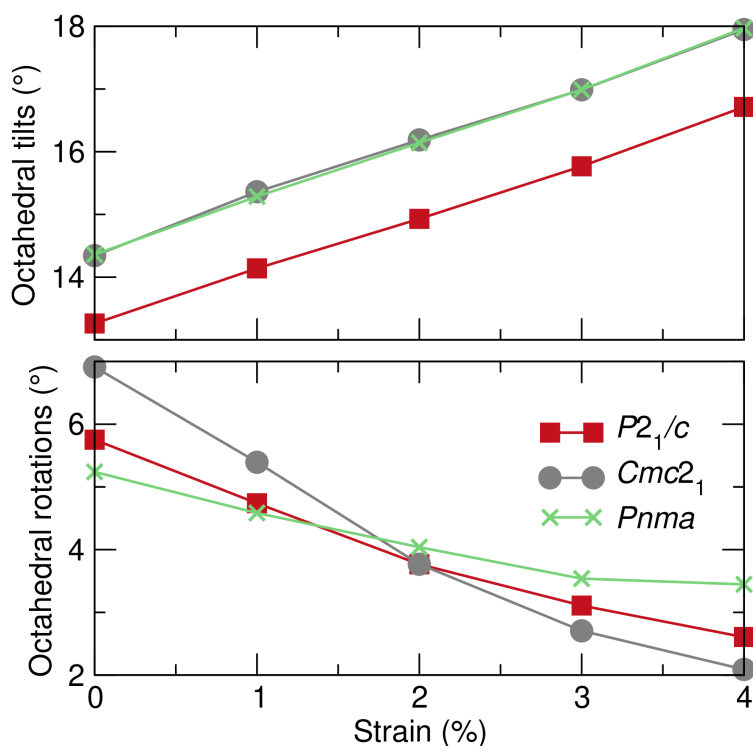


FIGURE 7.6: Octahedral tilt (top) and rotation (bottom) angles as a function of strain for $\text{Sr}_3\text{In}_2\text{O}_5\text{F}_2$ polymorphs.

7.4 Discussion

Previous research has indicated that decreasing the size for the A -site cation (or decreasing the tolerance factor) can induce further octahedral tilts and rotations into the structure [347]. In terms of the tolerance factor modified for RP compounds [369], this reduces the tolerance factor from 0.905 to 0.855 for the Ba and Sr compounds, respectively. Based on trends in homoanionic materials, I expect that the ground state structures with lower tolerance factors should exhibit in-phase octahedral tilts and either in-phase or out-of-phase octahedral rotations, generating structures with either $Cmc2_1$ or $Pbcn$ symmetry. In $\text{Ba}_3\text{In}_2\text{O}_5\text{F}_2$ and $\text{Sr}_3\text{In}_2\text{O}_5\text{F}_2$, I instead observe $P4_2/mnm$ and $P2_1/c$ ground state symmetries. The structure of $\text{Ba}_3\text{In}_2\text{O}_5\text{F}_2$ is commonly seen in $n = 2$ RP compounds which have two species of A site cation, however, to my knowledge the structure of

$\text{Sr}_3\text{In}_2\text{O}_5\text{F}_2$ is unique.

The instability of the typically observed structures $Cmc2_1$ and $Pbcn$ phases can be explained as a result of the fluorine substitution on the apical site. In Chapter 6 I established that out-of-plane polar distortions within octahedra will stabilize octahedral tilts about an in-plane direction, likely resulting in enhanced tilting in $\text{Ba}_3\text{In}_2\text{O}_5\text{F}_2$ and $\text{Sr}_3\text{In}_2\text{O}_5\text{F}_2$ compared to their homoanionic analogues. Recent research has indicated that a large octahedral tilt may suppress octahedral rotations and vice versa [350]. This can be explained phenomenologically by the cross term between octahedral rotations (whose amplitude is represented by R) and tilts (T) in the free energy, $\gamma T^2 R^2$ (see Chapter 6 for the full free energy expansion). For fixed values of T , this term renormalizes the coefficient of the T^2 term, αT^2 as $(\alpha + \gamma T^2)$. Hence, when $T^2 > -\alpha/\gamma$, the rotation instability is suppressed and it becomes energetically favorable to have no rotations.

The ground state structure of $\text{Sr}_3\text{In}_2\text{O}_5\text{F}_2$ is more mysterious, as this derivative structure has not been observed in any known $n = 2$ RP compounds. The most unique feature of this structure is the transverse, wave-like modulation of the equatorial oxides, induced by the condensation of the A_2 mode. This feature is reminiscent other oxyfluorides, such as K_3TiOF_5 , an incommensurate structure with many of these wave-like modulations [370], and $A_3\text{MoO}_3\text{F}_3$ ($A = \text{K}, \text{Rb}$), which has an extremely large unit cell with non-cooperative octahedral tilts [371]. These compounds suggest that complex distortions with wave-like atomic displacements or polyhedral precessions may be relatively common within oxyfluoride materials. Further research is necessary to understand the origin of these distortions.

The structural evolutions observed in $\text{Ba}_3\text{In}_2\text{O}_5\text{F}_2$ and $\text{Sr}_3\text{In}_2\text{O}_5\text{F}_2$ with epitaxial strain appear to be largely consistent with the trends observed in perovskite and perovskite-derived homoanionic

materials. Tensile strain increases octahedral tilt while compressive strain favors octahedral rotations. However, the origin of the stabilization of triclinic phases in $\text{Sr}_3\text{In}_2\text{O}_5\text{F}_2$ under compressive strain is still under investigation.

Chapter 8: Investigating Insulator-Metal Transitions in Anion Disordered and Ordered TiOF

8.1 Introduction

This thesis has thus far focused heavily on ferroelectricity. I now turn to electronic properties through an investigation of TiOF. Recently, a computational study of rutile-structured MoON was published which predicted a MIT in the anion ordered oxynitride MoON [372]. Through anion engineering principles, the MIT was designed and aided by *fac* configured $[\text{MoO}_3\text{N}_3]$ octahedra and a d^1 band filling of Mo^{5+} . Within oxyfluoride materials, TiOF, a rutile-type oxyfluoride with d^1 Ti^{3+} and disordered anions has been synthesized [373,374]. Magnetic measurements indicated it is paramagnetic down to 5 K and diffuse scattering suggest local *cis*- or *fac*-ordering of the octahedra [374]. However, transport measurements were not feasible due to the small size of the single crystals.

TiOF is therefore an excellent candidate for a computational investigation of how local atomic structure alters the electronic properties. In constructing a useful model, however, an accurate description of the anion disordered structure is also necessary. I choose to use a virtual crystal approximation (VCA) to simulate the 50/50 O/F mixed occupancy on the anion sites within density

functional theory (DFT) calculations [375–377]. Unlike the quasi-random structure models [378], where the anion disorder is modeled by appropriately decorating a large supercell, the VCAs simulate a mixed occupancy site by creating a virtual ion which is the interpolation between the component ions of the mixed site. VCAs have been evaluated and used to simulate heterovalent cation substitution in complex oxide materials [379,380], but have been rarely used for anion substitution [265,381]. Because oxygen and fluorine have similar bonding character to transition metals, I propose to use a 50/50 O/F VCA for the disordered model.

I investigate the ground state and electronics structures of the disordered and ordered variants of TiOF to predict if a thermally driven metal-insulator transition may occur. In the disordered case, I determine the ground state structure by calculating the phonon dispersions with the VCA and then assessing any dynamical instabilities. These modes are then frozen-in and relaxed, from which the lowest energy structure is determined to be the ground state. In the anion ordered case, I decorate supercells of TiOF with an appropriate statistical distribution of O and F sites, relax these anion ordered structures, and choose the lowest energy anion ordered configuration. Once we’ve obtained the lowest energy anion disordered structure and the lowest energy anion ordered configurations of TiOF, I calculate their electronic structures and compare and contrast the results.

8.2 Methods

Density functional theory (DFT) calculations are used to investigate the structure dynamics and electronic structure of both the anion ordered and anion disordered variants of TiOF. DFT calculations are performed using the projector-augmented wave (PAW) formalism [87,91] as implemented in the Vienna *Ab initio* Simulation Package (VASP) [43,44] within the generalized gradient approximation (GGA) of Perdew-Burke-Ernzerhof (PBE) for densely packed solids (PBEsol) [62], as

recommended for oxyfluorides [253]. For all calculations, total energies were converged to 10^{-8} eV. In all structural relaxations, forces on the ions were converged to within $1 \text{ meV } \text{\AA}^{-1}$ and lattice stresses to below 0.1 kbar. Non-spin polarized calculations were used as TiOF is expected to be paramagnetic down to low temperature [374].

For the anion disordered (primitive) cell, a virtual crystal approximation (VCA) was used to model the 50/50 O/F anion sites of the experimental structure of TiOF. The VCA was implemented using the built-in tools in VASP, which uses the formulation devised by Belliache and coworkers [376]. For the disordered cell, a 650 eV plane-wave cutoff was used, and k -space integrations were performed on a $7 \times 7 \times 7$ Monkhorst-Pack mesh [79] with Methfessel-Paxton smearing (150 meV width) for Brillouin zone integrations.

For the anion ordered configurations, supercells of the size $1 \times 2 \times 1$, $1 \times 1 \times 2$, $1 \times 2 \times 2$, and $2 \times 2 \times 1$ were used to generate anion ordered configurations of TiOF. The anion ordered structures were generated using SOCCR [192] which generates all symmetry unique anion configurations (excluding those with $P1$ symmetry). Only the structures with fac - $[\text{TiO}_3\text{F}_3]$ octahedral units are examined herein. For the ordered cell, a 650 eV plane-wave cutoff was also used, and k -space integrations were performed on an appropriate Monkhorst-Pack mesh [79] (i.e., $7 \times 4 \times 7$ for a $1 \times 2 \times 2$ supercell) with Methfessel-Paxton smearing (150 meV width) for Brillouin zone integrations.

A dense $13 \times 13 \times 13$ Monkhorst-Pack mesh was used for density of states (DOS) calculations on the primitive cell (with appropriate scaling for the supercells) to ensure adequate sampling of the Brillouin zone. Dynamical stability was evaluated using the frozen phonon method as implemented by PHONOPY [286]. Some adjustment to the PHONOPY source code was needed to take into account the VCA, e.g. a virtual atom with interpolated atomic mass (further details can be found in Appendix E. Additionally, for PHONOPY to correctly interpret the forces on the ions, the forces

on the virtual “ghost” ions (i.e. 50% O and 50% F) must be summed prior to post-processing with PHONOPY. The frozen phonon method was also used to determine the forces on the ions and generate the dynamical matrices with finite displacements of 0.02 Å.

8.3 Results and Discussion

8.3.1 Modeling Anion Disordered TiOF using a VCA

TABLE 8.1: Comparison of the experimental and DFT relaxed lattice parameters of the rutile ($P4_2/mnm$) anion disordered TiOF.

	$a = b$ (Å)	c (Å)	volume (Å ³)
Experimental structure (90 K) [374]	4.653	3.014	65.254
DFT relaxed	4.645	3.009	64.922

I first discuss the results of the anion disordered structure calculations which used a VCA to approximate the 50/50 O/F mixed occupancy sites. The lattice parameters of the DFT relaxed structure, shown in Figure 8.2a, are remarkably similar to the experimental TiOF cell (Table 8.1). As expected with PBEsol, the lattice is slightly overbonded however the error in the lattice parameters is around 0.17% (volume 0.50%), which is much less than the error of $\sim 2\%$ often found in other anion ordered oxyfluorides [253]. The remarkable similarity in the experimental and DFT VCA relaxed lattice parameters of disordered systems has been seen before with oxynitrides [382], so this is not unexpected. Although the similarity in lattice parameters does not validate the VCA model, it provides some assurance that the lattice dynamics and bonding of the mixed occupancy anion sites are grossly modeled appropriately.

To investigate the possibility of structural symmetry breaking in rutile TiOF, I first evaluate the dynamical stability of the rutile, anion disordered TiOF. The phonon dispersions of the rutile

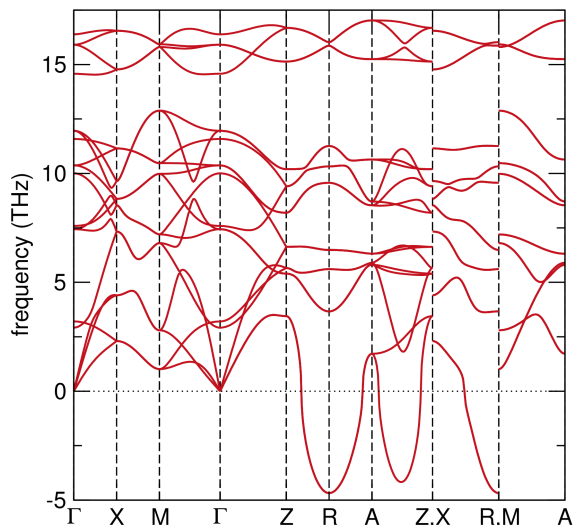


FIGURE 8.1: Phonon dispersions of rutile, anion disordered TiOF with the VCA

structure with the VCA are shown in Figure 8.1. I find three instabilities in this structure: two degenerate modes at R [$k = (0, 0.5, 0.5)$, irrep R_1^-] and one minimum at $k = (0.26, 0.26, 0.5)$, between the high symmetry k -points A and Z [$k = (0.5, 0.5, 0.5)$ and $(0, 0, 0.5)$, respectively]. The instability at R is expected as this instability is also observed in phonon calculations of d^1 VO_2 and is (at least partially) attributed to the origin of the MIT in the oxide [383,384]. Indeed, I find that the structure modulated with the unstable R mode shows many similar characteristics to the displacements observed in the MIT of VO_2 , such as dimerization of the Ti ions and zig-zagging of the Ti along the chains of octahedra parallel to the c -axis. However, the structure has a symmetry of $P2_1/m$, which is slightly lower than the insulating phase of VO_2 ($P2_1/c$). I also note that I am able to achieve softening at the R point without additional strong correlation effects (i.e. without the addition of a Hubbard U) which, to my knowledge, is not possible in VO_2 [385]. The band with a minimum at $k = (0.26, 0.26, 0.5)$ produces an incommensurate-like structure (shown in Appendix E). The largest displacements are octahedral shearing in (110) plane of $[\text{TiO}_3\text{F}_3]$ octahedra and slight dimerization of Ti ions.

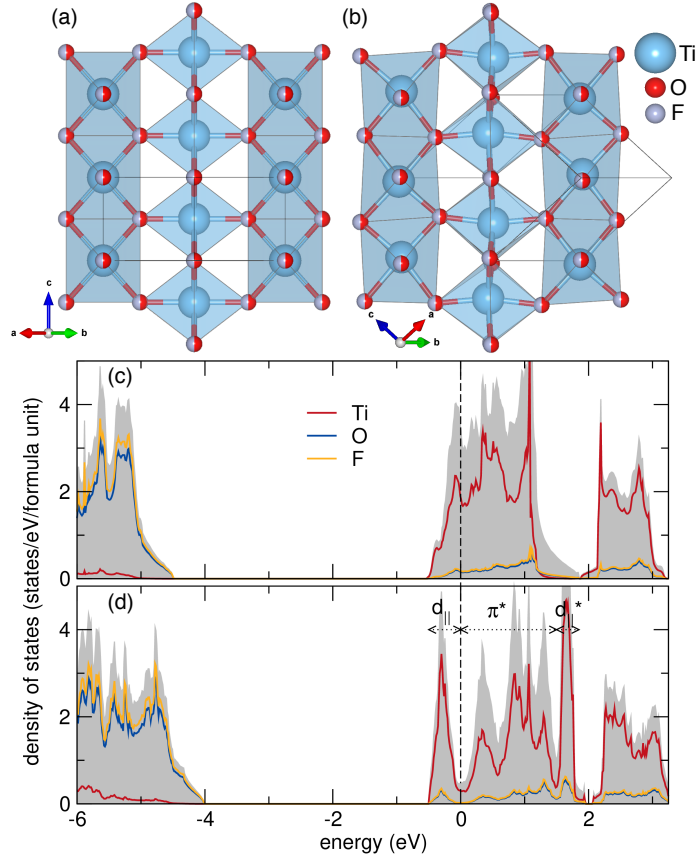


FIGURE 8.2: Atomic and electronic structures of the rutile and monoclinic phases of anion disordered TiOF. Relaxed anion disordered rutile $P4_2/mmm$ (a) and monoclinic $P2_1/c$ (b) structures of TiOF. The corresponding DOS of the rutile (c) and monoclinic (d) phases of TiOF. The gray shaded portion is the total DOS and the Fermi level is at 0 eV.

I confirm the degenerate R_1^- modes are generate a more stable structure than the incommensurate mode (Appendix E) and so proceed with relaxing the $P2_1/m$ structure. Upon relaxation, the structure relaxes to a monoclinic (M1) $P2_1/c$ space group (Figure 8.2b), which identical in symmetry to the low temperature structure of VO_2 . Additionally, the M1 phase of TiOF, like the M1 phase of VO_2 , also exhibits dimerization of the cations (3.01 Å in rutile and 2.74 and 3.267 Å in M1) and alternating displacements of the cations perpendicular to the direction of the edge-sharing chains. The difference in energy between the R and M1 phases is 59.4 meV per formula unit (~ 689.3 K).

The electronic structures of the R and M1 phases obtained from the VCA are shown in Figure 8.2c,d. The R phase is metallic, which agrees experiment as the synthesized samples are black (or extremely dark) in color [373,374]. The electronic structure of rutile TiOF appears very similar to that of VO₂ [386], where octahedral crystal field splitting (t_{2g} - e_g) is further split due to the elongation of the [TiOF₆] octahedra along the [001] direction. The e_g orbitals are split into two d_σ orbitals and the three t_{2g} orbitals are split into two d_π orbitals, which mix with anion $2p_\pi$ states, and a $d_{||}$ orbital [383]. In the rutile structure, the antibonding π^* overlaps with the $d_{||}$ states. I also note that because I am using a VCA, the O p and F p orbitals are fully “hybridized,” rather than the F p states appearing lower in energy as a narrow band below the O p states, which is typically expected in oxyfluorides [27].

The electronic structure of the M1 phase appears to be very similar to the M1 phase of VO₂ [383,386]. In VO₂, the monoclinic phase splits the $d_{||}$ band through bonding between the V-V pairs while simultaneously destabilizing the π^* orbital to obtain an insulating phase [383]. The M1 phase of TiOF shows splitting of the $d_{||}$ orbital, however it still appears to be metallic with no gap opening. Because the gap is nearly open, I assess whether strong correlations (i.e. $+U$) will open an insulating gap in the M1 phase.

Previous research has recommended a Hubbard U values ranging from 2-7 eV for Ti³⁺ with 2-3 eV found to be the best when studying catalytic systems as it accurately models both the electronic structure and energetics of catalytic reactions [387,388]. Because the compound is already very close to forming a gap, I relax the M1 phase of TiOF with a Hubbard $U = 1$ eV and 2 eV to capture enhanced Coulomb interactions in a Ti³⁺ compounds (Figure 8.3). Even with a small amount of correlation, a very small gap of 10 meV forms when $U = 1$ eV and a larger gap of 280 meV opens when $U = 2$ eV. When a Hubbard U is added to the M1 phase without a structural relaxation, no

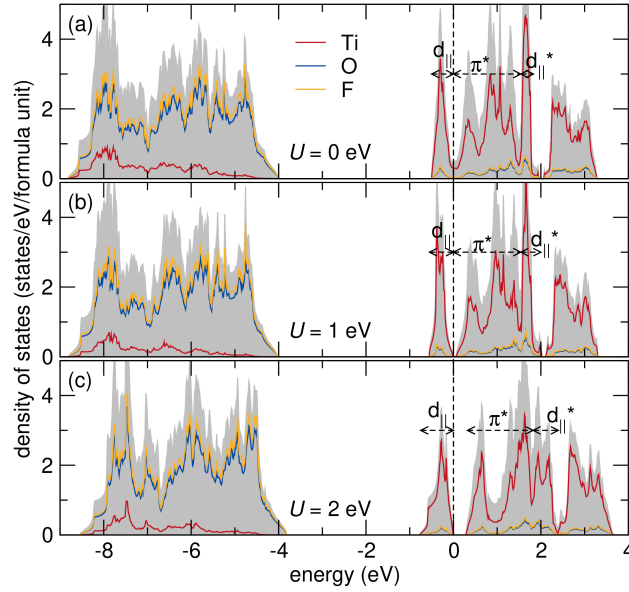


FIGURE 8.3: Density of states of the monoclinic phases of TiOF with varying Hubbard U . The gray shaded portion is the total DOS.

gap is formed when $U = 1$ eV and a gap of 180 meV opens when $U = 2$ eV.

In rutiles with d^1 transition metals, the axial ratio c/a has been linked to the structural instability that triggers the MIT [384]. In general, undistorted rutile compounds have a c/a ratio greater than 0.625 and distorted rutile compounds are less than 0.625. The axial ratio of the undistorted rutile MIT materials VO_2 and NbO_2 are both close to this critical value and the difference between the c/a ratios of the distorted and undistorted rutile structures are relatively small, suggesting that there is an inherent structural instability that causes a transition between the two structures. The c/a axial ratios of the rutile and monoclinic TiOF (as specified in Ref. [384]) are 0.648 and 0.571, respectively, crossing the structure stability boundary. However, the difference in the axial ratios between the two structures is quite large in comparison to the rutile and monoclinic axial ratios of VO_2 (0.626 and 0.635, respectively) and NbO_2 (0.626 and 0.618, respectively). In MoON, the *fac*-ordering of the octahedra enables an axial ratio that is close to the critical rutile structural stability ratio ($c/a = 0.609$) while alternative anion orders give ratios ≤ 0.590 [372].

Because the difference in the axial ratios of the phases are large and the rutile value is quite far from the critical ratio, the MIT may not be present in TiOF.

These results suggest that the anion disordered structure of TiOF, which has been synthesized, likely displays metal-insulating behavior with the insulating phase appearing at a relatively high temperature (~ 689 K). Our collaborators plan to refine their single crystal synthesis and conduct more detailed characterization of the local structure through pair distribution function (PDF). Their measurements have been delayed due to 2020 COVID19 pandemic.

8.3.2 Modeling Anion Ordered TiOF

I also explore the anion ordered variants of TiOF to determine if a similar structural transition could occur in the anion ordered structure. A computational study of anion ordered MoON, a similar rutile-like oxynitride, showed an isosymmetric MIT [372]. Although the low temperature phase of MoON exhibits the same dimerization and zig-zagging of the Mo ions as is seen in VO_2 and which is not seen in the high temperature phase, the transition is isosymmetry because the anion order lowers the symmetry of the rutile-like phase. I first use SOCCR [192] to generate anion ordered structures with only *fac*- $[\text{TiO}_3\text{F}_3]$ heteroleptic octahedra, as this is the most commonly observed isomer for $[\text{MO}_3\text{F}_3]$ octahedra [27]. The energetics of the alternative anion orders can be found in Appendix E. In contrast to MoON, whose lowest energy phases have symmetry Pc , the lowest energy anion configuration in TiOF is $P2_1/c$ (Figure 8.4a).

The crystal structure of the ground state anion ordered variant is similar to the anion disordered structure. The $P2_1/c$ ordered phase shows similar Ti-Ti dimerization (2.61 Å) and slight zig-zagging of the Ti ions along the *c*-axis. A symmetry analysis on the homoanionic analogues of the structure (i.e. with only one ligand species) shows that the anion ordered and disordered equilibrium structures

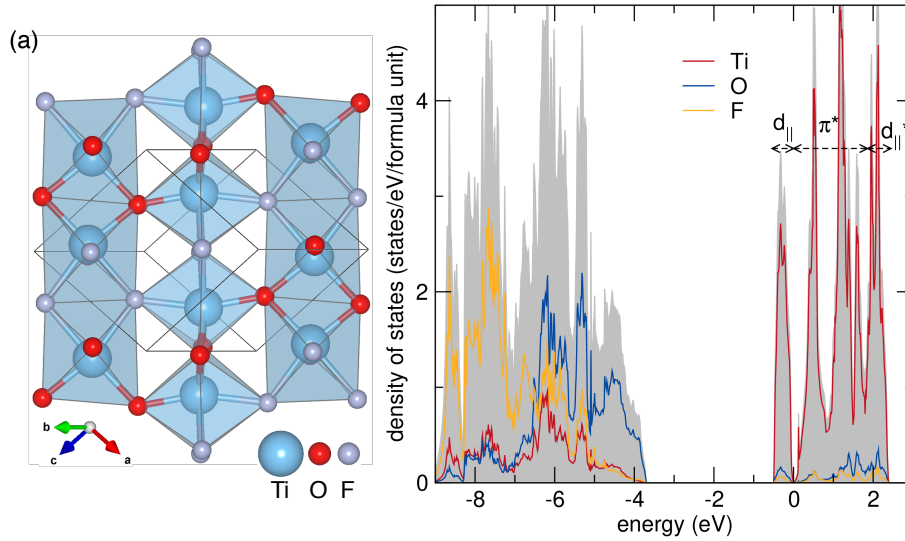


FIGURE 8.4: (a) Atomic and (b) electronic structures of the ground state configuration of anion ordered TiOF.

are derived from the same symmetry-adapted modes (primarily R_1^-) driving the transition between the rutile and respective monoclinic phases. The dimerization distance of the ordered phase is slight closer than the disordered phase, 2.61 Å and 2.74 Å, respectively. The a and c axes are about 0.5 Å larger than the disordered cell, although it is difficult to compare them due to the difference between lattice parameter errors when using a VCA. The c/a ratios are also very similar at 0.571 and 0.578 for the disordered and ordered phases, respectively.

The DOS of the ordered phase (calculated without $+U$) is shown in Figure 8.4b and the conduction band states appear very similar to the anion disordered phase. Unlike the disordered phase, I also see that the ordered phase is barely insulating, with a gap of $E_g = 10$ meV. I also see that the gap between the π^* and/or d_{\parallel}^* and e_g states is absent in the ordered phase. These two features are likely related, as the missing gap between the π^* and/or d_{\parallel}^* and e_g states suggests a destabilization of the π^* orbital, which increases the separation between it and the d_{\parallel} states, producing a gap. This is supported by the respective structures, as the ordered phase shows shorter Ti–O bond distances compared to the Ti–F, which should destabilize the π^* orbital [383].

The disordered phase shows similar short and long Ti–O/F bond lengths, but their difference is not as large as in the ordered phase.

Of the remaining phases that were higher in energy than $P2_1/c$, none have anion orders that are compatible with a small displacive phase transition from the $P2_1/c$ phase. Because the electronic structure suggests that this material is close to both conducting and insulating states, anion ordered TiOF may exhibit a metal-insulator transition, although there is clear structural distinction between the insulating and metallic phases as in VO_2 , NbO_2 , and MoON . Interestingly, nearly all of the ordered phases at the DFT level are clearly metallic, except for the $P2_1/c$ phase and the next lowest energy phase Cm (Appendix E). This clearly shows that anion order strongly affects the electronic structure of these materials.

Chapter 9: Conclusions and Outlook

In this dissertation, I sought to improve our theoretical understanding of oxyfluorides by using density functional theory calculations to identify structure-property relationships and leverage them to design oxyfluorides with functional properties. Anion engineering offers a way to expand the design space of functional materials by adapting crystal-chemistry principles established in transition metal oxides into the design of novel heteroanionic materials. To this end, I addressed the following aspects of materials design in oxyfluorides:

In Chapter 4, I evaluated existing crystal chemistry principles, the bond valence sum and global instability index (GII), for heteroanionic materials and adapted them into a workflow which screens for highly unstable candidate compositions in a given structure type. The GII of stable heteroanionic materials was found to be slightly higher than transition metal oxide compounds. Using this workflow, I predicted $\text{Sr}_2\text{AlO}_3\text{F}$ to be stable and attempted to synthesize it, however due to a small driving force, the material did not appear through solid state synthetic methods. The workflow I developed reduces the computational cost for similar high-throughput DFT-based predictions of new heteroanionic materials, enabling faster and accurate predictions of synthesizable heteroanionic materials. This will enable experimentalists to implement more targeted syntheses of new oxyfluorides, which are challenging due to the toxicity of their reactants.

In Chapter 5 and Chapter 6, I investigated how ferroelectricity may be induced into oxyfluoride structures. Chapter 5 describes my analysis of a potential switchable ferroelectric in a known oxyfluoride, noncentrosymmetric KNaNbOF_5 , which exhibits a phase transition to a centrosymmetric, high temperature phase. Based on our computational model of the transition, I predict that an intermediate phase should appear between the known phases and confirmed this through in-situ ^{19}F MAS NMR. I then modeled potential ferroelectric switching pathways and find that switchable ferroelectricity is feasible and the polarization originates from the anions, which may be unique to heteroanionic materials. This then led to results reported in Chapter 6, in which I proposed a new mechanism for ferroelectricity called improper anion-ordered ferroelectricity which couples anion order and octahedral tilts to polar distortions in $n = 1$ Ruddlesden-Popper compounds. Based on *ab initio* calculations, I predicted that this mechanism is possible in $\text{Ca}_2\text{ScO}_3\text{F}$ and showed that its anion order configuration is different than $\text{Sr}_2\text{ScO}_3\text{F}$. The following significant insights into structure-property relationships in heteroanionic materials and TMO were also made: (i) The anion order may be tunable based on the degree of octahedral tilts in the system and (ii) local polar displacements within transition metal octahedra stabilize octahedral tilts or rotations about an axis orthogonal to the polar displacements due to the pseudo-Jahn-Teller effect. Because anion order often facilitates properties in heteroanionic materials, finding (i) is important because it will aid materials engineers in achieving desired phases and properties through the selection of chemical compositions. Since (ii) is a general result, it may spark interest in the ultrafast laser spectroscopy community, where polar displacement modes can be pumped and used to tune properties reliant on the degree of octahedral rotations, such as magnetism. Given that our proposed mechanism for ferroelectricity relies on the anions for the electronic polarization, heteroanionic materials may also be interesting candidates to support multiferroism. I anticipate that these studies will prompt

further exploration of heteroanionic materials for ferroelectric properties.

Next, I investigated the coupling of anharmonicity with strain in $n = 2$ RP oxyfluorides. First, I found that as the tolerance factor in oxyfluorides decreases, the oxyfluorides adopt unique structures from their oxide analogues. In particular, there is a tendency in these materials to condense transverse wave-like modulations of the anions as the tolerance factor decreases and under compressive strain. The trends in octahedral tilting and rotations as a function of strain are the same as in oxides and the oxyfluorides studied here. Specifically, the frequency and amplitude of these transverse wave-like modulations increases with compressive strain. I also observed that these octahedral rotations are energetically unfavorable in these oxyfluorides, likely because of the enhanced stability of octahedral tilts as described in the previous chapter. To complete this description and motivate advancements in the synthesis of thin film oxyfluorides, the stability of structures with alternate anion orders should be evaluated as a function of epitaxial strain.

Using design principles for metal-insulator transition materials, first established in rutile transition metal oxides, I investigated the electronic and atomic structures of TiOF in Chapter 8. Using virtual crystal approximations (VCA), I predicted that the anion disordered variant of TiOF will show a metal-insulator transition with structural phase transition similar to VO_2 . Importantly, I showed that an added Hubbard U correction is not necessary to drive the phase transition, unlike VO_2 , suggesting that heteroanionic materials can be used as a tool to gain important insights into complex transitions of transition metal oxides. The anion ordered variant of TiOF exhibits structural features that are similar to the monoclinic, insulating phase of VO_2 , however I find that it is most likely metallic. The ordered variant may exhibit MIT as it close to the phase boundary between insulating and metallic states, although I do not find an accompanying structural phase transition. Although I justified the use of a VCA in this compound as it accurately predicts the

lattice parameters of disordered TiOF, further work to confirm the application of VCA to HAMS would enable accurate prediction of properties in many anion disordered heteroanionic compounds. Comparing calculated properties between quasi-random structure models and VCAs of oxynitrides and oxyfluorides would provide valuable insight into the importance of accurately modeling local structural distortions in disordered heteroanionic materials. I also note that today, VCAs cannot be used in the context of order-disorder transitions, as the energies of the virtual atoms are not interpolated correctly, which has been noted elsewhere [382].

This dissertation provides insights into the changes in atomic and electronic structures due to anion substitution. It also demonstrates how the unique structural features of heteroanionic materials due to anion ordering that can be leveraged to design new mechanisms for desirable properties. I anticipate that this will spark more interest into important fundamental aspects of heteroanionic materials design, such as anion ordering, and motivate researchers to adopt anion engineering as a new tool in the repertoire for the design of novel functional materials.

Bibliography

- [1] T Mizokawa, A Fujimori, H Namatame, K Akeyama, and N Kosugi. Electronic structure of the local-singlet insulator NaCuO₂. *Phys. Rev. B*, 49(11):7193–7204, mar 1994.
- [2] Vladimir V. Gapontsev, Daniel I. Khomskii, and Sergey V. Streltsov. Magnetism and charge ordering in high- and low-temperature phases of Nb₂O₂F₃. *J. Magn. Magn. Mater.*, 420:28–32, 2016.
- [3] C T Chen, G. L. Wang, X Y Wang, and Z Y Xu. Deep-UV nonlinear optical crystal KBe₂BO₃F₂—discovery, growth, optical properties and applications. *Appl. Phys. B*, 97(1):9–25, sep 2009.
- [4] Won Bin Im, Nathan George, Joshua Kurzman, Stuart Brinkley, Alexander Mikhailovsky, Jerry Hu, Bradley F. Chmelka, Steven P. DenBaars, and Ram Seshadri. Efficient and Color-Tunable Oxyfluoride Solid Solution Phosphors for Solid-State White Lighting. *Adv. Mater.*, 23(20):2300–2305, may 2011.
- [5] Jinhyuk Lee, Daniil A Kitchaev, Deok-hwang Kwon, Chang-wook Lee, Joseph K Papp, Yisheng Liu, Zhengyan Lun, Raphaële J. Clément, Tan Shi, Bryan D. McCloskey, Jinghua Guo,

- Mahalingam Balasubramanian, and Gerbrand Ceder. Reversible Mn²⁺/Mn⁴⁺ Double Redox in Lithium-Excess Cathode Materials. *Nature*, 556(7700):185–190, apr 2018.
- [6] Po-Hsiu Chien, Jaye K. Harada, Haoyu Liu, Sawankumar Patel, Chen Huang, James M. Rondinelli, Kenneth R. Poeppelmeier, and Yan-Yan Hu. Microscopic Insights into the Reconstructive Phase Transition of KNaNbOF₅ with ¹⁹F NMR Spectroscopy. *Chem. Mater.*, 32(13):5715–5722, jul 2020.
- [7] Michael Holland, Nenian Charles, James M. Rondinelli, and Kenneth R. Poeppelmeier. Reconstructive Transitions from Rotations of Rigid Heteroanionic Polyhedra. *J. Am. Chem. Soc.*, 138(36):11882–11889, 2016.
- [8] Gerhard Pfaff. *Inorganic Pigments*. De Gruyter, Berlin/Boston, sep 2017.
- [9] Paul Anthony Cox. *Transition metal oxides: an introduction to their electronic structure and properties*, volume 27. Oxford University Press, 2010.
- [10] Leila Ghadbeigi, Jaye K Harada, Bethany R. Lettiere, and Taylor D. Sparks. Performance and resource considerations of Li-ion battery electrode materials. *Energy Environ. Sci.*, 8(6):1640–1650, 2015.
- [11] J. Georg Bednorz and K. Alex Müller. Perovskite-type oxides—The new approach to high-T_c superconductivity. *Rev. Mod. Phys.*, 60(3):585–600, 1988.
- [12] Masatoshi Imada, Atsushi Fujimori, and Yoshinori Tokura. Metal-insulator transitions. *Rev. Mod. Phys.*, 70(4):1039–1263, oct 1998.
- [13] Sang Wook S.-W. Cheong and Maxim Mostovoy. Multiferroics: A magnetic twist for ferroelectricity. *Nat. Mater.*, 6(1):13–20, 2007.

- [14] A P Ramirez. Colossal magnetoresistance. *J. Phys.: Condens. Matter*, 9(39):8171–8199, sep 1997.
- [15] Eric Bousquet, Matthew Dawber, Nicolas Stucki, Céline Lichtensteiger, Patrick Hermet, Stefano Gariglio, Jean-Marc Triscone, and Philippe Ghosez. Improper ferroelectricity in perovskite oxide artificial superlattices. *Nature*, 452(7188):732–736, apr 2008.
- [16] Jak Chakhalian, John W. Freeland, Andrew J. Millis, Christos Panagopoulos, and James M. Rondinelli. Colloquium: Emergent properties in plane view: Strong correlations at oxide interfaces. *Rev. Mod. Phys.*, 86(4), 2014.
- [17] Kenneth R. Poeppelmeier and James M. Rondinelli. Mismatched lattices patched up. *Nat. Chem.*, 8(4):292–294, apr 2016.
- [18] S Catalano, M Gibert, J Fowlie, J Íñiguez, J-M Triscone, and J Kreisel. Rare-earth nickelates R NiO 3 : thin films and heterostructures. *Reports Prog. Phys.*, 81(4):046501, apr 2018.
- [19] J Chakhalian, J W Freeland, H.-U. Habermeier, G Cristiani, G Khaliullin, M. van Veenendaal, and B Keimer. Orbital Reconstruction and Covalent Bonding at an Oxide Interface. *Science*, 318(5853):1114–1117, nov 2007.
- [20] Marita O’Sullivan, Joke Hadermann, Matthew S. Dyer, Stuart Turner, Jonathan Alaria, Troy D. Manning, Artem M. Abakumov, John B. Claridge, and Matthew J. Rosseinsky. Interface control by chemical and dimensional matching in an oxide heterostructure. *Nat. Chem.*, 8(4):347–353, apr 2016.
- [21] A Ohtomo and H Y Hwang. A high-mobility electron gas at the LaAlO₃/SrTiO₃ heterointerface. *Nature*, 427(6973):423–426, jan 2004.

- [22] Julie A. Bert, Beena Kalisky, Christopher Bell, Minu Kim, Yasuyuki Hikita, Harold Y. Hwang, and Kathryn A. Moler. Direct imaging of the coexistence of ferromagnetism and superconductivity at the LaAlO₃/SrTiO₃ interface. *Nat. Phys.*, 7(10):767–771, oct 2011.
- [23] James M. Rondinelli and Craig J. Fennie. Octahedral Rotation-Induced Ferroelectricity in Cation Ordered Perovskites. *Adv. Mater.*, 24(15):1961–1968, apr 2012.
- [24] Nicole A. Benedek, James M. Rondinelli, Hania Djani, Philippe Ghosez, and Philip Lightfoot. Understanding ferroelectricity in layered perovskites: new ideas and insights from theory and experiments. *Dalt. Trans.*, 44(23):10543–10558, 2015.
- [25] J. Paul Attfield. Principles and Applications of Anion Order in Solid Oxynitrides. *Cryst. Growth Des.*, 13(10):4623–4629, 2013.
- [26] Hiroshi Kageyama, Katsuro Hayashi, Kazuhiko Maeda, J. Paul Attfield, Zenji Hiroi, James M. Rondinelli, and Kenneth R. Poeppelmeier. Expanding Frontiers in Materials Chemistry and Physics with Multiple Anions. *Nat. Commun.*, 9(1):772, dec 2018.
- [27] Jaye K Harada, Nenian Charles, Kenneth R Poeppelmeier, and James M Rondinelli. Heteroanionic Materials by Design: Progress Toward Targeted Properties. *Adv. Mater.*, 31(19):1805295, may 2019.
- [28] Jared T. Incorvati, Liwen F. Wan, Baris Key, Dehua Zhou, Chen Liao, Lindsay Fuoco, Michael Holland, Hao Wang, David Prendergast, Kenneth R. Poeppelmeier, and John T. Vaughey. Reversible Magnesium Intercalation into a Layered Oxyfluoride Cathode. *Chem. Mater.*, 28(1):17–20, 2016.

- [29] Liwen F. Wan, Jared T. Incorvati, Kenneth R. Poeppelmeier, and David Prendergast. Building a fast lane for Mg diffusion in $\text{Mg}_{1-x}\text{MoO}_3$ by fluorine doping. *Chem. Mater.*, 28(19):6900–6908, 2016.
- [30] Allison Wustrow, Baris Key, Patrick J. Phillips, Niya Sa, Andrew S. Lipton, Robert F. Klie, John T. Vaughey, and Kenneth R. Poeppelmeier. Synthesis and Characterization of MgCr_2S_4 Thiospinel as a Potential Magnesium Cathode. *Inorg. Chem.*, 57(14):8634–8638, 2018.
- [31] Frédéric Sauvage, Vincent Bodenez, Hervé Vezin, Thomas A Albrecht, Jean-Marie Tarascon, and Kenneth R Poeppelmeier. $\text{Ag}_4\text{V}_2\text{O}_6\text{F}_2$ (SVOF): A High Silver Density Phase and Potential New Cathode Material for Implantable Cardioverter Defibrillators. *Inorg. Chem.*, 47(19):8464–8472, oct 2008.
- [32] Yu Pan, Sheng-Ping Guo, Bin-Wen Liu, Huai-Guo Xue, and Guo-Cong Guo. Second-order nonlinear optical crystals with mixed anions. *Coord. Chem. Rev.*, 374:464–496, nov 2018.
- [33] Anant A Setlur, Emil V Radkov, Claire S Henderson, Jae-Hyuk Her, Alok M Srivastava, Nagaveni Karkada, M Satya Kishore, N Prasanth Kumar, Danny Aesram, Anirudha Deshpande, Boris Kolodin, Ljudmil S Grigorov, and Uwe Happek. Energy-Efficient, High-Color-Rendering LED Lamps Using Oxyfluoride and Fluoride Phosphors. *Chem. Mater.*, 22(13):4076–4082, 2010.
- [34] Nathan C. George, Kristin A. Denault, and Ram Seshadri. Phosphors for Solid-State White Lighting. *Annu. Rev. Mater. Res.*, 43(1):481–501, 2013.
- [35] Akira Chikamatsu, Yuji Kurauchi, Keisuke Kawahara, Tomoya Onozuka, Makoto Minohara, Hiroshi Kumigashira, Eiji Ikenaga, and Tetsuya Hasegawa. Spectroscopic and theoretical

- investigation of the electronic states of layered perovskite oxyfluoride $\text{Sr}_2\text{RuO}_3\text{F}_2$ thin films. *Phys. Rev. B*, 97(23):2–8, 2018.
- [36] Shishin Mo, Yuji Kurauchi, Tsukasa Katayama, Yasushi Hirose, and Tetsuya Hasegawa. Theoretical Investigation of the Role of the Nitride Ion in the Magnetism of Oxynitride MnTaO_2N . *J. Phys. Chem. C*, 123(41):25379–25384, 2019.
- [37] Bramhachari Khamari and B R K Nanda. Shifting of Fermi level and realization of topological insulating phase in the oxyfluoride BaBiO_2F . *Mater. Res. Express*, 6:066309, mar 2019.
- [38] Clarina de la Cruz, Q Huang, J W Lynn, Jiying Li, W Ratcliff II, J L Zarestky, H A Mook, G F Chen, J L Luo, N L Wang, and Pengcheng Dai. Magnetic order close to superconductivity in the iron-based layered $\text{LaO}_{1-x}\text{F}_x\text{FeAs}$ systems. *Nature*, 453(7197):899–902, 2008.
- [39] Richard M Martin. *Electronic Structure - Basic Theory and Practical Methods*. Cambridge University Press, New York, NY, 2nd edition, apr 2020.
- [40] R. O. Jones and O. Gunnarsson. The density functional formalism, its applications and prospects. *Rev. Mod. Phys.*, 61(3):689–746, jul 1989.
- [41] David J Singh and Lars Nordström. *Planewaves, Pseudopotentials, and the LAPW Method*. Springer, 2nd edition, 2006.
- [42] David Sholl and Janice A Steckel. *Density Functional Theory: A Practical Introduction*. John Wiley & Sons, Inc., 2011.
- [43] G Kresse and J Furthmüller. Efficient Iterative Schemes for Ab Initio Total-Energy Calculations Using a Plane-Wave Basis Set. *Phys. Rev. B*, 54(16):11169–11186, oct 1996.

- [44] G Kresse and J Furthmüller. Efficiency of ab-initio total energy calculations for metals and semiconductors using a plane-wave basis set. *Comput. Mater. Sci.*, 6(1):15–50, jul 1996.
- [45] M. Born and R. Oppenheimer. Zur Quantentheorie der Molekeln. *Ann. Phys.*, 389(20):457–484, 1927.
- [46] L. H. Thomas. The calculation of atomic fields. *Math. Proc. Cambridge Philos. Soc.*, 23(5):542–548, jan 1927.
- [47] E. Fermi. Atti Accad. Naz. Lincei, Cl. *Sci. Fis. Mat. Nat. Rend.*, 6:602, 1927.
- [48] P. A. M. Dirac. Note on Exchange Phenomena in the Thomas Atom. *Math. Proc. Cambridge Philos. Soc.*, 26(3):376–385, jul 1930.
- [49] P. Hohenberg and W. Kohn. Inhomogeneous Electron Gas. *Phys. Rev.*, 136(3B):B864–B871, nov 1964.
- [50] W. Kohn and L. J. Sham. Self-Consistent Equations Including Exchange and Correlation Effects. *Phys. Rev.*, 140(4A):A1133–A1138, nov 1965.
- [51] John P. Perdew and Karla Schmidt. Jacob’s ladder of density functional approximations for the exchange-correlation energy. In *AIP Conf. Proc.*, volume 577, pages 1–20. AIP, 2001.
- [52] John P. Perdew, Adrienn Ruzsinszky, Jianmin Tao, Viktor N. Staroverov, Gustavo E. Scuseria, and Gábor I. Csonka. Prescription for the design and selection of density functional approximations: More constraint satisfaction with fewer fits. *J. Chem. Phys.*, 123(6):062201, aug 2005.
- [53] Jianwei Sun, Richard C. Remsing, Yubo Zhang, Zhaoru Sun, Adrienn Ruzsinszky, Haowei Peng, Zenghui Yang, Arpita Paul, Umesh Waghmare, Xifan Wu, Michael L. Klein, and

- John P. Perdew. Accurate first-principles structures and energies of diversely bonded systems from an efficient density functional. *Nat. Chem.*, 8(9):831–836, sep 2016.
- [54] J. C. Slater. A simplification of the Hartree-Fock method. *Phys. Rev.*, 81(3):385–390, 1951.
- [55] D M Ceperley and B J Alder. Ground State of the Electron Gas by a Stochastic Method. *Phys. Rev. Lett.*, 45(7):566–569, 1980.
- [56] A. van de Walle and G. Ceder. Correcting overbinding in local-density-approximation calculations. *Phys. Rev. B*, 59(23):14992–15001, 1999.
- [57] John P. Perdew and Wang Yue. Accurate and simple density functional for the electronic exchange energy: Generalized gradient approximation. *Phys. Rev. B*, 33(12):8800–8802, 1986.
- [58] John P. Perdew and Yue Wang. Accurate and simple analytic representation of the electron-gas correlation energy. *Phys. Rev. B*, 45(23):13244–13249, jun 1992.
- [59] John P. Perdew, Matthias Ernzerhof, and Kieron Burke. Rationale for mixing exact exchange with density functional approximations. *J. Chem. Phys.*, 105(22):9982–9985, 1996.
- [60] John P. Perdew and Kieron Burke. Comparison shopping for a gradient-corrected density functional. *Int. J. Quantum Chem.*, 57(3):309–319, 1996.
- [61] Kurt Lejaeghere, Gustav Bihlmayer, T. Bjorkman, Peter Blaha, S. Blugel, Volker Blum, Damien Caliste, Ivano E. Castelli, Stewart J. Clark, Andrea Dal Corso, S. de Gironcoli, Thierry Deutsch, John Kay Dewhurst, Igor Di Marco, Claudia Draxl, M. Du ak, Olle Eriksson, José A. Flores-Livas, Kevin F. Garrity, Luigi Genovese, Paolo Giannozzi, Matteo Giantomassi, Stefan Goedecker, Xavier Gonze, O. Granas, E. K. U. Gross, Andris Gulans, François Gygi, D. R. Hamann, Phil J. Hasnip, N. A. W. Holzwarth, D. Iu an, Dominik B. Jochym, François

- Jollet, Daniel Jones, Georg Kresse, Klaus Koepernik, E. Kucukbenli, Yaroslav O. Kvashnin, I. L. M. Locht, Sven Lubeck, Martijn Marsman, Nicola Marzari, Ulrike Nitzsche, L. Nordstrom, Taisuke Ozaki, Lorenzo Paulatto, Chris J. Pickard, Ward Poelmans, M. I. J. Probert, Keith Refson, Manuel Richter, G.-M. Rignanese, Santanu Saha, Matthias Scheffler, Martin Schlipf, Karlheinz Schwarz, Sangeeta Sharma, Francesca Tavazza, P. Thunstrom, Alexandre Tkatchenko, Marc Torrent, David Vanderbilt, M. J. van Setten, Veronique Van Speybroeck, John M. Wills, Jonathan R. Yates, G.-X. Zhang, and Stefaan Cottenier. Reproducibility in density functional theory calculations of solids. *Science*, 351(6280):aad3000–aad3000, mar 2016.
- [62] John P Perdew, Adrienn Ruzsinszky, Gábor I Csonka, Oleg A Vydrov, Gustavo E Scuseria, Lucian A Constantin, Xiaolan Zhou, and Kieron Burke. Restoring the Density-Gradient Expansion for Exchange in Solids and Surfaces. *Phys. Rev. Lett.*, 100(13):136406, apr 2008.
- [63] B Silvi and A Savin. Classification of Chemical-Bonds Based on Topological Analysis of Electron Localization Functions, 1994.
- [64] Viktor N Staroverov, Gustavo E Scuseria, Jianmin Tao, and John P Perdew. Tests of a ladder of density functionals for bulk solids and surfaces. *Phys. Rev. B*, 69(7):75102, feb 2004.
- [65] Jianwei Sun, Adrienn Ruzsinszky, and John P. Perdew. Strongly Constrained and Appropriately Normed Semilocal Density Functional. *Phys. Rev. Lett.*, 115(3):036402, jul 2015.
- [66] Philipp Haas, Fabien Tran, and Peter Blaha. Calculation of the lattice constant of solids with semilocal functionals. *Phys. Rev. B*, 79(8):085104, feb 2009.

- [67] Jianwei Sun, Bing Xiao, Yuan Fang, Robin Haunschuld, Pan Hao, Adrienn Ruzsinszky, Gábor I Csonka, Gustavo E Scuseria, and John P Perdew. Density Functionals that Recognize Covalent, Metallic, and Weak Bonds. *Phys. Rev. Lett.*, 111(10):106401, sep 2013.
- [68] Bharat Medasani, Maciej Haranczyk, Andrew Canning, and Mark Asta. Vacancy formation energies in metals: A comparison of MetaGGA with LDA and GGA exchange-correlation functionals. *Comput. Mater. Sci.*, 101:96–107, 2015.
- [69] Yubo Zhang, Jianwei Sun, John P. Perdew, and Xifan Wu. Comparative first-principles studies of prototypical ferroelectric materials by LDA, GGA, and SCAN meta-GGA. *Phys. Rev. B*, 96(3):1–16, 2017.
- [70] Julia H. Yang, Daniil A. Kitchaev, and Gerbrand Ceder. Rationalizing accurate structure prediction in the meta-GGA SCAN functional. *Phys. Rev. B*, 100(3):1–10, 2019.
- [71] Andrew S. Rosen, Justin M. Notestein, and Randall Q. Snurr. Comparing GGA, GGA+U, and meta-GGA functionals for redox-dependent binding at open metal sites in metal-organic frameworks. *J. Chem. Phys.*, 152(22), 2020.
- [72] Jochen Heyd, Gustavo E. Scuseria, and Matthias Ernzerhof. Hybrid functionals based on a screened Coulomb potential. *J. Chem. Phys.*, 118(18):8207–8215, 2003.
- [73] Aliaksandr V. Krukau, Oleg A. Vydrov, Artur F. Izmaylov, and Gustavo E. Scuseria. Influence of the exchange screening parameter on the performance of screened hybrid functionals. *J. Chem. Phys.*, 125(22), 2006.
- [74] Miguel A L Marques, Julien Vidal, Micael J T Oliveira, Lucia Reining, and Silvana Botti. Density-based mixing parameter for hybrid functionals. *Phys. Rev. B*, 83(3):035119, jan 2011.

- [75] P. García-Fernández, S. Ghosh, Niall J. English, and J. A. Aramburu. Benchmark study for the application of density functional theory to the prediction of octahedral tilting in perovskites. *Phys. Rev. B*, 86(14):144107, oct 2012.
- [76] Gaoyang Gou, Min Zhao, Jing Shi, Jaye K. Harada, and James M. Rondinelli. Anion Ordered and Ferroelectric Ruddlesden–Popper Oxynitride $\text{Ca}_3\text{Nb}_2\text{N}_2\text{O}_5$ for Visible-Light-Active Photocatalysis. *Chem. Mater.*, 32(7):2815–2823, 2020.
- [77] Felix Bloch. Über die Quantenmechanik der Elektronen in Kristallgittern. *Zeitschrift für Phys.*, 52(7-8):555–600, 1929.
- [78] A. Baldereschi. Mean-Value Point in the Brillouin Zone. *Phys. Rev. B*, 7(12):5212–5215, jun 1973.
- [79] Hendrik J. Monkhorst and James D. Pack. Special Points for Brillouin-Zone Integrations. *Phys. Rev. B*, 13(12):5188–5192, jun 1976.
- [80] Juana Moreno and José M. Soler. Optimal meshes for integrals in real- and reciprocal-space unit cells. *Phys. Rev. B*, 45(24):13891–13898, 1992.
- [81] Pandu Wisesa, Kyle A. McGill, and Tim Mueller. Efficient generation of generalized Monkhorst-Pack grids through the use of informatics. *Phys. Rev. B*, 93(15):1–10, 2016.
- [82] Wiley S. Morgan, John E. Christensen, Parker K. Hamilton, Jeremy J. Jorgensen, Branton J. Campbell, Gus L.W. Hart, and Rodney W. Forcade. Generalized regular k-point grid generation on the fly. *Comput. Mater. Sci.*, 173(December 2019):109340, 2020.

- [83] Yunzhe Wang, Pandu Wisesa, Adarsh Balasubramanian, Shyam Dwaraknath, and Tim Mueller. Rapid generation of optimal generalized Monkhorst-Pack grids. *Comput. Mater. Sci.*, 187(August 2020):110100, 2021.
- [84] D. R. Hamann, M. Schlüter, and C. Chiang. Norm-Conserving Pseudopotentials. *Phys. Rev. Lett.*, 43(20):1494–1497, 1979.
- [85] Peter E. Blöchl. Generalized separable potentials for electronic-structure calculations. *Phys. Rev. B*, 41(8):5414–5416, 1990.
- [86] David Vanderbilt. Soft self-consistent pseudopotentials in a generalized eigenvalue formalism. *Phys. Rev. B*, 41(11):7892–7895, apr 1990.
- [87] P. E. Blöchl. Projector Augmented-Wave Method. *Phys. Rev. B*, 50(24):17953–17979, dec 1994.
- [88] Steven G. Louie, Sverre Froyen, and Marvin L. Cohen. Nonlinear ionic pseudopotentials in spin-density-functional calculations. *Phys. Rev. B*, 26(4):1738–1742, aug 1982.
- [89] Jürgen Hafner. Materials simulations using VASP—a quantum perspective to materials science. *Comput. Phys. Commun.*, 177(1-2):6–13, jul 2007.
- [90] P. Blaha, K. Schwarz, P. Sorantin, and S. B. Trickey. Full-potential, linearized augmented plane wave programs for crystalline systems. *Comput. Phys. Commun.*, 59(2):399–415, 1990.
- [91] G Kresse and D Joubert. From Ultrasoft Pseudopotentials to the Projector Augmented-Wave Method. *Phys. Rev. B*, 59(3):1758–1775, jan 1999.

- [92] Yoshihiro Tsujimoto, Yoshitaka Matsushita, Naoaki Hayashi, Kazunari Yamaura, and Tetsuo Uchikoshi. Anion Order-to-Disorder Transition in Layered Iron Oxyfluoride $\text{Sr}_2\text{FeO}_3\text{F}$ Single Crystals. *Cryst. Growth Des.*, 14(9):4278–4284, sep 2014.
- [93] Frank J Brink, Ray L Withers, and John G Thompson. An Electron Diffraction and Crystal Chemical Investigation of Oxygen/Fluorine Ordering in Rutile-Type Iron Oxyfluoride, FeOF . *J. Solid State Chem.*, 155(2):359–365, 2000.
- [94] Vincent L. Chevrier, Geoffroy Hautier, Shyue Ping Ong, Robert E. Doe, and Gerbrand Ceder. First-Principles Study of Iron Oxyfluorides and Lithiation of FeOF . *Phys. Rev. B*, 87:094118, mar 2013.
- [95] R G Pearson. *Chemical Hardness*. Wiley-VCH, Weinheim, Germany, 1997.
- [96] Holger Wolff and Richard Dronskowski. First-principles and molecular-dynamics study of structure and bonding in perovskite-type oxynitrides ABO_2N ($A = \text{Ca}, \text{Sr}, \text{Ba}$; $B = \text{Ta}, \text{Nb}$). *J. Comput. Chem.*, 29(13):2260–2267, oct 2008.
- [97] C M Fang, G A de Wijs, E Orhan, G de With, R A de Groot, H T Hintzen, and R Marchand. Local structure and electronic properties of BaTaO_2N with perovskite-type structure. *J. Phys. Chem. Solids*, 64(2):281–286, 2003.
- [98] Karl O Christe and R D Wilson. Cis- and trans- iodine (VII) oxytetrafluoride hypofluorite, OIF_4OF . *Inorg. Nucl. Chem. Lett.*, 15(9):375–376, 1979.
- [99] E I Voit, A V Voit, A A Mashkovskii, N M Laptash, and V Ya. Kavun. Dynamic disorder in ammonium oxofluorotungstates $(\text{NH}_4)_2\text{WO}_2\text{F}_4$ and $(\text{NH}_4)_3\text{WO}_3\text{F}_3$. *J. Struct. Chem.*, 47(4):642–650, 2006.

- [100] G Pausewang and W Rüdorff. Über Alkali-oxofluorometallate der Übergangsmetalle. $\text{Al}_3\text{MeO}_x\text{F}_{6-x}$ -Verbindungen mit $x = 1, 2, 3$. *Z. Anorg. Allg. Chem.*, 364(1-2):69–87, jan 1969.
- [101] Cody R Morelock, Benjamin K Greve, Mehmet Cetinkol, Karena W Chapman, Peter J Chupas, and Angus P Wilkinson. Role of Anion Site Disorder in the Near Zero Thermal Expansion of Tantalum Oxyfluoride. *Chem. Mater.*, 25(9):1900–1904, may 2013.
- [102] Margaret E Welk, Alexander J Norquist, Frederick P Arnold, Charlotte L Stern, and Kenneth R Poeppelmeier. Out-of-Center Distortions in d0 Transition Metal Oxide Fluoride Anions. *Inorg. Chem.*, 41(20):5119–5125, oct 2002.
- [103] Minghui Yang, Judith Orò-Solè, Jennifer A Rodgers, Ana Belén Belèn Jorge, Amparo Fuertes, and J Paul Attfield. Anion order in perovskite oxynitrides. *Nat. Chem.*, 3(1):47–52, 2011.
- [104] S. C. Abrahams, P. Marsh, and J. Ravez. Ferroelectric structure and related properties of $\text{Pb}_5\text{W}_3\text{O}_9\text{F}_{10}$. *J. Chem. Phys.*, 87(10):6012–6020, nov 1987.
- [105] David W Aldous, Richard J Goff, J Paul Attfield, and Philip Lightfoot. Novel vanadium (IV) oxyfluorides with 'spin-ladder'-like structures, and their relationship to $(\text{VO})_2\text{P}_2\text{O}_7$. *Inorg. Chem.*, 46(4):1277–1282, feb 2007.
- [106] William B. Jensen. Crystal Coordination Formulas: A Flexible Notation for the Interpretation of Solid-State Structures. In J. Hafner, F. Hulliger, W. B. Jense, J. A. Majewski, K. Mathis, P. Villars, and P. Vogl, editors, *Cohesion and Structure*, volume 2, chapter 2, pages 105–146. Elsevier Science Publishers, Amsterdam, jan 1989.

- [107] Heather K Izumi, Janet E Kirsch, Charlotte L Stern, and Kenneth R Poeppelmeier. Examining the Out-of-Center Distortion in the $[\text{NbOF}_5]^{2-}$ Anion. *Inorg. Chem.*, 44(4):884–895, feb 2005.
- [108] Rachelle Ann F. Pinlac, Charlotte L. Stern, and Kenneth R. Poeppelmeier. New Layered Oxide-Fluoride Perovskites: KNaNbOF_5 and KNaMO_2F_4 ($M = \text{Mo}^{6+}, \text{W}^{6+}$). *Crystals*, 1(4):3–14, mar 2011.
- [109] Jamal Dabachi, Monique Body, Cyrille Galven, Florent Boucher, and Christophe Legein. Preparation-Dependent Composition and O/F Ordering in NbO_2F and TaO_2F . *Inorg. Chem.*, 56(9):5219–5232, may 2017.
- [110] L K Frevel and H W Rinn. The crystal structure of NbO_2F and TaO_2F . *Acta Crystallogr.*, 9(8):626–627, aug 1956.
- [111] F.J. Brink, R.L. Withers, K Friese, G Madariaga, and L. Norén. An Electron Diffraction and XRPD Study of Superlattice Ordering in the Elpasolite-Related Oxyfluoride $\text{K}_3\text{MoO}_3\text{F}_3$. *J. Solid State Chem.*, 163(1):267–274, jan 2002.
- [112] Michael R Marvel, Rachelle Ann F Pinlac, Julien Lesage, Charlotte L Stern, and Kenneth R Poeppelmeier. Chemical Hardness and the Adaptive Coordination Behavior of the d_0 Transition Metal Oxide Fluoride Anions. *Z. Anorg. Allg. Chem.*, 635(6-7):869–877, may 2009.
- [113] P Shiv Halasyamani. *Noncentrosymmetric Inorganic Oxide Materials: Synthetic Strategies and Characterisation Techniques*. John Wiley & Sons, Inc., 2010.
- [114] A M Glazer. The classification of tilted octahedra in perovskites. *Acta Crystallogr. Sect. B: Struct. Crystallogr. Cryst. Chem.*, 28(11):3384–3392, nov 1972.

- [115] Kengo Oka and Katsuyoshi Oh-ishi. Observation of Anion Order in $\text{Pb}_2\text{Ti}_4\text{O}_9\text{F}_2$. *Inorg. Chem.*, 54(21):10239–10242, nov 2015.
- [116] Amnon Aharony, R J Birgeneau, A Coniglio, M A Kastner, and H E Stanley. Magnetic phase diagram and magnetic pairing in doped La_2CuO_4 . *Phys. Rev. Lett.*, 60(13):1330–1333, mar 1988.
- [117] Ayako Kubo, Giacomo Giorgi, and Koichi Yamashita. Anion Ordering in CaTaO_2N : Structural Impact on the Photocatalytic Activity. Insights from First-Principles. *Chem. Mater.*, 29(2):539–545, jan 2017.
- [118] Ronghuan Zhang, Mark S Senn, and Michael A Hayward. Directed Lifting of Inversion Symmetry in Ruddlesden-Popper Oxide-Fluorides: Toward Ferroelectric and Multiferroic Behavior. *Chem. Mater.*, 28(22):8399–8406, 2016.
- [119] F Di Quarto, C Sunseri, S Piazza, and M C Romano. Semiempirical Correlation between Optical Band Gap Values of Oxides and the Difference of Electronegativity of the Elements. Its Importance for a Quantitative Use of Photocurrent Spectroscopy in Corrosion Studies. *J. Phys. Chem. B*, 101(14):2519–2525, apr 1997.
- [120] A R Denton and N W Ashcroft. Vegard’s law. *Phys. Rev. A*, 43(6):3161–3164, 1991.
- [121] Yong-Nian Xu and W. Y. Ching. Electronic structure and optical properties of α and β phases of silicon nitride, silicon oxynitride, and with comparison to silicon dioxide. *Phys. Rev. B*, 51(24):17379–17389, jun 1995.

- [122] J. Etourneau, J. Portier, and F. M enil. The Role of the Inductive Effect in Solid State Chemistry: How the Chemist Can Use It to Modify Both the Structural and the Physical Properties of the Materials. *J. Alloys Compd.*, 188(0):1–7, 1992.
- [123] J. Zaanen, G. A. Sawatzky, and J. W. Allen. Band gaps and electronic structure of transition-metal compounds. *Phys. Rev. Lett.*, 55(4):418–421, jul 1985.
- [124] Daniel I. Khomskii. *Transition metal compounds*. Cambridge University Press, 2014.
- [125] George Sawatzky and Robert Green. The Explicit Role of Anion States in High-Valence Metal Oxides. In Sawatzky G. Pavarini, E., Koch E., van den Brink J., editor, *Quantum Materials: Experiments and Theory Modeling and Simulation*, volume 6, chapter 1, pages 1–36. Forschungszentrum Julich GmbH, 2016.
- [126] M A Korotin, V I Anisimov, D I Khomskii, and G A Sawatzky. CrO₂: A Self-Doped Double Exchange Ferromagnet. *Phys. Rev. Lett.*, 80(19):4305–4308, may 1998.
- [127] M Sathiya, G Rousse, K Ramesha, C P Laisa, H Vezin, M T Sougrati, M-L. Doublet, D Foix, D Gonbeau, W Walker, A S Prakash, M Ben Hassine, L Dupont, and J-M. Tarascon. Reversible anionic redox chemistry in high-capacity layered-oxide electrodes. *Nat. Mater.*, 12:827, jul 2013.
- [128] Dong-Hwa Seo, Jinhyuk Lee, Alexander Urban, Rahul Malik, ShinYoung Kang, and Gerbrand Ceder. The structural and chemical origin of the oxygen redox activity in layered and cation-disordered Li-excess cathode materials. *Nat. Chem.*, 8:692, may 2016.
- [129] Kun Luo, Matthew R Roberts, Rong Hao, Niccol o Guerrini, David M Pickup, Yi-Sheng Liu, Kristina Edstr om, Jinghua Guo, Alan V Chadwick, Laurent C Duda, and Peter G

- Bruce. Charge-compensation in 3d-transition-metal-oxide intercalation cathodes through the generation of localized electron holes on oxygen. *Nat. Chem.*, 8(7):684–691, jul 2016.
- [130] U Staub, G I Meijer, F Fauth, R Allenspach, J G Bednorz, J Karpinski, S M Kazakov, L Paolasini, and F. D’Acapito. Direct Observation of Charge Order in an Epitaxial NdNiO₃. *Phys. Rev. Lett.*, 88(12):126402, mar 2002.
- [131] T. Mizokawa, H. Namatame, A. Fujimori, K. Akeyama, H. Kondoh, H. Kuroda, and N. Kosugi. Origin of the band gap in the negative charge-transfer-energy compound NaCuO₂. *Phys. Rev. Lett.*, 67(12):1638–1641, sep 1991.
- [132] Valentina Bisogni, Sara Catalano, Robert J Green, Marta Gibert, Raoul Scherwitzl, Yaobo Huang, Vladimir N Strocov, Pavlo Zubko, Shadi Balandeh, Jean-marc Triscone, George Sawatzky, and Thorsten Schmitt. Ground-state oxygen holes and the metal–insulator transition in the negative charge-transfer rare-earth nickelates. *Nat. Commun.*, 7:13017, 2016.
- [133] Hidenori Hiramatsu, Hiroshi Yanagi, Toshio Kamiya, Kazushige Ueda, Masahiro Hirano, and Hideo Hosono. Crystal Structures, Optoelectronic Properties, and Electronic Structures of Layered Oxychalcogenides MCuOCh (M=Bi, La; Ch=S, Se, Te): Effects of Electronic Configurations of M³⁺ Ions. *Chem. Mater.*, 20(1):326–334, jan 2008.
- [134] Hidenori Hiramatsu, Kazushige Ueda, Hiromichi Ohta, Masahiro Hirano, Toshio Kamiya, and Hideo Hosono. Degenerate p-type conductivity in wide-gap LaCuOS_{1-x}Sex (x=0–1) epitaxial films. *Appl. Phys. Lett.*, 82(7):1048–1050, feb 2003.
- [135] Hideo Hosono. Recent progress in transparent oxide semiconductors: Materials and device application. *Thin Solid Films*, 515(15):6000–6014, may 2007.

- [136] K Ueda, S Inoue, H Hosono, N Sarukura, and M Hirano. Room-temperature excitons in wide-gap layered-oxysulfide semiconductor: LaCuOS. *Appl. Phys. Lett.*, 78(16):2333–2335, apr 2001.
- [137] Shin-Ichiro Inoue, Kazushige Ueda, Hideo Hosono, and Noriaki Hamada. Electronic structure of the transparent p-type semiconductor (LaO)CuS. *Phys. Rev. B*, 64(24):245211, dec 2001.
- [138] A V Ushakov, S V Streltsov, and D I Khomskii. Crystal field splitting in correlated systems with negative charge-transfer gap. *J. Phys.: Condens. Matter*, 23(44):445601, 2011.
- [139] Yoshihiro Tsujimoto, Clastin I I Sathish, Kun-pyo Hong, Kengo Oka, Masaki Azuma, Yanfeng Guo, Yoshitaka Matsushita, Kazunari Yamaura, and Eiji Takayama-Muromachi. Crystal Structural, Magnetic, and Transport Properties of Layered Cobalt Oxyfluorides, Sr₂CoO_{3+x}F_{1-x} (0 ≤ x ≤ 0.15). *Inorg. Chem.*, 51(8):4802–4809, apr 2012.
- [140] F Menil, N Kinomura, L Fournes, J Portieb, and P. Hagenmuller. Investigation of the K₂NiF₄-type layer oxide fluorides Sr₂FeO_{3+x}F_{1-x} (0 ≤ x ≤ 0.20). *Phys. Status Solidi A*, 64(1):261–274, mar 1981.
- [141] M. Goga, R. Seshadri, V. Ksenofontov, P. Gülich, and W. Tremel. Ln₂Ti₂S₂O₅ (Ln = Nd, Pr, Sm): a novel series of defective Ruddlesden–Popper phases. *Chem. Commun.*, (11):979–980, 1999.
- [142] Akio Ishikawa, Tsuyoshi Takata, Junko N Kondo, Michikazu Hara, Hisayoshi Kobayashi, and Kazunari Domen. Oxysulfide Sm₂Ti₂S₂O₅ as a Stable Photocatalyst for Water Oxidation and Reduction under Visible Light Irradiation (λ = 650 nm). *J. Am. Chem. Soc.*, 124(45):13547–13553, nov 2002.

- [143] Yu Su, Yoshihiro Tsujimoto, Yoshitaka Matsushita, Yahua Yuan, Jianfeng He, and Kazunari Yamaura. High-Pressure Synthesis, Crystal Structure, and Magnetic Properties of Sr₂MnO₃F: A New Member of Layered Perovskite Oxyfluorides. *Inorg. Chem.*, 55(5):2627–2633, mar 2016.
- [144] Yoshihiro Tsujimoto, Jun J Li, Kazunari Yamaura, Yoshitaka Matsushita, Yoshio Katsuya, Masahiko Tanaka, Yuichi Shirako, Masaki Akaogi, and Eiji Takayama-Muromachi. New Layered Cobalt Oxyfluoride, Sr₂CoO₃F. *Chem. Commun.*, 47(11):3263–3265, 2011.
- [145] Yoshihiro Tsujimoto, Kazunari Yamaura, and Tetsuo Uchikoshi. Extended Ni(III) Oxyhalide Perovskite Derivatives: Sr₂NiO₃X (X = F, Cl). *Inorg. Chem.*, 52(17):10211–10216, 2013.
- [146] Yan Yongkun Wang, Kaibin Tang, Baichuan Zhu, Dake Wang, Qiaoyan Hao, and Yan Yongkun Wang. Synthesis and Structure of a New Layered Oxyfluoride Sr₂ScO₃F with Photocatalytic Property. *Mater. Res. Bull.*, 65:42–46, may 2015.
- [147] Francis Galasso and Wilda Darby. Preparation and Properties of Sr₂FeO₃F. *J. Phys. Chem.*, 67(7):1451–1453, 1963.
- [148] Rajasekarakumar Vadapoo, Muhtar Ahart, Maddury Somayazulu, Nicholas Holtgrewe, Yue Meng, Zuzana Konopkova, Russell J. Hemley, and R. E. Cohen. Synthesis of a polar ordered oxynitride perovskite. *Phys. Rev. B*, 95(21):214120, 2017.
- [149] Albrecht Rabenau. The Role of Hydrothermal Synthesis in Preparative Chemistry. *Angew. Chemie Int. Ed. English*, 24(12):1026–1040, 1985.

- [150] Richard L. Needs, Sandra E. Dann, Mark T. Weller, Julian C. Cherryman, and Robin K. Harris. The structure and oxide/fluoride ordering of the ferroelectrics $\text{Bi}_2\text{TiO}_4\text{F}_2$ and $\text{Bi}_2\text{NbO}_5\text{F}$. *J. Mater. Chem.*, 15(24):2399, 2005.
- [151] Michael R. Marvel, Julien Lesage, Jaewook Baek, P. Shiv Halasyamani, Charlotte L. Stern, and Kenneth R. Poeppelmeier. Cation-Anion Interactions and Polar Structures in the Solid State. *J. Am. Chem. Soc.*, 129(45):13963–13969, nov 2007.
- [152] William C. Sheets, Evan S. Stampler, Houria Kabbour, Mariana I. Bertoni, Laurent Cario, Thomas O. Mason, Tobin J. Marks, and Kenneth R. Poeppelmeier. Facile synthesis of BiCuOS by hydrothermal methods. *Inorg. Chem.*, 46(25):10741–10748, 2007.
- [153] Adele L. Pacquette, Hidehisa Hagiwara, Tatsumi Ishihara, and Andrew A. Gewirth. Fabrication of an oxysulfide of bismuth $\text{Bi}_2\text{O}_2\text{S}$ and its photocatalytic activity in a $\text{Bi}_2\text{O}_2\text{S}/\text{In}_2\text{O}_3$ composite. *J. Photochem. Photobiol. A Chem.*, 277:27–36, mar 2014.
- [154] Ian Saratovsky, Michelle A. Lockett, Nicholas H. Rees, and Michael A. Hayward. Preparation of $\text{Sr}_7\text{Mn}_4\text{O}_{13}\text{F}_2$ by the Topotactic Reduction and Subsequent Fluorination of $\text{Sr}_7\text{Mn}_4\text{O}_{15}$. *Inorg. Chem.*, 47(12):5212–5217, jun 2008.
- [155] Y W Cho and J A Charles. Synthesis of nitrogen ceramic powders by carbothermal reduction and nitridation Part 2 Silicon aluminium oxynitride (sialon). *Mater. Sci. Technol.*, 7(5):399–406, may 1991.
- [156] Mary McHughes, Roger D Willett, H B Davis, and G L Gard. Chromium oxide trifluoride (CrOF_3). Preparation and crystal structure. *Inorg. Chem.*, 25(4):426–427, feb 1986.

- [157] C. Greaves, J. L. Kissick, M. G. Francesconi, L. D. Aikens, and L. J. Gillie. Synthetic strategies for new inorganic oxide fluorides and oxide sulfates. *J. Mater. Chem.*, 9:111–116, 1999.
- [158] P.R. Slater, J.P. Hodges, M.G. Francesconi, P.P. Edwards, C. Greaves, I. Gameson, and M. Slaski. An improved route to the synthesis of superconducting copper oxyfluorides $\text{Sr}_{2x}\text{A}_x\text{CuO}_{2+x}$ (A=Ca, Ba) using transition metal difluorides as fluorinating reagents. *Phys. C Supercond.*, 253(1-2):16–22, oct 1995.
- [159] Kun Luo, Roger D. Johnson, Thao T. Tran, P. Shiv Halasyamani, Paolo G. Radaelli, and Michael A. Hayward. $\text{Ba}_2\text{YFeO}_{5.5}$: A ferromagnetic pyroelectric phase prepared by topochemical oxidation. *Chem. Mater.*, 25(9):1800–1808, 2013.
- [160] P. R. Slater. Poly(vinylidene fluoride) as a reagent for the synthesis of K_2NiF_4 -related inorganic oxide fluorides. *J. Fluor. Chem.*, 117(1):43–45, 2002.
- [161] Eun Ju Moon, Yujun Xie, Eric D. Laird, David J. Keavney, Christopher Y. Li, and Steven J. May. Fluorination of epitaxial oxides: Synthesis of perovskite oxyfluoride thin films. *J. Am. Chem. Soc.*, 136(6):2224–2227, 2014.
- [162] Yoji Kobayashi, Mingliang Tian, Miharu Eguchi, and Thomas E Mallouk. Ion-Exchangeable, Electronically Conducting Layered Perovskite Oxyfluorides. *J. Am. Chem. Soc.*, 131(28):9849–9855, jul 2009.
- [163] Yasushi Hirose and Tetsuya Hasegawa. Exploring Metastable Oxynitrides by Thin Film Growth Approach. *Bull. Chem. Soc. Jpn.*, page bcsj.20210033, mar 2021.

- [164] Young Il Kim, Weidong Si, Patrick M. Woodward, Eli Sutter, Sangmoon Park, and Thomas Vogt. Epitaxial thin-film deposition and dielectric properties of the perovskite oxynitride BaTaO₂N. *Chem. Mater.*, 19(3):618–623, 2007.
- [165] Daichi Oka, Yasushi Hirose, Tomoteru Fukumura, and Tetsuya Hasegawa. Heteroepitaxial Growth of Perovskite CaTaO₂N Thin Films by Nitrogen Plasma-Assisted Pulsed Laser Deposition. *Cryst. Growth Des.*, 14(1):87–90, 2014.
- [166] Daichi Oka, Yasushi Hirose, Fumihiko Matsui, Hideyuki Kamisaka, Tamio Oguchi, Naoyuki Maejima, Hiroaki Nishikawa, Takayuki Muro, Kouichi Hayashi, and Tetsuya Hasegawa. Strain Engineering for Anion Arrangement in Perovskite Oxynitrides. *ACS Nano*, 11(4):3860–3866, 2017.
- [167] Yu Lu, Claire Le Paven, Hung V. Nguyen, Ratiba Benzerga, Laurent Le Gendre, Stéphane Rioual, Franck Tessier, François Cheviré, Ala Sharaiha, Christophe Delaveaud, and Xavier Castel. Reactive sputtering deposition of perovskite oxide and oxynitride lanthanum titanium films: Structural and dielectric characterization. *Cryst. Growth Des.*, 13(11):4852–4858, 2013.
- [168] F. Marlec, C. Le Paven, L. Le Gendre, R. Benzerga, F. Cheviré, F. Tessier, F. Gam, and A. Sharaiha. Deposition and dielectric study as function of thickness of perovskite oxynitride SrTaO₂N thin films elaborated by reactive sputtering. *Surf. Coatings Technol.*, 324:607–613, 2016.
- [169] Takuto Wakasugi, Yasushi Hirose, Shoichiro Nakao, Yuki Sugisawa, Yuki Sugisawa, Daiichiro Sekiba, Daiichiro Sekiba, and Tetsuya Hasegawa. High-Quality Heteroepitaxial Growth of Thin Films of the Perovskite Oxynitride CaTaO₂N: Importance of Interfacial Symmetry Matching between Films and Substrates. *ACS Omega*, 5(22):13396–13402, 2020.

- [170] Prasert Sinsersuksakul, Katy Hartman, Sang Bok Kim, Jaeyeong Heo, Leizhi Sun, Helen Hejin Park, Rupak Chakraborty, Tonio Buonassisi, and Roy G. Gordon. Enhancing the efficiency of SnS solar cells via band-offset engineering with a zinc oxysulfide buffer layer. *Appl. Phys. Lett.*, 102(5), 2013.
- [171] Jiayi Wang, Yongjin Shin, Elke Arenholz, Benjamin M. Lefler, James M. Rondinelli, and Steven J. May. Effect of fluoropolymer composition on topochemical synthesis of SrMnO₃- δ F γ oxyfluoride films. *Phys. Rev. Mater.*, 2(7):073407, jul 2018.
- [172] T. Katayama, A. Chikamatsu, Y. Hirose, R. Takagi, H. Kamisaka, T. Fukumura, and T. Hasegawa. Topotactic fluorination of strontium iron oxide thin films using polyvinylidene fluoride. *J. Mater. Chem. C*, 2(27):5350–5356, 2014.
- [173] Tsukasa Katayama, Akira Chikamatsu, Yasushi Hirose, Tomoteru Fukumura, and Tetsuya Hasegawa. Topotactic reductive fluorination of strontium cobalt oxide epitaxial thin films. *J. Sol-Gel Sci. Technol.*, 73(3):527–530, 2015.
- [174] Tsukasa Katayama, Akira Chikamatsu, Hideyuki Kamisaka, Hiroshi Kumigashira, and Tetsuya Hasegawa. Experimental and theoretical investigation of electronic structure of SrFeO₃-xFx epitaxial thin films prepared via topotactic reaction. *Appl. Phys. Express*, 9(2):2–6, 2016.
- [175] Tomoya Onozuka, Akira Chikamatsu, Tsukasa Katayama, Yasushi Hirose, Isao Harayama, Daiichiro Sekiba, Eiji Ikenaga, Makoto Minohara, Hiroshi Kumigashira, and Tetsuya Hasegawa. Reversible Changes in Resistance of Perovskite Nickelate NdNiO₃ Thin Films Induced by Fluorine Substitution. *ACS Appl. Mater. Interfaces*, 9(12):10882–10887, 2017.

- [176] Akash Nair, Stephan Wollstadt, Ralf Witte, Supratik Dasgupta, Philipp Kehne, Lambert Alff, Philipp Komissinskiy, and Oliver Clemens. Synthesis and characterisation of fluorinated epitaxial films of BaFeO₂F: Tailoring magnetic anisotropy: Via a lowering of tetragonal distortion. *RSC Adv.*, 9(64):37136–37143, 2019.
- [177] Junjie Li, Haoliang Huang, Peiqi Qiu, Zhaolong Liao, Xierong Zeng, Yalin Lu, and Chuanwei Huang. Topotactic fluorination induced stable structure and tunable electronic transport in perovskite barium ferrite thin films. *Ceram. Int.*, 46(7):8761–8765, 2020.
- [178] K. Kawahara, A. Chikamatsu, T. Katayama, T. Onozuka, D. Ogawa, K. Morikawa, E. Ike-naga, Y. Hirose, I. Harayama, D. Sekiba, T. Fukumura, and T. Hasegawa. Topotactic fluorination of perovskite strontium ruthenate thin films using polyvinylidene fluoride. *CrystEngComm*, 19(2):313–317, 2017.
- [179] Ray L. Withers, F. J. Brink, Yun Liu, and Lasse Norén. Cluster chemistry in the solid state: Structured diffuse scattering, oxide/fluoride ordering and polar behaviour in transition metal oxyfluorides. *Polyhedron*, 26(2):290–299, 2007.
- [180] N Diot, R Marchand, J Haines, J M Léger, P Macaudière, and S Hull. Crystal Structure Determination of the Oxynitride Sr₂TaO₃N. *J. Solid State Chem.*, 146(2):390–393, 1999.
- [181] Kamila M. Wiaderek, Olaf J. Borkiewicz, Elizabeth Castillo-Martínez, Rosa Robert, Nathalie Pereira, Glenn G. Amatucci, Clare P. Grey, Peter J. Chupas, and Karena W. Chapman. Comprehensive Insights into the Structural and Chemical Changes in Mixed-Anion FeOF Electrodes by Using Operando PDF and NMR Spectroscopy. *J. Am. Chem. Soc.*, 135(10):4070–4078, mar 2013.

- [182] Kristin A. Denault, Nathan C. George, Sara R. Paden, Stuart Brinkley, Alexander A. Mikhailovsky, Jörg Neufeind, Steven P. DenBaars, and Ram Seshadri. A green-yellow emitting oxyfluoride solid solution phosphor $\text{Sr}_{1-x}\text{Ba}_x(\text{AlO}_4)_x(\text{SiO}_5)_{1-x}:\text{Ce}^{3+}$ for thermally stable, high color rendition solid state white lighting. *J. Mater. Chem.*, 22(35):18204, 2012.
- [183] F J Brink, L Norén, and R L Withers. Synthesis, electron diffraction, XRD and DSC study of the new elpasolite-related oxyfluoride, $\text{Ti}_3\text{MoO}_3\text{F}_3$. *J. Solid State Chem.*, 174(1):44–51, 2003.
- [184] Frank J. Brink, Lasse Norén, Darren J. Goossens, Ray L. Withers, Yun Liu, and Chao-Nan Xu. A combined diffraction (XRD, electron and neutron) and electrical study of $\text{Na}_3\text{MoO}_3\text{F}_3$. *J. Solid State Chem.*, 174(2):450–458, sep 2003.
- [185] Y. Yamamoto, A.K.R. Ang, K. Kimura, T. Matsushita, Y. Hirose, D. Oka, and K. Hayashi. Anion arrangement analysis of oxynitride perovskite thin film with inverse photoelectron holography. *J. Electron Spectros. Relat. Phenomena*, 246(October 2020):147018, jan 2021.
- [186] L. F. Huang, M. J. Hutchison, R. J. Santucci, J. R. Scully, and J. M. Rondinelli. Improved Electrochemical Phase Diagrams from Theory and Experiment: The Ni-Water System and Its Complex Compounds. *J. Phys. Chem. C*, 121(18):9782–9789, 2017.
- [187] Stefano Curtarolo, Gus L W Hart, Marco Buongiorno Nardelli, Natalio Mingo, Stefano Sanvito, and Ohad Levy. The high-throughput highway to computational materials design. *Nat. Mater.*, 12:191, feb 2013.

- [188] Hongping Wu, Hongwei Yu, Zhihua Yang, Xueling Hou, Xin Su, Shilie Pan, Kenneth R Poepelmeier, and James M Rondinelli. Designing a Deep-Ultraviolet Nonlinear Optical Material with a Large Second Harmonic Generation Response. *J. Am. Chem. Soc.*, 135(11):4215–4218, mar 2013.
- [189] Gus L W Hart and Rodney W Forcade. Algorithm for Generating Derivative Structures. *Phys. Rev. B*, 77(22):224115, jun 2008.
- [190] Gus L. W. Hart and Rodney W. Forcade. Generating Derivative Structures from Multilattices: Algorithm and Application to HCP Alloys. *Phys. Rev. B*, 80(1):014120, jul 2009.
- [191] Gus L.W. Hart, Lance J Nelson, and Rodney W Forcade. Generating Derivative Structures at a Fixed Concentration. *Comput. Mater. Sci.*, 59:101–107, jun 2012.
- [192] Nenian Charles, Richard J. Saballos, and James M. Rondinelli. Structural Diversity from Anion Order in Heteroanionic Materials. *Chem. Mater.*, 30(10):3528–3537, may 2018.
- [193] A C W P James, D W Murphy, and S M Zahurak. Superconductivity at 27 K in fluorine-doped Nd₂CuO₄. *Nature*, 338:240–241, mar 1989.
- [194] Yuya Haraguchi, Chishiro Michioka, Hiroaki Ueda, and Kazuyoshi Yoshimura. Tetramer spin singlet instability in the fluorine-substituted pyrochlore superconducting system Cd₂Re₂O_{7-x}F_x. *J. Phys.: Condens. Matter*, 28(35):355602, sep 2016.
- [195] T Hanaguri, C Lupien, Y Kohsaka, D. H. Lee, M Azuma, M Takano, H Takagi, and J C Davis. A 'checkerboard' electronic crystal state in lightly hole-doped Ca_{2-x}NaxCuO₂Cl₂. *Nature*, 430(7003):1001–1005, aug 2004.

- [196] N McGlothlin, D Ho, and R J Cava. Sr₃Co₂O₅Cl₂ and Sr₂CoO₃Cl: two layered cobalt oxychlorides. *Mater. Res. Bull.*, 35(7):1035–1043, 2000.
- [197] Christopher S Knee, Daniel J Price, Martin R Lees, and Mark T Weller. Two- and three-dimensional magnetic order in the layered cobalt oxychloride Sr₂CoO₃Cl. *Phys. Rev. B*, 68(17):174407, nov 2003.
- [198] Yoshihiro Tsujimoto, Satoshi Nakano, Naoki Ishimatsu, Masaichiro Mizumaki, Naomi Kawamura, Takateru Kawakami, Yoshitaka Matsushita, and Kazunari Yamaura. Pressure-Driven Spin Crossover Involving Polyhedral Transformation in Layered Perovskite Cobalt Oxyfluoride. *Sci. Rep.*, 6(August):36253, 2016.
- [199] T. Thao Tran, Melissa Gooch, Bernd Lorenz, Alexander P. Litvinchuk, Maurice G. Sorolla, Jakoah Brgoch, Paul C W Chu, and Arnold M. Guloy. Nb₂O₂F₃: A reduced niobium (III/IV) oxyfluoride with a complex structural, magnetic, and electronic phase transition. *J. Am. Chem. Soc.*, 137(2):636–639, 2015.
- [200] T. S. Ercit. Refinement of the structure of γ -Nb₂O₅ and its relationship to the rutile and thoreaulite structures. *Mineral. Petrol.*, 43(3):217–223, feb 1991.
- [201] J F Nye. *Physical Properties of Crystals: Their Representation by Tensors and Matrices*. Oxford University Press, New York, NY, 1985.
- [202] Alec Belsky, Mariette Hellenbrandt, Vicky Lynn Karen, and Peter Luksch. New developments in the Inorganic Crystal Structure Database (ICSD): accessibility in support of materials research and design. *Acta Crystallogr. Sect. B: Struct. Sci.*, 58(3):364–369, jun 2002.

- [203] Z. G. G Ye, J. Ravez, J.-P. Rivera, J.-P. Chaminade, and H. Schmid. Optical and dielectric studies on ferroelectric oxyfluoride $K_3MoO_3F_3$ single crystals. *Ferroelectrics*, 124(1):281–286, dec 1991.
- [204] Jean Ravez. The Inorganic Fluoride and Oxyfluoride Ferroelectrics. *J. Phys. III*, 7(6):1129–1144, 1997.
- [205] J. Ravez, G. Peraudeau, H. Arend, S. C. Abrahams, and P. Hagenmuller. A new family of ferroelectric materials with composition $A_2BMO_3F_3$ ($A, B = K, Rb, Cs$, for $rA + rB +$ and $M = Mo, W$). *Ferroelectrics*, 26(1):767–769, jan 1980.
- [206] Paul A Maggard, Tiffany S Nault, Charlotte L Stern, and Kenneth R Poeppelmeier. Alignment of acentric MoO_3F_3 anions in a polar material: $(Ag_3MoO_3F_3)(Ag_3MoO_4)Cl$. *J. Solid State Chem.*, 175(1):27–33, oct 2003.
- [207] R.L. Withers, T.R. Welberry, F.J. Brink, and L. Norén. Oxygen/fluorine ordering, structured diffuse scattering and the local crystal chemistry of $K_3MoO_3F_3$. *J. Solid State Chem.*, 170(2):211–220, feb 2003.
- [208] J F Scott. Ferroelectrics go bananas. *J. Phys.: Condens. Matter*, 20(2):021001, jan 2008.
- [209] Abhishek Kumar Mishra, Michael R. Marvel, Kenneth R. Poeppelmeier, and Umesh V. Waghmare. Competing Cation–Anion Interactions and Noncentrosymmetry in Metal Oxide-Fluorides: A First-Principles Theoretical Study. *Cryst. Growth Des.*, 14(1):131–139, jan 2014.
- [210] H H Wieder. Electrical behavior of barium titanate single crystals at low temperatures. *Phys. Rev.*, 99(4):1161–1165, aug 1955.

- [211] Kelvin B. Chang, Bryce W. Edwards, Laszlo Frazer, Erik J. Lenferink, Teodor K. Stanev, Nathaniel P. Stern, Juan C. Nino, and Kenneth R. Poeppelmeier. Hydrothermal crystal growth, piezoelectricity, and triboluminescence of KNaNbOF_5 . *J. Solid State Chem.*, 236:78–82, 2016.
- [212] Chen Chuang-Tian. AN IONIC GROUPING THEORY OF THE ELECTRO-OPTICAL AND NON-LINEAR OPTICAL EFFECTS OF CRYSTALS ()—A THEORETICAL CALCULATION OF ELECTRO-OPTICAL AND SECOND OPTICAL HARMONIC COEFFICIENTS OF BARIUM TITANATE CRYSTALS BASED ON A DEFORMED OXYGEN-OCTAHEDRA. *Acta Phys. Sin.*, 25(2):146, 1976.
- [213] S K Kurtz and T T Perry. A Powder Technique for the Evaluation of Nonlinear Optical Materials. *J. Appl. Phys.*, 39(8):3798–3813, jul 1968.
- [214] Martin D Donakowski, Romain Gautier, Hongcheng Lu, T Thao Tran, Jacqueline R Cantwell, P Shiv Halasyamani, and Kenneth R Poeppelmeier. Syntheses of Two Vanadium Oxide-Fluoride Materials That Differ in Phase Matchability. *Inorg. Chem.*, 54(3):765–772, feb 2015.
- [215] T. Thao Tran, Joshua Young, James M. Rondinelli, and P. Shiv Halasyamani. Mixed-Metal Carbonate Fluorides as Deep-Ultraviolet Nonlinear Optical Materials. *J. Am. Chem. Soc.*, 139(3):1285–1295, 2017.
- [216] Guangsai Yang, Guang Peng, Ning Ye, Jiyang Wang, Min Luo, Tao Yan, and Yuqiao Zhou. Structural Modulation of Anionic Group Architectures by Cations to Optimize SHG Effects: A Facile Route to New NLO Materials in the ATCO_3F ($\text{A} = \text{K}, \text{Rb}$; $\text{T} = \text{Zn}, \text{Cd}$) Series. *Chem. Mater.*, 27(21):7520–7530, nov 2015.

- [217] Hongwei Huang, Jiyong Yao, Zheshuai Lin, Xiaoyang Wang, Ran He, Wenjiao Yao, Naixia Zhai, and Chuangtian Chen. NaSr₃Be₃B₃O₉F₄: A Promising Deep-Ultraviolet Nonlinear Optical Material Resulting from the Cooperative Alignment of the [Be₃B₃O₁₂F]₁₀ Anionic Group. *Angew. Chem. Int. Ed.*, 50(39):9141–9144, sep 2011.
- [218] Hongwei Yu, Hongping Wu, Shilie Pan, Zhihua Yang, Xin Su, and Fangfang Zhang. A novel deep UV nonlinear optical crystal Ba₃B₆O₁₁F₂, with a new fundamental building block, B₆O₁₄ group. *J. Mater. Chem.*, 22(19):9665, 2012.
- [219] Hongwei Huang, Jiyong Yao, Zheshuai Lin, Xiaoyang Wang, Ran He, Wenjiao Yao, Naixia Zhai, and Chuangtian Chen. Molecular Engineering Design to Resolve the Layering Habit and Polymorphism Problems in Deep UV NLO Crystals: New Structures in MMBe₂B₂O₆F (M′=Na, M=Ca; M= K, M=Ca, Sr). *Chem. Mater.*, 23(24):5457–5463, dec 2011.
- [220] D Eimerl, L Davis, S Velsko, E K Graham, and A Zalkin. Optical, mechanical, and thermal properties of barium borate. *J. Appl. Phys.*, 62(5):1968–1983, 1987.
- [221] Baichang Wu, Dingyuen Tang, Ning Ye, and Chuangtian Chen. Linear and nonlinear optical properties of the KBe₂BO₃F₂ (KBBF) crystal. *Opt. Mater. (Amst.)*, 5(1-2):105–109, jan 1996.
- [222] Colin D McMillen and Joseph W Kolis. Hydrothermal crystal growth of ABe₂BO₃F₂ (A=K, Rb, Cs, Tl) NLO crystals. *J. Cryst. Growth*, 310(7-9):2033–2038, apr 2008.
- [223] Ning Ye and Dingyaun Tang. Hydrothermal growth of KBe₂BO₃F₂ crystals. *J. Cryst. Growth*, 293(2):233–235, aug 2006.

- [224] Hui Zhang, Min Zhang, Shilie Pan, Zhihua Yang, Zheng Wang, Qiang Bian, Xueling Hou, Hongwei Yu, Fangfang Zhang, Kui Wu, Feng Yang, Qinjun Peng, Zuyan Xu, Kelvin B Chang, and Kenneth R Poeppelmeier. Na₃Ba₂(B₃O₆)₂F: Next Generation of Deep-Ultraviolet Birefringent Materials. *Cryst. Growth Des.*, 15(1):523–529, jan 2015.
- [225] Won Bin Im, Stuart Brinkley, Jerry Hu, Alexander Mikhailovsky, Steven P. Denbaars, and Ram Seshadri. Sr_{2.975-x}Ba_xCe_{0.025}AlO₄F: A highly efficient green-emitting oxyfluoride phosphor for solid state white lighting. *Chem. Mater.*, 22(9):2842–2849, 2010.
- [226] Alexander Kraytsberg and Yair Ein-Eli. A critical review-promises and barriers of conversion electrodes for Li-ion batteries. *J. Solid State Electrochem.*, 21(7):1907–1923, 2017.
- [227] Erin M Sorensen, Heather K Izumi, John T Vaughey, Charlotte L Stern, and Kenneth R Poeppelmeier. Ag₄V₂O₆F₂: An Electrochemically Active and High Silver Density Phase. *J. Am. Chem. Soc.*, 127(17):6347–6352, may 2005.
- [228] Jaye K. Harada, Kenneth R. Poeppelmeier, and James M. Rondinelli. Predicting the Structure Stability of Layered Heteroanionic Materials Exhibiting Anion Order. *Inorg. Chem.*, 58(19):13229–13240, 2019.
- [229] Yoji Kobayashi, Yoshihiro Tsujimoto, and Hiroshi Kageyama. Property Engineering in Perovskites via Modification of Anion Chemistry. *Annu. Rev. Mater. Res.*, 48(1):303–326, jul 2018.
- [230] Ryu Abe, Masanobu Higashi, and Kazunari Domen. Facile Fabrication of an Efficient Oxynitride TaON Photoanode for Overall Water Splitting into H₂ and O₂ under Visible Light Irradiation. *J. Am. Chem. Soc.*, 132(34):11828–11829, sep 2010.

- [231] Michael W. Gaultois, Anton O. Oliynyk, Arthur Mar, Taylor D. Sparks, Gregory J. Mulholland, and Bryce Meredig. Perspective: Web-Based Machine Learning Models for Real-Time Screening of Thermoelectric Materials Properties. *APL Mater.*, 4(5), 2016.
- [232] Ya Zhuo, Aria Mansouri Tehrani, Anton O. Oliynyk, Anna C. Duke, and Jakoah Brgoch. Identifying an Efficient, Thermally Robust Inorganic Phosphor Host via Machine Learning. *Nat. Commun.*, 9(1), 2018.
- [233] M. V. Talanov, V. B. Shirokov, and V. M. Talanov. Anion Order in Perovskites: A Group-Theoretical Analysis. *Acta Crystallogr. Sect. A: Found. Adv.*, 72(2):222–235, mar 2016.
- [234] P P Ewald. Die Berechnung Optischer und Elektrostatischer Gitterpotentiale. *Ann. Phys.*, 369(3):253–287, 1921.
- [235] I. D. Brown and R. D. Shannon. Empirical bond-strength–bond-length curves for oxides. *Acta Crystallogr. Sect. A*, 29(3):266–282, 1973.
- [236] I David Brown and Kenneth R Poeppelmeier, editors. *Bond Valences*, volume 158 of *Structure and Bonding*. Springer-Verlag Berlin Heidelberg, Berlin, Heidelberg, 2014.
- [237] Amparo Fuertes. Prediction of Anion Distributions Using Pauling’s Second Rule. *Inorg. Chem.*, 45(24):9640–9642, nov 2006.
- [238] James A. Enterkin, Andres E. Becerra-Toledo, Kenneth R. Poeppelmeier, and Laurence D. Marks. A Chemical Approach to Understanding Oxide Surfaces. *Surf. Sci.*, 606(3-4):344–355, 2012.

- [239] Ikuya Yamada, Akihiko Takamatsu, and Hidekazu Ikeno. Complementary Evaluation of Structure Stability of Perovskite Oxides Using Bond-Valence and Density-Functional-Theory Calculations. *Sci. Technol. Adv. Mater.*, 19(1):101–107, 2018.
- [240] I. D. Brown. Chemical and Steric Constraints in Inorganic Solids. *Acta Crystallogr. Sect. B: Struct. Sci.*, 48(5):553–572, oct 1992.
- [241] A. Salinas-Sanchez, J. L. Garcia-Muñoz, J. Rodriguez-Carvajal, R. Saez-Puche, and J. L. Martinez. Structural Characterization of R_2BaCuO_5 ($R = Y, Lu, Yb, Tm, Er, Ho, Dy, Gd, Eu$ and Sm) Oxides by X-Ray and Neutron Diffraction. *J. Solid State Chem.*, 100(2):201–211, 1992.
- [242] Prasanna V Balachandran, Danilo Puggioni, and James M. Rondinelli. Crystal-Chemistry Guidelines for Noncentrosymmetric A_2BO_4 RuddlesdenPopper Oxides. *Inorg. Chem.*, 53(1):336–348, jan 2014.
- [243] Harold T. Stokes, Branton J. Campbell, and Dorian M. Hatch. ISOTROPY Software Suite, 2015.
- [244] Harold T. Stokes, Dorian M. Hatch, and Branton J. Campbell. ISODISTORT.
- [245] S C Miller and W F Love. *Tables of Irreducible Representations of Space Groups and Co-Representations of Magnetic Space Groups*. Pruett Press, Boulder, Co, 1967.
- [246] I David Brown. Bond Valence Parameters, 2016.
- [247] N. E. Brese and M. O’Keeffe. Bond-Valence Parameters for Solids. *Acta Crystallogr. B*, 47(2):192–197, 1991.

- [248] I. D. Brown and D. Altermatt. Bond-valence Parameters Obtained from a Systematic Analysis of the Inorganic Crystal Structure Database. *Acta Crystallogr. Sect. B: Struct. Sci.*, 41(4):244–247, aug 1985.
- [249] Michael W Lufaso and Patrick M Woodward. Prediction of the Crystal Structures of Perovskites Using the Software Program SPuDS. *Acta Crystallogr. Sect. B: Struct. Sci.*, 57(6):725–738, dec 2001.
- [250] Joshua Young, Parth Lalkiya, and James M Rondinelli. Design of Noncentrosymmetric Perovskites From Centric and Acentric Basic Building Units. *J. Mater. Chem. C*, 4(18):4016–4027, 2016.
- [251] Young Han Shin, Valentino R. Cooper, Ilya Grinberg, and Andrew M. Rappe. Development of a Bond-Valence Molecular-Dynamics Model for Complex Oxides. *Phys. Rev. B*, 71(5):1–4, 2005.
- [252] Eric Jones, Travis Oliphant, Pearu Peterson, and Others. SciPy: Open Source Scientific Tools for Python, 2001.
- [253] Nenan Charles and James M. Rondinelli. Assessing Exchange-Correlation Functional Performance for Structure and Property Predictions of Oxyfluoride Compounds From First Principles. *Phys. Rev. B*, 94(17):174108, nov 2016.
- [254] Shyue Ping Ong, William Davidson Richards, Anubhav Jain, Geoffroy Hautier, Michael Kocher, Shreyas Cholia, Dan Gunter, Vincent L Chevrier, Kristin A Persson, and Gerbrand Ceder. Python Materials Genomics (pymatgen): A robust, open-source python library for materials analysis. *Comput. Mater. Sci.*, 68:314–319, 2013.

- [255] Allyson M Fry, Harry A Seibel, Indunil N Lokuhewa, and Patrick M Woodward. $\text{Na}_{1.5}\text{Ag}_{1.5}\text{MO}_3\text{F}_3$ (M = Mo, W): An Ordered Oxyfluoride Derivative of the LiNbO_3 Structure. *J. Am. Chem. Soc.*, 134(5):2621–2625, 2012.
- [256] R Marchand, R Pastuszak, and Y Laurent. Structure Cristalline de $\text{Nd}_2\text{AlO}_3\text{N}$. Dtermination de L'ordre Oxygène-Zzote par Diffraction de Neutrons. *Rev. Chim. Miner.*, 19:684–489, 1982.
- [257] François Cheviré, Arthur Pallu, Erwan Ray, and Franck Tessier. Characterization of $\text{Nd}_2\text{AlO}_3\text{N}$ and $\text{Sm}_2\text{AlO}_3\text{N}$ Oxynitrides Synthesized by Carbothermal Reduction and Nitridation. *J. Alloys Compd.*, 509(19):5839–5842, may 2011.
- [258] Andrew L. Hector, John A. Hutchings, Richard L. Needs, Michael F. Thomas, and Mark T. Weller. Structural and Mössbauer Study of $\text{Sr}_2\text{FeO}_3\text{X}$ (X = F, Cl, Br) and the Magnetic Structure of $\text{Sr}_2\text{FeO}_3\text{F}$. *J. Mater. Chem.*, 11(2):527–532, 2001.
- [259] Christopher S. Knee, Alexander A. Zhukov, and Mark T. Weller. Crystal Structures and Magnetic Properties of the Manganese Oxide Chlorides $\text{Sr}_2\text{MnO}_3\text{Cl}$ and $\text{Sr}_4\text{Mn}_3\text{O}_8 \cdot \text{Cl}_2$. *Chem. Mater.*, 14(10):4249–4255, oct 2002.
- [260] Richard L Needs and Mark T Weller. Synthesis and structure of $\text{Ba}_2\text{InO}_3\text{F}$: oxide/fluoride ordering in a new K_2NiF_4 superstructure. *J. Chem. Soc. Chem. Commun.*, (3):353, 1995.
- [261] Richard L. Needs, Mark T. Weller, Ulrich Scheler, and Robin K. Harris. Synthesis and Structure of $\text{Ba}_2\text{InO}_3\text{X}$ (X = F, Cl, Br) and $\text{Ba}_2\text{ScO}_3\text{F}$; Oxide/Halide Ordering in K_2NiF_4 -Type Structures. *J. Mater. Chem.*, 6(7):1219, 1996.

- [262] Gilles Le Flem, Gérard Demazeau, and Paul Hagemuller. Relations Between Structure and Physical Properties in K_2NiF_4 -Type Oxides. *J. Solid State Chem.*, 44(1):82–88, aug 1982.
- [263] C.N.R. Rao, P Ganguly, K.K. Singh, and R.A.Mohan Ram. A Comparative Study of the Magnetic and Electrical Properties of Perovskite Oxides and the Corresponding Two-Dimensional Oxides of K_2NiF_4 Structure. *J. Solid State Chem.*, 72(1):14–23, jan 1988.
- [264] Nathalie Vonrüti and Ulrich Aschauer. Anion Order and Spontaneous Polarization in $LaTiO_{2N}$ Oxynitride Thin Films. *Phys. Rev. Lett.*, 120(4):046001, jan 2018.
- [265] Maria Bouri and Ulrich Aschauer. Bulk and Surface Properties of the Ruddlesden–Popper Oxynitride Sr_2TaO_3N . *Phys. Chem. Chem. Phys.*, 20(4):2771–2776, 2018.
- [266] J. A. Alonso, M. J. Martínez-Lope, C. De La Calle, and V. Pomjakushin. Preparation and Structural Study From Neutron Diffraction Data of $RCoO_3$ ($R = Pr, Tb, Dy, Ho, Er, Tm, Yb, Lu$) Perovskites. *J. Mater. Chem.*, 16(16):1555–1560, 2006.
- [267] Stefan Adams. Relationship Between Bond Valence and Bond Softness of Alkali Halides and Chalcogenides. *Acta Crystallogr. Sect. B: Struct. Sci.*, 57(3):278–287, 2001.
- [268] Todd A. Yee, Leopoldo Suescun, and Federico A. Rabuffetti. Bond Valence Parameters for Alkali- and Alkaline-Earth–Oxygen Pairs: Derivation and Application to Metal–Organic Compounds. *J. Solid State Chem.*, 270(November 2018):242–246, 2019.

- [269] Karin M. Rabe, Matthew Dawber, Céline Lichtensteiger, Charles H. Ahn, and Jean-Marc Triscone. Modern Physics of Ferroelectrics: Essential Background. In *Phys. Ferroelectr.*, pages 1–30. Springer Berlin Heidelberg, Berlin, Heidelberg, 2007.
- [270] P Shiv Halasyamani and Kenneth R Poeppelmeier. Noncentrosymmetric Oxides. *Chem. Mater.*, 10(10):2753–2769, oct 1998.
- [271] J. M. Perez-Mato, P. Blaha, K. Schwarz, M. Aroyo, D. Orobengoa, I. Etxebarria, and Alberto García. Multiple instabilities in $\text{Bi}_4\text{Ti}_3\text{O}_{12}$: A ferroelectric beyond the soft-mode paradigm. *Phys. Rev. B*, 77(18):1–11, 2008.
- [272] Nicole A. Benedek and Craig J. Fennie. Hybrid Improper Ferroelectricity: A Mechanism for Controllable Polarization-Magnetization Coupling. *Phys. Rev. Lett.*, 106(10):107204, mar 2011.
- [273] Andrew T Mulder, Nicole A Benedek, James M Rondinelli, and Craig J Fennie. Turning ABO_3 Antiferroelectrics into Ferroelectrics: Design Rules for Practical Rotation-Driven Ferroelectricity in Double Perovskites and $\text{A}_3\text{B}_2\text{O}_7$ Ruddlesden-Popper Compounds. *Adv. Funct. Mater.*, 23(38):4810–4820, may 2013.
- [274] Joshua Young, Eun Ju Moon, Debangshu Mukherjee, Greg Stone, Venkatraman Gopalan, Nasim Alem, Steven J. May, and James M. Rondinelli. Polar Oxides without Inversion Symmetry through Vacancy and Chemical Order. *J. Am. Chem. Soc.*, 139(7):2833–2841, 2017.
- [275] Romain Gautier and Kenneth R. Poeppelmeier. Preservation of chirality and polarity between chiral and polar building units in the solid state. *Inorg. Chem.*, 51(20):10613–10618, 2012.

- [276] Martin D. Donakowski, Romain Gautier, Jeongho Yeon, Donald T. Moore, Juan C. Nino, P. Shiv Halasyamani, and Kenneth R. Poeppelmeier. The role of polar, lambda (λ)-shaped building units in noncentrosymmetric inorganic structures. *J. Am. Chem. Soc.*, 134(18):7679–7689, 2012.
- [277] Daichi Oka, Yasushi Hirose, Hideyuki Kamisaka, Tomoteru Fukumura, Kimikazu Sasa, Satoshi Ishii, Hiroyuki Matsuzaki, Yukio Sato, Yuichi Ikuhara, and Tetsuya Hasegawa. Possible ferroelectricity in perovskite oxynitride SrTaO₂N epitaxial thin films. *Sci. Rep.*, 4(1):4987, may 2015.
- [278] Shinichi Kikkawa, Shikuan Sun, Yuji Masubuchi, Yuki Nagamine, and Takeshi Shibahara. Ferroelectric Response Induced in cis-Type Anion Ordered SrTaO₂N Oxynitride Perovskite. *Chem. Mater.*, 28(5):1312–1317, mar 2016.
- [279] Gaoyang Gou, Min Zhao, Jing Shi, Jaye K. Harada, and James M. Rondinelli. Anion Ordered and Ferroelectric Ruddlesden-Popper Oxynitride Ca₃Nb₂N₂O₅ for Visible-Light-Active Photocatalysis. *Chem. Mater.*, 32(7):2815–2823, apr 2020.
- [280] Zbigniew Tylczyński. A collection of 505 papers on false or unconfirmed ferroelectric properties in single crystals, ceramics and polymers. *Front. Phys.*, 14(6):63301, dec 2019.
- [281] A. D. Vasiliev and N. M. Laptash. Polymorphism of KNaNbOF₅ crystals. *J. Struct. Chem.*, 53(5):902–906, sep 2012.
- [282] Kelvin B. Chang, Anastasiya Vinokur, Rachele Ann F Pinlac, Matthew R. Suchomel, Michael R. Marvel, and Kenneth R. Poeppelmeier. How Lewis Acidity of the Cationic Framework Affects KNaNbOF₅ Polymorphism. *Inorg. Chem.*, 53(13):6979–6984, jul 2014.

- [283] Urko Petralanda and I. Etxebarria. Structural instabilities and sequence of phase transitions in SrBi₂Nb₂O₉ and SrBi₂Ta₂O₉ from first principles and Monte Carlo simulations. *Phys. Rev. B*, 91(18):184106, may 2015.
- [284] Charlotte A.L. Dixon, Jason A. McNulty, Kevin S. Knight, Alexandra S. Gibbs, and Philip Lightfoot. Phase transition behavior of the layered perovskite Csbi_{0.6}La_{0.4}Nb₂O₇: A hybrid improper ferroelectric. *Crystals*, 7(5):1–11, 2017.
- [285] Daniel Sheppard, Penghao Xiao, William Chemelewski, Duane D. Johnson, and Graeme Henkelman. A generalized solid-state nudged elastic band method. *J. Chem. Phys.*, 136(7):74103, 2012.
- [286] Atsushi Togo and Isao Tanaka. First principles phonon calculations in materials science. *Scr. Mater.*, 108:1–5, 2015.
- [287] Arash A. Mostofi, Jonathan R. Yates, Giovanni Pizzi, Young Su Lee, Ivo Souza, David Vanderbilt, and Nicola Marzari. An updated version of wannier90: A tool for obtaining maximally-localised Wannier functions. *Comput. Phys. Commun.*, 185(8):2309–2310, 2014.
- [288] Chris J. Pickard and Francesco Mauri. All-electron magnetic response with pseudopotentials: NMR chemical shifts. *Phys. Rev. B*, 63(24):2451011–2451013, 2001.
- [289] Jonathan R. Yates, Chris J. Pickard, and Francesco Mauri. Calculation of NMR chemical shifts for extended systems using ultrasoft pseudopotentials. *Phys. Rev. B*, 76(2):1–11, 2007.
- [290] Branton J Campbell, Harold T Stokes, David E Tanner, and Dorian M Hatch. ISODISPLACE : A Web-Based Tool for Exploring Structural Distortions. *J. Appl. Crystallogr.*, 39(4):607–614, jul 2006.

- [291] Harold T. Stokes, Dorian M. Hatch, and Branton J. Campbell. INVARIANTS.
- [292] Dorian M Hatch and Harold T Stokes. INVARIANTS : program for obtaining a list of invariant polynomials of the order-parameter components associated with irreducible representations of a space group. *J. Appl. Crystallogr.*, (36):951–952, 2003.
- [293] Eileen B Segal. First aid for a unique acid, HF: A sequel. *Chem. Heal. Saf.*, 7(1):18–23, 2000.
- [294] D. Peters and R. Miethchen. Symptoms and treatment of hydrogen fluoride injuries. *J. Fluor. Chem.*, 79(2):161–165, 1996.
- [295] John C. Bertolini. Hydrofluoric acid: A review of toxicity. *J. Emerg. Med.*, 10(2):163–168, 1992.
- [296] William T. A. Harrison, Tina M. Nenoff, Thurman E. Gier, and Galen D. Stucky. Tetrahedral-atom 3-ring groupings in 1-dimensional inorganic chains: beryllium arsenate hydroxide hydrate ($\text{Be}_2\text{AsO}_4\text{OH}\cdot 4\text{H}_2\text{O}$) and sodium zinc hydroxide phosphate hydrate ($\text{Na}_2\text{ZnPO}_4\text{OH}\cdot 7\text{H}_2\text{O}$). *Inorg. Chem.*, 32(11):2437–2441, 2005.
- [297] Horst Ernst, Dieter Freude, Toralf Mildner, and Ingo Wolf. Laser-supported high-temperature MAS NMR for time-resolved in situ studies of reaction steps in heterogeneous catalysis. *Solid State Nucl. Magn. Reson.*, 6(2):147–156, apr 1996.
- [298] Danel Orobengoa, Cesar Capillas, Mois I. Aroyo, and J. Manuel Perez-Mato. AMPLIMODES: symmetry-mode analysis on the Bilbao Crystallographic Server. *J. Appl. Crystallogr.*, 42(5):820–833, oct 2009.
- [299] J. M. Perez-Mato, D. Orobengoa, and M. I. Aroyo. Mode crystallography of distorted structures. *Acta Crystallogr. Sect. A Found. Crystallogr.*, 66(5):558–590, sep 2010.

- [300] Nicola A Spaldin. A beginner's guide to the modern theory of polarization. *J. Solid State Chem.*, 195:2–10, nov 2012.
- [301] R. D. King-Smith and David Vanderbilt. Theory of polarization of crystalline solids. *Phys. Rev. B*, 47(3):1651–1654, 1993.
- [302] Paul A. Maggard, Tiffany S. Nault, Charlotte L. Stern, and Kenneth R. Poeppelmeier. Alignment of acentric MoO_3F_3^- anions in a polar material: $(\text{Ag}_3\text{MoO}_3\text{F}_3)(\text{Ag}_3\text{MoO}_4)\text{Cl}$. *J. Solid State Chem.*, 175(1):27–33, 2003.
- [303] Y. Noel, C. M. Zicovich-Wilson, B. Civalleri, Ph D'Arco, and R. Dovesi. Polarization properties of ZnO and BeO: An ab initio study through the Berry phase and Wannier functions approaches. *Phys. Rev. B*, 65(1):1–9, 2002.
- [304] Claude Ederer and Nicola A. Spaldin. Origin of ferroelectricity in the multiferroic barium fluorides BaM_2F_4 : A first principles study. *Phys. Rev. B*, 74(2):1–8, 2006.
- [305] Ronald E. Cohen. Origin of ferroelectricity in perovskite oxides. *Nature*, 358(6382):136–138, jul 1992.
- [306] Orlando Auciello, James F Scott, and Ramamoorthy Ramesh. The Physics of Ferroelectric Memories. *Phys. Today*, 51(7):22–27, jul 1998.
- [307] James F Scott. *Ferroelectric Memories*. Springer Berlin Heidelberg, 2000.
- [308] Yoon Seok Oh, Xuan Luo, Fei Ting Huang, Yazhong Wang, and Sang Wook Cheong. Experimental demonstration of hybrid improper ferroelectricity and the presence of abundant charged walls in $(\text{Ca,Sr})_3\text{Ti}_2\text{O}_7$ crystals. *Nat. Mater.*, 14(4):407–413, 2015.

- [309] Joshua Young, Alessandro Stroppa, Silvia Picozzi, and James M Rondinelli. Anharmonic lattice interactions in improper ferroelectrics for multiferroic design. *J. Phys.: Condens. Matter*, 27(28):283202, jul 2015.
- [310] Jeremy K. Burdett. Use of the Jahn-Teller Theorem in Inorganic Chemistry. *Inorg. Chem.*, 20(7):1959–1962, 1981.
- [311] Isaac B. Bersuker. Pseudo-Jahn-Teller Effect—A Two-State Paradigm in Formation, Deformation, and Transformation of Molecular Systems and Solids. *Chem. Rev.*, 113(3):1351–1390, mar 2013.
- [312] V Polinger, P. Garcia-Fernandez, and I.B. Bersuker. Pseudo Jahn-Teller origin of ferroelectric instability in BaTiO₃ type perovskites: The Green’s function approach and beyond. *Phys. B Condens. Matter*, 457:296–309, jan 2015.
- [313] Bas B. Van Aken, Thomas T.M. Palstra, Alessio Filippetti, and Nicola A. Spaldin. The origin of ferroelectricity in magnetoelectric YMnO₃. *Nat. Mater.*, 3(3):164–170, mar 2004.
- [314] Ke Xu, Xue-Zeng Lu, and Hongjun Xiang. Designing new ferroelectrics with a general strategy. *npj Quantum Mater.*, 2(1):1, dec 2017.
- [315] L. Bellaiche and Jorge Íñiguez. Universal collaborative couplings between oxygen-octahedral rotations and antiferroelectric distortions in perovskites. *Phys. Rev. B*, 88(1):014104, jul 2013.
- [316] Nicole A. Benedek. Origin of ferroelectricity in a family of polar oxides: The dion-jacobson phases. *Inorg. Chem.*, 53(7):3769–3777, 2014.
- [317] Hong Jian Zhao, Jorge Íñiguez, Wei Ren, Xiang Ming Chen, and L. Bellaiche. Atomistic theory of hybrid improper ferroelectricity in perovskites. *Phys. Rev. B*, 89(17):1–7, 2014.

- [318] Hong Jian Zhao, L. Bellaiche, Xiang Ming Chen, and Jorge Íñiguez. Improper electric polarization in simple perovskite oxides with two magnetic sublattices. *Nat. Commun.*, 8:1–11, 2017.
- [319] Hanna L.B. Boström, Mark S. Senn, and Andrew L. Goodwin. Recipes for improper ferroelectricity in molecular perovskites. *Nat. Commun.*, 9(1):1–7, 2018.
- [320] Judith Oró-Solé, Ignasi Fina, Carlos Frontera, Jaume Gàzquez, Clemens Ritter, Marina Cunqueiro, Pablo Loza-Alvarez, Sergio Conejeros, Pere Alemany, Enric Canadell, Josep Fontcuberta, and Amparo Fuertes. Engineering Polar Oxynitrides: Hexagonal Perovskite BaWON 2. *Angew. Chem. Int. Ed.*, 59(42):18395–18399, oct 2020.
- [321] Ghanshyam Pilania, Ayana Ghosh, Steven T. Hartman, Rohan Mishra, Christopher R. Stanek, and Blas P. Uberuaga. Anion order in oxysulfide perovskites: origins and implications. *npj Comput. Mater.*, 6(1):71, dec 2020.
- [322] X. Gonze, J. C. Charlier, D. C. Allan, and M. P. Teter. Interatomic force constants from first principles: The case of α -quartz. *Phys. Rev. B*, 50(17):13035–13038, 1994.
- [323] Richard Dronskowski and Peter E. Blöchl. Crystal orbital hamilton populations (COHP). Energy-resolved visualization of chemical bonding in solids based on density-functional calculations. *J. Phys. Chem.*, 97(33):8617–8624, 1993.
- [324] Volker L. Deringer, Andrei L. Tchougréeff, and Richard Dronskowski. Crystal orbital Hamilton population (COHP) analysis as projected from plane-wave basis sets. *J. Phys. Chem. A*, 115(21):5461–5466, 2011.

- [325] Stefan Maintz, Volker L. Deringer, Andrei L. Tchougréeff, and Richard Dronskowski. Analytic projection from plane-wave and PAW wavefunctions and application to chemical-bonding analysis in solids. *J. Comput. Chem.*, 34(29):2557–2567, nov 2013.
- [326] Stefan Maintz, Marc Esser, and Richard Dronskowski. Efficient rotation of local basis functions using real spherical harmonics. *Acta Phys. Pol. B*, 47(4):1165–1175, 2016.
- [327] G Simon Case, Andrew L Hector, William Levason, Richard L Needs, Michael F Thomas, and Mark T Weller. Syntheses, powder neutron diffraction structures and Mössbauer studies of some complex iron oxyfluorides: Sr₃Fe₂O₆F_{0.87}, Sr₂FeO₃F and Ba₂InFeO₅F_{0.68}. *J. Mater. Chem.*, 9(11):2821–2827, 1999.
- [328] S. M. Loureiro, C. Felser, Q. Huang, and R. J. Cava. Refinement of the Crystal Structures of Strontium Cobalt Oxochlorides by Neutron Powder Diffraction. *Chem. Mater.*, 12(10):3181–3185, oct 2000.
- [329] Patrick M. Woodward. Octahedral Tilting in Perovskites. II. Structure Stabilizing Forces. *Acta Crystallogr. Sect. B: Struct. Sci.*, 53(1):44–66, feb 1997.
- [330] P Garcia-Fernandez, J.A. Aramburu, M.T. Barriuso, and M Moreno. Key Role of Covalent Bonding in Octahedral Tilting in Perovskites. *J. Phys. Chem. Lett.*, 1(3):647–651, feb 2010.
- [331] Pablo Aguado-Puente, Pablo García-Fernández, and Javier Junquera. Interplay of Couplings between Antiferrodistortive, Ferroelectric, and Strain Degrees of Freedom in Monodomain PbTiO_3 SrTiO_3 Superlattices. *Phys. Rev. Lett.*, 107(21):217601, nov 2011.

- [332] Antonio Cammarata and James M. Rondinelli. Covalent dependence of octahedral rotations in orthorhombic perovskite oxides. *J. Chem. Phys.*, 141(11):114704, sep 2014.
- [333] Nicole A Benedek and Craig J Fennie. Why Are There So Few Perovskite Ferroelectrics? *J. Phys. Chem. C*, 117(26):13339–13349, 2013.
- [334] Yasuhide Mochizuki, Takayuki Nagai, Hirokazu Shirakuni, Akitoshi Nakano, Fumiyasu Oba, Ichiro Terasaki, and Hiroki Taniguchi. Coexisting Mechanisms for the Ferroelectric Phase Transition in $\text{Li}_2\text{SrNb}_2\text{O}_7$. *Chem. Mater.*, 33(4):1257–1264, feb 2021.
- [335] Ph Ghosez, E. Cockayne, U V Waghmare, and K M Rabe. Lattice dynamics of BaTiO_3 , PbTiO_3 , and PbZrO_3 : A comparative first-principles study. *Phys. Rev. B*, 60(2):836–843, jul 1999.
- [336] Ph Ghosez, X Gonze, and J.-P Michenaud. Coulomb interaction and ferroelectric instability of BaTiO_3 . *Europhys. Lett.*, 33(9):713–718, 1996.
- [337] Nathan Z Koocher, Liang-Feng Huang, and James M Rondinelli. Negative thermal expansion in the Ruddlesden-Popper calcium titanates. *Phys. Rev. Mater.*, 5(5):053601, may 2021.
- [338] Turan Birol, Nicole A. Benedek, and Craig J. Fennie. Interface control of emergent ferroic order in Ruddlesden-Popper $\text{Sr}_{n+1}\text{Ti}_n\text{O}_{3n+1}$. *Phys. Rev. Lett.*, 107(25):1–5, 2011.
- [339] Daniel Hickox-Young, Danilo Puggioni, and James M. Rondinelli. Persistent polar distortions from covalent interactions in doped BaTiO_3 . *Phys. Rev. B*, 102(1):1–11, 2020.
- [340] C. J. Ballhausen and Harry B. Gray. The Electronic Structure of the Vanadyl Ion. *Inorg. Chem.*, 1(1):111–122, feb 1962.

- [341] Jay R. Winkler and Harry B. Gray. Electronic Absorption and Emission Spectra of Dioxorhenium(V) Complexes. Characterization of the Luminescent $3E_g$ State. *Inorg. Chem.*, 24(3):346–355, 1985.
- [342] Karsten Meyer, Jesper Bendix, Eckhard Bill, Thomas Weyhermüller, and Karl Wieghardt. Molecular and Electronic Structure of Nitridochromium(V) Complexes with Macrocyclic Amine Ligands. *Inorg. Chem.*, 37(20):5180–5188, 1998.
- [343] Steven T. Hartman, Sung Beom Cho, and Rohan Mishra. Multiferroism in Iron-Based Oxyfluoride Perovskites. *Inorg. Chem.*, 57(17):10616–10624, 2018.
- [344] Yazhong Wang, Fei Ting Huang, Xuan Luo, Bin Gao, and Sang Wook Cheong. The First Room-Temperature Ferroelectric Sn Insulator and Its Polarization Switching Kinetics. *Adv. Mater.*, 29(2):1–5, 2017.
- [345] Suguru Yoshida, Hirofumi Akamatsu, Ryosuke Tsuji, Olivier Hernandez, Haricharan Padmanabhan, Arnab Sen Gupta, Alexandra S. Gibbs, Ko Mibu, Shunsuke Murai, James M. Rondinelli, Venkatraman Gopalan, Katsuhisa Tanaka, and Koji Fujita. Hybrid Improper Ferroelectricity in $(\text{Sr,Ca})_3\text{Sn}_2\text{O}_7$ and Beyond: Universal Relationship between Ferroelectric Transition Temperature and Tolerance Factor in $n = 2$ Ruddlesden–Popper Phases. *J. Am. Chem. Soc.*, 140(46):15690–15700, nov 2018.
- [346] Suguru Yoshida, Koji Fujita, Hirofumi Akamatsu, Olivier Hernandez, Arnab Sen Gupta, Forrest G. Brown, Haricharan Padmanabhan, Alexandra S. Gibbs, Toshihiro Kuge, Ryosuke Tsuji, Shunsuke Murai, James M. Rondinelli, Venkatraman Gopalan, and Katsuhisa Tanaka. Ferroelectric $\text{Sr}_3\text{Zr}_2\text{O}_7$: Competition between Hybrid Improper Ferroelectric and Antiferroelectric Mechanisms. *Adv. Funct. Mater.*, 28(30):1801856, jul 2018.

- [347] Michael J. Pitcher, Pranab Mandal, Matthew S. Dyer, Jonathan Alaria, Pavel Borisov, Hongjun Niu, John B. Claridge, and Matthew J. Rosseinsky. Tilt engineering of spontaneous polarization and magnetization above 300 K in a bulk layered perovskite. *Science*, 347(6220):420–424, 2015.
- [348] X. Q. Liu, J. W. Wu, X. X. Shi, H. J. Zhao, H. Y. Zhou, R. H. Qiu, W. Q. Zhang, and X. M. Chen. Hybrid improper ferroelectricity in Ruddlesden-Popper $\text{Ca}_3(\text{Ti,Mn})_2\text{O}_7$ ceramics. *Appl. Phys. Lett.*, 106(20):1–5, 2015.
- [349] Darrell G Schlom, Long-Qing Chen, Craig J Fennie, Venkatraman Gopalan, David A Muller, Xiaoqing Pan, Ramamoorthy Ramesh, and Reinhard Uecker. Elastic strain engineering of ferroic oxides. *MRS Bull.*, 39(02):118–130, 2014.
- [350] Shutong Li and Turan Birol. Suppressing the ferroelectric switching barrier in hybrid improper ferroelectrics. *npj Comput. Mater.*, 6(1):168, dec 2020.
- [351] Xue-Zeng Lu and James M. Rondinelli. Epitaxial-strain-induced polar-to-nonpolar transitions in layered oxides. *Nat. Mater.*, 15(9):951–955, sep 2016.
- [352] Jiayi Wang, Benjamin M. Lefler, and Steven J. May. Synthesis and Characterization of $\text{SrFexMn}_{1-x}(\text{O,F})_{3-\delta}$ Oxide ($\delta=0$ and 0.5) and Oxyfluoride Perovskite Films. *Inorg. Chem.*, 59(14):9990–9997, 2020.
- [353] Nathalie Vonrüti and Ulrich Aschauer. Epitaxial strain dependence of band gaps in perovskite oxynitrides compared to perovskite oxides. *Phys. Rev. Mater.*, 2(10):1–9, 2018.

- [354] Richard L Needs and Mark T Weller. Structure of Ba₃In₂O₅F₂ by combined powder X-ray and neutron diffraction analysis; oxide/fluoride ordering in a Ruddlesden–Popper phase. *J. Chem. Soc., Dalton Trans.*, (18):3015–3017, 1995.
- [355] Yu.O. Tyitov, N.M. Byilyavyina, V.Ya. Markyiv, M.S. Slobodyanik, Ya.A. Krajevs'ka, and V.P. Yashchuk. Synthesis and crystal structure of BaLn₂Sc₂O₇. *Dopov. Natsyional'noyi Akad. Nauk Ukrayini*, 5:172–178, 2009.
- [356] Yu.O. Titov, N.M. Bilyavina, V.Ya. Markiv, M.S. Slobodyanik, Ya.A. Kraevs'ka, and V.P. Yashchuk. Synthesis and crystal structure of Ba Ln₂ In₂ O₇. *Dopovidi Natsional'noi Akad. Nauk Ukr.*, 1:148–154, 2010.
- [357] Maité Caldes, Claude Michel, Thierry Rouillon, Maryvonne Hervieu, and Bernard Raveau. Novel indates Ln₂BaIn₂O₇, n = 2 members of the Ruddlesden–Popper family (Ln = La, Nd). *J. Mater. Chem.*, 12(3):473–476, 2002.
- [358] Naoki Kamegashira, Hirohisa Satoh, and Takeshi Mikami. Superstructure of tetragonal BaGd₂Mn₂O₇. *J. Alloys Compd.*, 311(1):69–73, oct 2000.
- [359] M. Drogenik, D. Kolar, and L. Golič. Crystal growth and crystallographic study of Sr₂EuFeO₅. *J. Cryst. Growth*, 21(2):305–306, feb 1974.
- [360] D. Samaras, A. Collomb, and J.C. Joubert. Determination des structures de deux ferrites mixtes nouveaux de formule BaLa₂Fe₂O₇ et SrTb₂Fe₂O₇. *J. Solid State Chem.*, 7(3):337–348, jul 1973.

- [361] M. Sánchez-Andújar and M. A. Señaris-Rodríguez. Cation ordering and electrical properties of the ruddlesden-popper $\text{Gd}_{2-2x}\text{Sr}_{1+2x}\text{Co}_2\text{O}_7$ compounds ($x = 0$ and 0.10). *Z. Anorg. Allg. Chem.*, 633(11-12):1890–1896, 2007.
- [362] Peter J. Hickey, Christopher S. Knee, Paul F. Henry, and Mark T. Weller. Spin-crossover structural transition in the layered perovskite $\text{Gd}_2\text{Sr}_2\text{Co}_2\text{O}_7$. *Phys. Rev. B*, 75(2):024113, jan 2007.
- [363] Peter D Battle, Julie E Millburn, Matthew J Rosseinsky, Lauren E Spring, Jaap F Vente, and Paolo G Radaelli. Neutron Diffraction Study of the Structural and Electronic Properties of $\text{Sr}_2\text{HoMn}_2\text{O}_7$ and $\text{Sr}_2\text{YMn}_2\text{O}_7$. *Chem. Mater.*, 9(12):3136–3143, dec 1997.
- [364] Peter D. Battle, Jonathan C. Burley, Daniel J. Gallon, Clare P. Grey, and Jeremy Sloan. Magnetism and structural chemistry of the $n=2$ Ruddlesden–Popper phase $\text{La}_3\text{LiMnO}_7$. *J. Solid State Chem.*, 177(1):119–125, jan 2004.
- [365] Y.-C. Hung, James C. Fettinger, and Bryan W. Eichhorn. $\text{Ba}_3\text{Zr}_2\text{S}_7$, the Low-Temperature Polymorph. *Acta Crystallogr. Sect. C: Cryst. Struct. Commun.*, 53(7):827–829, jul 1997.
- [366] Alison J. Hatt and Nicola A. Spaldin. Structural phases of strained LaAlO_3 driven by octahedral tilt instabilities. *Phys. Rev. B*, 82(19):195402, nov 2010.

- [367] S J May, J.-W. Kim, J M Rondinelli, E Karapetrova, N A Spaldin, A Bhattacharya, and P J Ryan. Quantifying octahedral rotations in strained perovskite oxide films. *Phys. Rev. B*, 82(1):14110, 2010.
- [368] Yajun Zhang, M. P.K. Sahoo, Takahiro Shimada, Takayuki Kitamura, and Jie Wang. Strain-induced improper ferroelectricity in Ruddlesden-Popper perovskite halides. *Phys. Rev. B*, 96(14):1–8, 2017.
- [369] Megan C Knapp. *Investigations into the Structure and Properties of Ordered Perovskites, Layered Perovskites, and Defect Pyrochlores*. PhD thesis, The Ohio State University, 2006.
- [370] Fenghua Ding, Nenian Charles, Jaye K. Harada, Christos D. Malliakas, Chi Zhang, M. L. Nisbet, W. Zhang, P. Shiv Halasyamani, Vinayak P. Dravid, James M. Rondinelli, and Kenneth R. Poeppelmeier. K₃TiOF₅ Exhibits an Incommensurate Structure Induced by Octahedrally Coordinated Potassium Ions. 2021.
- [371] Allyson M Fry and Patrick M Woodward. Structures of α -K₃MoO₃F₃ and α -Rb₃MoO₃F₃: Ferroelectricity from Anion Ordering and Noncooperative Octahedral Tilting. *Cryst. Growth Des.*, 13(12):5404–5410, dec 2013.
- [372] Nathan J. Szymanski, Lauren N. Walters, Danilo Puggioni, and James M. Rondinelli. Design of Heteroanionic MoON Exhibiting a Peierls Metal-Insulator Transition. *Phys. Rev. Lett.*, 123(23):236402, dec 2019.
- [373] B.L. Chamberland, A.W. Sleight, and W.H. Cloud. The preparation and properties of rutile-type transition metal oxyfluorides. *J. Solid State Chem.*, 2(1):49–54, jun 1970.

- [374] J. Cumby, M.B. Burchell, and J.P. Attfield. High pressure synthesis, crystal growth and magnetic properties of TiOF. *Solid State Sci.*, 80:35–38, jun 2018.
- [375] Nicholas J. Ramer and Andrew M. Rappe. Virtual-crystal approximation that works: Locating a composition phase boundary in $\text{Pb}(\text{Zr}_{1-x}\text{Ti}_x)\text{O}_3$. *Phys. Rev. B*, 62(2):5, 1999.
- [376] L. Bellaiche and David Vanderbilt. Virtual crystal approximation revisited: Application to dielectric and piezoelectric properties of perovskites. *Phys. Rev. B*, 61(12):7877–7882, 2000.
- [377] Chol-Jun Yu and Heike Emmerich. An efficient virtual crystal approximation that can be used to treat heterovalent atoms, applied to $(1-x)\text{BiScO}_3-x\text{PbTiO}_3$. *J. Phys.: Condens. Matter*, 19(30):306203, aug 2007.
- [378] Alex Zunger, S.-H. Wei, L. G. Ferreira, and James E. Bernard. Special quasirandom structures. *Phys. Rev. Lett.*, 65(3):353–356, jul 1990.
- [379] Jorge Íñiguez, David Vanderbilt, and L. Bellaiche. First-principles study of $(\text{BiScO}_3)_{1-x}(\text{PbTiO}_3)_x$ piezoelectric alloys. *Phys. Rev. B*, 67(22):224107, 2003.
- [380] Smritijit Sen and Haranath Ghosh. Electronic structures of doped BaFe_2As_2 materials: virtual crystal approximation versus super-cell approach. *Eur. Phys. J. B*, 89(12), 2016.
- [381] Changfeng Chen and E. Wang. Unexpected band-gap collapse in quaternary alloys at the group-III-nitride/GaAs interface: GaAlAsN . *Phys. Rev. B*, 57(7):3753–3756, 1998.
- [382] Roberta Poloni, Jorge Íñiguez, Alberto García, and Enric Canadell. An efficient computational method for use in structural studies of crystals with substitutional disorder. *J. Phys.: Condens. Matter*, 22(41):415401, oct 2010.

- [383] John B. Goodenough. The two components of the crystallographic transition in VO₂. *J. Solid State Chem.*, 3(4):490–500, nov 1971.
- [384] Zenji Hiroi. Structural instability of the rutile compounds and its relevance to the metal-insulator transition of VO₂. *Prog. Solid State Chem.*, 43(1-2):47–69, may 2015.
- [385] Sooran Kim, Kyoo Kim, Chang Jong Kang, and B. I. Min. Correlation-assisted phonon softening and the orbital-selective Peierls transition in VO₂. *Phys. Rev. B*, 87(19):1–5, 2013.
- [386] V. Eyert. The metal-insulator transitions of VO₂: A band theoretical approach. *Ann. Phys.*, 11(9):650–704, oct 2002.
- [387] Jess Stausholm-Møller, Henrik H. Kristoffersen, Berit Hinnemann, Georg K H Madsen, and Bjørk Hammer. DFT+U study of defects in bulk rutile TiO₂. *J. Chem. Phys.*, 133(14), 2010.
- [388] Anderson R. Albuquerque, Albert Bruix, Iêda M G Dos Santos, Julio R. Sambrano, and Francesc Illas. DFT study on Ce-doped anatase TiO₂: Nature of Ce³⁺ and Ti³⁺ centers triggered by oxygen vacancy formation. *J. Phys. Chem. C*, 118(18):9677–9689, 2014.

Appendix A: Predicting the Structure Stability of Layered Heteroanionic Materials Exhibiting Anion Order

TABLE A.1: Table of all published heteroanionic $n=1$ Ruddlesden-Popper compounds. RT = room temperature

Composition	Space group	Temperature	X Anion	Long range anion order?	DOI
Ba ₂ InO ₃ Br	<i>P4/nmm</i>	298 K	Br	ordered	10.1039/JM9960601219
Ca ₂ CuO ₂ Br ₂	<i>I4/nmm</i>	RT	Br	ordered	10.1002/zaac.19774290112
Sr ₂ CoO ₂ Br ₂	<i>I4/nmm</i>	RT	Br	ordered	10.1006/jssc.2002.9682
Sr ₂ FeO ₃ Br	<i>P4/nmm</i>	RT	Br	ordered	10.1039/B008321F
Ba ₂ CuO ₂ Cl ₂	<i>I4/nmm</i>	RT	Cl	ordered	10.1016/0921-4534(96)00332-2
Ba ₂ InO ₃ Cl	<i>P4/nmm</i>	298 K	Cl	ordered	10.1039/JM9960601219
Ca _{0.44} Sr _{0.56} SmCuO ₃ Cl	<i>P4/nmm</i>	RT	Cl	ordered	10.1016/0022-4596(91)90347-K
Ca _{0.72} Sr _{0.28} NdCuO ₃ Cl	<i>P4/nmm</i>	RT	Cl	ordered	10.1016/0022-4596(91)90347-K
Ca _{0.78} Sr _{0.22} NdCuO ₃ Cl	<i>P4/nmm</i>	RT	Cl	ordered	10.1016/0022-4596(91)90347-K
Ca _{0.79} Sr _{0.21} GdCuO ₃ Cl	<i>P4/nmm</i>	RT	Cl	ordered	10.1016/0022-4596(91)90347-K
Ca _{0.80} Sr _{0.20} EuCuO ₃ Cl	<i>P4/nmm</i>	RT	Cl	ordered	10.1016/0022-4596(91)90347-K
Ca _{0.83} Sr _{0.17} NdCuO ₃ Cl	<i>P4/nmm</i>	RT	Cl	ordered	10.1016/0022-4596(91)90347-K
Ca ₂ CuO ₂ Cl ₂	<i>I4/nmm</i>	RT	Cl	ordered	10.1002/zaac.19774290112
Ca ₂ ErCuO ₃ Cl	<i>P4/nmm</i>	RT	Cl	ordered	10.1016/S0921-4534(96)00510-2
Ca ₂ HoCuO ₃ Cl	<i>P4/nmm</i>	RT	Cl	ordered	10.1016/S0921-4534(96)00510-2
Ca ₂ YCuO ₃ Cl	<i>P4/nmm</i>	RT	Cl	ordered	10.1016/S0921-4534(96)00510-2
CaEuCuO ₃ Cl	<i>P4/nmm</i>	RT	Cl	ordered	10.1016/0022-4596(91)90347-K
CaGdCuO ₃ Cl	<i>P4/nmm</i>	RT	Cl	ordered	10.1016/0022-4596(91)90347-K
CaSmCuO ₃ Cl	<i>P4/nmm</i>	RT	Cl	ordered	10.1016/0022-4596(91)90347-K
Sr ₂ CoO ₂ Cl ₂	<i>I4/nmm</i>	RT	Cl	ordered	10.1006/jssc.2002.9682
Sr ₂ CoO ₃ Cl	<i>P4/nmm</i>	RT	Cl	ordered	10.1021/cm000410m
Sr ₂ CuO ₂ Cl ₂	<i>I4/nmm</i>	300,200,65,25 K	Cl	ordered	10.1103/PhysRevB.41.1921
Sr ₂ FeO ₃ Cl	<i>P4/nmm</i>	RT	Cl	ordered	10.1039/B008321F
Sr ₂ MnO ₃ Cl	<i>P4/nmm</i>	RT, 2K	Cl	ordered	10.1021/cm020280c
Sr ₂ NiO ₃ Cl	<i>P4/nmm</i>	RT	Cl	ordered	10.1021/ic402008n
SrNdCuO ₃ Cl	<i>P4/nmm</i>	RT	Cl	ordered	10.1016/0022-4596(91)90347-K
Ba ₂ InO ₃ F	<i>P4/nmm</i>	298 K	F	ordered	10.1039/JM9960601219
Ba ₂ ScO ₃ F	<i>I4/nmm</i>	298 K	F	disordered	10.1039/JM9960601219
K ₂ NbO ₃ F	<i>I4/nmm</i>	RT	F	disordered	10.1021/j100813a025
Sr ₂ CuO ₂ F ₂	<i>I4/nmm</i>	RT	F	disordered	10.1103/PhysRevB.56.2831
Sr ₂ ScO ₃ F	<i>I4/mmm</i>	RT	F	disordered	10.1016/j.materresbull.2015.01.042

$\text{Sr}_2\text{FeO}_3\text{F}$	$P4/nmm$	RT	F	ordered	10.1021/j100801a011
$\text{Sr}_2\text{MnO}_3\text{F}$	$I4/nmm$	RT	F	disordered	10.1021/acs.inorgchem.5b02984
$\text{Sr}_2\text{NiO}_3\text{F}$	$I4/nmm$	RT	F	disordered	10.1021/ic402008n
$\text{Sr}_2\text{CoO}_3\text{F}$	$I4/nmm$	RT	F	disordered	10.1039/C0CC05482H
$\text{Ba}_2\text{TaO}_3\text{N}$	$I4/nmm$	298 K	N	disordered	10.1021/cm011738y
$\text{Ce}_2\text{AlO}_3\text{N}$	$I4/nmm$	N/A	N	disordered	10.1007/BFb0036504
$\text{Eu}_2\text{AlO}_3\text{N}$	$I4/nmm$	N/A	N	disordered	10.1007/BFb0036504
$\text{La}_2\text{AlO}_3\text{N}$	Hexagonal	RT	N	unknown	10.1016/0025-5408(95)00015-1
$\text{La}_2\text{AlO}_3\text{N}$	$I4/nmm$	N/A	N	disordered	10.1007/BFb0036504
$\text{La}_2\text{VO}_3\text{N}$	Hexagonal	RT	N	unknown	10.1016/0025-5408(95)00015-1
$\text{Nd}_2\text{AlO}_3\text{N}$	$I4mm$	RT	N	ordered	10.1016/j.jallcom.2011.02.138
$\text{Pr}_2\text{AlO}_3\text{N}$	$I4/nmm$	N/A	N	disordered	10.1007/BFb0036504
$\text{Sm}_2\text{AlO}_3\text{N}$	$I4/nmm$	N/A	N	disordered	10.1016/j.jallcom.2011.02.138
$\text{Sr}_2\text{NbO}_{3.28}\text{N}_{0.72}$	$I4/nmm$	RT	N	disordered	10.1021/ic049236k
$\text{Sr}_2\text{TaO}_3\text{N}$	N/A	Theoretical	N	both available	10.1039/c7cp06791g
$\text{Sr}_2\text{TaO}_3\text{N}$	$I4/nmm$	298 K	N	disordered	10.1021/cm011738y

TABLE A.2: Summary of statistics from varying bond valence parameters by 0.05 Å. The “GII minimized” and “DFT” label in the first column indicate from which step of the materials discovery procedure the structure originates. All values are in units of v.u.

	Actual value	Avg.	St. Dev.	Maximum	Minimum
Sr2ScO3F (GII minimized)	0.433	0.492	0.136	0.811	0.127
Sr2ScO3F (DFT)	0.245	0.352	0.096	0.605	0.173
Sr2AlO3F (GII minimized)	0.106	0.293	0.105	0.618	0.082
Sr2AlO3F (DFT)	0.221	0.348	0.132	0.754	0.118
Ba2ScO3F (GII minimized)	0.164	0.366	0.119	0.660	0.086
Ba2ScO3F (DFT)	0.154	0.296	0.085	0.588	0.127
Ba2InO3F (GII minimized)	0.277	0.352	0.096	0.605	0.173
Ba2InO3F (DFT)	0.205	0.315	0.092	0.646	0.155

TABLE A.3: Attempted syntheses for Sr₂AlO₃F and products identified from powder x-ray diffraction. Starting materials for all synthetic attempts were stoichiometric amounts of SrCO₃, SrF₂, and Al₂O₃. Products are in order of weight percent.

Conditions	Products
Ground and heated in a Pt crucible at 1050°C for 12 hrs in air, repeated 3 times	Sr ₃ Al ₂ O ₆ , Sr ₃ AlO ₄ F, SrF ₂ , Sr ₇ Al ₁₂ O ₂₅ , Sr ₉ Al ₅ O ₁₈
Ground and heated in Pt crucible at 1400°C for 4 hrs in air	Sample vaporized, no powder to analyze
Ground and heated in a Pt crucible at 1050°C for 12 hrs in Ar, repeated 2 times	SrF ₂ , Sr ₇ Al ₁₂ O ₂₅ , Sr ₃ AlO ₄ F
Ground and pressed into pellets. Heated in an alumina crucible with sacrificial powder at 950°C	Sr ₃ Al ₂ O ₆ , Sr ₃ AlO ₄ F, SrF ₂

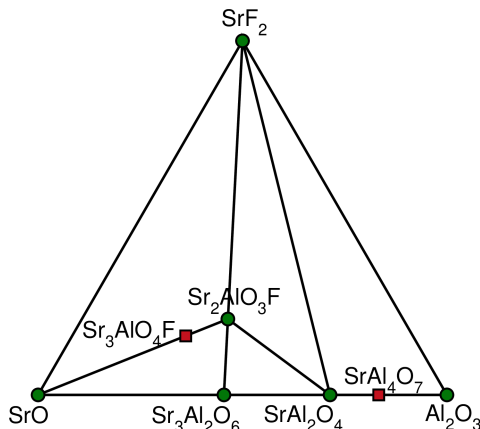


FIGURE A.1: The compound phase diagram from the binary phases, SrO, SrF₂, and Al₂O₃, which are used to create Sr₂AlO₃F. Green circles indicate that the compound is on the convex hull and red squares are above the hull. SrAl₄O₇ is 0.001 eV per atom above the hull and Sr₃AlO₄F is 0.172 eV per atom above hull.

Appendix B: Phase Transitions and Potential Ferroelectricity in Noncentrosymmetric KNaNbOF_5

We extracted the symmetry-adapted modes, Y_2^+ , Y_1^- , and Γ_2^- , from the fully relaxed $Pna2_1$ structure relative to the $Cmcm$ phase as described in the main text. These symmetry-adapted modes are energetically stable, indicating that these symmetry adapted modes are a linear combination of phonon eigenmodes with the same symmetry, but of different dynamical stability. We decomposed each symmetry-adapted mode, Q into its eigenvectors, e_i . Each mode has a different number of eigenvectors, n , with Y_2^+ , Y_1^- , and Γ_2^- having 7, 3, and 7 eigenvectors, respectively. The distortion mode of symmetry Q , u_Q , mode vector is described as:

$$u_Q = \sum_{i=1}^n a_i e_i$$

where a_i are coefficients. To more easily interpret the relative contributions of each mode, the coefficients were normalized such that the sum of their squares equals 1. A summary of the phonon frequencies and their linear combinations are show in Table B.1. In all cases, the unstable eigenmode contributes a significant amount to the symmetry adapted mode.

TABLE B.1: Summary of each eigenmode's contribution to the symmetry adapted modes using the force constant matrix of the $Cmcm$ phase.

Band no.	Y_2^+		Y_1^-		Γ_2^-	
	Freq. (cm^{-1})	a^2	Freq. (cm^{-1})	a^2	Freq. (cm^{-1})	a^2
1	69i	0.734	59i	0.951	38i	0.583
2	15	0.024	27i	0.016	0.1	0.000
3	105	0.056	239	0.034	43	0.004
4	143	0.155			112	0.020
5	247	0.006			134	0.337
6	288	0.007			195	0.028
7	515	0.020			260	0.028

TABLE B.2: Crystallographic information for the DFT relaxed structures of $Pna2_1$ (NCS) and $Cmcm$ (HT) structures of KNaNbOF_5 .

Atom	$Pna2_1$				$Cmcm$			
	Site	x	y	z	Site	x	y	z
		$a = 11.8868, b = 5.8746, c = 8.1581$				$a = 6.6179, b = 11.2953, c = 8.3046$		
K1	4a	0.5416	-0.0325	0.1160	4a	0	0	0
Na1	4a	0.1382	0.0509	0.3603	4c	0	0.3199	0.25
Nb1	4a	0.8491	-0.0410	0.3532	4c	0	0.6874	0.25
O1	4a	0.7221	0.0983	0.3109	4c	0	0.8448	0.25
F1	4a	0.8751	0.8509	0.1305	4c	0	0.5078	0.25
F2	4a	-0.0467	0.2154	0.3183	8g	0.2069	0.1624	0.25
F3	4a	0.8600	0.0388	0.5853	8f	0	0.6744	0.0169
F4	4a	0.7886	0.6650	0.4170				
F5	4a	0.0023	0.7838	0.3915				

TABLE B.3: Landau coefficients of the free energy expansion fit to DFT total energy calculations using different functionals.

	PBEsol	SCAN
$\alpha_{Y_2^+}$ (meV \AA^{-2})	-85.20	-96.01
$\alpha_{Y_1^-}$ (meV \AA^{-2})	-59.19	-76.38
$\alpha_{\Gamma_2^-}$ (meV \AA^{-2})	-10.21	-7.27
$\beta_{Y_2^+}$ (meV \AA^{-2})	46.80	75.86
$\beta_{Y_1^-}$ (meV \AA^{-2})	61.89	45.39
$\beta_{\Gamma_2^-}$ (meV \AA^{-2})	7.00	9.52
$\delta_{Y_2^+Y_1^-}$ (meV \AA^{-4})	56.46	51.59
$\delta_{Y_1^-\Gamma_2^-}$ (meV \AA^{-4})	8.50	6.32
$\delta_{\Gamma_2^-Y_2^+}$ (meV \AA^{-4})	7.85	7.01
$\gamma_{\Gamma_2^-Y_2^+Y_1^-}$ (meV \AA^{-3})	20.17	18.95

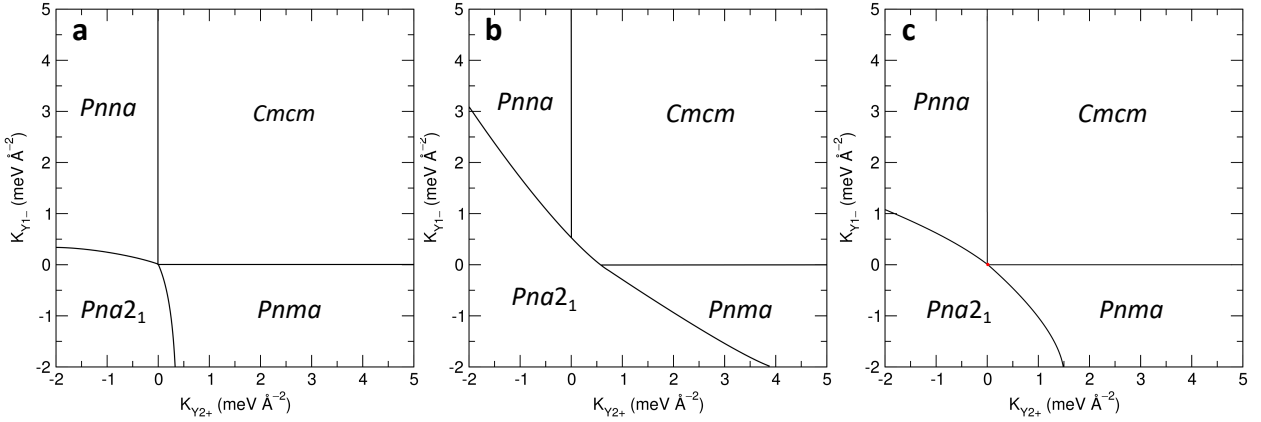


FIGURE B.1: Approximate phase diagrams of the transition upon parametrically changing the trilinear coupling coefficients $\gamma_{\Gamma_2^-Y_2^+Y_1^-}$ to be equal to **a** 15 meV \AA^{-3} , and **b** 27 meV \AA^{-3} . **c** Approximate phase diagram using Landau coefficients fit to SCAN energies. The third quadratic coefficient, $K_{\Gamma_2^-}$, is set to 0.6 meV \AA^{-2} , as described in the main text.

In the in-situ monitoring of the heating process (4 in the main text), a new ^{19}F peak resonating at -143.2 ppm appears at $\sim 360^\circ\text{C}$. This peak is assigned to an intermediate phase ($Pbcm$) in the irreversible reconstructive transition ($P4/nmm \rightarrow Cmcm$) on the basis of (1) $Pbcm$ is a proposed intermediate structure in the CS ($P4/nmm$) to HT ($Cmcm$) phase transition [7]; (2) the formation of the $Pbcm$ phase is detected at 358.8°C while the HT phase is not detected until 390°C (4 in the main text; further details below); (3) the same ^{19}F resonance is not detected at -143.2 ppm during cooling process (Figure B.8), which implies that the intermediate $Pbcm$ phase transition to $Cmcm$

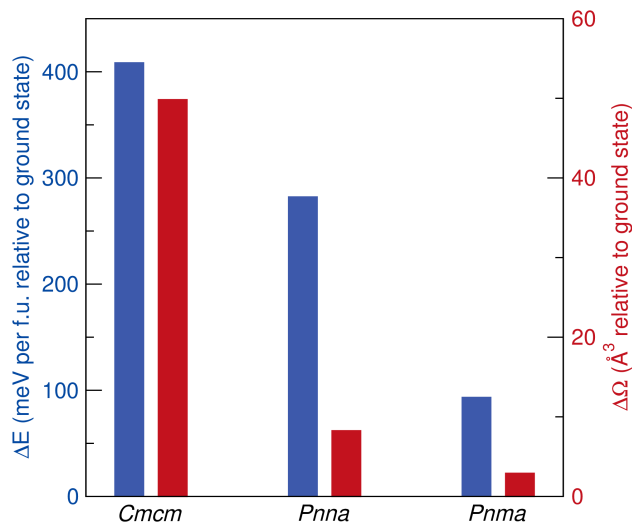


FIGURE B.3: Difference in energy (blue, left) and volume (red, right) between the various centrosymmetric phases of KNaNbOF_5 and the $Pna2_1$ phase.

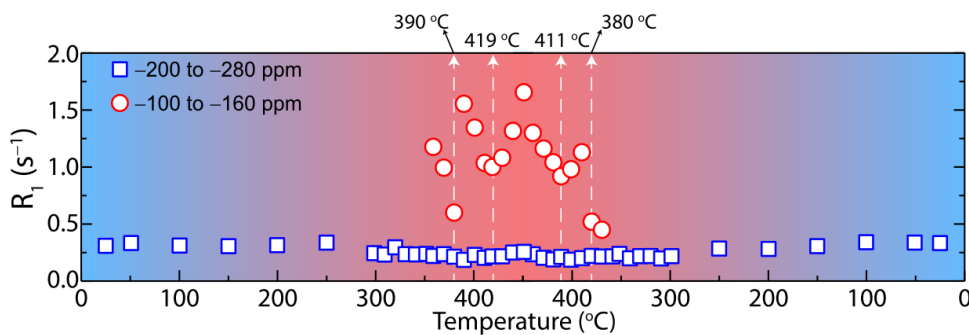


FIGURE B.4: In situ ^{19}F NMR spin-lattice relaxation rate ($R_1 = 1/T_1$) measurements on the NCS to HT phase transition upon heating (0°C to 450°C) and the HT to NCS transition upon cooling (450°C to 0°C) in KNaNbOF_5 . The apical F (blue square) experiences negligible motion as revealed by its unaltered ^{19}F T_1 throughout the measurements. In line with our previous studies [6], it suggests that the apical F_{NCS} ion stays as if it is static in the axial rotation about the $\text{F}_{\text{apical}}\text{-Nb-O}$ axis and no dynamic O/F disorder is expected for this fluoride ion. Note that the ^{19}F T_1 signals from the equatorial fluoride ions in the NCS phase is not traceable due to the interference of CSA. The jump in the ^{19}F T_1 signal (red circles) at $\sim 360^\circ\text{C}$ till about 390°C is associated with the reconstructive phase.

phase is not reversible, (4) the calculated ^{19}F NMR chemical shift of this signal at -140.6 ppm in the $Pbcm$ phase [6] is comparable with the experimental value at -143.2 ppm.

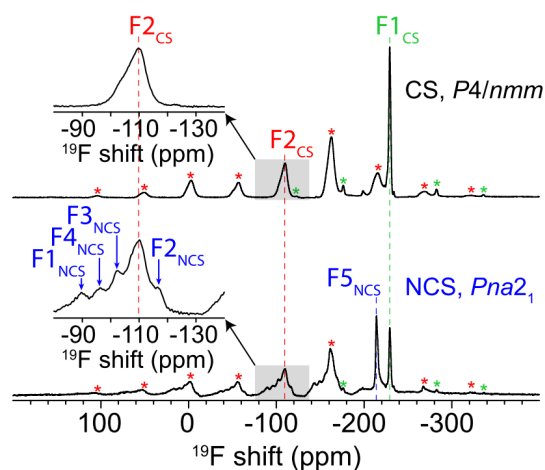


FIGURE B.5: High-resolution ^{19}F MAS (25 kHz) NMR spectra of noncentrosymmetric (NCS; bottom) and centrosymmetric (CS; top) KNaNbOF_5 . The assignment of ^{19}F NMR signals of CS KNaNbOF_5 can be found in literature. [6] Asterisks (*) denotes spinning side bands. Top panel is reproduced with permission from Chien, P.-H. et.al. Chem. Mater., DOI: 10.1021/acs.chemmater.0c01439. Copyright 2020 American Chemical Society.

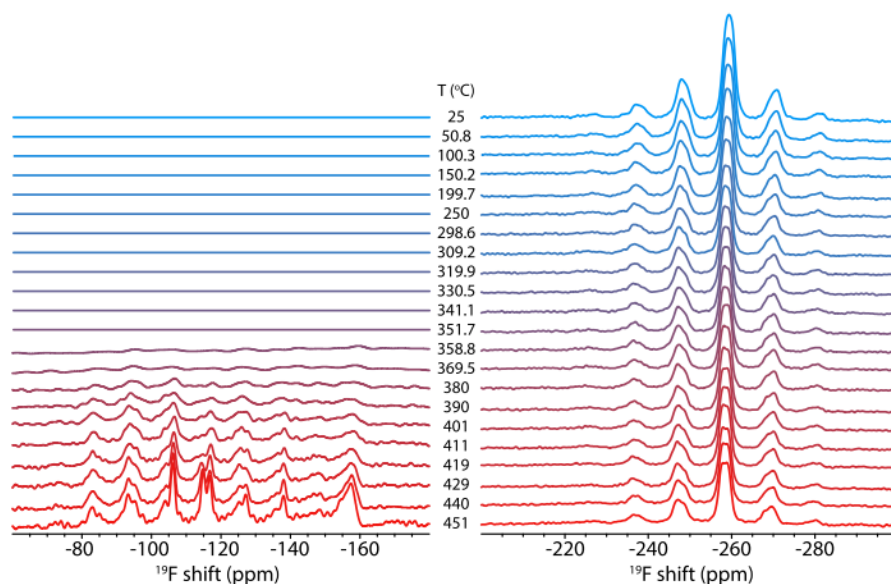


FIGURE B.6: In situ monitoring (cooling process) of the phase transition in KNaNbOF_5 from non-centrosymmetric (NCS) phase ($Pna2_1$) to the high-temperature (HT) phase ($Cmcm$) by variable-temperature ^{19}F MAS (5 kHz) NMR. Note that the ^{19}F resonance at -143.2 ppm is not identified at 358.8 °C (cf. Fig. 2). The removal of this ^{19}F chemical shift during the cooling process indicates that the reconstructive phase transition from $P4/nmm$ to $Cmcm$ (a secondary phase transition from the $P4/nmm$ polymorph of KNaNbOF_5 , not the focus of this article) is irreversible, as confirmed previously [6, 7].

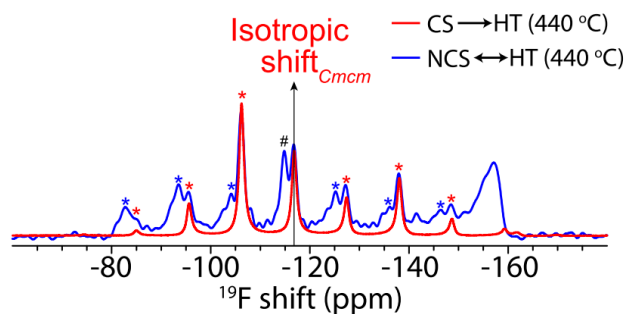


FIGURE B.7: ^{19}F MAS (5 kHz) NMR spectra of KNaNbO_5 acquired at 440 °C in different phase transition routes ($P4/nmm$ to HT and $Pna2_1$ to HT). The new signal (marked with # to indicate the isotropic shift) detected in the transition from NCS to HT route is shown in blue. Asterisks (*) denotes the spinning side bands.

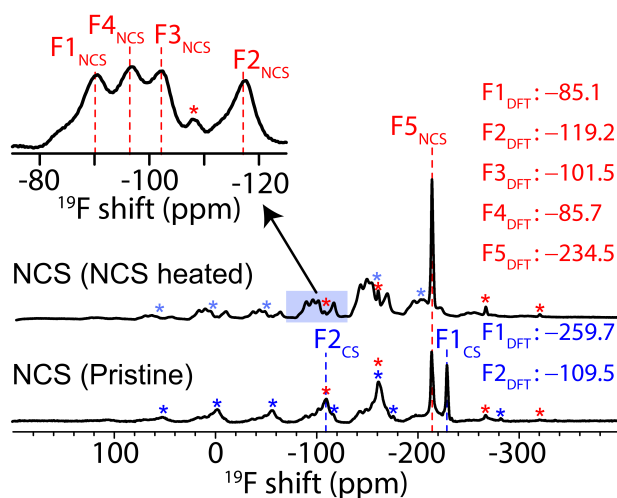


FIGURE B.8: High-resolution ^{19}F MAS (25 kHz) NMR spectra of $Pna2_1$ KNaNbO_5 before/after in situ high-temperature ^{19}F MAS NMR experiments. Calculated ^{19}F NMR chemical shifts are also shown for reference. Asterisks (*) denote spinning side bands.

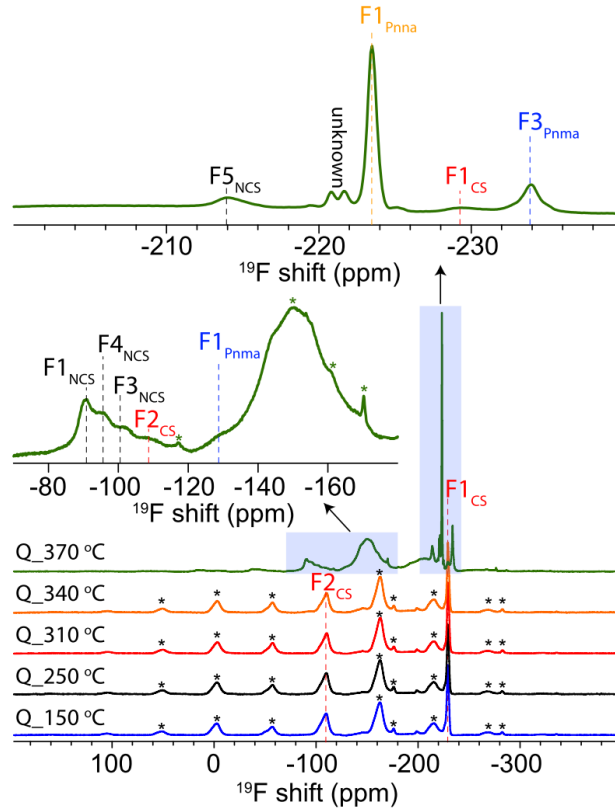


FIGURE B.9: High-resolution ^{19}F MAS (25 kHz) NMR spectra of the perovskite-derived polymorph of KNaNbOF_5 with symmetry $P4/nmm$ quenched at 150 °C, 250 °C, 310 °C, 340 °C, and 370 °C. Asterisks (*) denote spinning side bands. The spectra of the $P4/nmm$ samples quenched at 340 °C, 310 °C, 250 °C, and 150 °C do not show any additional phases other than the $P4/nmm$ phase. Multiple phases appear in the spectra of the sample quenched at 370 °C. In order of highest to lowest percentage of the sample, we see the $Pnna$, $Pnma$, NCS phases along with a small amount of remaining $P4/nmm$ sample. This is distinctive from the results of the NCS quenching experiment, as the $Pnna$ phase makes up by far the largest percentage of the sample when the $P4/nmm$ sample is quenched.

TABLE B.6: Summary of the calculated Born effective charges in KNaNbOF_5 in units of e at the DFT-PBESol level.

$Pna2_1$				$Pnma$			
Site	Z_{xx}	Z_{yy}	Z_{zz}	Site	Z_{xx}	Z_{yy}	Z_{zz}
K	1.19	1.33	1.20	K	1.19	1.30	1.25
Na	1.23	1.06	1.20	Na	1.19	1.09	1.22
Nb	4.15	4.35	4.36	Nb	4.17	4.32	4.29
O	-2.04	-1.20	-0.89	O	-2.01	-1.19	-0.83
F1	-0.58	-0.73	-1.86	F1	-1.11	-1.46	-0.70
F2	-1.19	-1.33	-0.71	F2	-0.66	-1.77	-0.62
F3	-0.67	-0.75	-1.72	F3	-1.65	-1.03	-0.84
F4	-0.72	-1.66	-0.73	F4	-0.60	-0.64	-1.89
F5	-1.58	-1.07	-0.87				

Appendix C: Heteroanionic Ruddlesden-Popper Ferroelectrics From Anion Order and Octahedral Tilts

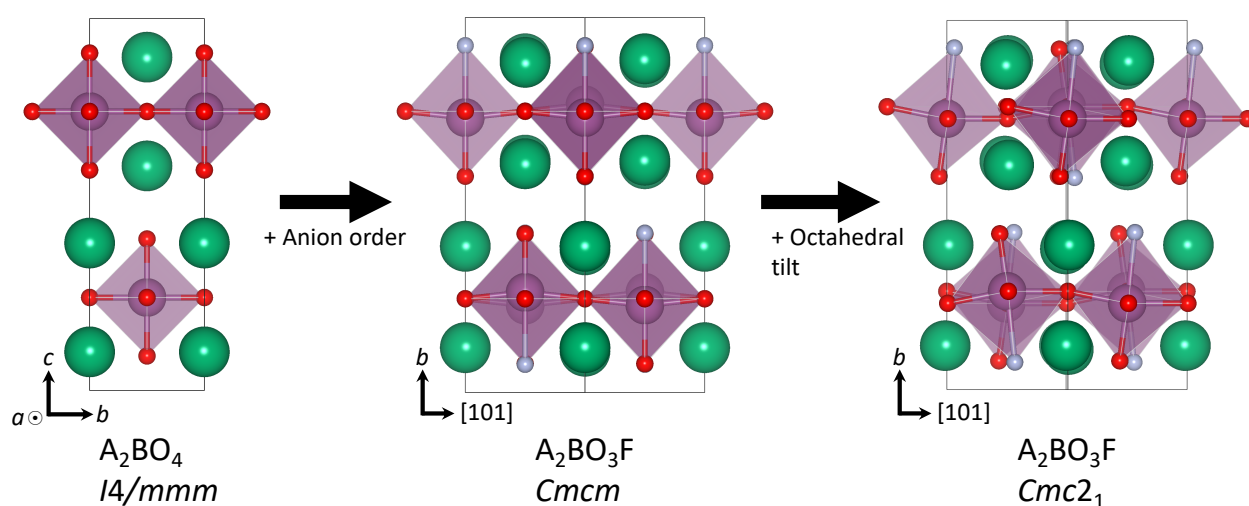


FIGURE C.1: Potential derivative structure path to obtain a polar phase ($Cmc2_1$) from a centrosymmetric anion ordered structure ($Cmcm$) from the homoanionic parent phase ($I4/mmm$). The polarization in the $Cmc2_1$ structure arises as the fluorides all move to the right while the apical oxides all move to the left. The calculated Berry phase polarizations for the relaxed polar structures are 2.70 and $2.58 \mu\text{C cm}^{-2}$ for the $Cmc2_1$ and $Pna2_1$ phases of $\text{Sr}_2\text{ScO}_3\text{F}$, respectively, and $4.82 \mu\text{C cm}^{-2}$ for the $Cmc2_1$ phase of $\text{Ca}_2\text{ScO}_3\text{F}$.

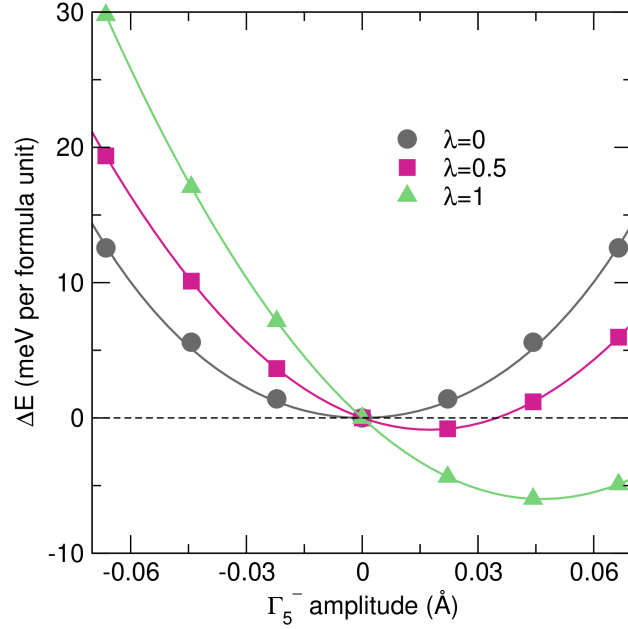


FIGURE C.2: Relative energies of the $\text{Sr}_2\text{ScO}_3\text{F}$ $Cmc2_1$ structure as a function of the polar (Γ_5^-) mode with varying amounts of a hybrid order parameter, $\lambda Q_{X_3^+} Q_{X_2^-}$.

TABLE C.1: The energetics of the prototypical anion ordered structures and their equilibrium structures relative to the highest energy anion order of $\text{Ca}_2\text{ScO}_3\text{F}$. $\Delta E_{\text{anion orders}}$ is the energy of the relaxed anion ordered structures relative to the highest energy anion ordered structure (intralayer antipolar). ΔE_{eq} (meV/f.u.) is the energy of the equilibrium structures relative to the highest energy anion ordered structure.

	$\Delta E_{\text{anion orders}}$ (meV/f.u.)	Equilibrium structure	ΔE_{eq} (meV/f.u.)
Polar	-117.4	Cm	-546.5
Interlayer antipolar	-204.8	$P\bar{4}2_1m$	-591.0
Intralayer antipolar	0	$P2_12_12_1$	-679.7

TABLE C.2: The energetics of the prototypical anion ordered structures and their equilibrium structures relative to the highest energy anion order of $\text{Sr}_2\text{ScO}_3\text{F}$. $\Delta E_{\text{anion orders}}$ is the energy of the relaxed anion ordered structures relative to the highest energy anion ordered structure (intralayer antipolar). ΔE_{eq} (meV/f.u.) is the energy of the equilibrium structures relative to the highest energy anion ordered structure.

	$\Delta E_{\text{anion orders}}$ (meV/f.u.)	Equilibrium structure	ΔE_{eq} (meV/f.u.)
Polar	-36.6	$P4_2cm$	-112.1
Interlayer antipolar	-76.0	$P\bar{4}2_1m$	-154.5
Intralayer antipolar	0	$Pna2_1$	-66.8

TABLE C.3: Separation of dipole-dipole and short-range contributions to the total change in energy in the Sr_2SnO_4 structure with tilts relative to the prototypical $I4/mmm$ structure.

	<i>Cmca</i>
Total change in energy (meV)	-25.9
Dipole-dipole contribution (meV)	8.3
Short-range contribution (meV)	-34.2

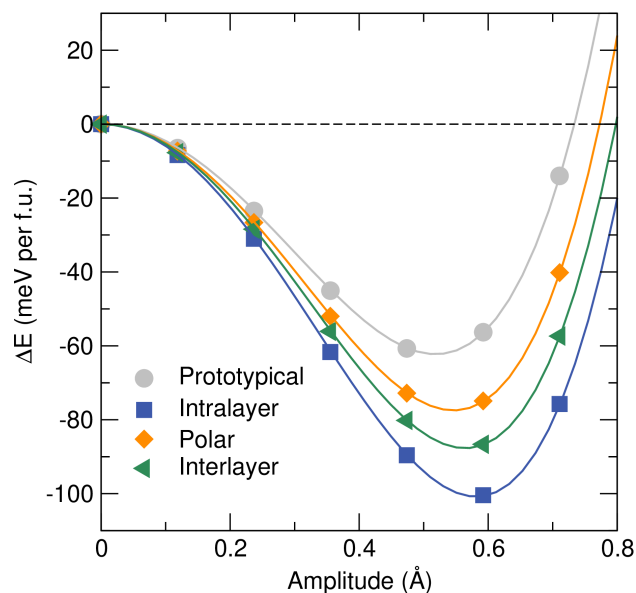


FIGURE C.3: Energetics of Ca_2TiO_4 with octahedral tilts. The anion order labels indicate the pattern of B -site displacements and all B -site displacements are 0.178 \AA .

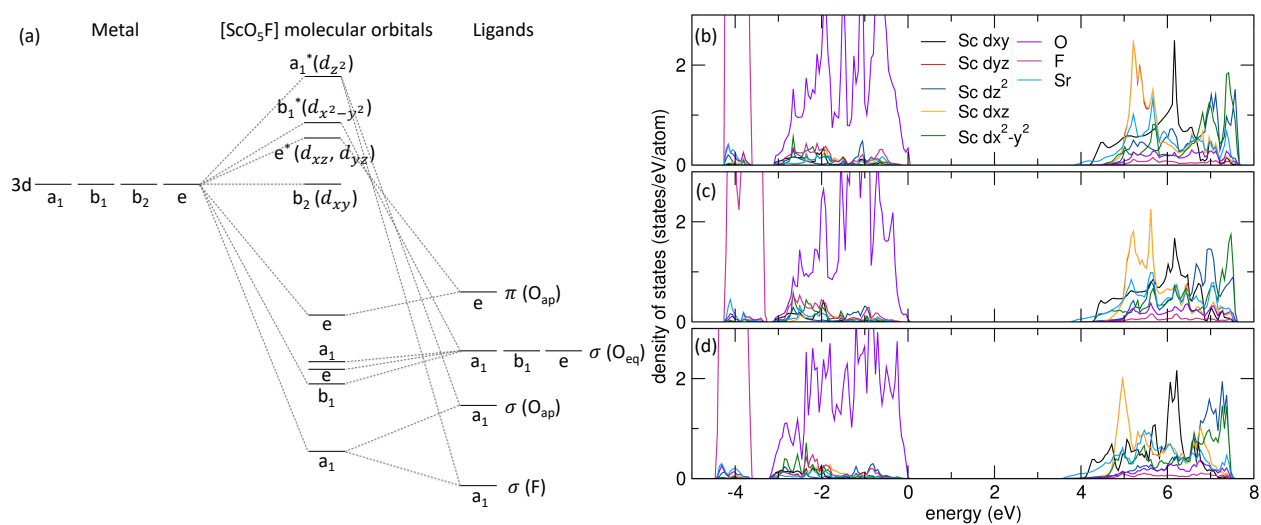


FIGURE C.4: (a) Schematic of the molecular orbital diagram for a $[\text{ScO}_5\text{F}]$ octahedra. The diagram is not drawn to scale. Partial density of states of the relaxed (b) polar, (c) interlayer, and (d) intralayer anion ordered structures of $\text{Sr}_2\text{ScO}_3\text{F}$ on a per atom basis.

Appendix D: Exploring the Phase Space of Epitaxially Strained $n = 2$ Ruddlesden-Popper Oxyfluorides

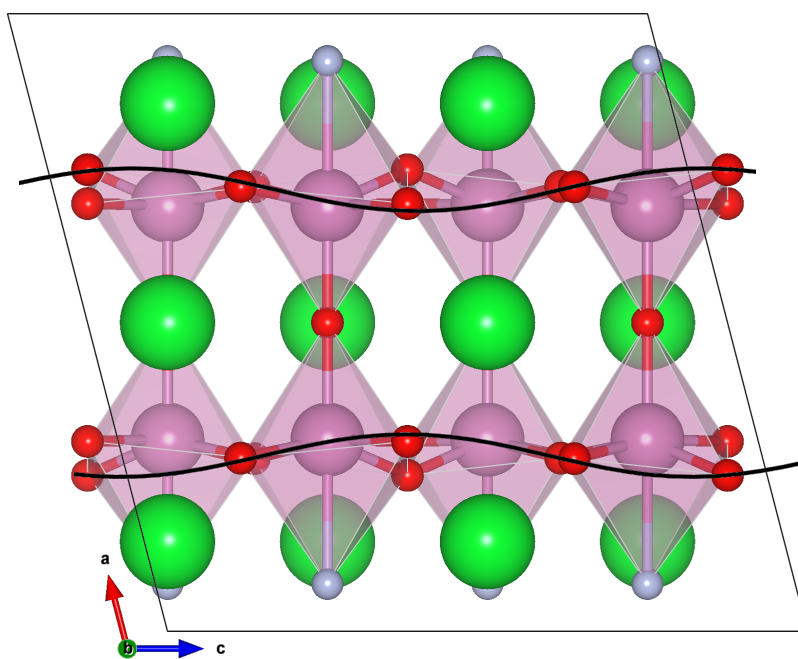


FIGURE D.1: Structure with condensed $A2$ mode from the $\text{Sr}_3\text{In}_2\text{O}_5\text{F}_2$ ground state $P2_1/c$ structure. The lines show the wave-like displacive modulation of the equatorial O ions in the foreground on the (101) plane.

TABLE D.1: Lowest energy phases obtained from derivative structure search of $\text{Sr}_3\text{In}_2\text{O}_5\text{F}_2$.

space group	ΔE (meV per formula unit)
$I4/mmm$	0.00
$P2_1/c$	-729.9
$P2_1$	-716.6
$Cmc2_1$	-700.8
$Pnma$	-695.6
Pm	-681.7
$P\bar{1}$	-674.5
$P2_1/c$	-673.7
Cc	-673.6
$P\bar{1}$	-670.5
$P2_1/m$	-667.4

TABLE D.2: Lowest energy phases obtained from derivative structure search of $\text{Sr}_3\text{In}_2\text{O}_5\text{F}_2$.

Space group	Irrep	Amplitude (\AA)	
		$P\bar{1}$	$P1$
$I4/mmm$	Γ_1^+	0.107	0.178
$Immm$	Γ_2^+	0.002	0.014
$P\bar{1}$	Γ_5^+	0.376	0.202
$I4mm$	Γ_3^-	-	0.048
$I\bar{4}m2$	Γ_4^-	-	0.005
Cm	Γ_5^-	-	0.355
$Cmmm$	X_1^+	-	0.010
$Cmca$	X_2^+	-	0.106
$Cmca$	X_3^+	-	0.003
$Cccm$	X_4^+	-	0.016
$Ccca$	X_1^-	0.173	0.160
$Cmcm$	X_2^-	0.002	0.200
$Cmcm$	X_3^-	1.328	1.282
$Cmma$	X_4^-	0.003	0.024
$P2_1/m$	$A1$	0.064	0.139
$P2_1/c$	$A2$	0.380	1.543

Appendix E: Investigating Insulator-Metal Transitions in Anion Disordered and Ordered TiOF

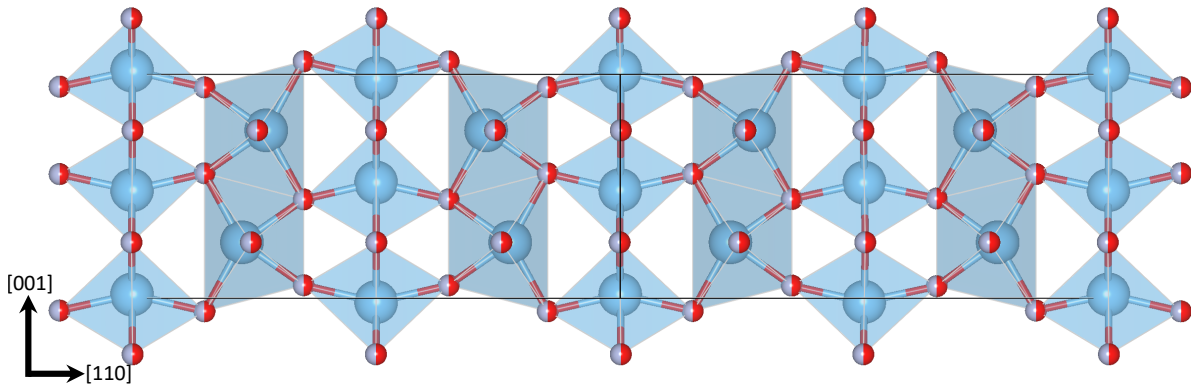


FIGURE E.1: Disordered TiOF with condensed instability at $k = (0.26, 0.26, 0.6)$ on a $4 \times 4 \times 2$ supercell. The distortions are exaggerated to make them clearer.

TABLE E.1: Energetics of alternative anion ordered configurations of TiOF. All structures have only *fac*-[TiO₃O₃] octahedral units.

space group	ΔE (meV per formula unit)	electronic state
$P2_1/c$	0.00	metallic
$P4_21m$	64.0	insulating
Cm	73.5	insulating
$Amm2$	117.8	metallic
$P2_1(1)$	123.8	metallic
$P2_1(2)$	169.6	metallic
Pc	177.6	metallic
$Pmc2_1$	191.9	metallic
$C2/m$	268.5	metallic

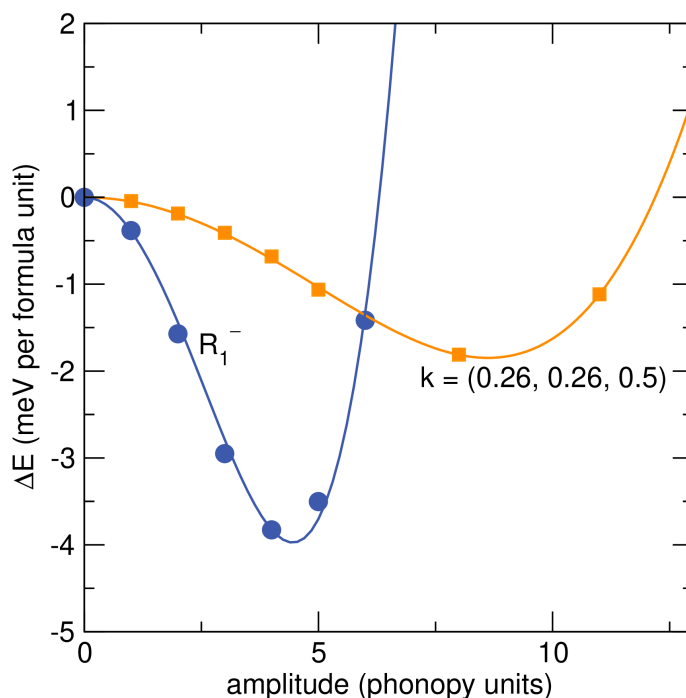


FIGURE E.2: Energetics of anion disordered TiOF structures modulated with the unstable phonon modes from VCA phonon dispersions.

This appendix contains a short description of the input files needed to perform VCA calculations in VASP, at this time the official VASP documentation does not have a guide on how to do this. A presentation with a how-to guide and the python scripts printed here can also be found in the MTD group share or in the archive. Disclaimer: As a general rule, the components of the VCA must have masses that are close to one another. However, thorough testing is needed to confirm that a VCA will accurately model your system.

The POSCAR for your VCA must duplicate the ionic positions of the VCA ions and add their associate element species. For our rutile TiOF, the POSCAR appears as follows:

```
TiOF rutile
1.0000000000000000
 4.6454683013242928  0.0000000000000000  0.0000000000000000
 0.0000000000000000  4.6454683013242928  0.0000000000000000
 0.0000000000000000  0.0000000000000000  3.0092011362285902
Ti   O   F
 2   4   4
Direct
0.0000000000000000  0.0000000000000000  0.0000000000000000
0.5000000000000000  0.5000000000000000  0.5000000000000000
```

```

0.2968582686327679  0.2968582686327679  0.0000000000000000
0.7031417063672336  0.7031417063672336  0.0000000000000000
0.2031417313672321  0.7968582936327664  0.5000000000000000
0.7968582936327664  0.2031417313672321  0.5000000000000000
0.2968582686327679  0.2968582686327679  0.0000000000000000
0.7031417063672336  0.7031417063672336  0.0000000000000000
0.2031417313672321  0.7968582936327664  0.5000000000000000
0.7968582936327664  0.2031417313672321  0.5000000000000000

```

In addition, the VCA weights must be added to the INCAR file. The weights for all ions must be specified (ie non-VCA ions must be 1.0). For TiOF, it appears as,

```
VCA = 1.0 0.5 0.5
```

If you want to calculate the phonons of a structure with VCAs, the Phonopy source code must be modified to take into account the mass of the virtual atom. In particular, `atoms.py` must be modified to add the virtual atom (which we name “Of” for TiOF) to the `atom_data`, `symbol_mat`, and `isotope_data` lists. The `atom_data` element must contained the weighted average of the VCA atom components. Additionally, if using the frozen phonon method and using Phonopy to create the displaced structures, you must use a virtual atom POSCAR for it to work. (N.B. I did not try the density functional perturbation theory with the VCA) The TiOF virtual atom POSCAR is as follows:

TiOF for Phonopy

```

1.0000000000000000
  4.6454683013242928  0.0000000000000000  0.0000000000000000
  0.0000000000000000  4.6454683013242928  0.0000000000000000
  0.0000000000000000  0.0000000000000000  3.0092011362285902

```

```

Ti   Of
  2   4

```

Direct

```

0.0000000000000000  0.0000000000000000  0.0000000000000000
0.5000000000000000  0.5000000000000000  0.5000000000000000
0.2968582686327679  0.2968582686327679  0.0000000000000000
0.7031417063672336  0.7031417063672336  0.0000000000000000
0.2031417313672321  0.7968582936327664  0.5000000000000000
0.7968582936327664  0.2031417313672321  0.5000000000000000

```

The procedure to calculate phonons with the VCA is as follows (custom scripts to automate these steps are shown in parentheses and can be found in the MTD group share drive):

1. Start with the virtual atom POSCAR
2. Proceed as normal in creating the displaced POSCAR
3. Edit the displaced POSCARs so that the VCA can run in VASP (`make_vasp_VCA_files.sh`)
4. Run self-consistent calculations using the VCA tag
5. Create `FORCE_SETS` using a custom script, which automatically determines the net forces on the virtual atoms (`VCA_force_sets.py`)
6. From here, postprocessing is as usual

Vita

Publications before PhD

1. S. H. Donaldson, M. Valtiner, M. A. Gebbie, **J. Harada**, J. N. Israelachvili. Interactions and visualization of bio-mimetic membrane detachment at smooth and nano-rough gold electrode surfaces. *Soft Matter*. 9 (2013) 5231-5238 [doi]
2. M. C. Kemei, **J. K. Harada**, R. Seshadri, M. R. Suchomel. Structural change and phase coexistence upon magnetic ordering in the magnetodielectric spinel Mn_3O_4 . *Phys. Rev. B*. 90 (2014) 064418 [doi]
3. K. Kristiansen, P. Stock, T. Baimpos, S. Raman, **J. K. Harada**, J. N. Israelachvili, M. Valtiner. Influence of molecular dipole orientations on long-range exponential interaction forces at hydrophobic contacts in aqueous solutions. *ACS Nano*. 8 (2014) 10870-10877 [doi]
4. M. W. Gaultois, M. C. Kemei, **J. K. Harada**, R. Seshadri. Rapid preparation and magnetodielectric properties of trirutile Cr_2WO_6 . *J. Appl. Phys.* 117 (2015) 014105 [doi]
5. L. Ghadbeigi, **J. K. Harada**, B. R. Lettiere, T. D. Sparks. Performance and resource considerations of Li-ion battery electrode materials. *Energy Environ. Sci.* 8 (2015) 1640-1650 [doi]
6. **J. K. Harada**, L. Balhorn, J. Hazi, M. C. Kemei, R. Seshadri. Magnetodielectric coupling in ilmenites $M\text{TiO}_3$ ($M = \text{Co}, \text{Ni}$). *Phys. Rev. B*. 93 (2016) 104404 [doi]

Publications during PhD

1. **J. K. Harada**, N. Charles, K. R. Poeppelmeier, J. M. Rondinelli. Heteroanionic Materials by Design: Progress Towards Targeted Properties. *Adv. Mater.* 31 (2019) 1805295. [doi]
2. **J. K. Harada**, K. R. Poeppelmeier, J. M. Rondinelli. Predicting the Structure Stability of Layered Heteroanionic Materials Exhibiting Anion Order. *Inorg. Chem.* 58, 19 (2019) 13229-13240. [doi]
3. G. Gou, M. Zhao, J. Shi, **J. K. Harada**, J. M. Rondinelli. Anion Ordered and Ferroelectric Ruddlesden–Popper Oxynitride $\text{Ca}_3\text{Nb}_2\text{N}_2\text{O}_5$ for Visible-Light-Active Photocatalysis. *Chem. Mater.* 32, 7 (2020) [doi]
4. P.-H. Chien,* **J. K. Harada**,* H. Liu, S. Patel, C. Huang, J. M. Rondinelli, K. R. Poeppelmeier, Y.-Y. Hu. Microscopic Insights into the Reconstructive Phase Transition of KNaNbOF_5 with ^{19}F MAS NMR Spectroscopy. *Chem. Mater.* 32, 13 (2020) 5715-5722. [doi]
* Co-first authors
5. K. Chatterjee, R. D. Rios, **J. K. Harada**, J. K. Mathiesen, S. L. A. Bueno, K. M. Ø. Jensen, J. M. Rondinelli, V. Dravid, S. E. Skrabalak. Durable Multimetal Oxychloride Intergrowths for Visible Light-Driven Water Splitting. *Chem. Mater.* 33, 1 (2021) 347-358 [doi]
6. F. Ding, N. Charles, **J. K. Harada**, C. D. Malliakas, C. Zhang, M. L. Nisbet, W. Zhang, P. S. Halasyamani, V. P. Dravid, J. M. Rondinelli, K. R. Poeppelmeier. K_3TiOF_5 Exhibits an Incommensurate Structure Induced by Octahedrally Coordinated Potassium Ions. *In preparation*
7. **J. K. Harada**, K. R. Poeppelmeier, J. M. Rondinelli. Designing heteroanionic Ruddlesden–Popper ferroelectrics through the coupling of anion orders and covalently-driven octahedral tilts. *In preparation*
8. **J. K. Harada**, P.-H. Chien, H. Liu, S. Patel, C.-H. A. Chen, N. Charles, Y.-Y. Hu, K. R. Poeppelmeier, J. M. Rondinelli. Investigations of Switchable Ferroelectricity and the Sequence of Phase Transitions in Noncentrosymmetric KNaNbOF_5 . *In preparation*

9. **J. K. Harada** & J. M. Rondinelli. Effects of Epitaxial Strain on the Lattice Dynamics of $A_3\text{In}_2\text{O}_5\text{F}_2$ (A=Sr, Ba). *In preparation*